Electro-Optic Effects in Multiple Quantum Well GaAs/AlGaAs Stripe Waveguides.

A Thesis submitted to the
Faculty of Engineering of the
University of Glasgow for the degree of
Doctor of Philosophy by

John Andrew Jennings M.Sc., B.Sc. (A.R.C.S.)

August 1990

SUMMARY.

The quantum confined Stark effect (QCSE) has been studied in multiple quantum well GaAs/AlGaAs, with a large electric field (10^5V/cm) applied in a direction normal to the plane of the wells, concentrating on the associated electro-absorption and electro-optic effects at wavelengths close to the excitonic absorption edge. The electro-optic effect has been resolved into two components: the linear electro-optic (LEO) effect and electro-refraction which manifests as a quadratic electro-optic (QEO). The LEO has been shown to be quantitatively very similar to bulk GaAs. The LEO coefficient $r_{63} = -1.75 \times 10^{-12}$cm/V in MQW with 8.5nm wide wells and barriers for light polarised parallel to the plane of the wells and shows no wavelength dependance for photon energies in the range 105meV to 34meV from the excitonic absorption edge. The effect is absent for light polarised perpendicular to the plane of the wells. The QEO, however, is seen to be very different to that observed in bulk GaAs, with the QEO dominating the electro-optic effect. There is an increase in the QEO coefficient s_{33} of two orders of magnitude, from 1×10^{-20}m^2/V^2 to 140×10^{-20}m^2/V^2 over the range of wavelengths from 105meV to 34meV below the lowest energy exciton. Below the band gap, the QEO is dominated by the Stark shift of the lowest energy exciton.

Stripe waveguide modulator devices in MQW GaAs/AlGaAs material compatible with integration of diode lasers have been fabricated. A directional coupling switch in MQW GaAs/AlGaAs material has allowed the enhanced electro-optic effect in the material to be utilised, without experiencing the large electro-absorption in the material associated with the QCSE. The device operates at low voltages (≈4volts) and can give an on/off ratio of 30dB. Photocurrent spectroscopy on samples have shown a shift of the e1-hh1 and e1-lh1 exciton transitions which is quadratic with electric field strength and demonstrated the dominance of forbidden transitions in the absorption spectrum at large electric field strengths.

Acknowledgements.

I would like to thank Professor J. Lamb for the use of the facilities in the Department of Electronics and Electrical Engineering and the support given during my PhD, and I must also thank my supervisor Professor C.D.W. Wilkinson. Financial support during the PhD was from SERC and also BTRL through a CASE award, with industrial supervisor Dr. Ian Henning who encouraged me through out the PhD.

The excellent technical support in the department must be acknowledged: Andy Stark, Dave Gourlay and Helen Wallace in the USSL lab, Jimmy Young and Dave Clifton for making dry etching and evaporations more fun, Lois Hobbs for 'running a tight ship' in the cleanroom and Robert Harkins for prompt manufacture of photolithography masks.

I am indebted to Ray Hutchins; without his moral support and and assistance when times were hard, this work would not been finished and the thesis would never have been written. The understanding of the theoretical parts of the work was made possible for me with the help of John Davies through lectures and discussions for which I am very greatful. The labo rious proof reading by Ray Hutchins, John Davies and John Marsh was greatly appreciated. Liaising with Chris has been made a great deal easier with the help of Catherine Parker who has always been supportive.

Life in the department would not have been the same without the companions in my office: Ken Thomas, Jim Adams and Scott McMeekin (who shared the pains of writing a thesis), Robert Lind (who's help in printing and distributing chapters to the "proof readers" was greatly appreciated) and Rory McLeod. I thank Bindi Bhumbra for the use of computer modelling programs and practical help, and also Iain Thaine for his enthusiasm. In the early days of this PhD, encouragement from Kim Lee and Clive Reeves was a great help.

The second half of this thesis was written in Dublin where Ali was suffering the same agonies in writing a thesis; the support given from her was much needed. It is the support from Mary that has kept me going throughout the time of writing this thesis.

Finally, my parents have been a great source of support through my life in education and I can never thank them enough.

CONTENTS

Chapter 3.

Multiple Quantum Well Waveguide Design,

Material Characterisation and

Initial Waveguide Analysis.

Chapter 4
Electro– Absorption In MQW GaAs/AlGaAs.

Chapter 5
Electro– Optic Effects in Multiple Quantum well Stripe Waveguides.

Chapter 6
Electro– Optic Directional Coupling Switch.

Chapter 1
INTRODUCTION.

Present optical fibre communication systems operate at speeds in excess of 200MHz by modulating the output of the light source, a laser diode. Although acceptable modulation is achieved using this method it is not the ideal method. This is partly because amplitude modulating the laser diode leads to frequency modulation (otherwise known as chirp) in the laser output, which is undesirable in spectral regions where the fibre has non zero dispersion. For coherent communication systems, a well defined laser frequency and narrow linewidth is required and the laser is best operated c.w. with an external modulator.

The desire to improve the operating capabilities of fibre optic communication systems and develop the technology of integrated optics has generated a great deal of interest in the optical properties of multiple quantum well (MQW) material. The 2 dimensional density of states of the material and the presence of excitons at room temperature leads to a steep optical absorption edge in the material, which is advantageous to the performance of absorption modulators. Also, the enhanced electro–optic and electro–absorption effects exhibited as a result of the quantum confined Stark effect (QCSE) have potential for the development of electro–optic devices. Devices of interest include amplitude modulators which utilise the enhanced electro–absorption, allowing the laser to be operated c.w. This removes the problem of chirp in the diode laser output, allowing the data rate in fibre systems to be increased. The enhanced electro–optic effect can also be utilised in phase modulators, which have applications in coherent communications.

However, in an absorption modulator, the large refractive index changes (Δn) associated with the changes in absorption ($\Delta\alpha$) introduces its own component of chirp in the propagating pulse. Conversely, the $\Delta\alpha$ associated with the Δn in the phase modulators leads to amplitude modulation in the phase modulated signal. The electro–absorption and electro–refraction experienced in MQW waveguide devices therefore have to be fully characterised in order to develop external modulators.

In the work presented in this thesis, both electro–absorption modulator and phase modulator devices have been studied in a stripe waveguide configuration which is compatible with present laser diode and fibre optic systems. Present epitaxial techniques of III–V semiconductors are most advanced in the AlGaAs material and although the operating wavelength does not coincide with the low loss and low

dispersion wavelengths of 1.3μm (which is used in present optical fibre communication systems) and 1.55μm (which is at present being considered for the next generation of fibre systems), devices have potential applications in short distance communication such as data transfer between boards or computer networks. The aim of this work has been to characterise both electro–absorption and electro–refraction in MQW GaAs/AlGaAs stripe waveguides at wavelengths close to the excitonic absorption edge.

The structure of the thesis is set out below. The basic optical properties of MQW GaAs/AlGaAs are discussed in chapter 2, concentrating on the excitonic effects and the effect of an electric field on the optical properties of the material which were exploited in waveguide devices. The design of the waveguide structures, characterisation of the grown wafers and fabrication of the active stripe waveguides is described in chapter 3. Investigations of the electro–absorption and electro–optic properties of MQW GaAs/AlGaAs waveguide devices are described in chapters 4 and 5 respectively. To take advantage of the enhanced electro–optic effect in the MQW material, as demonstrated in chapter 5, an electro–optic directional coupling switch was designed. The device operation, fabrication and characterisation are presented in chapter 6. A conclusion of the main results is given at the end of each chapter. However, general concluding remarks and recommendations for further work are presented in chapter 7.

Chapter 2
MULTIPLE QUANTUM WELL STRUCTURES.

Section 2.1 INTRODUCTION.

This thesis reports on an experimental study of the electro-optic properties of multiple quantum well (MQW) GaA. /AlGaAs waveguides. Before describing the specific waveguide devices and electro-optic effects being studied, this chapter gives an introduction to the optical properties of quantum well structures in III-V semconductors, concentrating on the GaAs/AlGaAs system and properties relavent to the experimental work carried out. To begin, the band structure of bulk GaAs material is studied in section 2.2 before discussing the optical properties of multiple quantum well material. The model for a single, finite potential well is presented, followed by a discussion of the optical absorption of quantum well GaAs/AlGaAs material. Within the discussion, the excitonic features and effects of the band structure of GaAs on the material properties are discussed.

The electro-optic devices studied in this thesis are based upon the quantum confined Stark effect (QCSE) [Miller et al '84], an effect observed in quantum well material when a large D.C. electric field (10^5V/cm) is applied to the quantum well layers. The QCSE is discussed in section 2.4 and finally the associated electro-optic effect as applied to III-V materials is discussed in section 2.5

Section 2.2 BAND STRUCTURE OF GALLIUM ARSENIDE.

As a direct band-gap III-V semiconductor, Gallium Arsenide (GaAs) has become an important material in optoelectronics. This section gives a brief description of the band structure of GaAs, concentrating on the features that are of importance to the optical properties of the material. The band structure of GaAs obtained from a pseudopotential calculation [Chelikowski et al '76] is shown in figure 2.1.

The most important feature of the band structure of GaAs in terms of its optical properties is the coincidence of the minimum of the conduction band (Γ_6 point) and the maximum of the valence band (Γ_8 point) at $k=0$, making GaAs a direct band gap semiconductor. The conduction band of GaAs is a non degenerate band (excluding spin) and also parabolic and isotropic near $k=0$. Thus the energy of the band, measured from the top of the valence band, as a function of k is:

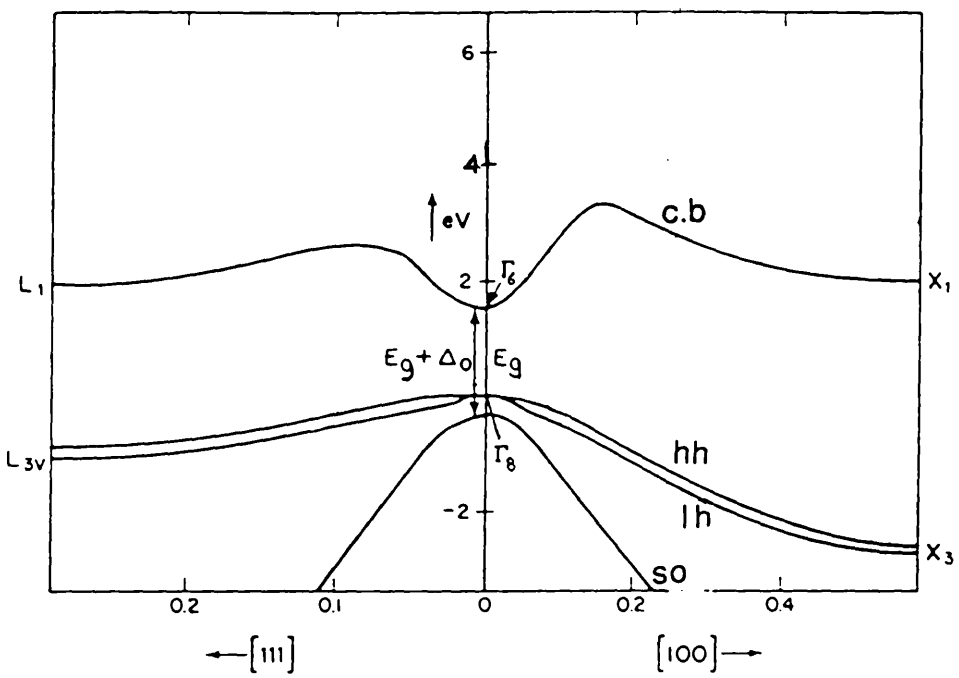

Figure 2.1
Band structure of Gallium Arsenide, showing the conduction band (cb), heavy hole (hh) and light hole (lh) valence bands and the split-off (so) band.

$$\epsilon(k) = \epsilon_g + \frac{\hbar^2 k^2}{2m^*} \qquad (2.1)$$

where ϵ_g is the band gap energy, $\hbar$ is Plank's constant divided by 2π and m^* is the electron effective mass given by:

$$m^* = \frac{1}{\hbar^2} \frac{d^2\epsilon}{dk^2} \qquad (2.2)$$

Because of the parabolic nature of the conduction band, the effective mass of electrons near k= 0 can be considered to be constant. Away from k= 0, the band becomes non parabolic and there are other minima at the edge of the Brillouin zone at the L and X points. These minima have higher energies than the Γ_6 minimum in GaAs. However, as a general trend in III– V semiconductors, the heavier the cation, the more likely it is to find the conduction band minimum at the Γ point [Bastard '88]. Thus, inclusion of Al in the Ga sites forming $Ga_xAl_{1-x}As$ lifts the Γ_6 minimum relative to the X minimum, such that for x= 0.41 the material becomes indirect [Oelgart et al '87].

The band structure of the valence band of GaAs is more complicated than the conduction band. In the absence of spin– orbit coupling, the valence band is 6– fold degenerate (including spin). Of these 6 states, four have total angular momentum J= 3/2 and z components J_z= ±3/2 and J_z= ±1/2 and the remaining two have J= 1/2 and J_z= ±1/2. The latter band is depressed in energy by an amount Δ_0 relative to the J= 3/2 bands due to spin– orbit coupling, giving rise to the split– off (so) band (Γ_7) which lies 350meV below the Γ_8 maximum [Pankove '71]. The two J= 3/2 bands remain degenerate at k= 0, but are non– degenerate at k≠0 because of the different band curvatures. These different band curvatures in turn lead to different effective masses for holes in the two bands. The J_z= ±3/2 band, having the smaller curvature, is refered to as the heavy hole (hh) and the J_z= ±1/2 band is refered to as the light hole (lh).

The dispersion of the valence bands are often approximated to being parabolic near k= 0, though in reality they are highly non parabolic even close to k= 0 [Bastard et al '86]. However, within the parabolic band approximation, the carriers in the hh and lh bands are assigned effective masses as summarised in table 2.1 [Thomas et al '86]:

Band	Effective Mass
Conduction Γ_6	$0.067m_0$
Valence hh	$0.47\ m_0$
Valence lh	$0.082m_0$
Valence so	$0.16\ m_0$

Table 2.1: Effective mass of carriers in the bands of GaAs.

It is worth while noting that these effective mass values refer to the values associated with motion in the crystal direction [100] and that for motion in the pependicular direction the effective mass of the hh is in fact less than that of the lh.

Section 2.3 QUANTUM WELL MODELLING.

Section 2.3.1 Finite Potential Well.

To introduce the ideas of multiple quantum well structures in III– V semiconductors, it is useful to begin by discussing the solutions to the time independent Schroedinger equation for a finite potential well. Consider the single potential well of depth V_0 and width 'a' with confinement in the z direction as shown in figure 2.2.

$$H\ \psi(z) = E\ \psi(z) \qquad (2.3)$$

where $\psi(z)$ is the wavefunction of the particle in the potential well such that $|\psi(z)|^2$ gives the probability of the particle being at position 'z' and E is the energy of the particle, measured from the bottom of the well. The Hamiltonian H of the potential well is given by:

$$H = \frac{\hbar^2}{2m^*}\ \frac{\partial^2}{\partial z^2} + V(z) \qquad (2.4)$$

where m^* and $\hbar$ are the effective mass of the particle and Planks constant divided by 2π respectively and the potential V(z) is defined as:

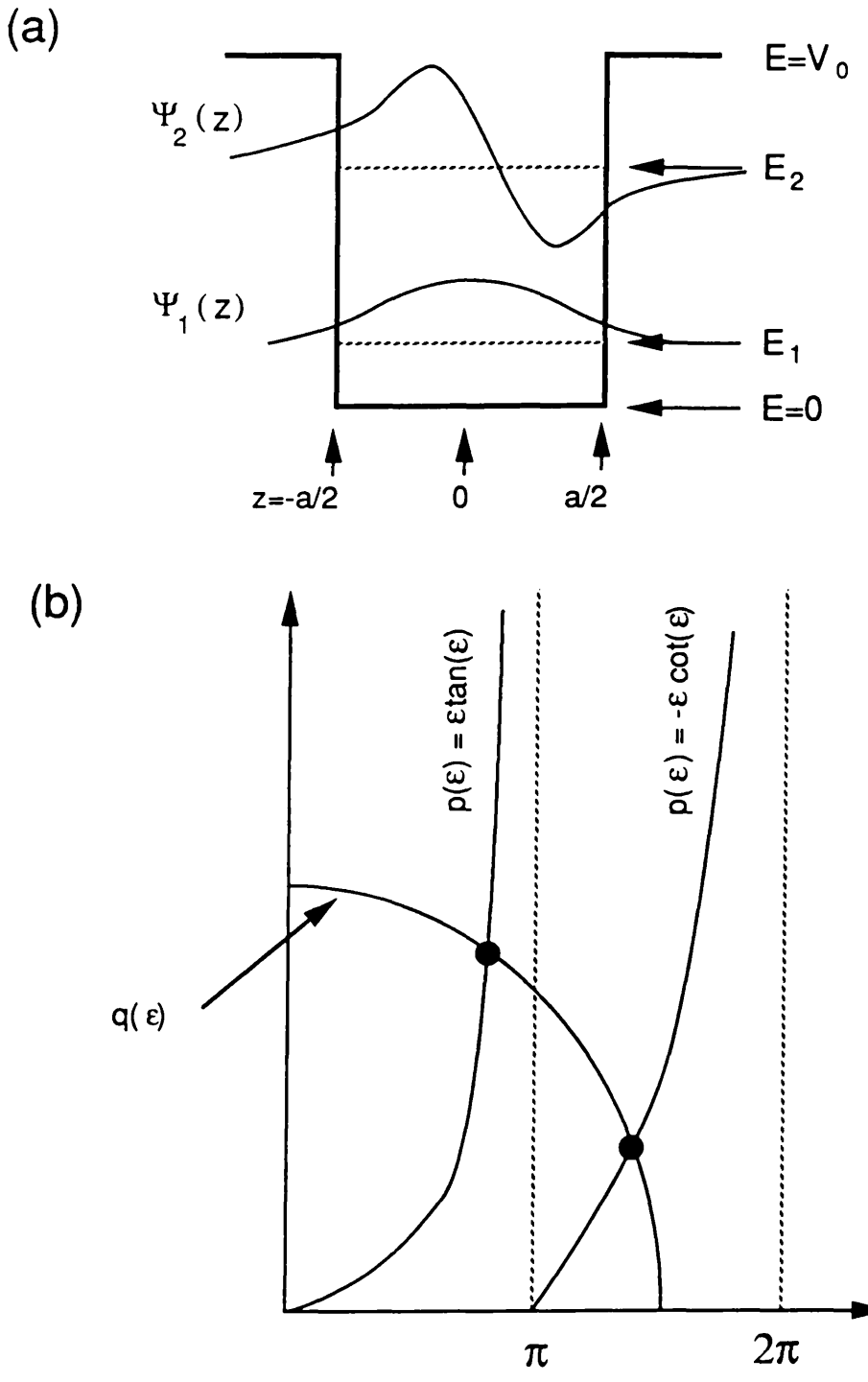

Figure 2.2
(a) Schematic diagram of a finite square potential well of depth V_0 and width 'a'. The eigenfunctions and energy eigenvalues of the lowest two energy states (n=1 and 2) are shown.

(b) Graphical solution of the single finite potential well model, showing the functions $p(\varepsilon)$ and $q(\varepsilon)$. The two intersection points of the graphs give the energy eigenvalues, this particular example having two confined states.

$$V(z) = 0 \qquad |z| < a/2$$
$$= V_0 \qquad |z| > a/2.$$

Solving equation 2.4 for the three regions of the potential well yields the solutions:

$$\psi(z) = A \exp(k_2 z) \qquad z < -a/2 \qquad (2.5a)$$
$$\psi(z) = C \sin(k_1 z) + D \cos(k_1 z) \qquad |z| < a/2 \qquad (2.5b)$$
$$\psi(z) = F \exp(-k_2 z) \qquad z > a/2. \qquad (2.5c)$$

where A, C, D, and F are arbitrary constants set by the boundary conditions of the system. The negative exponential term for $z < -a/2$ and positive exponential for $z > a/2$ have been dropped to ensure that $\psi(z)$ is finite at all values of z. The constants k_1 and k_2 are given by:

$$k_1 = [2m^* E]^{\frac{1}{2}}/\hbar \qquad (2.6a)$$
$$k_2 = [2m^*(V_0 - E)]^{\frac{1}{2}}/\hbar \qquad (2.6b)$$

The wave functions of particles confined to the potential well are therefore standing waves in the region of the potential well, with exponentially decaying amplitudes in the potential barriers. Taking into account the symmetry of the potential well, the solutions must be either symmetric or antisymmetric about $x = 0$. The boundary conditions that the wavefunction and its first derivative must be continuous at all values of z, coupled with the symmetry of the solutions, leads to 4 equations which can then be expressed as two transcendentals, eliminating the arbitrary constants:

$$k_1 \tan\left[\frac{k_1 a}{2}\right] = k_2 \qquad (2.7a)$$
$$-k_1 \cot\left[\frac{k_1 a}{2}\right] = k_2 \qquad (2.7b)$$

Since equations 2.7 (a) and (b) cannot be satisfied simultaneously, k_1 and k_2 must be solved graphically or numerically. The result is a set of symmetric eigenfunctions from solving 2.7a and an antisymmetric set of eigenfunctions from solving 2.7b. Considering the symmetric solutions first, the eigenfunctions are of the form:

$$\psi(z) = B \cos(k_1 z) \qquad |z| < a/2 \qquad (2.8a)$$
$$\psi(z) = B' \exp[k_2(a/2 - |z|)] \qquad |z| < -a/2 \qquad (2.8b)$$

Similarly the antisymmetric eigenfunctions, which result from solving 2.7b are of the form:

$$\psi(z) = A \sin(k_1 z) \qquad |z| < a/2 \qquad (2.9a)$$

$$\psi(z) = -A' \exp[\, k_2(a/2-z)\,] \qquad z < -a/2 \qquad (2.9b)$$

$$\psi(z) = A' \exp[\, -k_2(a/2-z)\,] \qquad z > a/2 \qquad (2.9c)$$

where $A' = A\sin(k_1 a/2)$

$B' = B\cos(k_1 a/2)$

and the constants A and B normalise the eigenfunctions. The normalised eigenfunctions form a complete orthogonal set, thus forming an orthonormal basis set, a property which becomes important when discussing transition rules in a quantum well semiconductor. In order to fully solve the eigenvalue problem, the eigenvalues E of equation 2.3 must be evaluated either graphically or numerically. The graphic solutions will be discussed here to illustrate the features of the potential well. Substituting the full expression for k_1 and k_2 into equation 2.7a and multiplying by a/2 leads to the equation:

$$\sqrt{[\, m^* E a^2/2\hbar^2 \,]} \tan[\, \sqrt{(m^* E a^2/2\hbar^2)} \,] = \sqrt{[\, m^*(V_0 - E) a^2/2\hbar^2 \,]}$$

and making the substitution $\varepsilon = \sqrt{[\, m^* E a^2/2\hbar^2 \,]}$ gives:

$$\varepsilon \tan(\varepsilon) = \sqrt{[\, (m^* V_0 a^2/2\hbar^2) - \varepsilon^2 \,]} \qquad (2.10a)$$

and similarly for the antisymetric eigenfunctions:

$$-\varepsilon \cot(\varepsilon) = \sqrt{[\, (m^* V_0 a^2/2\hbar^2) - \varepsilon^2 \,]} \qquad (2.10b)$$

To solve equations 2.10a and 2.10b and obtain the energy eigenvalues of the potential well, the functions $p(\varepsilon)$ and $q(\varepsilon)$ are defined and these functions are plotted in figure 2.2:

$$p(\varepsilon) = \varepsilon\tan(\varepsilon) \qquad \text{(for symmetric eigenfunction)}$$

$$= -\varepsilon\cot(\varepsilon) \qquad \text{(for antisymmetric eigenfunction)}$$

and $$q(\varepsilon) = \sqrt{[\, (m^* V_0 a^2/2\hbar^2) - \varepsilon^2 \,]} \equiv \sqrt{(\gamma^2 - \varepsilon^2)}$$

The solutions to the eigenvalue problem are given by the intersections of the two functions $p(\epsilon)$ and $q(\epsilon)$ and are discrete eigenvalues which give the allowed energies of a particle confined to the potential well (see figure 2.2). The number of solutions and hence the number of bound states in the potential well is dependent on the radius of the circle defined by $q(\epsilon)$ refered to as the strength parameter γ. In the example shown in figure 2.2 there are 2 confined states, and the eigenfunctions associated with these states are represented in figure 2.2b. The energy eigenvalues are labelled E_n with $n=1$ for the ground state and n increasing for increasing energy. The corresponding eigenfunctions contain $(n-1)$ nodes within the potential well.

The penetration of the eigenfunction into the potential barrier is dependent upon the term k_2: the higher the energy of the state in a potential well being considered, the larger the amount of penetration. In considering the width of the potential wells, narrower wells exhibit greater penetration into the barrier because k_2 decreases as energy increases leading to larger penetration and also the wavefunction at the barrier increases with decreasing a/2 (equations 2.8 and 2.9). The confinement of the eigenfunctions to the potential well therefore decreases with well width and this becomes an important consideration in designing quantum well material.

In the limit that the potential well becomes infinitely deep ($V_0=\infty$), the strength parameter γ of the well tends to infinity. The solutions to equations 2.10a and b can therefore be evaluated exactly, occuring at $\epsilon=n\pi/2$, so that the energy eigenvalues occur at:

$$E_n = \frac{(\hbar\pi n)^2}{2m^*a^2}$$

which are the solutions to the infinite potential square well problem [Pankove '71]. The separation of the energy eigenvalues therefore increases quadratically with n in the infinite potential well. For the finite well, the energy separation is less than for the infinite potential well, but still increases with energy.

Section 2.3.2 Multiple Quantum Well Structures.

In the discussion above, the solution to a single quantum well was considered. In a multiple quantum well (MQW) structure consisting of a number of finite potential wells of depth V_0, width 'a' and barrier width 'd', interaction between adjacent wells needs to be taken into account.

If the barrier width between adjacent potential wells is comparable to the penetration depth of the eigenfunction, then the adjacent wells cannot have the same energy eigenvalues because of resonsant coupling of the wells. The resultant eigenfunctions are approximately linear combinations of the two eigenfunctions of the wells, with a symmetric and an anti-symmetric combination [Chen et al '87(b)]. These two eigenfunctions have different energies, the energy difference increasing with increasing interaction. As more wells are included in a structure, further splitting of the energy states occurs (one level per well), until the energy levels of the single finite quantum well become broadened into minibands within the potential well. The magnitude of the broadening increases with an increase in the interaction between the eigenfunctions so that the broadening experienced by the higher lying eigenfunctions is greatest [Shik '75].

The interaction between individual potential wells leads to an important distinction between superlattices (SL) and MQW's. In a SL, there is a large overlap of the eigenfunctions of adjacent wells, caused by having thin barriers layers. The eigenstates therefore broaden into wide minibands and there is significant tunneling through the barrier material. The carriers are not confined to indvidual wells, but can drift through the extended lattice. In MQW material, thicker barriers greatly reduce the interaction between adjacent wells and the broadening is therefore less significant so that the minibands can be considered as discrete states. The broadening of the levels through well to well interaction can be satisfactorly modelled using the Kronig-Penney model [Kittel '86]. In modelling the effects of both the barrier width and well depth on the broadening of the energy states, a potential well with a strength parameter γ of 2π and barrier width equal to the well width showed negligible broadening of the first two energy states [MacBean '86].

The model of quantum confinement in potential wells presented so far gives a picture of confined carriers that can have only a few discrete energies which correspond to the eigenvalues of the potential well. Whilst this is true for the energy in the z direction, for the in-plane motion the carriers can move freely under the normal dispersion law, so that the total energy E of a confined particle is given by:

$$E = \frac{\hbar^2}{2m^*}\left[k_x^2 + k_y^2\right] + E_n \qquad (2.11)$$

and any energy of the particle greater than E_n is taken up by the in-plane motion.

The density of states g(E) of a 2 dimensional system, is given by:

$$g(E) = \frac{dn}{dE} = \frac{dn}{dk} \cdot \frac{dk}{dE} \qquad (2.12)$$

where n is the number of states with energy less than E and k is the wavevector. With the reduced dimensionality of the system, there are only 2 degrees of freedom in k space and so $n \propto k^2$. If the bands are assumed to be parabolic, then from equation (2.12) g(E)= constant. For each sub– band the density of states is therefore a constant, so that the density of states of the potential well consists of a series of steps:

$$g(E) = \frac{m^*_{x,y}}{\pi\hbar^2} \sum_n \Theta(E-E_n) \qquad (2.13)$$

where the summation is over all the bound states of energy E_n in the potential well, $\Theta(x)$ is the Heaviside step function and $m^*_{x,y}$ is the in– plane effective mass of the confined carriers.

In reality the density of states does not follow a sharp step, but is smeared out by the finite width of the minibands. The resultant density of states as a function of energy are shown schematically in figure 2.3. The smearing of the step increases with energy since the well to well interaction increases with energy as discussed in the Kronig– Penney analysis [Shik et al '74].

In interband optical absorption in quantum wells, absorption of a photon leads to the excitation of an electron from a confined state in the valence band to a confined state in the conduction band. The optical absorption spectum therefore follows the density of states as a function of energy, since the electron must be excited from one allowed energy level to another allowed energy level. A further consideration in the absorption spectrum is that there must be a non– zero transition probability between the two states. This is equivalent to saying that there must be a finite overlap of the envelope functions of the initial and final eigenfunctions. When the strength parameters (γ) of the quantum wells in the conduction and valence bands are equal, this leads to the strict selection rule that $\Delta n = 0$ for an allowed transition. The optical absorption therefore has a series of steps, following to the steps in the density of states, which can be expressed as:

$$\alpha(\hbar\omega) \propto \sum_{n,n'} |\langle u_{n'} | u_n \rangle|^2 \quad \theta(\hbar\omega - E_g - E_n - E_{n'}) \qquad (2.14)$$

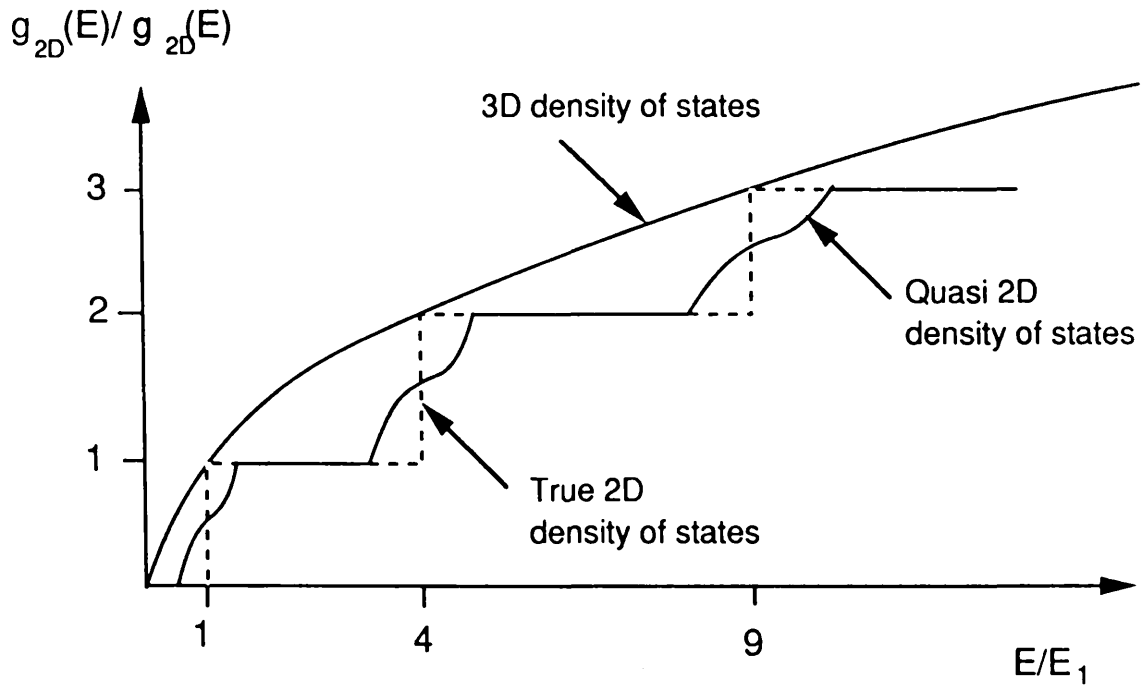

Figure 2.3
Density of states of a quasi-2D semiconductor, where $g_{2D}(E)$ is the density of states of a 2 dimensional system and E_1 is the energy eigenvalue of the ground state.
The density of states in true 2D system (dotted line) and a 3D system has been included for comparison.

where u_n and $u_{n'}$ are the eigenfunctions of the initial and final states, E_g is the material band gap and E_n and $E_{n'}$ are the eigenvalues of the initial and final states in the wells.

Section 2.3.3 Effects of Material Band Structure on MQW GaAs/AlGaAs.

The multiple quantum well structures studied in this thesis consist of thin layers of GaAs (≈10nm) which act as potential wells when sandwiched between layers of the larger band–gap $Al_xGa_{1-x}As$ material. Some of the features of this material will be discussed in this section to illustrate the optical properties of multiple quantum well (MQW) GaAs/AlGaAs.

One important feature of the potential wells in MQW GaAs/AlGaAs material is that potential wells in both the conduction and valence bands occur in the GaAs layers. A consequence of the confinement of carriers in the same layers is an increase in the interband transition probability from confined states. The fact that the carriers in the GaAs wells and AlGaAs barriers have different effective masses affects the energy eigenvalues of the wells. To conserve momentum at the well/barrier interface in the boundary conditions of the eigenvalue problem, $(1/m^*)(d\psi/dz)$ must be continous at the well/barrier, rather than $(d\psi/dz)$ [Kawai et al '84].

The well strength parameter γ is dependent upon the depth of the potential well (i.e. the difference in the band gap of the well and barrier materials) and also the effective mass of the confined carriers. For a barrier material consisting of $Al_{0.3}Ga_{0.7}As$ and GaAs wells, the potential well depth is 240meV and 160meV for the conduction and valence bands respectively. The difference in the well depths is a result of the 60:40 band offset for the ratio of conduction to valence bands in GaAs/AlGaAs [Schmitt–Rink et al '89]. Allowing for the different well depths and the different m^* for carriers in the conduction and valence bands leads to the ratio of γ between the bands cb:hh:lh to be 1:4.7:0.82.

It is the large well strength for the hh band (as a result of the large hh effective mass) that leads to an eigenfunction which is tightly confined to the wells. The large hh effective mass pushes the energy eigenvalue deeper in the well, and increases the decay constant k_2 (equation 2.6). For the light hole eigenstates, the combination of the shallower valence band potential well and the small effective mass means that the confinement of carriers to the well is much less than the either the heavy hole or conduction band eigenfunctions.

It is the different well strengths of the hh and lh bands that leads to the degeneracy at k= 0 being lifted, since the $1/m^*$ factor in the kinetic energy term of the Hamiltonian (equation 2.1) leads to the hh energy eigenvalues being smaller than the lh energy eigenvalues. There are therefore two sets of eigenstates within the valence band potential well, as illustrated in figure 2.4.

The points raised in this section lead to a modification of the selection rules which govern the interband transitions and hence the absorption spectrum. If the potential wells in the conduction and valence bands were identical, then interband transitions other than $\Delta n = 0$ would also be forbidden because of the orthogonality of the eigenfunctions. However, the combination of the different well depths and carrier effective masses of the conduction and valence bands means that, whilst eigenstates of a particular band remain orthogonal, for eigenfunctions of different bands and with $\Delta n \neq 0$, the eigenfunctions are not necessarily orthogonal. As a result, transitions of $\Delta n =$ even integer are observed as weak peaks in the absorption and luminescence [Miller et al '80] spectra of MQW material.

The confinement of the heavy hole eigenfunctions to the potential well is greater than both the light hole and conduction band eigenfunctions, which have comparable confinement. As a result, the overlap between the heavy hole eigenfunctions and the conduction band eigenfunctions for $\Delta n \neq 0$ is larger than for the light hole and conduction band eigenfunctions. The heavy hole forbidden transitions are therefore more prominent than light hole forbidden transitions in the absorption spectrum [Miller et al '81(b)].

Section 2.3.4 Excitonic Effects in GaAs/AlGaAs Quantum Well Structures.

Interband optical absorption always involves the creation of an electron–hole pair, which interact through their Coulomb attraction. This interaction means that the optically created electrons and holes cannot be fully described in terms of single particle states and so the concept of an exciton must be introduced. An exciton is an electron–hole pair which, whilst being bound to one another as a hydrogenic system, are free to move through the lattice. Peaks associated with the creation of excitons are observed in the optical absorption edge of bulk semiconductors [Dow et al '70], but only at low temperatures since the weakly bound electron–hole pair are easily ionised by phonon interaction. The diameter of orbit for excitons in GaAs is approximately 30nm and so the confinement of an optically created electron hole pair in a quantum well of 10nm width confines the electron hole pair and increases the binding energy of the exciton. As a result, the

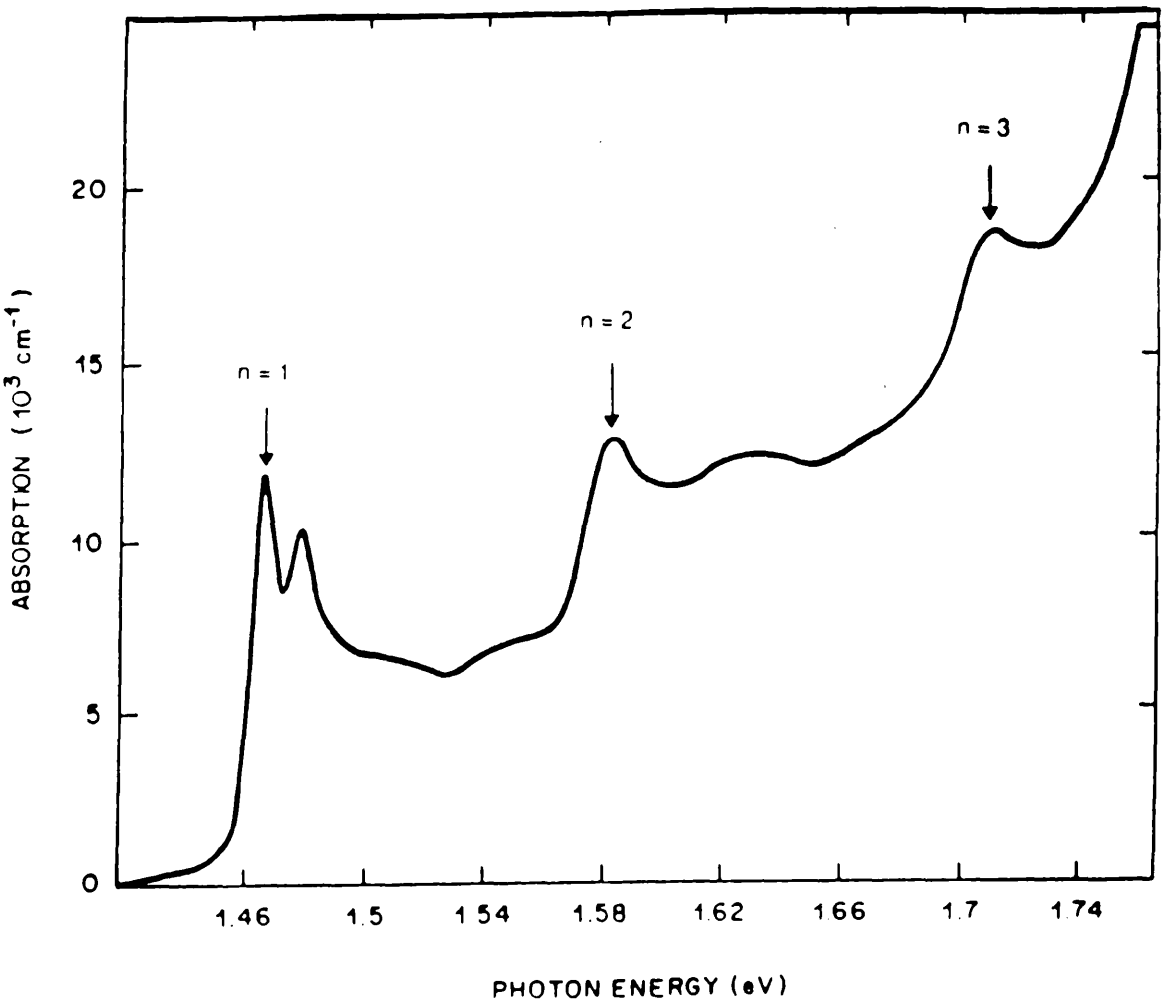

Figure 2.4
Absorption spectrum of MQW GaAs/AlGaAs, illustrating the step-like density of states at the n=1, 2 and 3 inter band transitions. Exciton peaks are well resolved at each of the interband transitions.
(After Chemla et al '86)

optical absorption edge of quantum well GaAs is dominated by the exciton peaks, even at room temperature [Dingle et al '74].

There are exciton states associated with each of the steps in the optical absorption spectrum as shown in fig 2.4, where two peaks are observed at the n=1 step. The low energy peak at the n=1 step originates from the creation of an exciton associated with the heavy hole subband, and the high energy peak from the creation of an exciton associated with the light hole subband. In general, the observed excitons are in the ground, 1s like hyrogenic, state with the energy of these states lying approximately 8meV below the step in the density of states. Excited states such as 2s and 2p do however exist, but are observed only at low temeratures (≈4K) in the luminescence spectra of high quality GaAs/AlGaAs quantum well samples [Miller at al '81(b), Dawson et al '86, Masumoto '85].

The confinement of carriers in the quantum well layers modifies the spherically symmetric orbits of bulk GaAs by compressing the orbits in the plane of the wells. The reduced average separation of the electron and hole of the exciton increases their coulombic attraction and leads to an increase in the exciton binding energy. In the 3 dimensional case, the exciton binding energy B_{3D} is given by:

$$B_{3D} = -R_y = -\frac{e^2\mu^*}{2\epsilon^2\hbar^2} \qquad (2.15)$$

In the limit of a purely 2 dimensional exciton, the binding energy is increased by a factor of 4 [Chemla et al '84] such that the binding energy is modified to B_{2D}:

$$B_{2D} = -4R_y = -\frac{2e^2\mu^*}{\epsilon^2\hbar^2} \qquad (2.16)$$

In reality, both the finite width of the quantum well layers and the penetration of the electron and hole wavefunctions into the barrier layers results in a quasi 2D exciton with a binding energy lying within the B_{2D} and B_{3D} limits. It is this increase in the exciton binding energy that leads to the exciton resonances still being observable at room temperature in MQW materials. For an exciton peak to be distinguishable from the continuum, the binding energy (B) must be larger than the exciton linewidth (Γ). There is a well width for which the exciton binding energy in a finite potential well is maximum [Greene et al '83, Bastard et al '82] since the penetration of the wavefunctions into the barrier materials increases with decreasing well width, thus increasing the average separation of the electron and hole. For instance, with an Al concentration of x=0.3 in the barrier material and using a band–offset ratio of 85:15, the heavy hole exciton binding energy peaks at

approximately 9meV for a well width of 3.5nm and at 5nm for the light hole binding energy.

Although the exciton resonances are still much more pronounced at the band edge of MQW material compared to bulk material, the line width of exciton peaks in high quality bulk GaAs is actually less than in MQW GaAs/AlGaAs [Chemla et al '85, Dow et al '70]. The lineshape of excitons has been modelled semiempirically to a Gaussian lineshape [Chemla et al '85] because the dominant broadening mechanisms are inhomogenous, the most significant being well/barrier interface roughness. This is especially so for thin wells since the energy eigenvalue fluctuation is given by:

$$\frac{\delta E}{E_i} \propto \frac{\delta L_z}{L_z} \qquad (2.17)$$

where E_i is the energy of the i'th eigenstate and L_z is the width of the well [Chemla et al '84]. The dominant mechanism limiting the exciton lifetime and so leading to homogenous broadening is longitudinal optical phonon (LO−phonon) interaction, which lead to an estimated exciton lifetime at room temperature of 300fs [Chemla et al '84].

The in−plane motion of the electron and hole pair of an exciton in GaAs/AlGaAs quantum wells is complicated by the lifting of the degeneracy at k=0 of the heavy and light hole bands and coupling between these bands. These lead to the bands having highly non−parabolic dispersion. The non−parabolicity of the bands arises from the fact that at k=0 the in−plane effective mass m^* of the heavy hole is in fact less than that of the "light" hole, because the heavy hole band curvature is greater than the lower energy light hole band, band crossing would occur at some finite value of k. However, coupling of the two bands occurs leading to anticrossing of the bands. The anticrossing of the excitons in excited states has been demonstrated from luminescence measurements of GaAs/AlGaAs in an electric field [Vina et al '87]. Also, by including mixing between the heavy hole and light hole states for the in−plane motion, variational calculations [Bastard et al '86] show divergence of the sub−bands at finite k, thus avoiding the band crossing. It is worth noting that the confinement of carriers in quantum wells therefore changes the in−plane dispersion of GaAs through coupling of the $J_z = \pm 1/2$ and $J_z = \pm 3/2$ bands whilst dispersion along the direction of confinement is left unchanged. To fully describe the dynamics of an exciton in a quantum well, the in plane dispersion of the bands should be taken into account. It is, however, usual to neglect the coupling of the bands and assign a mean

effective mass to the holes of the exciton, averaged over the dispersion in the Brillouin zone.

Measurements of the optical absorption spectrum of GaAs/AlGaAs quantum wells have shown it to be highly polarisation dependent [Weiner et al '85(a)]. The spectra show that for light polarised in the plane of the quantum well, there are two excitonic peaks: one associated with the the heavy hole band $|3/2, \pm 3/2\rangle$ and a second associated with the light hole band $|3/2, \pm 1/2\rangle$. The relative absorption strength of the peaks are 3:1 for the heavy and light hole respectively. However, for light polarised perpendicular to the wells, the transitions from the heavy hole band become forbidden, so that only the light hole exciton appears in the absorption spectrum giving relative absorption strengths 0:1 for the heavy hole and light hole transitions. Although the polarisation dependent absorption is more apparent in MQW materials because of the lifted degeneracy of the heavy and light hole bands, the polarisation dependence is also present in bulk GaAs [Sell et al '73]. The selection rule is related to crystal symmetry and can be explained in terms of the angular momentum of the bands involved in the transition.

The transition probability of an electron from an initial state u_i to a final state u_f which involves absorption of a photon is given by

$$P_{if} \propto | \langle u_f | \epsilon.p | u_i \rangle |^2 \qquad (2.18)$$

where u_f and u_i are the wavefunctions of the electron after and before the transition respectively, ϵ is the unit vector of the optical electric field and p is the momentum operator. The states of an electron in the conduction and valence bands of GaAs can be expressed as [Schuurmans et al '85]:

$$u_e = |1/2, \pm 1/2\rangle = |s\rangle \qquad 2.19(a)$$

$$u_{hh} = |3/2, \pm 3/2\rangle = 1/\sqrt{2}\,|(x + iy)\rangle \qquad 2.19(b)$$

$$u_{lh} = |3/2, \pm 1/2\rangle = 1/\sqrt{6}\,|(x + iy)\rangle - \sqrt{(2/3)}\,|z\rangle \qquad 2.19(c)$$

u_e is the state of an electron in the conduction band which is a spherically symmetric s−type orbit. The hh and lh states are p−type orbits with the two bands having different projections of angular momentum.

Consider an optical transition from a state $|z\rangle$ to a state $|s\rangle$ involving an

optical electric field ϵ_z. The operator $\epsilon.p$ becomes$\epsilon_z p_z$ (ie $\epsilon_z i\hbar$ d/dz), and since $|z\rangle$ is an odd function of z its derivative is even. Since $|s\rangle$ is also even, the matrix element (2.18) is non−zero and there is a finite transition probability. However, if the initial state is $|x\rangle$ or $|y\rangle$ (even functions in z), then the derivative is odd in z giving a zero matrix element (2.18). In conclusion, only the component of the $|p\rangle$ states parallel to the optical field couples with $|s\rangle$ states.

Now consider the optical absorption involving a transition from the hh to the cb, such that u_i and u_f are represented by u_{hh} and u_e respectively. If the polarisation of the incident light is in the plane of the quantum well (ie ϵ_x or ϵ_y), then there is coupling between the $|x\rangle$ or $|y\rangle$ states and the $|s\rangle$ state and there is a finite transition probability P_{if}. However, for polarisation ϵ_z perpendicular to the plane of the well, there is no $|z\rangle$ component to couple to and the transition from the hh to cb is forbidden for this polarisation.

For absorption processes involving the excitation from the lh to the cb, u_i represented by u_{lh} and there is coupling from the lh band to $|s\rangle$ type cb for all polarisations. As a result the transitions from the lh to cb is allowed for polarisation both perpendicular and parallel to the plane of the well.

The relative oscillation strength of the transitions from the two valence bands is given by the ratio of the projection of the heavy and light states in the direction of the light polarisation (the conduction band being spherically symmetric is unaffected by the direction of polarisation). For polarisation in the plane of the quantum well, the only difference the calculation of P_{if} from the heavy and light hole states is the factors $1/\sqrt{2}$ and $1/\sqrt{6}$ in the wavefunctions. Squaring these in P_{if} leads to a relative oscillator strength of 3:1 for the transitions as measured by [Weiner et al '85(a)]. Since the heavy hole transition is forbidden for polarisation perpendicular to the plane of the well the relative oscililation strengths will be 0:1. This argument assumes that the heavy and light hole bands are completely decoupled. This is however not the case and measurements by [Sooryakumar '86] suggest that there is mixing of states of up to 30% at k= 0.

Section 2.3.5 Refractive Index of Multiple Quantum Well GaAs/AlGaAs.

The optical absorption edge of MQW GaAs/AlGaAs has been shown to be qualitatively very different to that of bulk GaAs [Chemla et al '84]. It therefore follows that there must be a corresponding modification to the refractive index of the material at photon energies close to the band gap, since the absorption

spectrum of a material and its refractive index are inter-related, as represented by the Kramers-Kronig transformation. The differences in refractive index between bulk and MQW materials are mainly (a) large dispersion close to the band gap and (b) large birefringence resulting from both the multilayer dielectric nature of the material and the exciton polarisation sensitive selection rules described in section 2.3.4.

Beginning with the large dispersion, the presence of the exciton peaks in the absorption spectrum of MQW material at room temperature and also the changes in absorption associated with the 2 dimensional density of states lead to a corresponding change in refractive index. The changes are dominated by the exciton resonances, which lead to a large dispersion of refractive index [Chen et al '87(a)], although the step-like 2 dimensional density of states also radically changes the refractive index of the MQW compared with the bulk material. Considering the birefringence, at wavelengths away from band gap, the birefringence of MQW material is dominated by the multilayer dielectric nature of the material. However, at wavelengths close to the band gap, the birefringence originating from the anisotropic absorption of the material [Weiner et al '85(a)] dominates, with the loss of the heavy hole transition leading to large birefringence [Chen et al '87(a)].

In order to model and design optical devices such as waveguides in MQW GaAs/AlGaAs, it is necessary to be able to calculate the material's refractive index at the device's operating wavelengths. The simplest model used is the weighted rms model [Ohke et al '85], in which the refractive index is given by:

$$n_{rms}(TE) = \frac{\sqrt{[n_1^2 L_1 + n_2^2 L_2]}}{\sqrt{[L_1 + L_2]}} \qquad (2.20)$$

where $n_1(\omega)$ and $n_2(\omega)$ are the refractive indices of the well and barrier material of width L_1 and L_2 and at the photon frequency of ω. The values of n_1 and n_2 can either be calculated from the semi empirical method [Adachi '85] for a frequency ω and Al concentration of x in $Al_xGa_{1-x}As$ or alternatively the values can be taken from the published values measure experimentally [Cassey et al '74, Jensen et al '83].

Because the rms method neglects any effects on the refractive index arising from the 2-dimensional density of states and the exciton resonances, there are discrepances between the indices measured experimentally and those calculated from the rms model [MacBean '86]. A more refined method of calculating the indices, which takes into account the detailed electronic band structure of the material has been used [Kahen et al '85] giving values which agree well with the values

measured experimentally [Suzuki et al '83]. However, since the rms model is much simpler to implement and agrees well with measured values other than at wavelengths close to the exciton resonances, this method was used here when designing waveguide devices.

Section 2.4 QUANTUM WELLS IN AN ELECTRIC FIELD.

The previous sections of this chapter have shown that the band structure of GaAs is radically changed by the formation of thin (≈10nm) quantum well layers and that with this change there is a corresponding change in the optical absorption and the persistence of excitons at room temperature. It has also been demonstrated experimentally [Miller et al '85] that the quantum well material behaves very differently in a D.C. electric field, giving rise to a new effect in semiconductors which has been termed the quantum confined Stark shift (QCSE) [Miller et al '84]. The effect was first observed in the luminescence behaviour of GaAs/AlGaAs quantum wells [Mendez et al '82] and later in transmission through the quantum well layers [Chemla '83].

The electric field can be applied such that the field is either parallel or perpendicular to the plane of the quantum well layers. The latter configuration leads to the most radical change in the absorption compared with the effect observed in bulk material. Before explaining the effects observed in quantum well material, it is worthwhile briefly discussing the effects observed in bulk semiconductors in an electric field, ie the Franz– Keldysh effect [Keldysh '58].

Section 2.4.1 The Franz– Keldysh Effect.

When a large uniform DC electric field (≈10^5V/cm) is applied to an insulating or semiconducting crystal, the optical absorption edge is seen to broaden, inducing a tail in the absorption at photon energies below the band gap and oscillations in the absorption spectrum at energies above the absorption edge [Dow et al '70].

The effective decrease in the band gap of the material can be explained in terms of photon assisted tunnelling of electrons from the valence band to the conduction band. In the presence of an electric field, the bands tilt, but remaining parallel and maintaining the same vertical band gap as shown in figure 2.5(a). The wavefunctions of the carriers in the conduction and valence bands are now

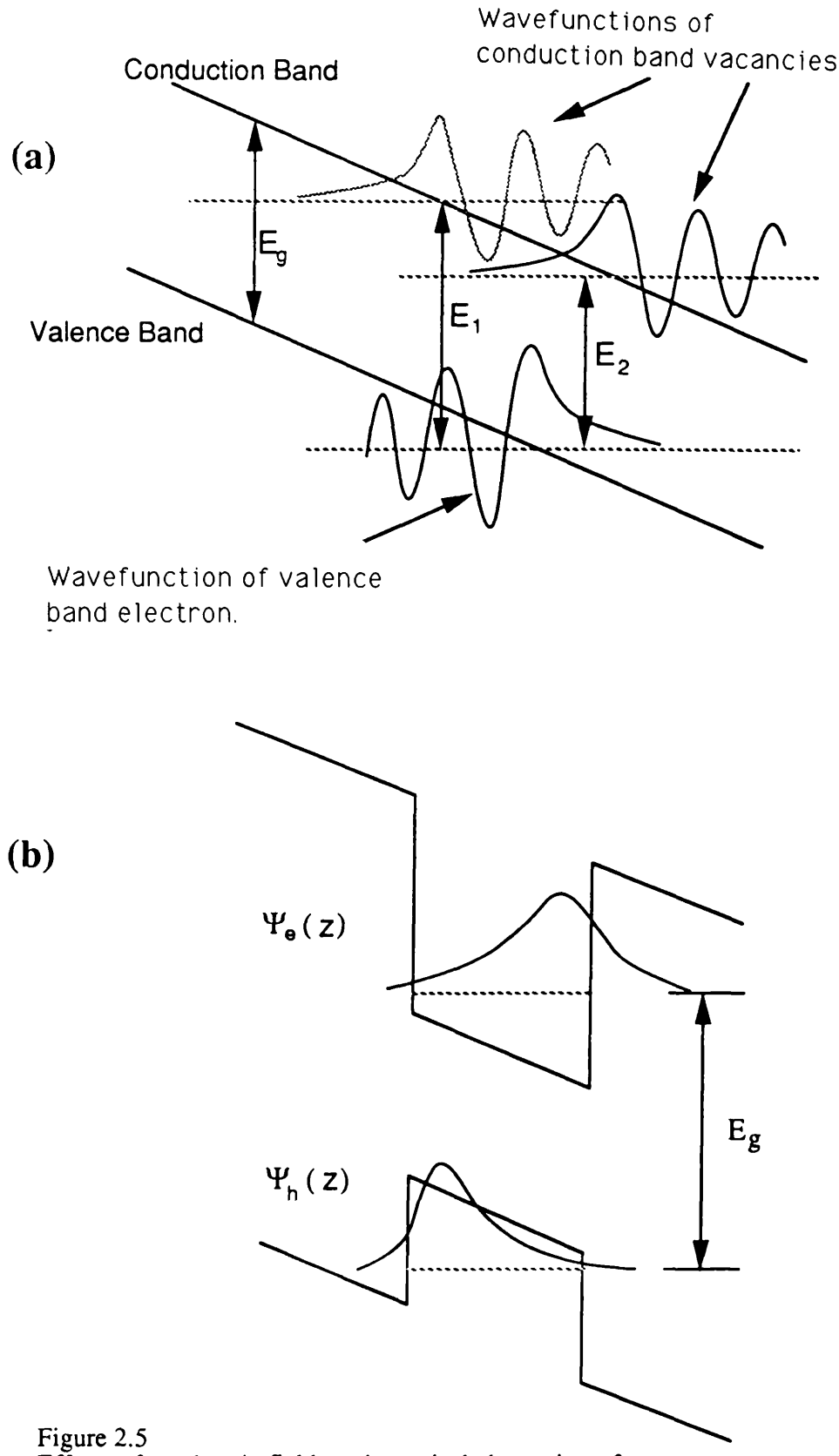

Figure 2.5
Effects of an electric field on the optical absorption of:
(a) Bulk semiconductors,
(b) Quantum Well material, with the electric field applied perpendicular to the plane of the wells.

asymmetric and are descibed by Airy functions, decaying into the band–gap and oscillating into the bands, as shown in figure 2.5(a). It is apparent fom the wavefunctions that an electron in the valence band can now tunnel into the band gap and be excited into the conduction band by absorption of a photon of energy ϵ_1, less than the band gap E_g. Equally, the electron can exist in the region where the wavefunction is oscillatory and be excited into the conduction band by a photon of energy ϵ_2, greater than E_g. It is the oscillatory nature of the wavefunction that leads to the oscillations in the optical absorption spectrum at energies above E_g.

The qualitative description of the Franz–Keldysh effect given above (and the original analysis by Franz and Keldysh) neglects any effects arising from the coulomb interaction of the electron and hole pair which are created by the absorption of a photon. In later studies, [Dow et al '70] took the Coulomb interaction into account, thus accounting for exciton resonances in the absorption spectrum. In bulk material the exciton peaks are seen to broaden rapidly with electric field strength and also shift slightly to lower energies. The broadening is mainly the result of rapid field ionisation in the presence of an electric field and the small exciton binding in the bulk material. The exciton resonance is soon lost as the electron are rapidly ionised by the electric field.

Section 2.4.2 Quantum Wells in an Electric field.

Field Parallel to the Plane of the Wells.

The effect of an electric field on the absorption spectrum of a quantum well GaAs/AlGaAs was studied experimentally by [Miller et al '85], who demonstrated that the effect was qualitatively similar to that seen in bulk GaAs. They observed large broadening of the exciton peaks at the band edge, with a slight shift to higher energies at low electric fields. This was similar to the effect predicted by [Dow et al '70] when modelling a 2–dimensional exciton in an electric field. The large broadening of the peak observed is due to the field ionisation since the electric field polarises the exciton, reducing the coulomb interaction. The broadening is however less rapid than with a 3 dimensional exciton because of the large binding enegry of the quasi 2 dimensional exciton.

Field perpendicular to the plane of the wells

When a uniform electric field is applied perpendicular to the plane of the quantum wells, the changes in the absorption spectrum are radically different to those seen when the field is applied parallel to the plane of the well or in bulk GaAs. A new effect is observed which has been termed the quantum confined Stark effect (QCSE) [Miller et al '84], and it is important to note that this is not an enhancement or modification of an effect observed in bulk material. The main features observed in the QCSE are that the exciton resonances associated with the n= 1 transition shift to lower energies [Whitehead et al '88(a)] and the exciton resonances remain resolvable for fields up to 50 times the classical exciton ionisation field [Miller et al '85]. The exciton peaks are also observed to shift by energies up to 5 times the exciton binding energy [Miller et al '85]]. The most remarkable feature is the persistence of the exciton resonances at large electric fields. The main mechanisms leading to the QCSE will be described as reported in the literature.

In section 2.3, it was shown that the carriers in a finite potential well exist in eigenstates with discrete energies given by the solutions to the eigenvalue problem [Bastard et al '86]. When an electric field is applied perpendicular to the plane of the wells, the bands of the material slope as shown in figure 2.5(b), and the Hamiltonian of equation 2.6 is redefined:

$$H = \frac{-\hbar^2}{2m^*} \cdot \frac{d^2}{dz^2} + V(z) - eF_z z \qquad (2.21)$$

where e = electronic charge

F_z = Electric field

and V(z) is the potential of the quantum well in the absence of the electric field.

Solving the Schroedinger equation for this Hamiltonian amounts to perturbing the eigenfunctions in the quantum well as shown in figure 2.5(b), whilst neglecting any coulomb interaction between electron and hole created, and hence neglecting excitonic effects. A variety of methods have been used to solve this eigenvalue problem: variational [Mendez et al '82, Sanders et al '87], perturbation [Bastard et al '83] and Airy solutions [Miller et al '84]. The methods all predict the shift of the n= 1 energy eigenvalue to lower energies, with the energy shift being quadratic for field strengths in the regime $eF_zL_z < \Delta E_1$, ie the potential drop across the well is less than the energy shift [Bastard et al '83]. For higher fields, the energy shifts more like $E^{3/2}$ as the wavefunction is squeezed into one side of the well, until the

field becomes large enough that field induced tunneling through the barriers removes the effect of shifting energies [Bastard et al '86]. Most of the theoretical studies have concentrated on the energy shift experienced by the n= 1 energy level. However, in calculating the energy shift of the higher lying states, [Matsuura et al '86] showed that the n= 2 an n= 3 states have an initial energy increases with applied electric field before they fall in energy at larger fields.

The results from the exact Airy solutions [Miller et al '86(b)] showed that in the limit of large GaAs quantum well widths (L_z> 30nm), then the effect of a perpendicular electric field on the absorption edge was qualitatively similar to the effect observed in bulk GaAs. The tail in the absorption spectrum at photon energies below the band gap and the oscillations at photon energies above the band gap are both predicted. However, for small wells (L_z< 10nm), the effect of the electric field on the absorption edge is qualitatively very different to bulk material. The energy eigenvalues of the n= 1 states shift to lower energies, and the eigenfunctions become asymmetric, with the penetration into the barrier material being much larger on one side of the well (figure 2.5(b)). The asymmetry of the eigenfunctions of the electron and hole states are in opposite directions, decreasing the overlap of the envelope functions and therefore reducing the oscillator strength of the corresponding absorption. At the same time, a finite overlap between states $\Delta n \neq 0$ increases with field, and the oscillator strength of these transitions which are forbidden at zero field increase. In this model the coulomb interaction of the created electron hole pair is completely neglected. Because of the similarity of the effect observed in bulk material and quantum wells of width greater than 30nm, the effect was named the quantum confined Franz– Keldysh (QCFK) effect [Miller et al '86(b)]. The theory was later extended to model the effect of electric field on lower dimensional systems: quantum wires and dots [Miller et al '88].

The QCFK effect models the shift of the energy eigenvalues of a quantum well in an electric field, completely neglecting any exciton effects. Since the absorption edge of MQW material is dominated by exciton resonances even at room temperature, the coulomb interaction of the electron and hole obviously have to be included in the full model of the QCSE. Also, an explanation of the persistence of the exciton resonances up to such high field strengths must be given.

To include excitonic effects in the model of quantum wells in electric fields, the Hamiltonian must now include terms accounting for the coulombic electron– hole interaction. The resulting exciton wavefunction can be described approximately by the separable wavefunction:

$$\Phi = \psi_e(z_e).\psi(z_h).\varphi_{eh}(r), \qquad (2.22)$$

where $\psi_{e(h)}(z)$ are the solutions to the potential well problem in an electric field in the absence of coulomb interaction and $\varphi_{eh}(r)$ is a $1-S$ like orbital describing the hydrogenic nature of the exciton [Miller et al '84]. The confinement of the exciton in the well perturbs the orbits, leading to the quasi $2-$ dimensional exciton. On application of an electric field perpendicular to the plane of the wells, an induced dipole between the electron and hole separates the particles. The exciton can therefore be considered as two particles orbiting in two different planes. The increased separation of the particles reduces the coulomb attraction of the particles, thereby reducing the exciton binding energy. The reduced binding energy increases the exciton energy so that the exciton shift actually works against the shift of the energy eigenvalues. At low fields strengths ($F \leqslant 3x10^4$V/cm), the increase in the binding energy can reduce the resonance shift predicted by the QCFK analysis by a factor of two [Miller et al '85]. For large fields, the total shift of the exciton peak is dominated by the change in the effective band gap with electric field (ie QCFK effect) and only a small shift in the exciton resonance energy is the result of the change in exciton binding energy. For instance, in a 10nm wide well at a field of $7.5x10^4$V/cm, there is a 10meV shift in the effective band gap and less than 2meV shift in the exciton binding energy [Brum et al '85]. At the larger field strengths, the potential barriers restrict the electron and hole separation, and the exciton binding energy decreases less rapidly. This is especially so for large wells ($L_z \geqslant 15$nm) where the initial decrease in the binding energy is most pronounced. [Brum et al '85].

It is the restriction on the separation of the electron and hole by the potential barriers that lead to the remarkable presistence of the excitonic resonances in electric field strengths up to 50 times the classical ionisation field. The rapid ionisation of the exciton is not experienced until the electric field strength reaches the regime of $eF/k \geqslant V_b - E_1$ ie when the drop in potential of the barrier over the penetation depth k is larger than the effective barrier height [Bastard '86]. At this field strength the exciton resonance is lost as the carriers ionise through electric field induced tunneling.

Finally, it is interesting to note that for electric fields perpendicular to the plane of the quantum well, the in$-$plane motion of the exciton is also affected due to reduced binding energy. For large well widths ($L_z \geqslant 15$nm) the orbit radius increases from approximately 30nm to approximately 40nm in electric fields of zero and $8x10^4$V/cm. The result is a decrease in the exciton oscillator strength due to

the increase separation and an increase in the broadening mechanisms such as interface roughness [Deveaud et al '87, Weisbuch et al '81].

Section 2.5 THE ELECTRO–OPTIC EFFECT.

When an electric field is applied to a transparent material, the material may experience a change in refractive index. The effect leading to the refractive index change is known as the electro–optic effect, and this effect can be separated into different effects. Gallium arsenide exhibits the electro–optic effect through three effects, all of which are described below in relation to MQW GaAs/AlGaAs.

Section 2.5.1 Linear Electro–Optic Effect.

The linear electo–optic effect (LEO) or Pockels effect can be exhibited by all non–centrosymmetric crystals and is observed as a linear change in the refractive index of the material with applied electric field. These materials also exhibit the piezo–electric effect which is an induced elastic strain in the material in the presence of an electric field. Associated with the strain, there is a change in the refractive index via the photoelastic effect. There are therefore two independently acting effects leading to a change in refractive index, sometimes refered to as the primary and secondary electro–optic effects respectively.

If a crystal is mechanically clamped whilst in the presence of the electric field and thus preventing any strain, then the refractive index change is purely from the primary electro–optic effect. However, if a crystal is unclamped an electric field will lead to a piezo–electric strain and hence a change in the refractive index through the photoelastic effect. Both the primary and secondary effects are therefore being experienced. It was Pockels who proved that the refractive index change in a crystal in an electric field was different to that experienced by a crystal under mechanical strain, the difference being the result of the primary electro–optic effect. This is therefore often refered to as the Pockels effect.

The change in refractive index is usually expessed in terms of changes in the optical indicatrix [Nye '57] which describes the polarisation dependance of refractive index of a crystal:

$$\sum_{i,j=1}^{3} B_{ij}\, x_i\, x_j = 1 \qquad (2.23)$$

where $B_{ij} = \epsilon_0/\epsilon_{ij}$

ϵ_0 = Permitivity of free space

ϵ_{ij} = Dielectric Constant

and i,j represent directions: 1=x, 2=y, 3=z.

The change in the refractive index of the material as a result of an applied electric field in the direction 'k' is represented by changes in the optical indicatrix:

$$\Delta B_{ij} = \Delta \left[\frac{\epsilon_0}{\epsilon_{ij}} \right] = \sum_{i,j,k=1}^{3} r_{ijk}\, E_k \qquad (2.24)$$

where E_k = applied electric field

r_{ijk} = Linear Electro-optic coefficient.

However, since r_{ijk} is symmetric in i and j, the coefficient is reduced to r_{ik}, with the suffix i, representing the polarisation direction, replacing ij as follows: 11=1, 22=2, 33=3, 23=32=4, 13=31=5 and 12=21=6. The resulting change in refractive index for the different polarisation directions is described using a 6x3 2nd Rank tensor. For cystals with point group symmetry $\bar{4}3m$ such as GaAs the only non zero terms are r_{41}, r_{52} and r_{63}, and so the index change in the material is given by:

$$\begin{bmatrix} \Delta(1/n_1^2) \\ \Delta(1/n_2^2) \\ \Delta(1/n_3^2) \\ \Delta(1/n_4^2) \\ \Delta(1/n_5^2) \\ \Delta(1/n_6^2) \end{bmatrix} = \begin{bmatrix} 0 & 0 & 0 \\ 0 & 0 & 0 \\ 0 & 0 & 0 \\ r_{41} & 0 & 0 \\ 0 & r_{52} & 0 \\ 0 & 0 & r_{63} \end{bmatrix} \begin{bmatrix} E_1 \\ E_2 \\ E_3 \end{bmatrix} \qquad (2.25)$$

The coefficients are all equal in $\bar{4}3m$ materials, and so the constant r_{41} is used to represent all 3 of them. However, in MQW material the suffixes are maintained since the crystal symmetry is disrupted along the direction perpendicular to the plane of the wells.

For an electric field applied perpendicular to the plane of the wells,

$E_1 = E_2 = 0$ and E_3 is finite. This reduces equation 2.25 to:

$$\Delta(1/n_6)^2 = r_{63} E_3 \qquad (2.26)$$

If the index change is small ie $\Delta n << n$, then the index of the material can be written

$$n \approx n_0 + \tfrac{1}{2} n_0^3 r_{63} E_3 \qquad (2.27)$$

where n_0 is the refractive index at zero field. The coefficient r_{63} gives the index change experienced by light polarised in the direction x= y. For quantum well material this represents light polarised in the crystalographic plane [1$\bar{1}$0] i.e. in the plane of the well. The change in refractive index experienced by light polarised perpendicular to the plane of the well is zero since there is no component of Δn acting in this direction.

To express the coefficient r_{63} of an unclamped crystal in terms of the primary and secondary linear electro– optic effect one can write:

$$r_{63} = r_{63}' + p_{66} d_{36} \qquad (2.28)$$

where r_{63}' = primary or strain free electro– optic coefficient

p_{66} = strain elasto– optic coefficient

d_{36} = piezo– electric coefficient.

For devices being considered in this thesis, all samples are unclamped and so that there is a strain component to the refractive index index change.

Section 2.5.2 Quadratic Electo Optic Effect.

The linear electro optic effect is exhibited only by crystals which are non– centrosymmetric. A second effect, the quadratic electro– optic effect, is however found in all transparent materials. As indicated by the name, the quadratic electro– optic effect leads to a change in refractive index which is proportional to the square of the electric field strength. As a result, there is no reversal in the sign of the index change when the field direction is reversed. The index change is again expressed in terms of the optical indicatrix:

$$\Delta n = aE_k + bE_kE_l + \ldots \qquad (2.29)$$

where a and b are coefficients giving the index changes which are linear and

quadratic with electric field strength respectively. E_k and E_l are the electric field strengths and they may be in the same or different directions. In the cases considered though out this thesis, the fields are such that k= l= 3.

As with the linear electro– optic effect, there are clamped and unclamped values of the quadratic electro– optic coefficient and the deformation of the crystal associated with the quadratic electic field is electro– striction. The changes in refractive index resulting from the quadratic electro– optic effect are usually negligible when compared to those observed from the LEO, and so the QEO does not receive a great deal of attention in non centrosymmetric crystals.

Section 2.5.3 Electrorefractive Effect.

The dielectric constant of a material is a frequency dependent complex number:

$$\epsilon(\omega) = \epsilon_r(\omega) - i\epsilon_i(\omega) \qquad (2.30)$$

By definition, the refractive index $n(\omega)$ and extinction cefficient $k(\omega)$ are related to the dielectric function:

$$\sqrt{\epsilon(\omega)} = n(\omega) - ik(\omega) \qquad (2.31)$$
$$= N(\omega)$$

where $N(\omega)$ is the complex refractive index.

The Kramers– Kronig relation enables $\epsilon_r(\omega)$ to be evaluated from $\epsilon_i(\omega)$, so long as the latter is known at all frequencies and vice versa. As a consequence, if the imaginary part of the dielectic function is changed by some perturbation, then there must be a corresponding change in the real part. This interdependence is passed on to an interdependence of the refractive index and absorption of the material. So that if there is a change in the absorption of a material, there must be a corresponding refractive index change. The effect leading to the refractive index change associated with absorption changes in an electric field is electro– refraction.

To calculate the change in refractive index, the change in absorption at all frequencies must be known:

$$\Delta n(\omega) = \frac{c}{\pi} P\int_0^{\infty} \frac{\Delta\alpha(\omega')}{\omega'^2 - \omega^2} \, d\omega' \qquad (2.32)$$

In reality, the absorption spectrum is never known across the whole frequency range and the change in refractive index at a fequency ω can be accurately calculated from knowing the change in absorption in the spectral region close to ω [Whitehead et al '88(a)]. In section 2.4 the large changes in absorption experienced in MQW material in an electric field perpendicular to the plane of the quantum wells was discussed. Studies of the electrorefractive effect in MQW material have been carried out in models which include the n= 1 exciton resonances [Nagai et al '86, Hiroshima et al '87], modelled to Gaussian line shapes in the absorption spectrum [Chemla et al '88]. Both these studies showed large changes in the refractive index ($\Delta n \approx 0.05$) associated with the Stark shifts of the exciton resonances in the material. The calculations by [Hiroshima et al '87] included effects arising from the forbidden transitions which become allowed in the presence of an electric field. The electrorefractive effect has also been shown to be highly polarisation dependent [Shimizu et al '88], as expected from the highly polarisation dependent absorption [Weiner et al '85(a)]. Also, because of the persistence of the excitonic resonances both at room temperature and large electric fields perpendicular to the plane of the quantum wells, the electrorefractive effect observed in MQW material is much larger than that observed in bulk material [Van Eck et al '86]. It therefore seems that the electrorefractive effect could have a role to play in optoelectronic devices.

Section 2.6 Conclusions.

A study of the optical properties of MQW GaAs/AlGaAs, looking at a single finite potential well has been given. The density of states of the material gives a steep step– like density of states, characteristic of a two dimensional system. The model was extended to describe the optical properties of a multiple quantum well system in a semiconductor. It was seen how the band structure of GaAs affects the energy eigenvalues of the quantum wells, with the degeneracy at k= 0 of the heavy and light holes of the valence bands being lifted by the confinement. The strict interband transition rule $\Delta n = 0$ in quantum wells, which results from the orthogonality of the eigenfunctions in the wells, was seen to be relaxed by the different band parameters in the valence and conduction bands, with transitions $\Delta n = 2m+1$ having weak oscillation strengths.

Most remarkable in the material is the persistence of excitonic resonances in the absorption spectrum at room temperature and it is these exciton resonances that have a profound affect on the optical properties of the material. The excitons make the material highly birefringent at wavelengths close to the absorption edge, since interband transitions involving the heavy hole bands are forbidden for light polarised perpendicular to the plane of the quantum well. Whilst this is also true for bulk GaAs, it is more apparent in MQW GaAs/AlGaAs because of the lifting of the degeneracy of the heavy and light holes.

The confinement of electrons and holes to the quantum wells in GaAs has a profound affect on the material's properties. When an electric field is applied perpendicular to the plane of the wells, it is found that the exciton resonances persist for field strengths 50 times the classical ionisation field of an exciton. This persistence is explained in terms of the potential barrier which hinders the separation of the electron and hole, and with the coulomb attraction of the electron and hole maintained, the exciton's binding energy is large enough for the electron and hole to complete an orbit before being ionised. When an electric field is applied in the plane of the quantum wells, the behaviour is qualitativly similar to that of bulk GaAs, since their are no potential barriers preventing ionisation.

The exciton resonances are also seen to shift to lower energies when the field is applied perpendicular to the plane of the wells, and this is described as a quantum confined Stark effect (QCSE). The effect is two fold: the energy eigenvalues of the quantum well in an electric field shift to lower energies for the n= 1 states and the binding energy of the excitons decrease. If the excitonic effects are neglected in modelling the quanatum wells in an electric field, the effect for large wells (30nm) becomes qualitatively similar to the Franz– Keldysh effect exhibited by bulk GaAs, with the quenching of the allowed transitions and dominance of the forbidden transitions giving the tail of the absorption edge characteristic of the Franz– Keldysh effect. In the smaller wells (10nm) the effect is qualitatively very different to the bulk material, and the effect has been termed the quantum confined Franz– Keldysh effect.

The optical properties of MQW GaAs/AlGaAs in an electric field thus affected should lead to an enhancement of the electro– optic effect at wavelengths close to the material band gap through electro– refraction. An experimental study of the electro– optic and electro– absorption effects in the material follow in the following chapters of this thesis.

CHAPTER 3
MULTIPLE QUANTUM WELL WAVEGUIDE DESIGN, MATERIAL CHARACTERISATION AND INITIAL WAVEGUIDE ANALYSIS

SECTION 3.1 INTRODUCTION.

In the discussion of the optical properties of MQW structures in chapter 2, it was indicated that the electro–absorption and electro–optic effects of the material are enhanced compared to bulk GaAs. In order to study the effects within a waveguide configuration which is compatable with integrated optics, a waveguide structure had to be designed and the grown structure characterised. These processes are explained in this chapter, followed by the processes involved in fabricating electro–optic stripe waveguides. Finally, the characterisation of the fabricated stripe waveguide structures is described including wavelength dependancy of absorption in the waveguides.

SECTION 3.2 DESIGN OF MULTIPLE QUANTUM WELL WAVEGUIDES.

Section 3.2.1 Quantum Well Design.

The design of the quantum well structure was based on the requirement that it should exhibit a steep optical absorption edge with the n= 1 heavy and light hole exciton peaks well resolved at room temperature, and that the exciton peaks should persist at high D.C. electric fields ($\approx 10^5 cmV^{-1}$).

The dominant mechanism for exciton broadening is through the interface roughness at the well/barrier interface, leading to variations in the well width ΔL_z which are of the order of crystal monolayers [Weisbuch et al '81]. The associated broadening of exciton peaks (ΔE_i) is given by [Chemla et al '84]:

$$\Delta E_i \propto E_i \, \Delta L_z / L_z$$

So interface roughness in narrow wells lead to substantial broadening as a result of L_z being small and the large energies of narrow wells. It would therefore appear that having large wells reduces the broadening of the exciton peaks. In considering exciton widths observed through optical absorption, the well width variation (ΔL_z) which varies in units of atomic spacing is averaged over the area of the sample

illuminated. To maintain the exciton peaks at large fields, the well width must be kept below 10nm since excitons in wells larger than this experience a large reduction in binding energy in the presence of an electic field [Brum et al '85]. It is therefore argued [Chemla et al '84] that for well widths of ≈10nm and a mole fraction of Al in the $Al_xGa_{1-x}As$ barrier material of x= 0.3 it is possible to maximise the exciton binding energy without excessive broadening.

Section 3.2.2 Waveguide Design.

For maximum efficiency of an electro-optic modulator, the waveguide should be a stripe, propagation should be in the fundamental mode and the confinement of light to the quantum well region should be maximised. The design procedure was first to design a single moded planar waveguide structure that could be grown by MBE or MOVPE techniques and then model the etch depth required to give a single moded stripe waveguide.

The planar waveguide consisted of a high index MQW guiding layer (≈0.5μm thick) with lower index AlGaAs cladding layer on either side, thus giving a symmetric waveguide structure. The MQW structure decided upon consisted of 25 GaAs quantum wells of width 10nm and 26 $Al_{0.3}Ga_{0.7}As$ barriers of width 10nm. Modelling the planar waveguide was done using the effective index method [Kogelnik et al '74, Hewak et al '87] and involved adjusting the Al concentration (and hence the refractive index) of the $Al_xGa_{1-x}As$ cladding layer in order to obtain a single mode planar waveguide. The refractive indices of the AlGaAs layers of the structure were calculated using the empirical formula given by [Adachi '85] and the refractive index of the MQW structure was calculated using the weighted rms model [Ohke et al '85]. This model does not account for the different dispersion of the refractive index of MQW GaAs/AlGaAs compared with bulk AlGaAs. However, other models [Kahen et al '85, Suzuki et al '83] which do account for the dispersion close to the excitonic band edge, predict an increase in refractive index of 0.01 close to the exciton peaks of the MQW compared with the values predicted by the rms model. This increase in refractive index was taken into account when designing waveguides.

To make single moded stripe waveguides, the depth to which the waveguides were to etched had to be calculated. The WAVE variational method [Wilkinson et al '80], which models the guided mode to a series of Hermite-Gaussian functions, was used for this under the following conditions: 14 basis functions in the z direction and 7 basis functions in the x direction. These conditions had previously

been demonstrated to converge accurately to the effective index of the waveguide structure [MacBean '86].

Figure 3.1(a) shows the intensity contour plot and figure 3.1(b) shows an intensity profile across the waveguide for an optimised stripe waveguide. The structure was as follows: an MQW structure consisting of 25 GaAs quantum wells of width 10nm and 26 $Al_{0.3}Ga_{0.7}As$ of width 10nm and 2μm thick cladding layers consisting of $Al_{0.25}Ga_{0.75}As$. The etch depth 1.6μm yields a guided mode which is tightly confined to the stripe, with the intensity of the mode falling to 10% of the peak intensity at the edge of the stripe.

Section 3.2.3 Electrical Design.

An essential requirement of the waveguide design was that it be configured in such a way as to make it possible to to apply a large uniform DC electric field ($\approx 10^5$V/cm) perpendicular to the quantum well layers. A convenient method of achieving this is to grow the MQW waveguide in the centre of a p–i–n diode [Marshal et al '85], so that by reverse biasing the diode, a large field is experienced in the intrinsic region. A low leakage current is necessary so that the measured electro–optic effects in the MQW waveguide are not mixed with plasma effects [Tsang et al '89] and thermal effects both of which have a slow response time.

The novel electro–optic properties of MQW materials depend on the presence of well resolved excitons at the material band edge. Since broadening of the excitonic peaks in a non uniform electric field occurs [Stevens et al '88], finite doping in the intrinsic region of the p–i–n diode causes peak broadening and leads to a degredation in the material quality. In deciding on an acceptable doping level for an MQW region of a p–i–n diode, [MacBean '86] used the criterion that the variation in electric field strength led to a variation in resonance energy of the wells of less than one quarter the exciton binding energy of 10meV [Chemla et al '84]. An acceptable doping level in the intrinsic region was thus calculated to be $\leqslant 3x10^{15}cm^{-3}$. The low doping in the guiding region was also compatible with the requirement that absorption in the waveguide be kept to a minimum, since the low doping reduces the free carrier absorption. The specification on the doping concentration in the intrinsic layer of the diode was therefore $3x10^{15}cm^{-3}$.

To maintain a low loss optical waveguide, the doping of the waveguide cladding should be kept to a minimum. However, in considering the diode

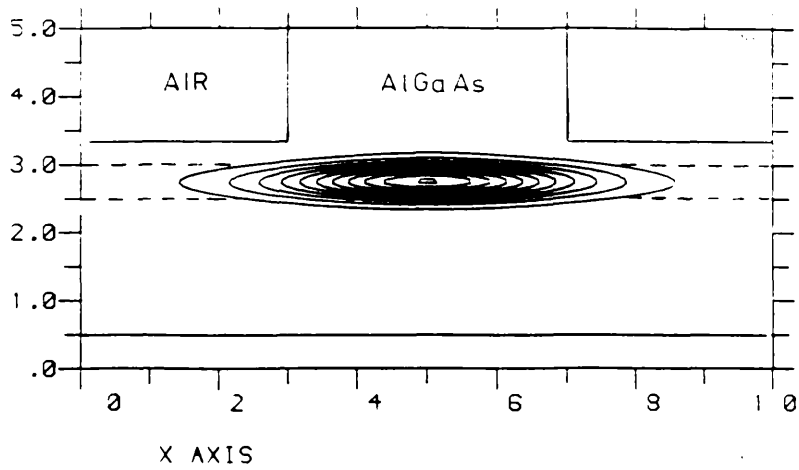

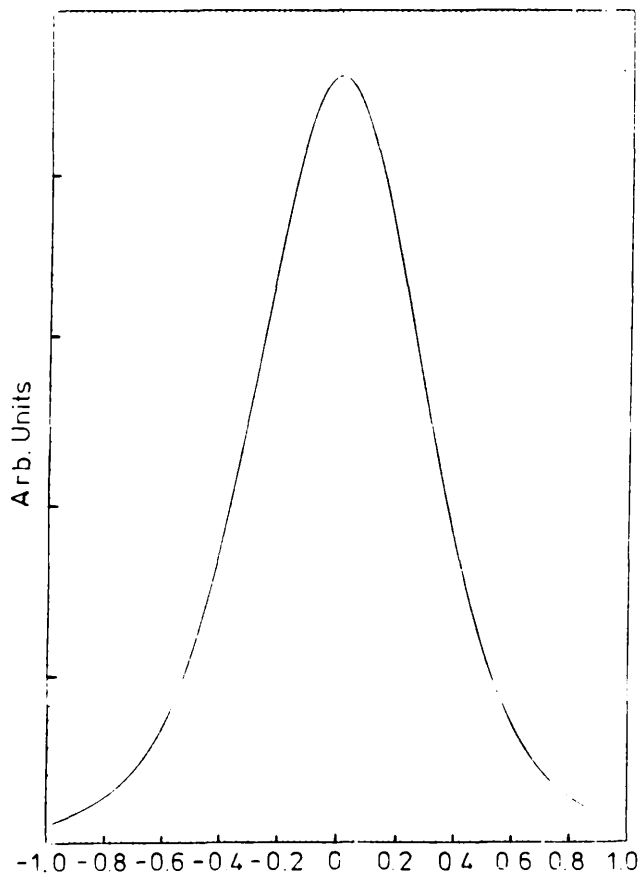

Figure 3.1
Modelling of stripe waveguides using the WAVE variational method.
(a) Intensity contour plot across the cross section of a stripe. The MQW region and stripe are indicated on the plot.
(b) Intensity profile across the stripe waveguide.

characteristics, if the doping concentration of the p− and n− regions are very low, then the depletion width of the diode will increase significantly as an increasing reverse bias voltage is applied. Hence, a compromise had to be made in the doping concentration of the cladding layers resulting in a specification on the doping concentration of $5x10^{16}cm^{-3}$. A highly doped p^+ GaAs layer was grown on the top of the p− doped cladding to allow fabrication of ohmic contacts to the waveguide diode.

Section 3.2.4 Depletion Width and Field Distribution in a P− I− N Diode.

To study the electro− absorption and electro− optic effects exhibited by the MQW material, both the electric field strength and distribution in the MQW region have to be known. This can be calculated for a p− i− n diode using the depletion width approximation.

Figure 3.2(a) shows the distribution of the space charge caused by the ionised impurities in the depletion region of a p− i− n diode, and the resulting electric field and potential are shown in figure 3.2(b) and (c) respectively. The intrinsic layer has a width D_i and a residual p− type doping concentration of N_i. The doping concentrations in the p− and n− regions are N_a and N_d and the depletion widths are L_a and L_d respectively. By Gauss's law, the field at any point within the depletion region is given by the integral of the enclosed charge from the depletion edge:

$$E(x) = \int_0^x \rho(x)/\epsilon\epsilon_0 \quad dx \qquad (3.1)$$

The charge density $\rho(x)$ is given by the doping concentration in the relevant region, and the resulting field distribution is shown in figure 3.2(b). The finite p− doping in the intrinsic region leads to the non− uniform field across the MQW region with the field strengths, E_1 and E_2, at the extremes of the i− region given by:

$$E_1 = \left[\frac{eN_d}{\epsilon\epsilon_0} \right] L_d \qquad (3.2a)$$

$$E_2 = \left[\frac{eN_d}{\epsilon\epsilon_0} \right] L_d - \left[\frac{eN_i}{\epsilon\epsilon_0} \right] D_i \qquad (3.2b)$$

The potential calculated across the diode from Lapla e equation is shown in figure 3.2(c), where φ_1, φ_2 and φ_3 are the potentials at the n− i and i− p

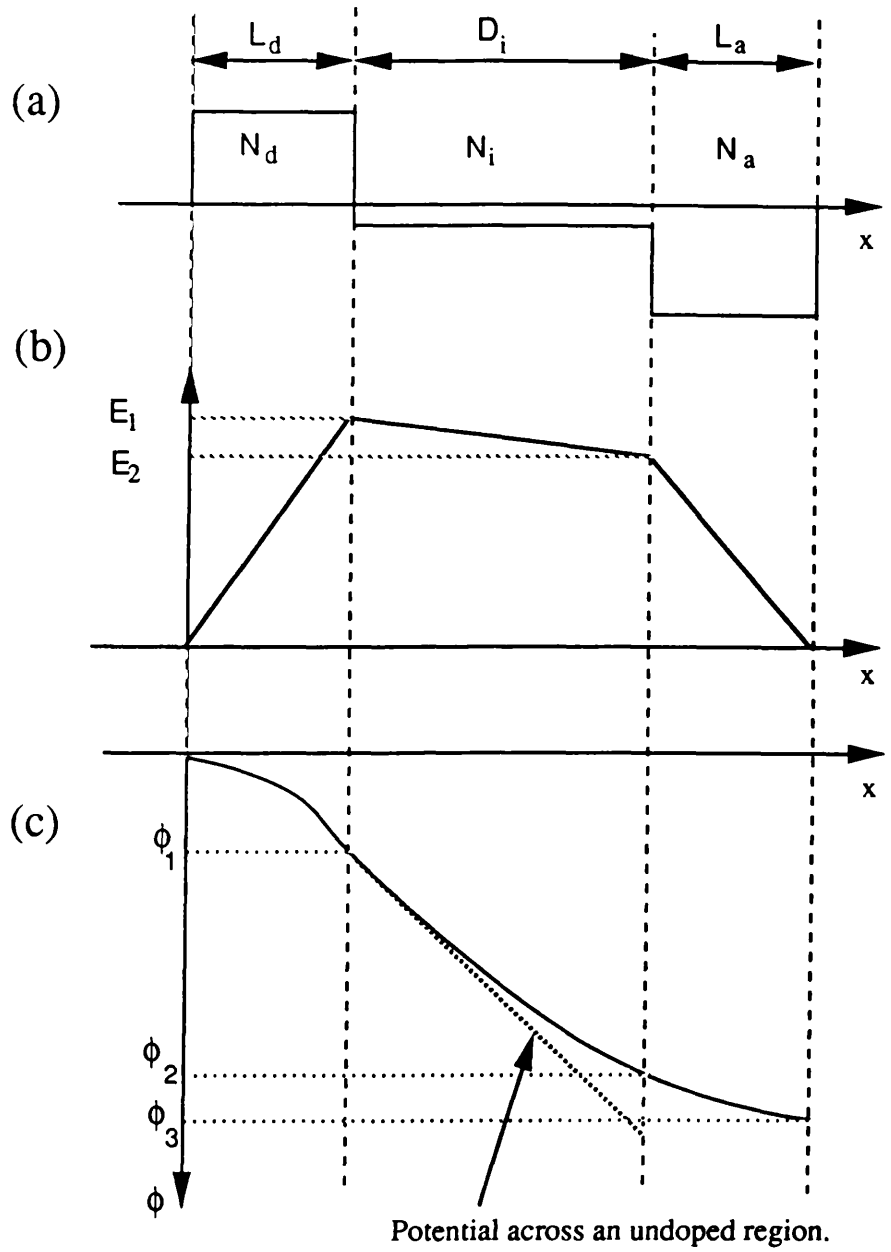

Figure 3.2
Depletion region of a p-i-n diode with p- and n- doping concentrations of N_a and N_d respectively and an intrinsic layer of thickness D_i and doping concentration N_i .

(a) Space charge distribution in the depletion region of a p-i-n diode. The depletion widths in the p- and n- doped regions are L_a and L_d respectively.

(b) Field distribution in the depletion region of a p-i-n diode, with field strengths E_1 and E_2 at the n-i and i-p interfaces respectively.

(c) Potential in the depletion region of a p-i-n diode. The potentials ϕ_1 , ϕ_2 and ϕ_3 are the potentials at the n-i interface, i-p interface and at the edge of the depletion region respectively.

junctions and at the edge of the p− depletion region respectively. These are given by:

$$\varphi_1 = \left[\frac{eN_d}{2\epsilon\epsilon_0} \right] L_d^2 \qquad (3.3a)$$

$$\varphi_2 - \varphi_1 = \left[\frac{eN_d}{2\epsilon\epsilon_0} \right] L_d D_i - \left[\frac{eN_i}{2\epsilon\epsilon_0} \right] D_i^2 \qquad (3.3b)$$

$$\varphi_3 - \varphi_2 = \left[\frac{eN_a}{2\epsilon\epsilon_0} \right] L_a^2 \qquad (3.3c)$$

The potential across the i−doped region would follow the straight line drawn in figure 3.2(c) if there was no residual doping in the i− region. However, the finite doping in the region leads to the deviation in the potential from a straight line. This variation appears in the second term of equation 3.3(b). The potential φ_3 is the potential across the entire depletion region of the diode, a potential which must include both the voltage applied to the diode and the built in potential of the p−i−n junction.

By charge neutrality, the net charge in the depletion region must be zero and the following relation must hold:

$$N_d.L_d = N_i.D_i + N_a.L_a \qquad (3.4)$$

Now substituting for L_a in the expression for φ_3 [the sum of equations 3.3(a), (b) and (c)] results in the following quadratic equation in L_d:

$$\frac{2\epsilon\epsilon_0}{e}\varphi_3 = N_d\left[1 + \frac{N_d}{N_a} \right]L_d^2 + 2N_dD_i\left[1 - \frac{N_i}{N_a} \right]L_d + N_i\left[1 + \frac{N_i}{N_a} \right]D_i^2 \qquad (3.5)$$

With L_d evaluated, L_a can be calculated from equation 3.5 and so the field strengths E_1 and E_2 in the diode can be calculated.

SECTION 3.3 MATERIAL CHARACTERISATION.

A number of MQW waveguide structures were grown for this work which, due to both design and growth problems, were not suitable for fabricating single mode stripe waveguides with optical confinement in the MQW region. The characterisation of the wafers included in the thesis has been limited to the wafers used sucessfully in the study of the electro−optic properties of MQW waveguides.

These include wafers to be refered to as MV348 (figure 3.3) grown by MOVPE techniques at the SERC Central Facility for III– V Semiconductors, Sheffield and A77 (figure 3.4) which was grown by MBE techniques in the Department of Electronics and Electrical Engineering, Glasgow. The characterisation of wafer A163 (figure 3.5) which was designed and used for fabricating electro– optic directional coupling switches which are described in chapter 6 has also been included in this section. To begin, section 3.3.1 dicusses a problem associated with the design in the waveguide.

Section 3.3.1 Slab Waveguide.

Each wafer was tested to ensure the planar waveguide structure grown supported a single planar guided mode, with confinement to the MQW region. In the early material design, an etch stop layer consisting of a 1μm layer of $Al_xGa_{1-x}As$ (x= 0.6) was grown below the waveguide structure. This enabled windows to be etched in the GaAs substrate, allowing devices to be fabricated with light propagating perpendicular to the layers. The etch stop layer, however, caused serious problems with the planar waveguide. A second planar waveguide was formed in this layer, making confinement to the MQW layer difficult to control. Since the devices to be studied were mainly waveguide devices, the etch stop layer was not necessary and so was removed from the design, solving the problem of the second planar waveguide in the material.

The three wafers: MV348, A77 and A163 all supported single planar modes for both TE and TM polarisation.

Section 3.3.2 Photoluminescence.

Photoluminescence analysis of the MQW samples was carried out to ensure the Al concentration in the waveguide cladding layers and the quantum well width were acceptably close to the original design and also to assess the quality of the material. A standard photoluminescence system was used. The samples taken from the grown wafer were mounted in a cryostat, cooled to a temperature of approximately 20K and illuminated with a HeNe laser operating at 632.8nm. The luminescence from the sample were collected by collimating lenses and focussed onto the slit of a monochromator. The luminescence spectrum was measured by scanning the monochromator through a wavelenth range and the signal at the output of the monochromator detected with a Ge detector. The signal was amplified using a lock– in amplifier and the amplified signal output to a chart

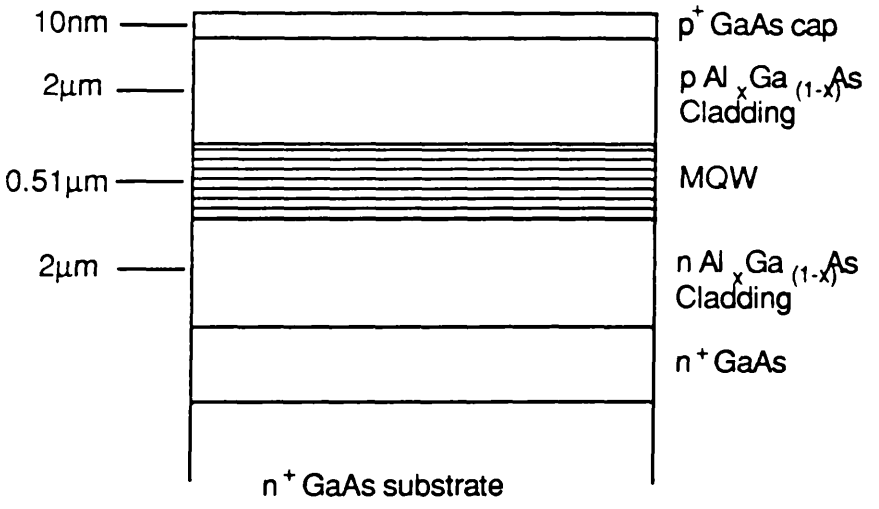

$p^+ > 10^{18} cm^{-3}$
$p = 5x10^{16} cm^{-3}$
$n = 5x10^{16} cm^{-3}$

$x = 0.25$

MQW Design: 25 wells of GaAs
26 barriers of $Al_yGa_{(1-y)}As$: y=0.3

Well width = 10nm
Barrrier width = 10nm

Doping $p^- < 10^{15} cm^{-3}$

Figure 3.3
Design of MQW planar waveguide structure MV348 grown by MOVPE.

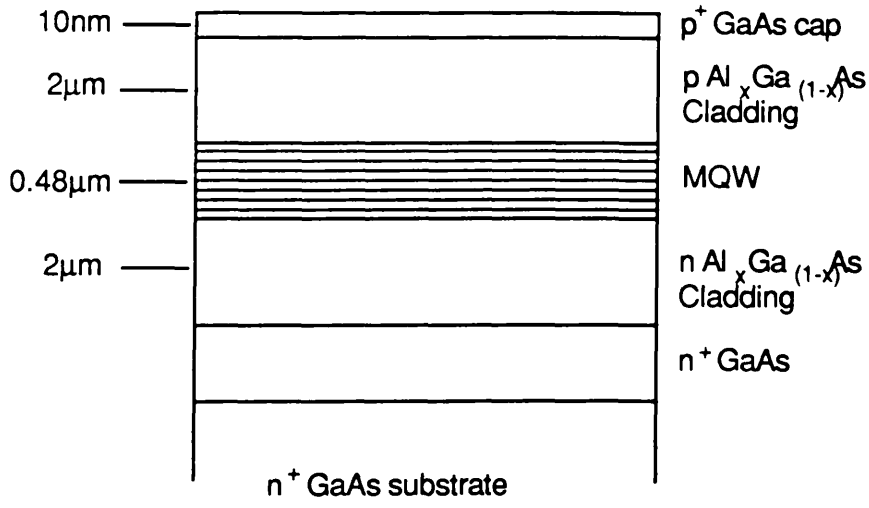

$p^+ > 10^{18}\ cm^{-3}$
$p = 5 \times 10^{16}\ cm^{-3}$
$n = 5 \times 10^{16}\ cm^{-3}$

$x = 0.35$

MQW Design: 7 wells of GaAs
8 barriers of $Al_y\ Ga_{(1-y)}\ As$: y=0.3

Well width = 10nm
Barrrier width = 60nm

Doping $p^- < 10^{15} cm^{-3}$

Figure 3.4
Design of MQW planar waveguide structure A77 grown by MBE.

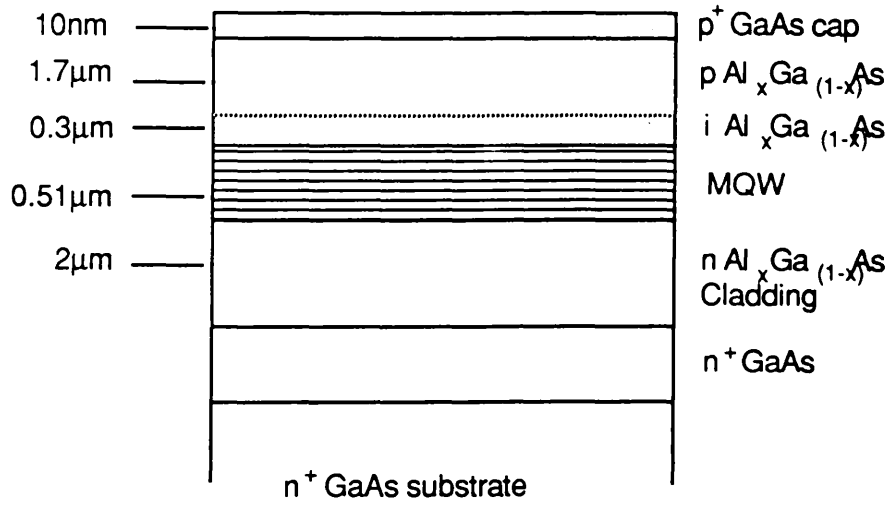

$p^+ > 10^{18}\ cm^{-3}$
$p = 5 \times 10^{16}\ cm^{-3}$
$n = 5 \times 10^{16}\ cm^{-3}$

$x = 0.25$

MQW Design: 25 wells of GaAs
26 barriers of $Al_y Ga_{(1-y)} As$: y=0.3

Well width = 10nm
Barrrier width = 10nm

Doping $p^- < 10^{15} cm^{-3}$

Figure 3.5
Design of MQW planar waveguide structure A163 grown by MBE.

recorder.

There were two features of interest in the photoluminescence spectra. Firstly a peak associated with bound excitons in the AlGaAs cladding layers from which the Al concentration in the AlGaAs could be calculated using the expression:

$$E_g = 1.512 + 1.455x \qquad (3.6)$$

where E_g is the photon energy of the luminescence peak in eV and x is the Al mole fraction in the AlGaAs. A second peak in the luminescence spectrum which was of interest was associated with the transition e1−lh1 in the quantum wells. From the energy of this luminescence peak, the well width in the sample was calculated using the finite quantum well model in GaAs/AlGaAs [Kawai et al '84].

Photoluminescence measurements were carried out on samples from the three wafers MV348, A77 and A163 and the material quality assessed from the results.

Photoluminescence results of wafer MV348

The photoluminescence spectrum obtained from measurements on sample MV348 at a temperature of 19k over the large spectral range of 635nm to 1.2μm are shown in figure 3.6(a), in which the two features of interest mentioned above are present. First a peak at a wavelength of 688.7nm associated with the bound exciton in the AlGaAs layers and second a peak at 797.5nm associated with the transition e1−lh1 in the quantum wells. These peaks are shown in greater detail in figures 3.6(b) and 3.6(c) resectively. The broad peak at approximately 830nm in figure 3.6(a) is luminescence from the GaAs substrate and capping layer of the sample.

From the peak at 688.7nm shown in figure 3.6(b), the mole fraction of Al in the cladding layer was calculated to be x= 0.2, slightly less than the value of x= 0.25 in the original design, although still acceptable. The well width calculated from the energy of the e1−lh1 transition (figure 3.6(b)) was 8.5nm, again less than the design had specified. The second peak shown in figure 3.6(c) was not properly identified, but was assigned to carbon impurities in the quantum wells.

Photoluminescence results of wafer A77

The photoluminescence measurements on wafer A77 were carried out at a

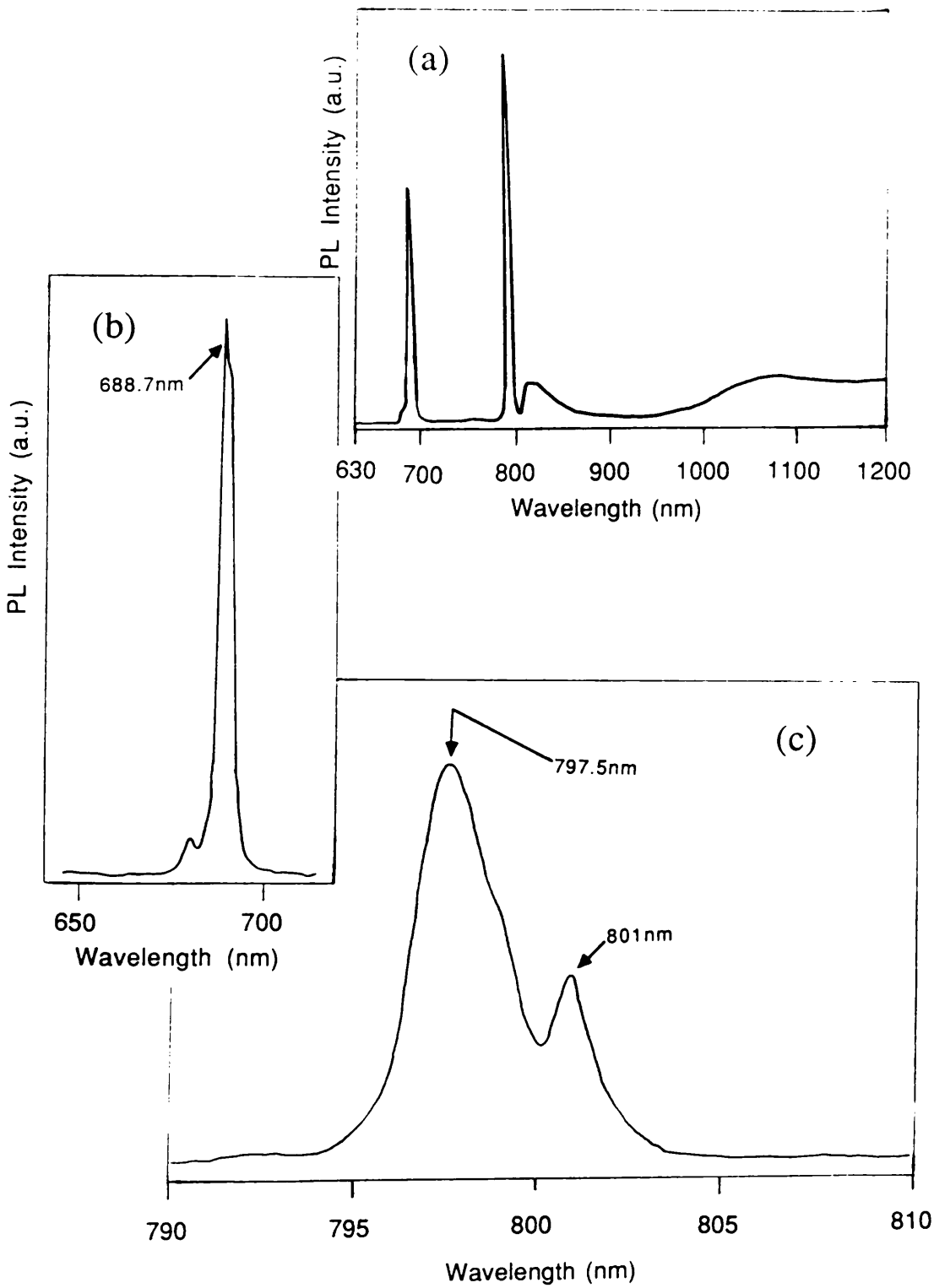

Figure 3.6
Photoluminescence spectra off wafer MV348.
(a) Luminescence showing peak at 868.7nm associated with bound exciton in AlGaAs cladding, and peak at 797.5nm from interband transitions in the MQW material.
(b) Expansion of peak at 868.7nm shown in (a).
(c) Expansion of peak at 797.5nm shown in (a).

temperature of 5k and, as with sample MV348, the luminescence spectrum showed the two peaks associated with the exciton in the AlGaAs cladding and the e1−lh1 transition in the quantum well. These features are shown in figures 3.7(a) and (b) respectively. The mole fraction of Al in the cladding layer was calculated from the peak at 617.5nm to be x= 0.34, very close to the design of x= 0.35 and the well width was calculated from the peak at 797.3nm in figure 3.7(b) to be 10.1nm. The small linewidth of 3.4meV of the peak in figure 3.7(b) indicates good quality of the well/barrier interface and that that the quantum wells are high quality. The shoulder on the low energy side of the peak shown in figure 3.7(b) is the result of luminescence from the e1− hh1 exciton transition.

Photoluminescence results of wafer A163

The two luminescence peaks resulting from the exciton in the AlGaAs cladding and recombination in the quantum well are again present in the luminescence spesctrum of sample A163. These measurements, taken at a temperature of 25k indicate a mole Al concentration of x= 0.3 from the peak at 641.9nm in figure 3.8(a). The well width was calculated to be 7.5nm from the peak at 785.8nm. However, measuring at a muber of points across the wafer indicated a variation in well width across the wafer of 6.7nm to 7.5nm. The large differences of Al mole fraction and well width from the the design was the result of excessive Ga desorption during growth [Stanley '89]. The sample was however still considered acceptable for fabrication directional coupling devices.

Section 3.3.3 Diode I− V Characterisation.

Electrical characterisation involved examining the reverse bias breakdown voltage and leakage current of the p− i− n diode by measuring the diode I− V characteristics. The diode was designed such that a d.c. electric field of greater than 10^5V/cm could be applied to the MQW region of the waveguide with a reverse bias voltage of ≈10V. Thus, a diode characteristic with a reverse bias break down voltage of greater than 10 volts and a leakage current of less than 100nA was required. The low leakage current was required to reduce thermal and plasma effects [Faist et al '87] whilst measuring the electro− optic effects in the waveguides. To calculate the field distribution across the p− i− n diode, the built− in potential of the diode had to be measured and this potential was taken from the I− V characteristic of the diode by measuring the forward bias voltage at which it began to conduct.

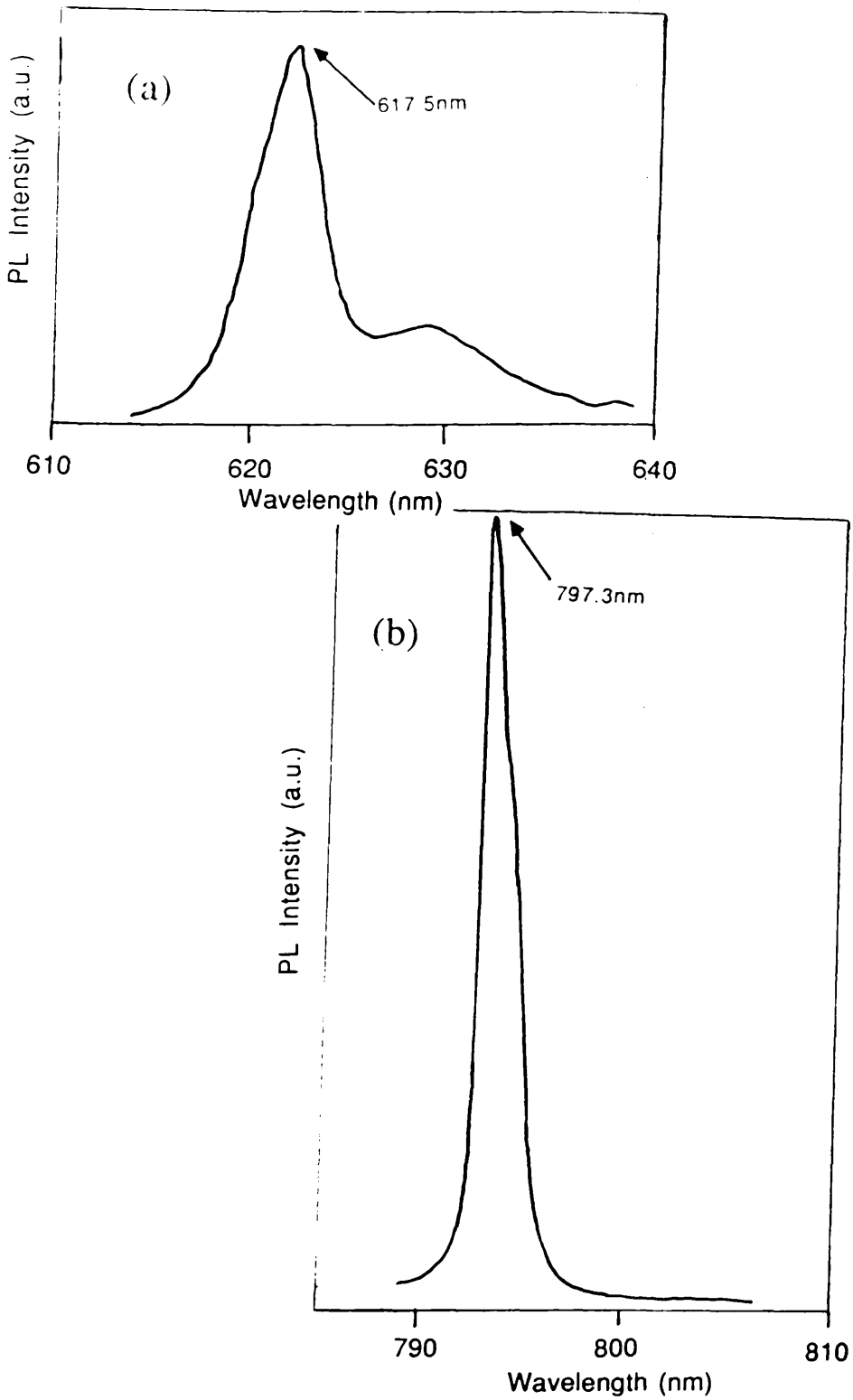

Figure 3.7
Photoluminescence spectra off wafer A77.
(a) Luminescence showing peak associated with bound excitons in the AlGaAs cladding.
(b) Luminescence peak from interband transitions in the MQW material.

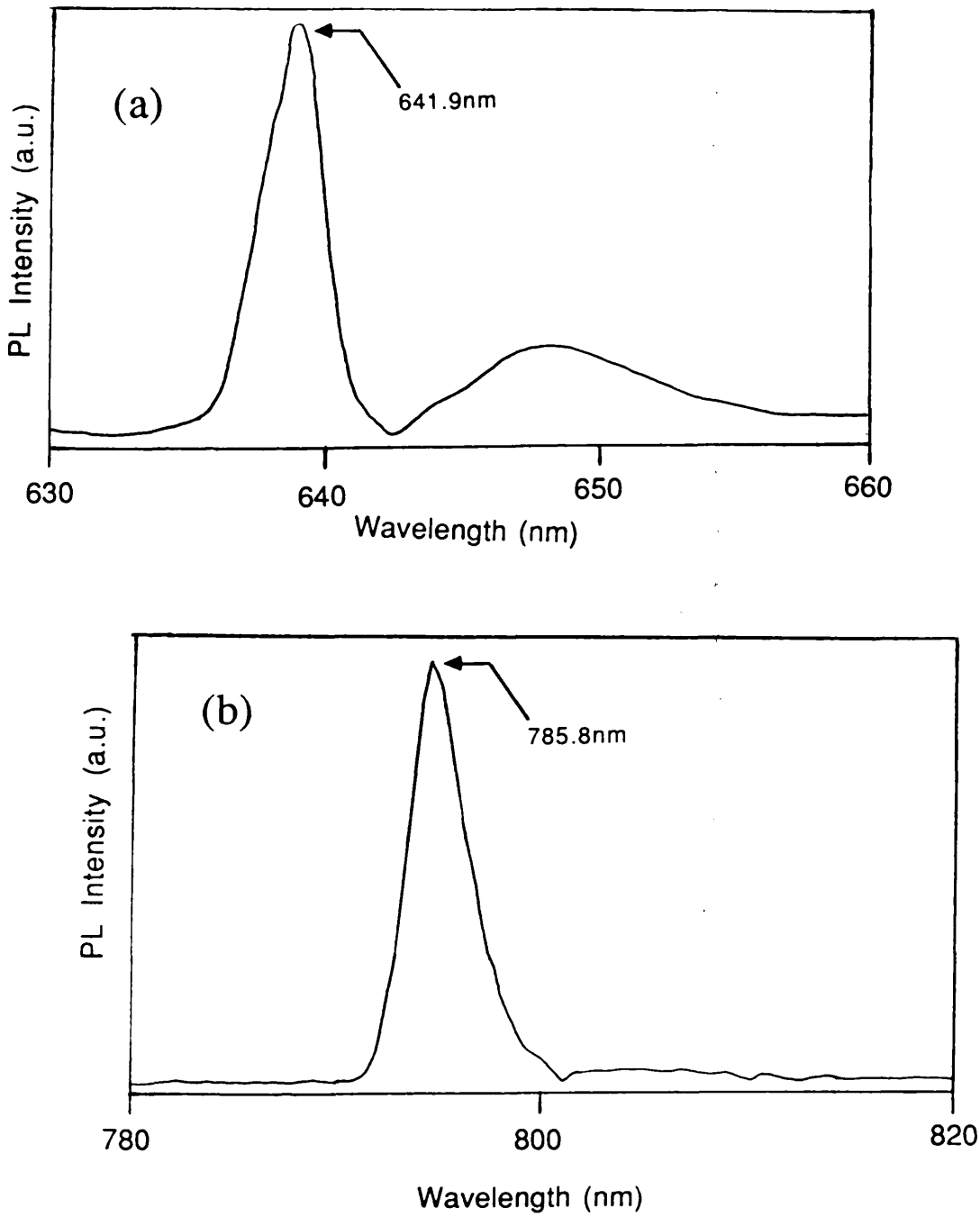

Figure 3.8
Photoluminescence spectra off wafer A163.
(a) Luminescence showing peak associated with bound excitons in the AlGaAs cladding.
(b) Luminescence peak from interband transitions in the MQW material.

The I–V characteristics of diode devices were measured using a Hewlett–Packard 4145 Parameter Analyser. The devices had 70μm diameter p–ohmic contact to the p^+ GaAs capping layer and an n–ohmic contact to the N^+ GaAs substrate. To isolate the devices, mesa structures were formed by etching to a depth below the p–i–n junctions, reducing the device area and so reducing the leakage current caused by material defects. If the ohmic contact was not protected with photoresist during the formation of the mesa structures, the reverse breakdown voltage of the diode was very low ($\approx$3 volts) probably due to the transportation of metal from the contact to the diode junction. The formation of ohmic contacts is discussed in more detail in section 3.4.2. The resultant I–V curves measured from the devices are shown in figure 3.9 for diodes fabricated on wafers MV348 and A163 and figure 3.10 for wafer A77.

Figure 3.9(a) shows the full rectifying I–V characteristic of a diode device fabricated on wafer MV348. The forward biased characteristic shows the diode conducting for voltages greater than 1.1 volt, indicating that this is the built in potential across the diode. The reverse bias characteristic shows that the diode experiences Zener breakdown at –42 volts, with the current increasing very sharply at breakdown. The breakdown voltage corresponds to an electric field of $8.6\text{x}10^5$ V/cm, assuming that the depletion region does not extend significantly beyond the i–region. The typical dark current for a reverse biased diode was 100pA.

The full rectifying I–V characteristic of a diode device fabricated on wafer A163 is shown in figure 3.9(b). The forward biased characteristic of the diode shows the conduction of the diode beginning at a voltage of 1.1 volts. The increase in voltage is not as rapid as in wafer MV348, and this could be due to poor ohmic contacts rather than the quality of the material. As with MV348 there is a sharp increase in current at the Zener breakdown, in this case at 39 volts reverse bias. Again, typical dark currents for the reverse biased diode were 100pA.

Figure 3.10(a) shows the forward and reverse bias characteristic of wafer A77. The figure shows the diode conducting when forward biased, but when reverse biased, the diode did not reach Zener breakdown even at 100 volts, conducting less than 500pA. To calculate the associated field in the diode at 100 volts reverse bias, doping concentations of $N_a = N_d = 1.8\text{x}10^{16}\text{cm}^{-1}$ and $N_i = 1.7\text{x}10^{15}\text{cm}^{-1}$ (taken from C–V measurements) were used. The depletion region was calculated to extend 1.7μm into both of the doped regions of the diode with a resultant field strength of $4.5\text{x}10^5$V/cm. The indication therefore was that the depletion region of the diode was extending significantly beyond the i–region at large reverse bias

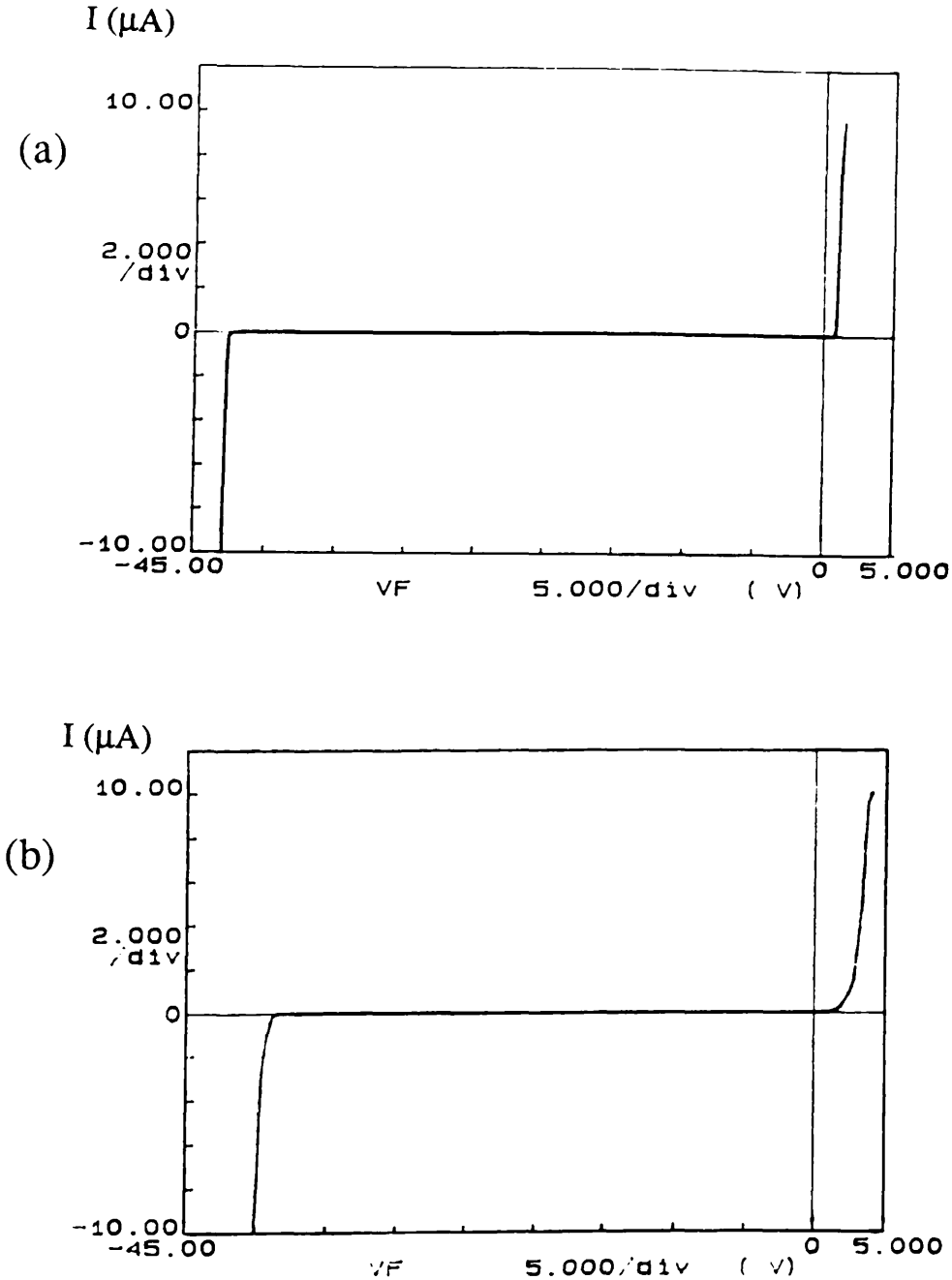

Figure 3.9
Diode characteristics of MQW p-i-n structures.
(a) Full rectifying characteristics of wafer MV348
(b) Full rectifying characteristics of wafer A163

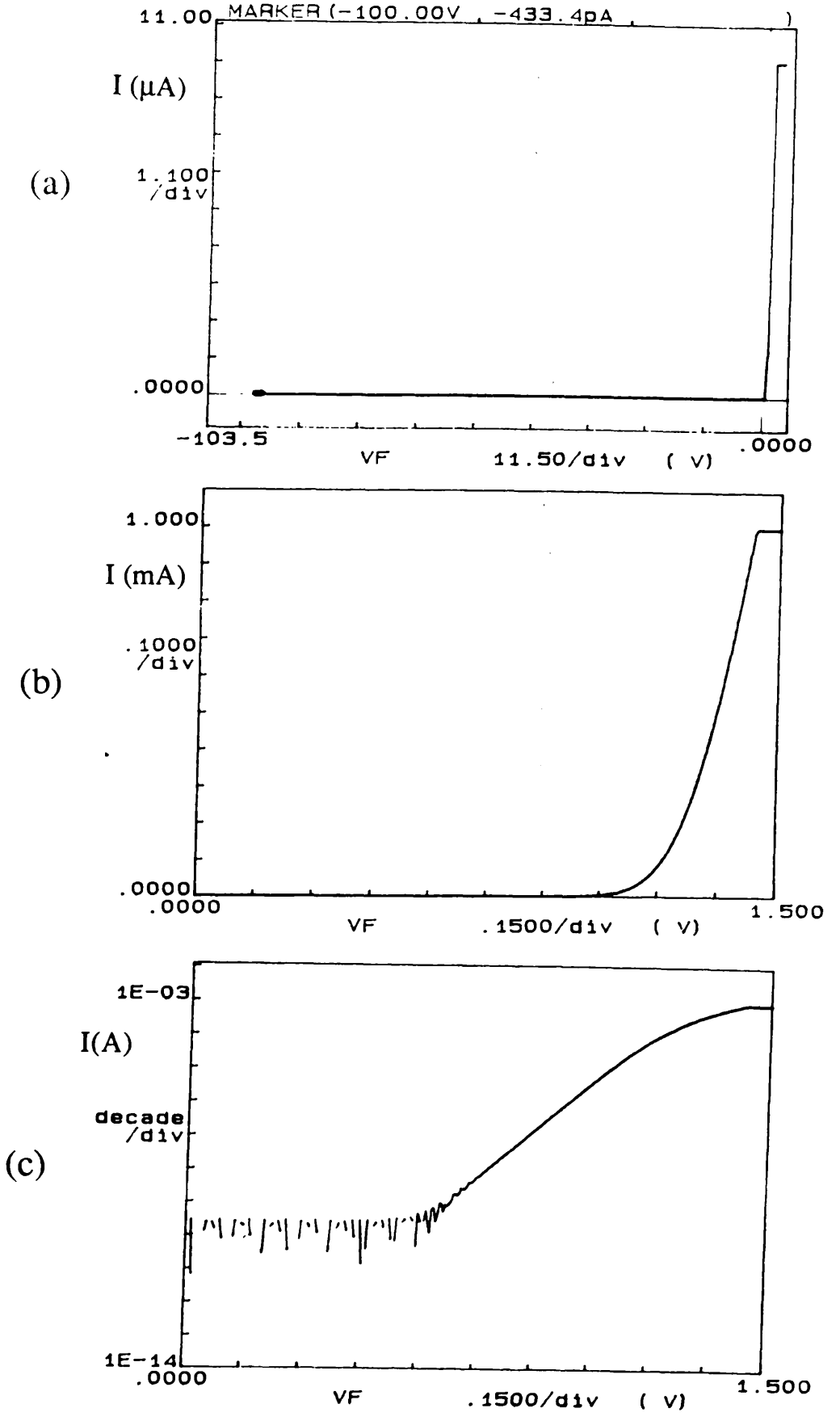

Figure 3.10
Diode characteristics of wafer A77.
(a) Full rectifying characteristics, (b) Forward bias characteristics (linear scales)
(c) Forward bias characteristics (current scale logarithmic).

voltages.

To confirm that the wafer did in fact contain a diode, the foward bias characteristic of the device was measured in more detail. Figure 3.10(b) and (c) show the forward biased I– V characteristic with the current plotted on a linear and logarithmic scales respectively. Figure 3.10(b) shows that the conduction across the diode does not begin to conduct significantly until a forward bias voltage of 1.05 volts is applied, indicating that this is the built in potential of the diode.

The current of less than 10^{-9}A and its random nature at voltages below 0.75V as shown in the logarithmic plot of figure 3.10(c) indicates that the conduction is dominated by generation– recombination [Sze '85]. For voltages larger than 0.75 volts and up to 1.2 volts, the conduction increases exponentially over 5 decades of current. In this regime, the current is dominated by carrier diffusion across the p– i– n diode. The calculated ideality factor (η) of 1.8 is the same as the value measured by [MacBean '86] in an MQW GaAs/AlGaAs p– i– n waveguide structure. For voltages greater than 1.2 volts, the diode is operating in a regime where the ohmic drop across the sample contacts and bulk semiconductor dominate the conduction, and current becomes proportional to voltage. The forward bias characteristics of the device therefore show that the material did contain a suitable diode, although the depletion width of the diode was likely to extend well beyond the i– region.

Section 3.3.5 Capacitance– Voltage Measurements.

The doping concentrations of the p– i– n diode had to be measured so that the electric field strength across the diode depletion region could be calculated. A standard method of measuring the doping concentrations at a p– n junction is through capacitance– voltage (C– V) measurements; a technique which was used through out this work for assesing the doping concentrations of the grown waveguide structures.

Theory of C– V Measurements.

When an increasing reverse bias voltage is applied to a p– i– n diode of doping concentrations N_a, N_i and N_d respectively, there is a corresponding increase in the depletion layer thickness by amounts ΔL_a and ΔL_d in the p– and n– doped regions respectively with a corresponding increase in the space charge of ΔQ at each side of the diode junction.

$$|\Delta Q| = |eN_d \Delta L_d| = |eN_a \Delta L_a| \qquad (3.6)$$

Thus, the junction capacitance C_j can be defined as the differential capacitance presented by the junction when a small a.c. voltage of amplitude ΔV_a is superimposed on a d.c. bias of V_a:

$$C_j = \left| \frac{dQ}{dV_a} \right|_{Va} \qquad (3.7)$$

The definition leads to the expression for the junction capacitance:

$$C_j = A \left[\frac{e \epsilon \epsilon_0}{2V_t} (N_a+N_d) \right]^{\frac{1}{2}} \left[(N_d/N_a)^{\frac{1}{2}} + (N_a/N_d)^{\frac{1}{2}} \right]^{-1} \qquad (3.8)$$

where A = Device area,

ϵ = Dielectric constant of the semiconductor,

ϵ_0= Permeability of free space,

V_t= Total junction voltage, including the built in voltage.

When the i− region, which in this case has residual p− doping, is not completely depleted of carriers, then $N_d >> N_a$ and equ 3.8 can be reduced to:

$$C_j = A \left[\frac{e \epsilon \epsilon_0}{2V_t} \right]^{\frac{1}{2}} \sqrt{N_a} \qquad (3.9)$$

However, when the i− doped region is completely depleted so that the two edges of the depletion region lie within the p− and n− layers, the equation 3.9 is no longer valid. The diodes for this work were designed to have $N_a = N_d = N$, so allowing the following approximation to be made:

$$C_j = A \left[\frac{e \epsilon \epsilon_0}{4V_t} \right]^{\frac{1}{2}} \sqrt{N} \qquad (3.10)$$

From equations 3.9 and 3.10, it is apparent that a plot of $(1/C^2)$ against V_t will yield straight lines from which the doping concentrations can be calculated.

Experiment.

The C− V measurements were carried out using an Hewlet Packard 4275A LCR meter. The devices measured, which were the same as those used for the I− V measurements, were probed between the p− and n− ohmic contacts and an a.c. voltage of 0.05V rms with a frequency of 1MHz applied to the device. This

was superimposed on a d.c. bias voltage swept from −10 volts to +2 volts and as the bias voltage was changed, the differential capacitance as defined in equation 3.8 was measured. The results of the C−V measurements obtained for each of the grown wafers and the doping concentrations calculated from these measurements are presented below.

C−V Results from Wafer MV348.

The capacitance against voltage results for wafer MV348 were taken from measurements on devices with a mesa diameter of 180μm. Figure 3.11(a) shows the results for voltages in the range −10 volts to +2 volts plotted as $1/C^2$ against voltage and figure 3.11(b) shows the results of measurements taken in the range −1 volt to + 1.4 volts, again plotted as $1/C^2$ against voltage.

The $1/C^2-V$ characteristic of figure 3.11(a) has two linear regions. As the bias voltage was decreased, a change in gradient occurred at +0.5V as the depletion region in the intrinsic region (residual p^- doping) extended into the p− doped cladding layer. The intrinsically doped region of the p−i−n diode was therefore shown to be fully depleted at zero volts, and the entire MQW region of the waveguide therefore experienced an electric field at all bias voltages less than +0.5 volts. At bias voltages less than +0.5 volts, the gradient of the linear region of the $1/C^2-V$ plot is related to the doping concentration in the p− doped region. Substituting the gradient into equation 3.10 indicates a doping concentration of $8.4\text{x}10^{16}\text{cm}^{-3}$. The second linear region, shown in more detail figure 3.11(b), is seen for bias voltages from 0.5 to 1.3 volts. This corresponds to the depletion region of the diode being in the intrinsically doped MQW region and a doping concentration in the i− region of $4.6\text{x}10^{15}\text{cm}^{-3}$ was calculated.

C−V Results from Wafer A77.

The capacitance against voltage measurements results for wafer A77 were taken from measurements on diode devices with a diameter of 200μm. Figure 3.12(a) shows a plot of $1/C^2$ against voltage in the range −10 volts to +1.2 volts and figure 3.12(b) shows the equivalent plot concentrating on the voltage range −2 volts to +1.2 volts.

As with wafer MV348, there are two linear regions in the $1/C^2-V$ characteristic associated with the doping concentrations in the p− doped and i− doped regions of the diode. The change in gradient occurs at zero bias voltage

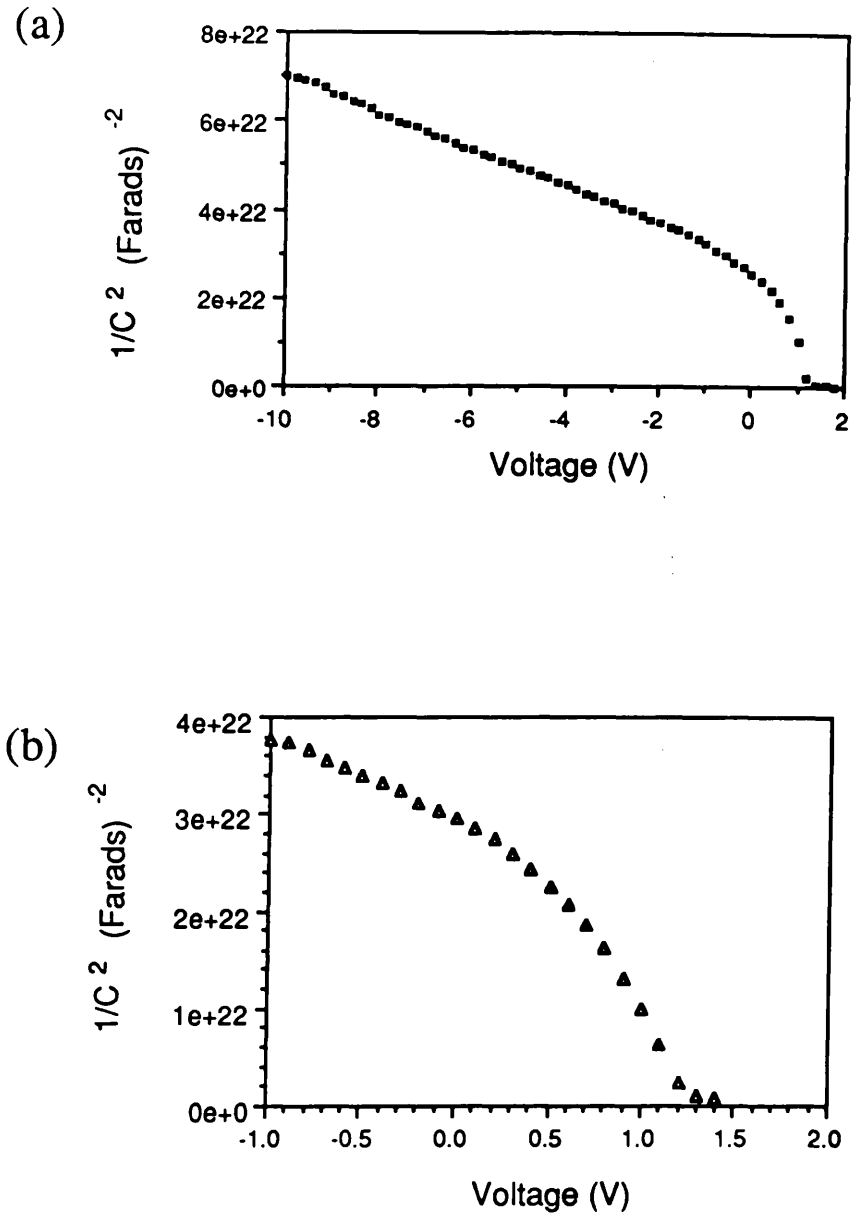

Figure 3.11
Capacitance against Voltage for p-i-n diode MV348 for assesing doping concentrations in the material
(a) C-V measurements to give doping concentration in n-doped cladding
(b) C-V measurements to give doping concentration in i-doped MQW.

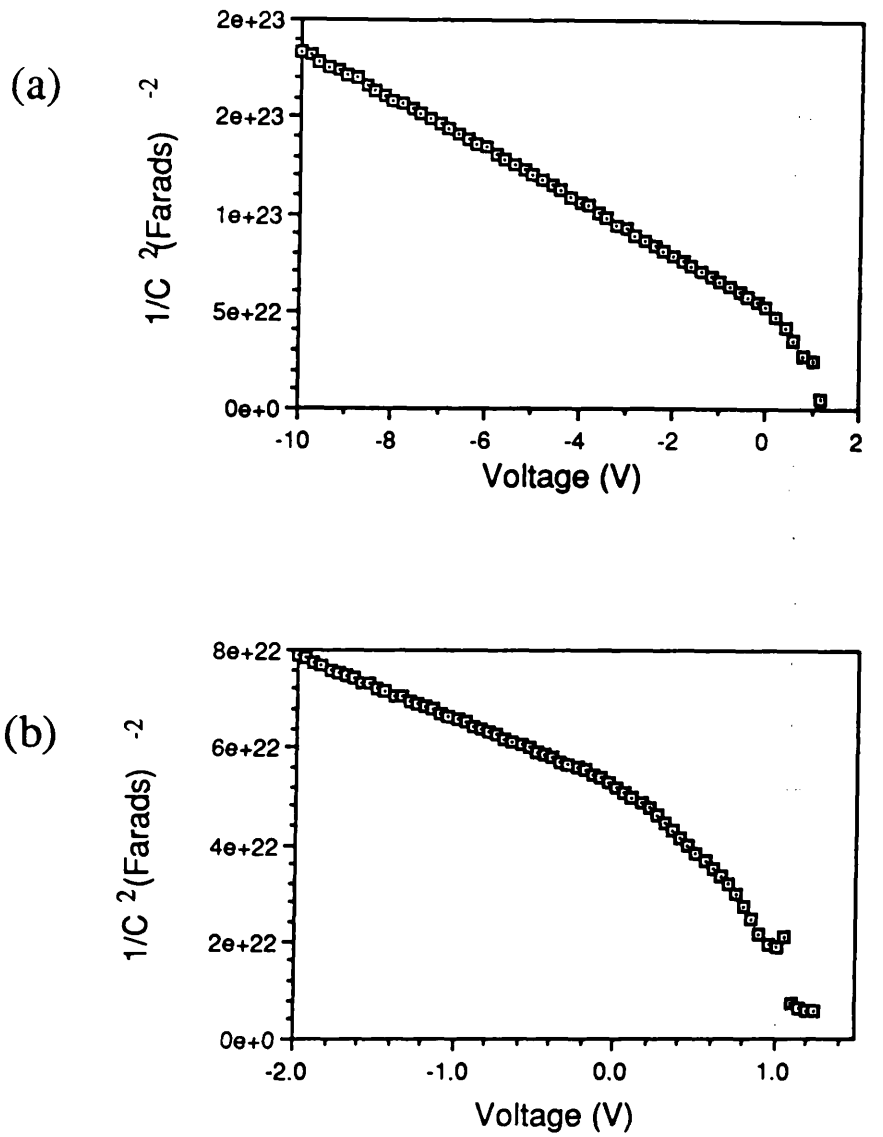

Figure 3.12
Capacitance against Voltage for p-i-n diode A77 for assesing doping concentrations in the material.
(a) C-V measurements to give doping concentration in the n-doped cladding.
(b) C-V measurements to give doping concentration in the i-doped MQW.

indicating that the i− doped region is just depleted with zero bias. Using equation 3.10, the gradient of figure 3.12(a) at reverse bias voltages leads to a calculated doping concentration of $1.8x10^{16}cm^{-3}$. Substituting the gradient of figure 3.12(b) for forward bias voltages up to 1.2 volts into equation 3.9 leads to a calculated doping concentration in the i− region of $1.7x10^{15}cm^{-3}$.

C− V Results from Wafer A163.

Diode devices of diameter 70μm were used to characterise the doping concentrations in the wafer A163. Figure 3.13(a) shows a plot of $1/C^2$ against voltage for bias voltages from −10 volts to +2 volts and figure 3.13(b) shows a plot of $1/C^2$ against voltage for bais voltages from −1 volt to +2 volts.

The two linear regions associated with the doping concentrations in the p− and i− doped regions are again present as shown in figure 3.13(a). The gradient of the plot for the reverse bias voltages is consistent with a doping concentration of $5x10^{15}cm^{-3}$ in the p− doped cladding region. Figure 3.13(b) shows a plot of $1/C^2$ against voltage for bias voltages in the range −1 volt to +2 volts, for which there is a change in gradient of the curve $1/C^2$ against voltage which occurs at two bias voltages. One change occurs at zero bias and a second change occurs at +1 volt bias. The change in gradient at zero volts is likely to be the result of a change in permitivity between the AlGaAs cladding and the MQW region since the calculated depletion width at zero volts is 0.75μm, consistent with the width of the intrinsic region in the design of wafer A163. The gradient is consistent with doping a concentration of $2.5x10^{14}cm^{-3}$.

Section 3.3.6 Depletion Width and Field Distribution of Wafer MV348.

Using the analysis of section 3.2.4 and the doping concentrations calculated from C− V measurements, a study of the field and depletion widths of wafer MV348 was carried out, both of these parameters being required for analysing the results of the electro− optic effects in the material.

The doping profile of the diode was shown, by C− V measurements, to be $N_d = 8.4x10^{16}cm^{-3}$, $N_i = 4.6x10^{15}cm^{-3}$ and $N_a = 8.4x10^{16}cm^{-3}$. The width of the intrinsic region was 0.55μm and the built in voltage was 1.1V. Using these values, the depletion width and the fields E_1 and E_2 were calculated for a range of applied reverse bias voltages from 0V to 10V. The resulting curves of depletion widths in the p− and n− regions against applied voltage is shown in figure

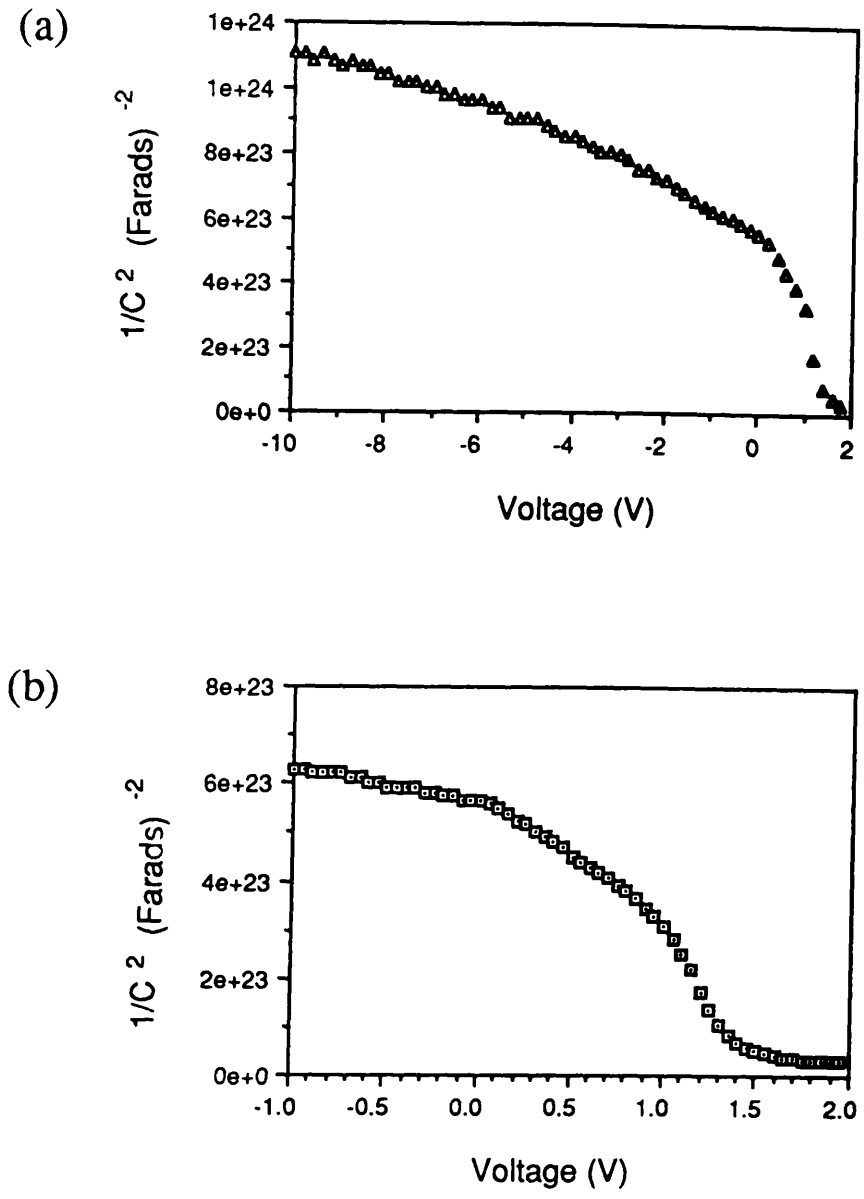

Figure 3.13
Capacitance against voltage measurements for p-i-n diode A163 for assesing doping concentrations in the material.
(a) C-V measurements to give doping concentration in n-doped cladding.
(b) C-V measurements to give doping concentration in i-doped MQW.

3.14(a), and the field strength E_1 against voltage is shown in figure 3.14(b).

It can be seen that the intrinsic region of the diode was completely depleted for zero volts bias in agreement with the results from the C– V measurements and that there is a significant increase in the depletion width with increasing reverse bias voltage. This is the result of the low doping concentration in both the p– and n– doped cladding layers of the waveguide, kept low to keep the free carrier absorption to a minimum. The variation in the field strength across the MQW region of $3.5x10^4$V/cm is also larger than desired, but still within the limits specified by [MacBean '86]. This is due to the doping in the i– region of the diode being higher than designed.

Section 3.3.7 Conclusion.

The MQW waveguide wafers which were designed as shown in figures 3.3– 5 and grown by either MOVPE or MBE techniques were characterised using photoluminescence techniques and I-V and C-V electrical probing. The results of the three succesfully grown wafers (MV348, A77 and A163) have been given and a summary of the structures of the grown wafers are shown in table 3.1 below.

Wafer	Well Width (nm)	Al mole Fraction	Doping Concentration p/n (cm^{-3})	i
MV348	8.5nm	0.2	$8.4x10^{16}$	$4.6x10^{15}$
A77	10.1nm	0.34	$1.8x10^{16}$	$1.7x10^{15}$
A163	6.7- 7.5nm	0.3	$5x10^{15}$	$2.5x10^{14}$

TABLE 3.1: Summary of the wafers grown for MQW waveguides.

3.4 FABRICATION OF ACTIVE STRIPE WAVEGUIDES.

The characterisation of the planar waveguiding structures MV348, A77 and A163 had shown that these waveguide structures were suitable for fabricating electrically active waveguides. The stripe guides were required to be single mode with ohmic contacts running continuously along the length of the guide. Standard photolithography techniques were used to define a negative pattern of the stripe

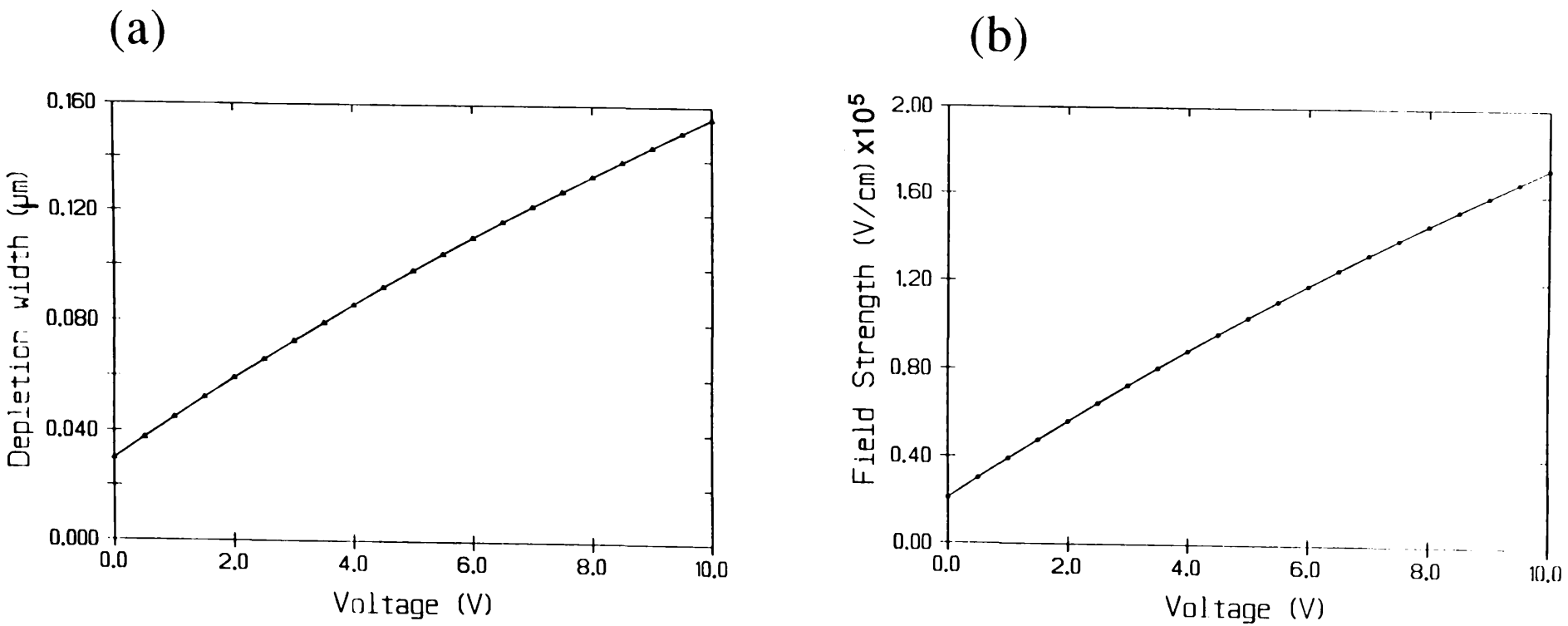

Figure 3.14
(a) Depletion width in the n region of diode MV348 as a function of applied reverse bias voltage. The depletion width is calculated from equation 3.5 using data from the material characterisation.
(b) Electric field strength in the intrinsic region of diode MV348 as a function of reverse bias voltage.

waveguides in photoresist, followed by thermal evaporation of the metal contacts and metal lift off. To form the stripes of the waveguides, dry etching techniques were used with the metal of the ohmic contact being used as an etch mask. Ohmic contacts were also evaporated on the reverse side (N+ doped) of the sample, allowing a voltage to be applied across the guide. The fabrication of the sripe waveguides is described in greater detail in the following sections.

Section 3.4.1 Photolithography.

The pattern of the stripe waveguides were defined onto samples of approximate size 6mm x 7mm using photolithography techniques. The sample first had to be thoroughly cleaned in analar grade organic solvents before beginning the photolithography. This reduced the amount of dust particles on the sample which would interupt the pattern of the waveguides in the photoresist. It also greatly increased the adhesion of metals evaporated onto the semiconductor surface at a later stage. The sample preparation is summarised in the following steps:

(a)Soaked in trichloroethelene in an ultrasonic bath for 5minutes
(b)Rinsed and soaked in methanol in an ultrasonic bath for 5 minutes.
(c)Rinsed and soaked in acetone in an ultrasonic bath for 5 minutes.
(d)Rinsed in de-ionised water and blown dry in dry nitrogen.

A positive photoresist (Shipley AZ1450J) dispensed onto the surface of the sample through a 0.45μm filter was then spun at a speed of 8000rpm for 30 seconds. This left a 2.5μm thick film on the sample, with a build up of photoresist at the sample corners of up to 50μm. The photoresist was cured by baking at 85°C for 15 minutes to drive off the solvents in the resist, soaking in chlorobenzene for 15 minutes, blown dry and finally baked for a further 5 minutes at 85°C. The sample could then be exposed to ultra– violet light through a shadow mask which defined the pattern of the waveguides. A diagram of the mask used for fabricating stripe waveguides is shown in fig 3.15. It consisted of sets of 3,4 and 5μm wide waveguides with 100μm x 200μm contact pads every 1mm along the length of the waveguide. The sample and mask were mounted on a mask aligner and the two brought into contact and exposed to 365nm u.v. light from a mercury lamp for approximately 10 seconds. The u.v. light acts upon the photoactive compound of the positive photoresist, rendering the exposed photoresist more soluble in the high pH developer. The exposed sample was then developed in Shipley microposit developer for 50 seconds, which removed exposed photoresist.

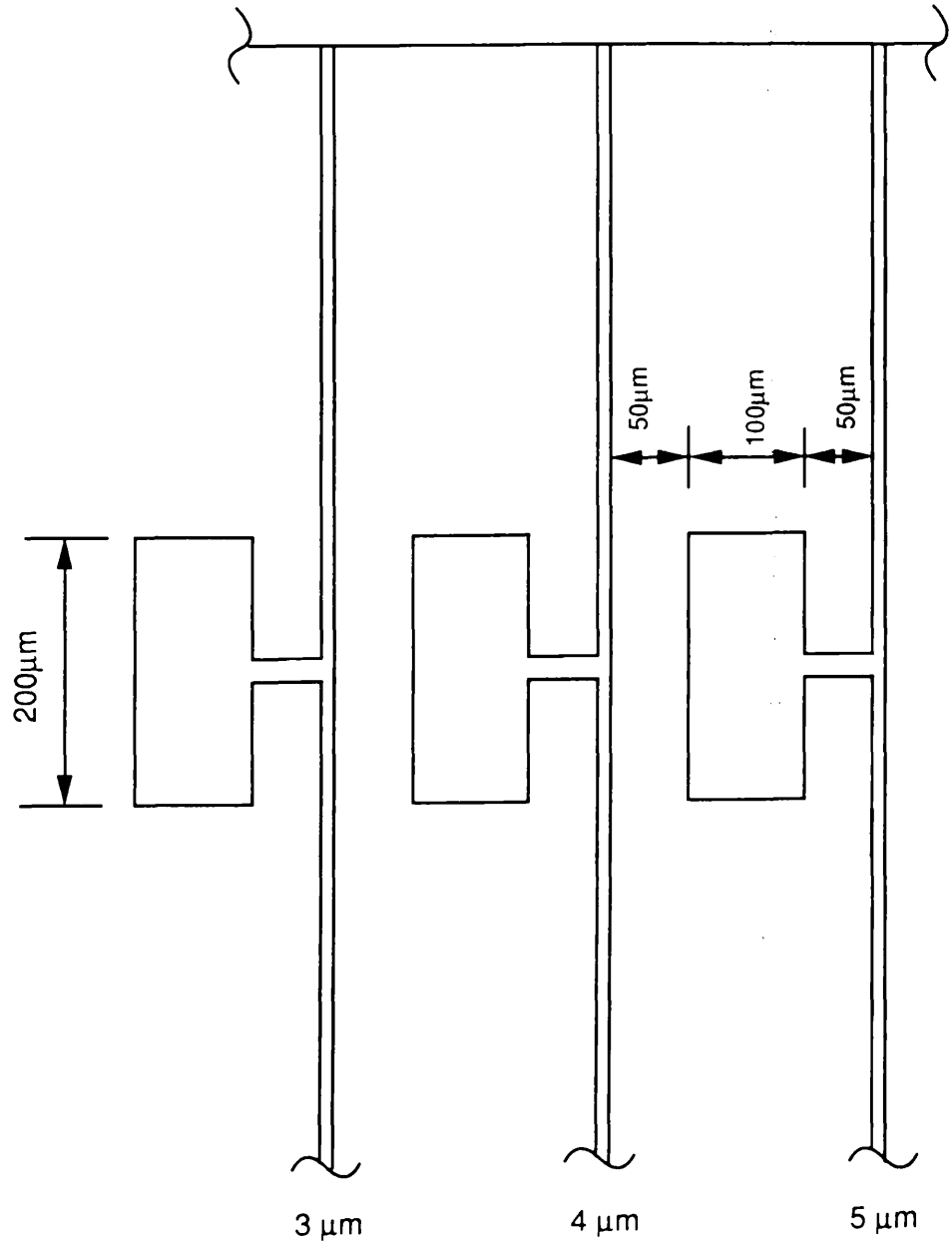

Figure 3.15
Schematic diagram of the waveguide mask used to define the waveguide patterns during photolithography.

Soaking the sample in Chlorbenzene affects the wall profile of the developed photoresist, which assists in the lift off process described later, by hardening the photoresist. After soaking the sample for 15 minutes, the photoresist is hardened to a depth of approximately 0.5μm from the surface of the film, so that the underlying photoresist is developed at a faster rate than the top surface, therby producing an overhang of the photoresist.

Whilst exposing the photoresist, the mask must be in intimate contact with the sample if small features such as 3μm wide stripe waveguides are to be defined. Any air gap between the sample and mask leads to poor quality line definition because of the diffraction of light between the mask and photoresist. The build up of resist at the sample corners during the spinning process prevented good contact being made, and so had to be removed by introducing the following extra step to the photolithography. Before exposing the sample to the waveguide pattern, the sample edges were exposed and developed, removing the build up of photoresist at the edge of the sample. In this way a larger area of the sample was in contact with the mask, reducing diffraction, and greatly improving the continuity of the waveguides.

Section 3.4.2 Fabrication of Ohmic Contacts to GaAs.

With a negative pattern of the waveguides defined in the photoresist, the next step was to thermally evaporate metal contacts onto the sample. The metal evaporated onto the semiconductor surface then formed a positive pattern of the waveguides and acted as an etch mask during the dry etching process as well as forming the electrical contacts to the waveguides. In addition to the contacts to the p− doped waveguide surface, contacts were required on the n− doped substrate, both of these contacts being required to be ohmic. In terms of metal/semiconductor contacts, an ohmic contact is defined as one in which the voltage drop across the contact is negligible compared with the voltage drop across the device [Roderick '88].

When a metal and semiconductor are brought into contact, the Fermi levels at the interface are pinned and band bending occurs. When the work function of the metal is greater than that of the semiconductor, as is generally the case for metal to n− doped GaAs, the bands bend upwards. For a metal with a work function less than that of the semiconductor, as is generally the case for a metal in contact with p− doped GaAs, the bands bend downwards. In both of these cases, the carriers encounter a Shottky barrier and the contact has a rectifying characteristic;

not the required ohmic characteristic.

In order to achieve the ohmic characteristic, the doping level in the GaAs at the metal/semiconductor interface must be increased such that the barrier width is reduced, and the barrier appears almost transparent to the carriers. Increasing the doping level was achieved by thermal evaporation of metals onto the GaAs and thermal annealing. A summary of the metals used and a brief explanation of the reactions taking place during the annealing for both n− ohmic and p− ohmic contacts are given below

N− Ohmic Contacts.

The metals used to form the n− ohmic contacts were the well established combination Ge/Au/Ni/Au [Patrick '86], thermally evaporated in a vacuum at a pressure of $2x10^{-6}$ Torr and to thicknesses of 1.6kHz/12kHz/700Hz/6kHz, as measured at a quartz crystal thickness monitor. The contact was then annealed at 340°C on a strip heater for 15 seconds in a reducing atmosphere of 5% H_2 in Ar. The reactions leading to the degenerate doping of the GaAs at the interface have been suggested by Ogawa et al '80 and is summarised below.

As the sample is heated (300°C), the GaAs begins to decompose, mainly by the reaction : Au + GaAs → AuGa + As. Ni takes a catalytic role, promoting the reaction by removal of As, forming NiAs. At the higher temperature of 340°C, the Ge diffuses inward, partly being captured by NiAs and partly doping the GaAs. With the metal/GaAs interface degenerately doped, the Shottky barrier is narrowed such that carriers can readily tunnel through. The top layer of Au on the contact is to reduce sheet resistance of the contact.

P− Ohmic Contacts.

A common p− dopant in GaAs is Zn, and so is a natural choice for p− ohmic contacts [Sharma '81]. The metal combination used in this work was Au/Zn/Au thermally evaporated to thicknesses of 30nm/30nm/80nm in a vacuum of $5x10^{-6}$ Torr. The sample was RF cleaned by an Ar plasma in the evaporation chamber for 15 minutes before the metals were evaporated [Hofler et al]. This removed the oxidised surface of the GaAs which would act to increase the potential barrier at the GaAs/metal interface [Roderick '88]. Annealing of the contacts was again at a temperature of 340°C for 15 seconds. At this temperature, the Zn diffuses into the GaAs, leading to a degenerately p− doped GaAs/metal interface, allowing carriers to

tunnel through the narrowed Shottky barrier.

Lift– off

To leave a positive pattern of the waveguides defined by the metal contacts, the metal evaporated onto photoresist on the sample had to be removed /lifted off, thus leaving a pattern of the stripe waveguide defined by metal on the GaAs surface and exposed GaAs else where. This lift off process was done by immersing the sample in acetone which disolves the photoresist and removes the metal not in direct contact with the GaAs. The break between the metal on the GaAs and the metal on the photoresist caused by the overhanging photoresist, speeds up the lift off and gives a better defined metal mask. Without the overhang, metal was evaporated onto the walls of the photoresist so that, after lift– off, thin trails of metal from the wall of the photoresist remained attached to the edges of the waveguide mask, degrading the quality of the mask.

Section 3.4.3 Dry Etching of Waveguides

Reactive Ion Etching (RIE) in $SiCl_4$ in a Plasma Tech 80 machine was used for the etching of the waveguides to define the stripes. RIE was chosen in preference to wet chemical etching because the directionality of RIE leads to more vertical wall profiles. The other available RIE system used the gas mixture of methane/hydrogen for the etching, but the etch rates obtained with this etch were considered to be too slow for etching 1.5μm of AlGaAs. The conditions used for etching the waveguides in $SiCl_4$ were as follows: gas flow 25 standard cc/min (sccm), chamber pressure 10 mtorr, dc bias of table 825 volts, RF power 100 Watts. The etch rate for these conditions was variable within the range 0.25μm/min to 0.33μm/min, so for each batch of waveguides etched, calibration samples were etched to establish the etch rate.

Once the waveguides were etched to the correct depth, a NiCr mask was removed from the sample by immersing it in concentrated HCl for 15 seconds, rinsing in de– ionised water for 30 seconds and finally blown dry in dry nitrogen. This left etched stripe waveguides with ohmic contacts exposed on the surface. Figure 3.16 shows an s.e.m. micrograph of a completed waveguide: figure 3.16(a) showing a 3μm wide waveguide with its 100μm x 200μm contact pad and figue 3.16(b) showing a close up of the waveguide, giving an indication of the vertical wall profile.

(a)

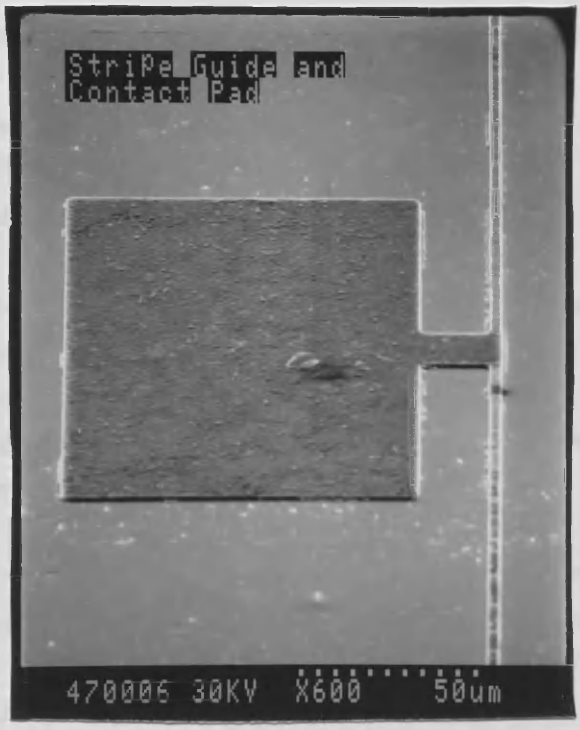

(b)

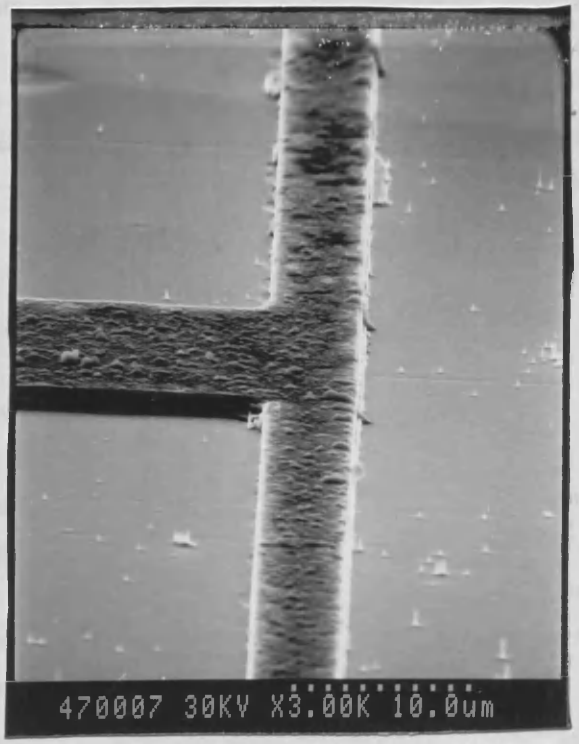

Figure 3.16
SEM micrographs of a fabricated stripe waveguide with an electrode running along the top of the stripe.
(a) Waveguide with contact pad
(b) Waveguide at the point where the contact pad joins.

The ohmic contacts on the top of the waveguides and on the reverse side of the sample could now be simultaneously annealed on a strip heater, by heating the sample to 330°C for 15 seconds as described in the previous section.

Section 3.4.4 Cleaving and Mounting Waveguides.

The proposed experiments to be carried out using the fabricated waveguides required guides of 1mm in length or less and with high quality facets at the guide ends to give a good coupling efficiency of light into the waveguide. These facets were obtained by cleaving the sample along the crystallographic planes [110] and [1$\bar{1}$0], using a diamond stylus scriber to initialise the cleave.

The guides also had to be mounted so that a voltage could be applied across them whilst light was end fire coupled into them. For this purpose, small pcb's were designed that would fit between the microscope objectives of the end fire rig whilst being held by a pcb edge connector. The waveguide sample was bonded onto the pcb, substrate down, using Johnson–Mathey silver epoxy, which remained nonconducting until it had been cured at 140°C for 15 minutes. This curing was done in a vacuum oven to reduce the deposition of organic contaminants from the heated pcb onto the sample. The waveguides fabricated and mounted were then ready for electro–optic probing of the MQW GaAs/AlGaAs.

SECTION 3.5 INITIAL TESTING OF WAVEGUIDES.

Section 3.5.1 Dye Laser System.

To study the wavelength dependence of the electro–optic properties of MQW material at wavelengths close to the material absorption edge, a c.w. Styryl–9 dye laser system was used as the light source. The tuning range of the laser was from 790nm to 920nm, allowing experiments to be carried out at photon energies close to the material absorption edge.

The dye laser was pumped by a c.w. argon ion laser operating at 514nm with an output power of 3.5W. The output of the argon ion laser was focused on to a high speed/high pressure jet of dye solution which passed through the folded cavity of the dye laser. The dye solution was made with 165cm^3 of propylene carbonate and 1010cm^3 of ethelyne glycol to 1g of dye. The wavelengths at which the dye lases is dependent on the wavelength at which the laser cavity is the least lossy

within the dye fluorescence range. In the Coherent 599 dye laser this was controlled by a 3 plate birefringent filter, with a 40GHz bandwidth, positioned at the Brewster's angle in the laser cavity. A full explanation of the lasing mechanism is given in reference [Schafer '77].

Section 3.5.2 End–Fire Coupling in Waveguides.

Of the three main techniques used for coupling light into waveguides i.e. grating coupling, prism coupling and end fire coupling, the latter was adopted. The principle behind end–fire coupling is to match the field profile of the light being coupled into a guide to that of the guided mode. Since the fundamental guided mode of a stripe waveguide is very similar to the Gaussian beam profile of the laser output, coupling can be obtained by focusing the input beam down to the dimensions of the waveguide at the cleaved facet.

A x40 microscope objective was used to focus the input beam from the dye laser onto the waveguide end facet. The coupling efficiency was highly sensitive to the focusing of the input beam since any mismatch between the beam profile and guided mode profile lead to loss from the guided mode into radiation modes. The microscope objective was therefore mounted onto a micromanipulation block with differential drives, allowing the positioning of the focused input beam to be controlled to a resolution of 0.1μm. Coupling losses were then limited by field mismatch and the quality of the cleaved facets. A microscope objective similar to the input objective was mounted on a second micromanipulating block at the output of the guide, allowing the waveguide output to be focused onto either a IR camera or Si detector. The fabricated waveguides were mounted on a device manipulator, which was positioned between the micromanipulating blocks as shown in figure 3.17. The device manipulator allowed sample movements of pitch, role, yaw and two degrees of movement in the plane perpendicular to the optical axis of the end fire rig.

Section 3.5.3 Mode Profiles of fabricated waveguides.

The fabricated stripe waveguides were required to be single moded and have tight confinement under the etched rib. Their mode profiles were therefore examined by end firing light from the Styryl–9 dye laser into the waveguides and observing the output mode using an I.R. camera and T.V. monitor.

Figure 3.18(a) shows a photograph of the output mode from a waveguide

(a)

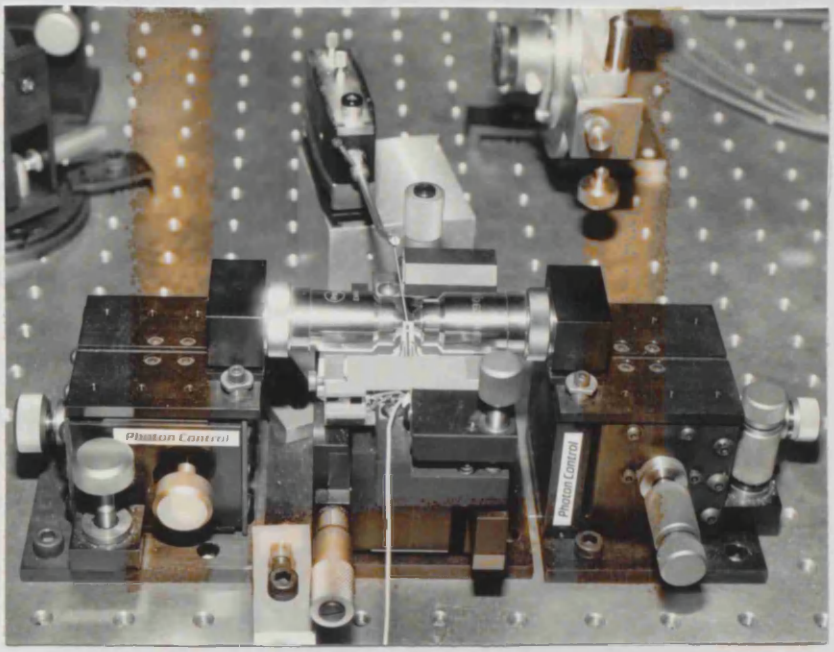

(b)

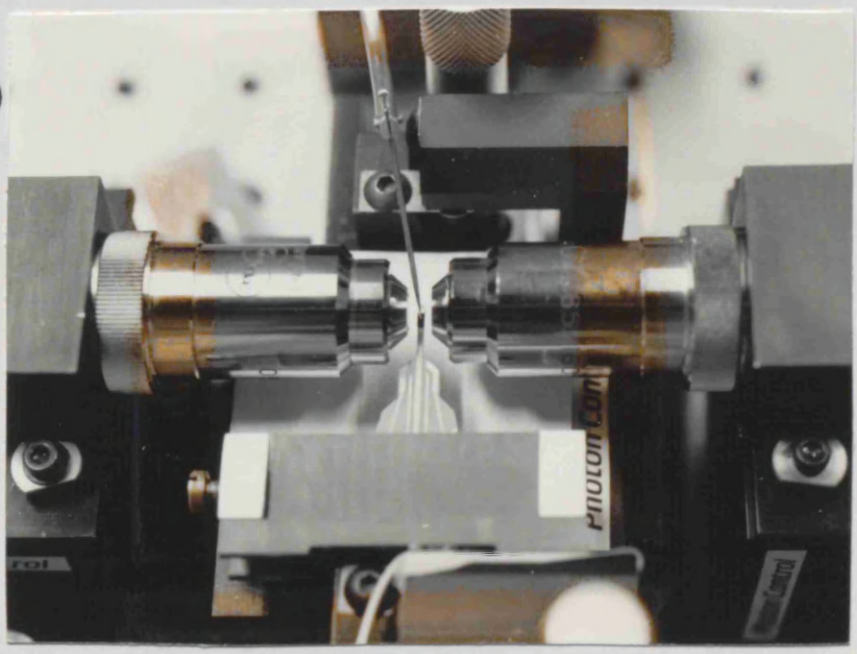

Figure 3.17
(a)Photograph of the end-fire rig used for coupling light into the waveguides.
(b)A stripe waveguide mounted on the end-fire rig with an electrical contact probe to the waveguide contact pad.

(a)

(b)

Figure 3.18
Photographs of the output mode of stripe waveguides taken from the monitor screen.
(a)TE_0 mode from 3 μm wide waveguide MV348.
(b)TE_0 mode from 3μm wide waveguide A77.

fabricated in wafer MV348. The width of the stripe was 3μm and the waveguide was etched to a depth of 1.6μm, leaving a cladding layer of thickness 0.2μm beyond the stripe. The waveguide propagated only the lowest order mode, and is seen here propagating the TE_0 mode. Figure 3.18(b) shows a similar photograph of the output mode from a 3μm wide stripe waveguide fabricated in wafer A77. The rib was etched to a depth of 1.5μm, leaving a cladding layer of 0.3μm beyond the stripe, and the waveguide is shown here propagating the TE_0 mode.

Section 3.5.4 Fabry–Perot Loss Measurements in Stripe Waveguides.

If the loss in a waveguide is low enough that multiple cavity transmissions through the waveguide cannot be neglected, then changing the optical path length of the waveguide results in Fabry–Perot resonances in the transmission. The transmission through the waveguide is represented by:

$$T = \frac{I_0 A}{(1-RA)^2 + 4RA\sin^2(\delta/2)} \qquad (3.11)$$

where A is the intensity loss per pass, R is the reflectivity at the facets and δ is the detuning off the high transmission resonance. A monochromatic light source is assumed in the above expression. The resonant transmission (T_r) and antiresonant transmission (T_a) are thus given by:

$$T_r = \frac{I_0 A}{(1-AR)^2} \qquad T_a = \frac{I_0 A}{(1+AR)^2} \qquad (3.12)$$

From the resonant and antiresonant transmissions, the absorption in the waveguide (Γ dB/cm) can be then calculated using the expression:

$$\Gamma = -10\log_{10}\left[\frac{1}{R}\frac{(k-1)^{\frac{1}{2}}}{(k+1)}\right] \qquad (3.13)$$

where k= Tr/Ta and R is the reflectivity at the waveguide facets.

To carry out the Fabry–Perot loss measurements, light from the dye laser at a wavelength of 900nm was end fired into the waveguide. The transmited light was focused onto a Si detector and the signal from the detector was amplified using a lock–in amplifier. Because of the short length of the waveguides and the low absorption in the GaAs substrate at this wavelength, radiation modes transmited through the device substrate were visible on an IR camera. A slit was therefore placed in front of the detector to prevent this light and light passing over the surface of the waveguide from being measured with the guided mode. The

transmission through the waveguide was then measured as the optical path length of the waveguide was changed as the waveguide was heated.

The experiment was carried out for 3μm wide stripe waveguides fabricated in wafer MV348 and the factor 'k' in equation 3.13 was calculated from the resonant and anti-resonant amplitudes in the transmission. From these measurements, an attenuation of 10.5dB/cm for TE and 10.1dB/cm for TM polarisation in the waveguides at a wavelength of 897nm was measured.

Section 3.5.4 Transmission Measurements In Stripe Waveguides.

With the absolute attenuation in the waveguide $\alpha(\lambda_0)$ known for one wavelength, the attenuation at other wavelengths could then be calculated by measuring the change in transmission as a function of wavelength.

Light from the Styryl-9 dye laser was endfired into the waveguide. The power from the laser varied with wavelength, and so a beam splitter and Si detector were used to monitor the incident power on the waveguide. The light transmitted through the waveguide was monitored using a similar detector, and the output of each detector was fed to lock-in amplifiers. This allowed measurements of input and output intensities at discrete wavelengths to be simultaneously recorded on a dual channel chart recorder, and the changes in transmission through the waveguide to be normalised.

Section 3.5.6 Absorption Near The Band-Gap Of MV348 MQW Stripe Waveguides.

The transmission as a function of wavelength in 3μm wide stripe waveguides fabricated in wafer MV348 was measured at wavelengths appoaching the absorption edge. The absorption for both TE_0 and TM_0 modes are shown in figure 3.19. The absolute loss values at 897nm were obtained using the Faby-Perot method and the change in absorption at subsequent wavelengths measured from this reference. The absorption for both TE_0 and TM_0 modes show the sharp rise associated with the quasi 2-dimensional density of states and the highly anisotopic absorption due to the loss of the heavy hole transition for TM polarisation [Weiner et al '85(a)] is demonstrated, with a subsequent shift in the absorption edge of approximately 8nm.

The high absorption measured at the long wavelengths ($\approx$10dB/cm) is likely to

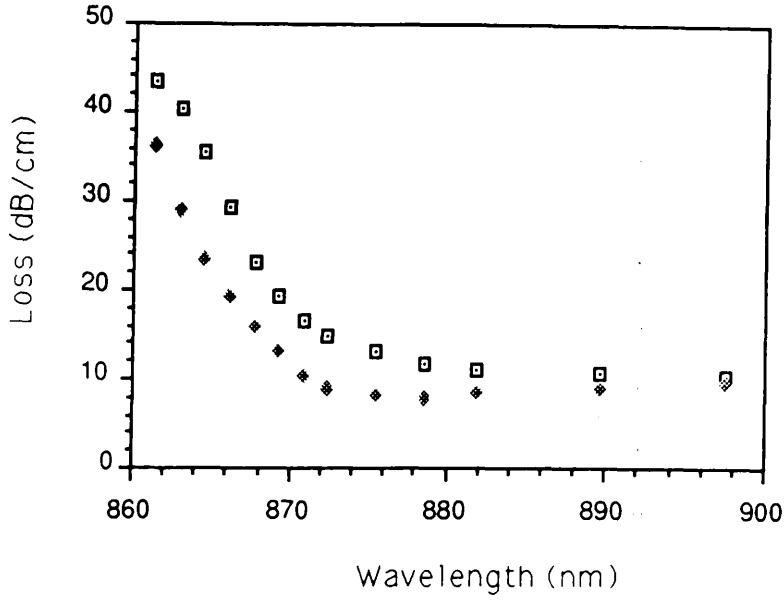

Figure 3.19
Absorption at wavelengths approaching the band gap of 3μm wide stripe waveguides in material MV348 for both TE polarisation (▫) and TM polarisation (◆).

be the result of the Fabry– Perot measuring technique, since using a light source with a relatively large bandwidth (40GHz for the dye laser) has the effect of reducing the peaks and toughs in the Fabry– Perot resonances. This then gives the appearance of high absorption.

Section 3.6 Conclusion.

MQW GaAs/AlGaAs waveguide structures were designed for the purpose of studying the electro– optic effects exhibited by the MQW structures. The characterisation of the wafers grown showned that they were suitable for the fabrication of electro– optic waveguides modulators. Stripe waveguides with ohmic contacts running along the stripe were fabricated on the material and shown to support the single modes TE_0 and TM_0. By studying the polarisation anisotropic absorption in the waveguides, it was demonstrated that there was suitable confinement of the guided mode to the MQW waveguide layer.

CHAPTER 4 ELECTRO- ABSORPTION IN MQW GaAs/AlGaAs.

Section 4.1 INTRODUCTION.

Multiple quantum well material has shown great potential in electro- optic devices in waveguide structures [Zucker et al '89(b)] using the electro- absorption and electro- optic effects at wavelengths close to the band- gap. Devices using electro- absorption have received a great deal of attention in recent years both experimentally through high speed devices [Wood et al '84], low loss devices [Koren et al '87(b)] and using intermixed quantum wells [Ralston et al '89].

The electro- absorption in MQW's at the band- gap is dominated by the quantum confined Stark effect (QCSE), as described in cahpter 2. The MQW waveguide material grown and characterised (chapter 3) was used to study the electro- absorption effect in quantum wells by measuring the photocurrent spectra from the material under reverse bias conditions. Also, the spectral variation of the absorption in a waveguide configuration is studied experimentally by measuring the transmission through a waveguide stucture in a large electric field.

Section 4.2 PHOTOCURRENT SPECTROSCOPY.

Photocurrent spectroscopy is an effective method of studying the absorption and electro- absorption in quantum well material [Collins et al '86, Yamanaka et al '86] which, in contrast to transmission measurements, gives a large signal at spectral regions of high absorption. Photocurrent measurements were carried out on devices fabricated on the wafers MV348 and A77 which were described in chapter 3. These measurements were carried out primarily to assess the quality of the material and examine the quantum confined Stark shift exhibited by the material. A discussion of the photocurrent spectroscopy measuring technique is given below followed by a dicussion of the results obtained from samples of MV348 and A77.

Section 4.2.1 Theory of Photocurrent Spectroscopy.

In photocurrent measurements, light incident on the sample creates free electron hole pairs and the resulting current is detected. The largest number of free carriers are created at the spectral regions of high absorption. Within the depletion region of a p- i- n junction, the electron- hole pairs created which would

normally recombine within the diffusion length, are swept apart by the Electric field, giving rise to a photocurrent [Whitehead et al '88(a)]:

$$i(F,\lambda) = P(\lambda)\ (1-R)\ (\lambda e/hc)\ \eta(F) \times \{1-\exp[-\alpha(F,\lambda)\,l\} \qquad (4.1)$$

where $P(\lambda)$= Incident Power at wavelength λ

R = Reflectivity of sample

η = Internal Quantum Efficiency

F = electric field strength

$\alpha(F,\lambda)$= Absorption coefficient.

$\lambda e/hc$= Conservation of charge and energy.

Measuring the resultant current gives a measure of the absorption in the material. In the case where $\alpha l << 1$, the photocurrent is directly proportional to the absorption coefficient in the material, allowing the wavelength dependence of α to be calculated from the photocurrent.

At low temperatures, tunneling of carriers through the potential barriers material of the MQW material in an electric field is thought to be responsible for the transport through the MQW [Collins et al '86] since η increases with decreasing barrier width [Yamanaka et al '86]. At room temperature, the high longitudinal optical (LO) phonon density is responsible for the transport of carriers over the barriers through collisions [Deveaud et al '88].

As the electric field applied to a sample is increased, η increases rapidly, since the transport efficiency of the free carriers increases with field strength. The presence of an electric field leads to the spatial separation of the electron and hole within a quantum well, increasing the radiative recombination time [Miyoshi et al '86, Mendez et al '82]. The phonon collision probability is thus increased and the creation of free electron hole pairs is increased.

Section 4.2.2 Features of Photocurrent Spectra In MQW Semiconductors.

The photocurrent spectra of MQW semiconductors in a large electric field show some distinct and interesting features. Before discussing the results obtained from the samples fabricated in this work, it is worth while introducing some of the features observed and the origins of these features.

Forbidden Transitions in Quantum Wells.

Photocurrent spectroscopy shows peaks associated with interband transitions which, for MQW material in a large electric field, include some transitions which are forbidden in zero field [Miller at al '81(b)]. In a MQW semiconductor, carriers are confined to the potential wells in eigenstates which form an orthonormal basis set. If the eigenfunctions in the conduction and valence bands are identical, then there is a strict selection rule for transitions governing interband transitions: $\Delta n = n_e - n_h = 0$ where n_e and n_h are the quantum numbers of the confined states. In a real semiconductor quantum well, the eigenfunctions of conduction band electrons and valence band heavy and light holes are not identical, and so the finite overlap of the eigenfunction leads to interband transitions corresponding to $\Delta n = 2p + 1$ becoming allowed, where p is an integer, although weakly as the overlap of the two states is small.

When an electric field is applied perpendicular to the plane of the quantum wells, the perturbed eigenfunctions become asymmetric. The perturbation leads to a further increase in the overlap of the eigenfunctions associated with interband transitions $\Delta n = 2p + 1$, and the oscillator strength between these transitions becomes increasingly strong. These transitions, refered to as forbidden transitions, become allowed in the presence of a large electric field. Forbidden transitions in quantum wells in an electric field were first observed in by photoluminescence measurements [Miller et al '81(b)] and later studied in greater detail by photocurrent measurements [Collins et al '86]

The appearance of forbidden transitions in the absorption spectrum of the material is accompanied by a corresponding quenching of the absorption of the zero field allowed transitions [Iwamaru et al '85]. This is a direct result of the absorption sum rules [Miller et al '86(a)] which states that the net change in absorption in the material must be zero. Assuming that the hh and lh transitions are completely decoupled, the sum rule for heavy hole and light hole transitions operate independently. This leads to a marked difference in the quantative behaviour of the oscillator strengths of these transitions in an electric field.

The well strength parameter (γ) of heavy hole eigenfunctions is large compared with the light hole and the conduction band eigenfunctions (which have comparable γ's). Since the penetration of the hh eigenfunction is smaller, the asymmetry of the heavy hole eigenfunctions in the presence of an electric field is larger than the lh and conduction eigenfunctions. The overlap of the heavy hole

and conduction band eigenfunctions associated with forbidden transitions therefore increases and the oscillator strength of these transitions becomes strong, and a decrease in the allowed heavy hole transitions occurs. In contrast, the oscillator strength of the light hole forbidden transitions do not increase greatly with field because penetration of the wavefunction into the barrier is reduced and the quenching of the light hole transitions with electric field is much less.

Exciton Broadening.

The excitonic peaks as measured by photocurrent have associated line widths which are the result of both homogenous and inhomogenous broadening. The inhomogenous broadening is dominant and is related to the material quality and the variations in the magnitude of the electric field across the i– doped region of the p– i– n diode [Stevens et al 88].

The homogenous broadening is mainly related to the life time of the exciton. Three possible mechanisms limiting the exciton life time are LO phonon interaction, tunnelling through the barrier and electron hole recombination [Stevens et al '88]. At room temperature, phonon interactions dominate the lifetime and lead to an estimated exciton life time of 300fs [Chemla et al '85]. With this lifetime there is a spread of exciton energies through the Heisenburg uncertainty principle and therefore an associated linewidth ($\Delta\nu$). In an electric field, the exciton lifetime is reduced since the electron and hole are spatially separated, thus leading to further homogeneous broadening of the exciton peak in an electric field.

The exciton broadening is, however, dominated by inhomogeneous broadening. The two main mechanisms leading to this broadening are variations in the well widths and variations in the electric field strength across the MQW structure in a p– i– n diode. Broadening through well width variation can occur in two ways. Firstly, there can be a variation in the width from well to well of one or two monolayers, giving the excitons of each well different resonant energies [Chemla et al '84]. The separation of these energies is small and leads to a broadening of the exciton peak of the MQW structure rather than giving a resolved peak for each well. Secondly, there can be well width fluctuations within a single well, as a result of interface roughness between the heterostructure layers. These take the form of monolayer islands or valleys [Weisbuch et al '81], and affect the resonant energy of the exciton. It is interesting to note that the line width of excitons in high purity bulk GaAs [Dow et al '70] is less than that measured in MQW GaAs/AlGaAs [Chemla at al '85], indicating that the interface roughness is the

dominant mechanism for exciton broadening [Juang et al '86].

The exciton broadening associated with the variation in the electric field strength across the MQW leads to a broadening of the peaks which increases with electric field strength. An MQW structure within the depletion region of a p– i– n diode experiences a variation in field strength due to residual doping in the intrinsic region [Newson et al '87], so each well experiences a different field strength and, since the resonant energy of the wells is strongly field dependent [Miller et al '84], there is a broadening in the absorption spectrum. As an increasing reverse bias voltage is applied to a p– i– n diode, the magnitude of the field increases, whilst the variation in field remains constant. However, because the resonant energy of the wells varies quadratically with field, the variation in resonant energies in wells across the depletion region increases, leading to a line width which increases with field strength [Stevens '88].

A field dependent homogeneous broadening of the excitons in quantum wells is observed which is related to the tunneling of electrons through the barriers and into adjacent wells [Hong et al '87(b)]. The tunneling increases with electric field strength and leads to a broadening similar to that of the Franz– Keldysh effect.

Section 4.2.3 Experimental Method.

Although photocurrent can be used to measure the absolute absorption coefficient in the material [Wood '86], in this work it was used to examine qualitatively the QCSE exhibited by the MQW wafers. Examining equation 4.1, it is apparent that to see fine structures in the absorption spectrum such as excitonic peaks of MQW material, a sample with a small αL is required. In a waveguide, the long interaction length (ie the length of the waveguide) and the large number of wells in the samples considered here lead to a large value of αL and to the loss of the fine structure in the photocurrent spectra [MacBean '86]. Devices were therefore fabricated such that the photocurrent could be measured with light at normal incidence to the MQW layers, thus reducing the interaction length to $0.5\mu m$ (the depth of the MQW region).

Device Fabrication.

The devices used for photocurrent measurements consisted of a $200\mu m$ diameter ohmic contact with a $50\mu m$ diameter aperture in the centre. Mesa structures were formed with the devices, etched to a depth below the i– n junction

Figure 4.1
S.E.M. micrograph of an array of photocurrent devices,
with one device contacted with ultrasonically bonded Al wire

in the material to isolate individual devices. The pattern of a device was defined photolithographically onto the p−doped surface of the sample as described in chapter 3 and a p−ohmic contact, identical to the contacts used on the waveguides, was evaporated onto the sample. After lift−off, the pattern of a 200μm diameter ohmic contact disc with 50μm diameter aperture was defined on the sample. Mesa structures containing individual devices were then formed by wet etching the samples in a solution of H_2SO_4:H_2O_2:H_2O (1:8:1 vol/vol)) for 30 seconds which etched the GaAs to a depth of approximately 3μm. The ohmic contacts and aperture were protected with a photoresist mask during the etching. An n−ohmic contact was then evaporated onto the back of the sample and both contacts simultaneously annealed.

The completed sample was bonded onto a p.c.b. mount with silver epoxy, and contacts of the individual devices were connected by ultrasonically bonded aluminium wires from the p.c.b. mount onto the top contact of the device. Figure 4.1 shows an S.E.M. micrograph of a complete bonded device. Typical electrical characteristics of the devices showed dark currents of 10nA for 10V reverse bias and the reverse bias breakdown voltages of devices on wafers MV348 and A77 were 42V and 80V respectively.

Experiment

The experimental arrangement for photocurrent measurements is shown figure 4.2 together with a diagram of the equivalent circuit of the device. Light from a tunable Styrly−9 dye laser was focused onto the aperture in the contact of a device at normal incidence using a microscope objective. The power incident on the sample was kept below 100μW (focused to a spot of diameter 50μm) to prevent both non linear effects and saturation of the exciton peak in the absorption [Chemla et al '85]. The polarisation of the light was in the plane of the well, so that transitions from both light and heavy holes were present in the absorption spectrum [Weiner et al '85(a)]. Absorption of light in the p−doped cladding layer of the waveguide structures was negligible because of the larger band−gap of the AlGaAs compared with that of the quantum well layers. Any absorption in the AlGaAs layer would not contribute to a net photocurrent because of the absence of an electric field outside the depletion region of the p−i−n structure.

The light absorbed in the depletion region of the diode gave rise to a photocurrent from the sample and hence a voltage V_0 across the 10kΩ load resistor. The laser light was chopped at 1kHz so that the voltage representing the

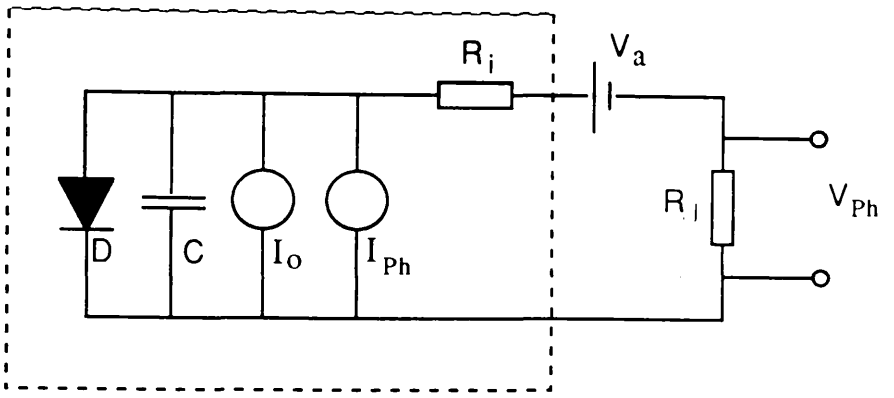

C = Junction Capacitance D= Ideal Diode
R = Internal Resistance
I_o = Dark Current I_{Ph} =Photocurrent.

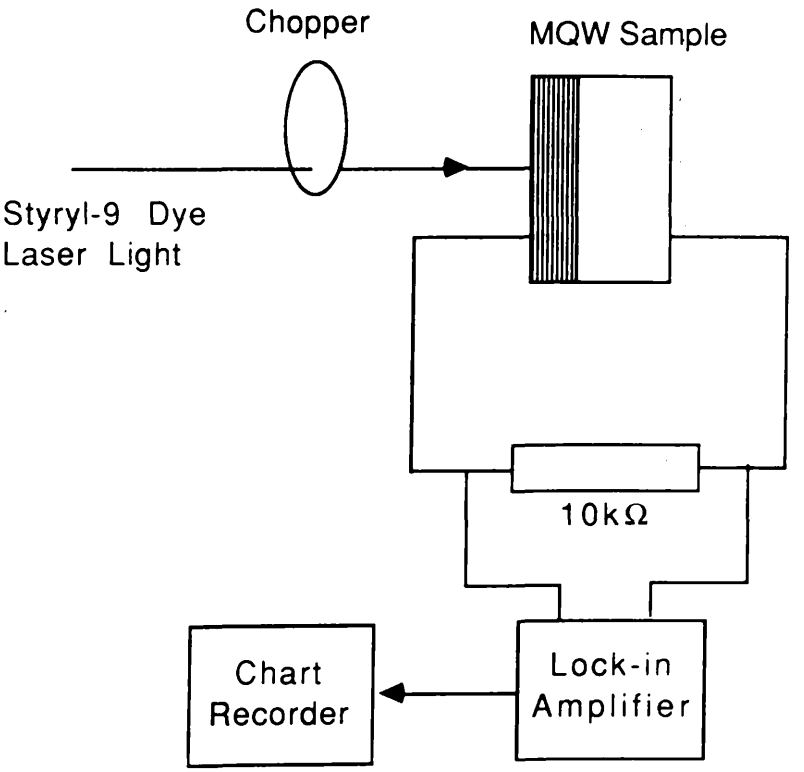

Figure 4.2
Photocurrent in MQW p-i-n diode
(a)The equivalent circuit of the device and experimental set-up
(b) Schematic diagram of the experimental arrangement.

photocurrent at the load resistor could be measured with a lock−in amplifier. The output signal from the lock−in amplifier was recorded on a chart recorder whilst the light from the Styryl−9 Dye laser was tuned through the absorption edge of the material at a rate of approximately 0.3nm/second. The photocurent spectrum was measured for a number of applied reverse bias voltages. The experiment was carried out for devices fabricated in samples from wafers MV348 and A77 to demonstrate qualitatively the effect of an electric field on the absorption of the material.

Section 4.2.4 Photocurrent in MV348: Results and Discussion.

The photocurrent spectra taken from a device fabricated on wafer MV348 sample at various reverse bias voltages is shown in figure 4.3. A copy of the trace of the zero volt spectrum is shown, and the spectra for other voltages show the outline of the absorption which are off set for clarity. The zero volt spectrum shows the excitonic absorption edge; the peaks of the e1−hh1 and e1−lh1 exciton transitions clearly resolved at wavelengths of 845nm and 839nm respectively. From the peak positions of the excitons, the well width was estimated to be 8.5nm using a computer program written by Mr. B.S. Bhumbra formulated on the model of [Kawai et al '84]. The heavy hole transition has a half width at half maximum (HWHM) of 5.5nm, as measured on the low energy side of the peak. Measuring the width of the light hole transition is made more difficult because of the presence of the 2−D continuum on one side and the heavy hole transition on the other. However, it is apparent that this transition is broader than the heavy hole transition. The peak of the light hole transition is lower than the heavy hole transition, but the ocsillator strength of the transition compared to the heavy hole transition does not demonstrate the 3:1 ratio expected [Weiner et al '85(a)].

Under a reverse bias voltage, an exciton peak associated with the forbidden transition e1−hh2 increases with increasing electric field strength, the exciton peaks begin to broaden and there is a reduction in the oscillation strength of the zero volt allowed transitions as expected. There is also the pronounced red shifting of the exciton peaks due to the quantum confined Stark effect [Miller et al '85]. The progression of the peak positions of the e1−hh1 and e1−lh1 transitions with field are shown in figure 4.4. Because the shift of the exciton peaks is quadratic with electric field strength E [Bastard et al '83], the energy shift of the peaks has been fitted to the quadratic:

$$\Delta E = aF^2 \qquad (4.2)$$

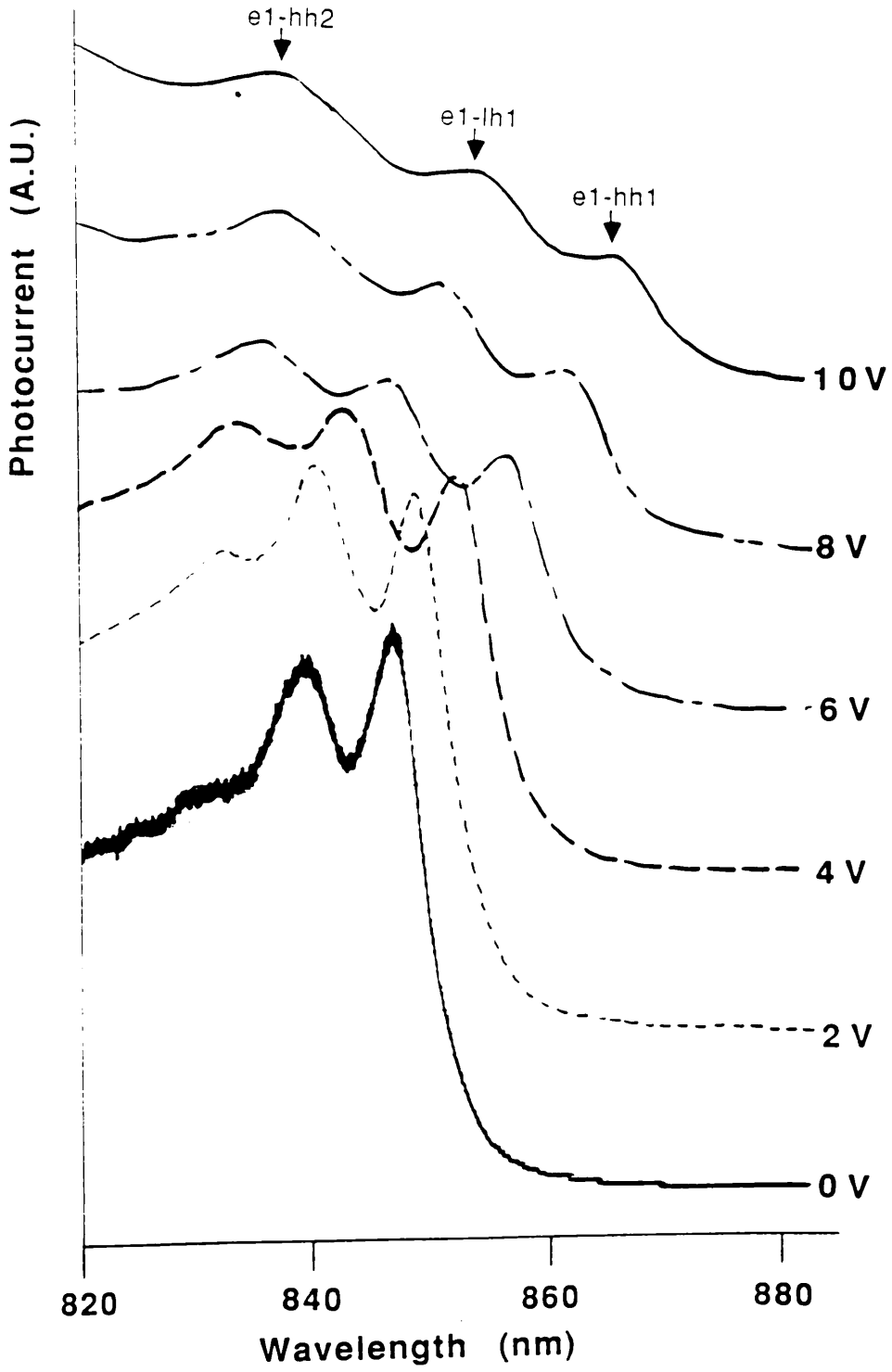

Figure 4.3
Photocurrent Spectra of MQW material MV348 under reverse bias conditions. The measured photocurrent is in arbitrary units. The different spectra are off set for clarity and the peaks are labeled according to the exciton transition.

(a)

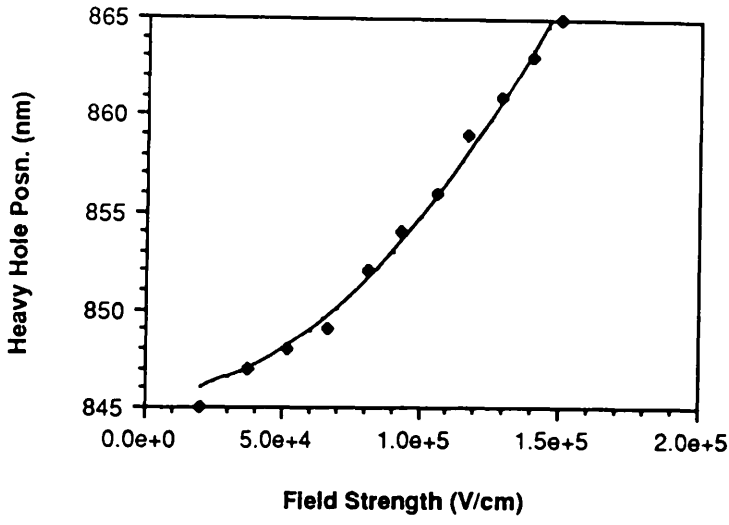

(b)

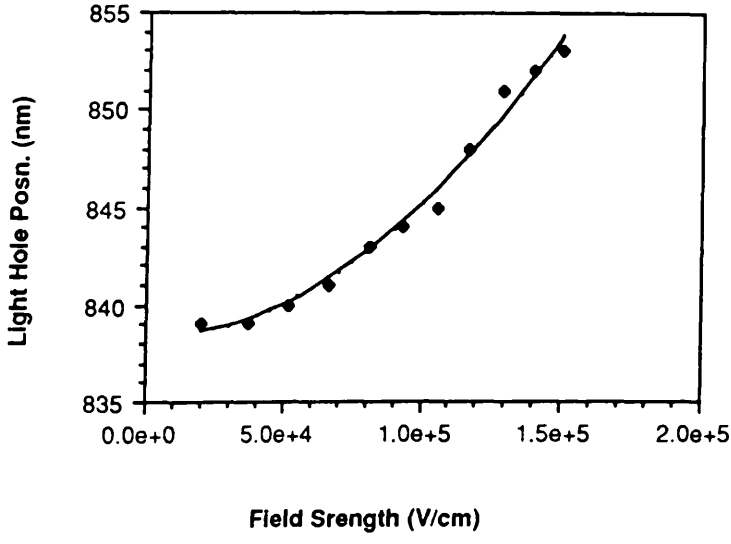

Figure 4.4
Peak position of exciton transition (a) e1-hh1 and (b)e1-lh1 as
a function of E field strength in MQW sample MV348.
In both cases the shift of the peak has been fitted to a quadratic: $\Delta E = aF^2$:

(a) For the heavy hole transition, $a=1.53\times10^{-9}$ meV/(V/cm)^2.

(b) For the light hole transition, $a=1.20\times10^{-9}$ meV/(V/cm)^2.

where ΔE is the shift of the peak in meV, F is the field strength and 'a' is a constant. There is a good fit for both transitions, with $a = 1.53 \times 10^{-9}$ meV/(V/cm)^2 and $a = 1.2 \times 10^{-9}$ meV/(V/cm)^2 for the heavy and light hole transitions respectively. Using data taken from [Miller et al '85], a comparable value of $a = 1.99 \times 10^{-9}$ meV/(V/cm)^2 was calculated [MacBean '86].

The energy of the heavy hole transition is seen to shift from 845nm at zero volts to 865nm at 10 volts reverse bias, whilst a slightly smaller shift from 839nm to 853nm is seen for the light hole transition. This difference, reflected in the values of the constant 'a' in equation 4.2, is to be expected since the energy shift is proportional to the effective mass [Bastard et al '83, Miller et al '84].

Section 4.2.5 Results and Discussion for Sample A77.

The absorption spectra of a photocurrent device fabricated on wafer A77 under different reverse bias conditions is shown in figure 4.5. Again, the zero volt trace is shown and with the outline of the reverse biased spectra off set for clarity. The positions of the zero volt excitons associated with the e1 − hh1 and e1 − lh1 transitions are at 851nm and 845nm respectively and from these positions, the well widths were calculated to be 9.7nm, close to the value of 10.1nm estimated from photoluminescence measurements. The HWHM line width of the heavy hole transition was measured to be 4.3nm and, as with MV348, the linewidth of the light hole transition was broader. In this material, the relative peaks of the two transitions are seen to be closer to having the 3:1 ratio predicted by symmetry [Weiner et al '85(a)]. The absorption spectrum also apears to have the shape close to the empirical fit [Chemla et al '85]: two Gaussian peaks, the light hole line width being larger than the heavy hole and the peak being lower.

The forbidden transitions are much more prominent in this material than in MV348, with exciton peaks associated with the transitions e1 − hh2 and e2 − hh1 showing strong oscillation strengths and the transition e1 − hh3 showing up weakly in the spectrum taken at a reverse bias voltage of 6 volts. Using the model presented by [Kawai et al '84], the peaks in the photocurrent spectra that were associated with the forbidden transitions were identified:

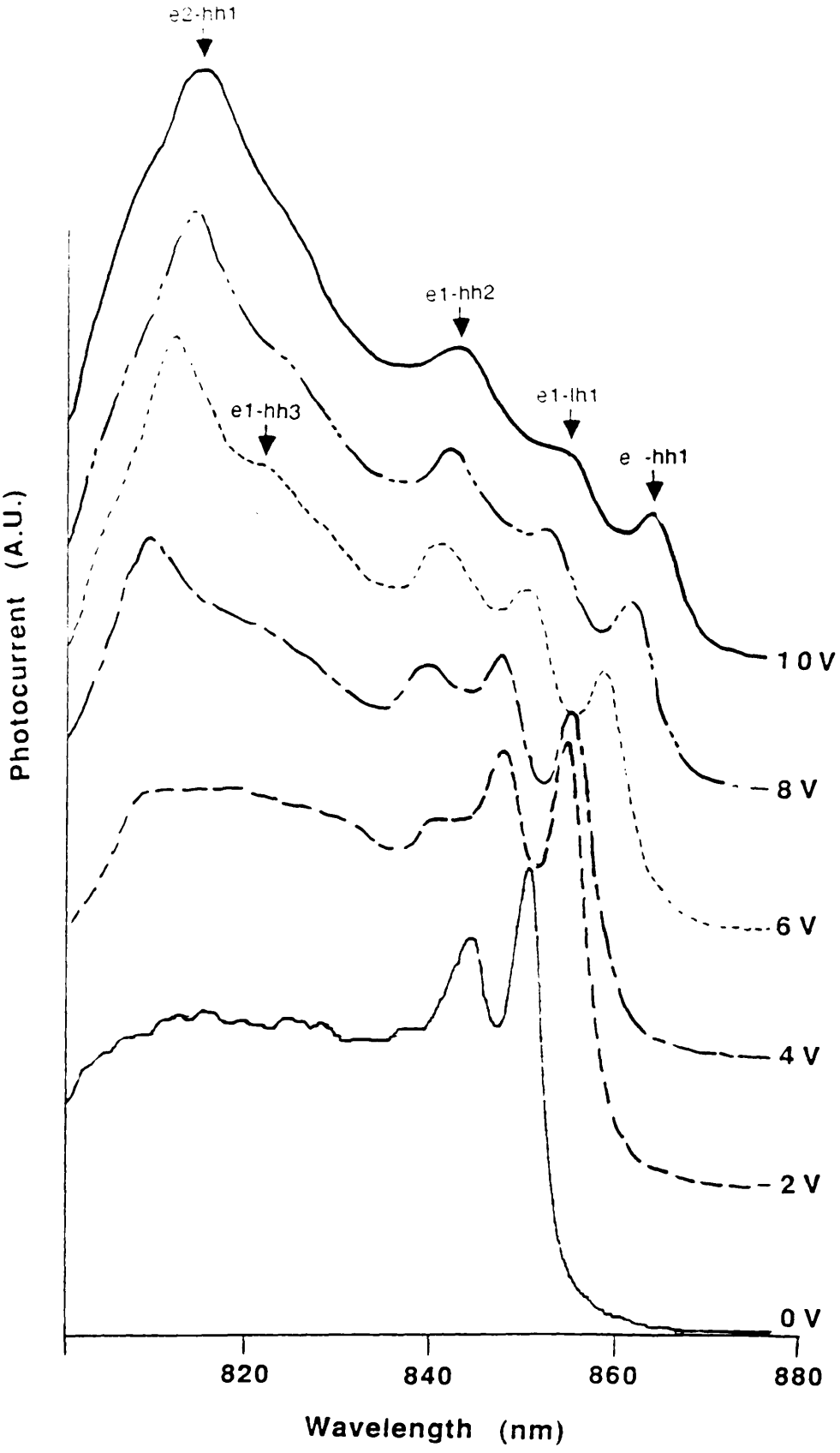

Figure 4.5
Photocurrent Spectra of MQW material A77 under reverse bias conditions. The measured photocurrent is in arbitrary units. The different spectra are off set for clarity and the peaks are labeled according to the exciton transition.

(a)

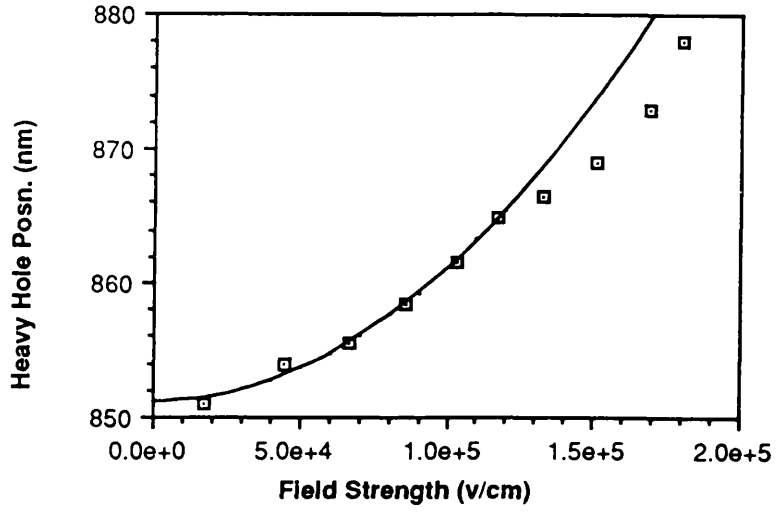

(b)

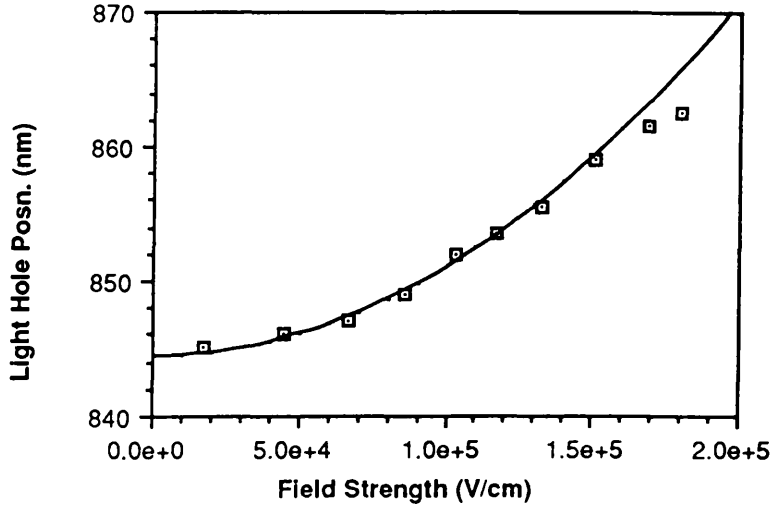

Figure 4.6
Peak position of exciton transition (a)e1-hh1 and (b)e1-lh1 as a function of E field strength in MQW sample A77.
In both cases the shift of the peak has beeen fitted to a quadratic: $\Delta E = aF^2$

(a) For the heavy hole transition, $a=1.68\times10^{-9}$ meV/(V/cm)^2

(b) For the light hole transition, $a=1.08\times10^{-9}$ meV/(V/cm).^{2}

Transition	Calculated Wavelength	Measured Wavelength
e1-hh2	839nm	838.5nm
e2-hh1	797nm	805.6nm
e1-hh3	822nm	820 nm

Table 4.1: Wavelengths of forbidden transitions in A77 MQW material, as calculated from Kawai et al '84 and measured from photocurrent spectra.

It is worth while noting that all the forbidden transitions observed involve heavy hole states. This is consistent with the larger asymmetry experienced by these eigenfunctions in an electric field. As a result of the large increase in heavy hole forbidden transitions compared with the light hole transitions, the e1−hh1 transition peak is rapidly quenched and the oscillation strength falls below that of the e1−lh1 transition, as the sum rule [Miller et al '86(a)] of the hh and lh transitions operate independently of one another.

The pronounced shifting of the exction peaks to lower energies is again present in the material, and plots of the position of the e1−hh1 and e1−lh1 exciton peaks against electric field strength are shown in figure 4.6, with the energy shift of the peaks fitted to equation 4.2. To obtain field strengths comparable to those applied to MV348 devices, larger voltages had to be applied because of the larger extension of the depletion region of A77 diodes into the p− and n− doped regions. Thus, a voltage of 10 volts leads to field strengths of $1.5\text{x}10^5$ V/cm and $1.1\text{x}10^5$ V/cm in samples MV348 and A77 respectively. This difference should be taken into account when comparing figures 4.3 and 4.5. In fitting the exciton resonance energies to equation 4.2, the energy of the e1−hh1 transition appears to vary quadratically only only up to field strengths of $1.1\text{x}10^5$ V/cm. However, this could be due to poor exciton peak resolution at high fields, since the transition is extensively quenched as the hh forbidden transitions begin to dominate. The curves are fitted with the coefficient 'a' with values of $a=1.68\text{x}10^{-9}\text{meV/(V/cm)}^2$ and $a=1.08\text{x}10^{-9}\text{meV/(V/cm)}^2$ for the heavy and light hole respectively. These are comparable with the values obtained for both MV348 and the data published by [Miller et al '84]. The shift of the heavy hole is again larger than the light hole transition and the shift quadratic with field strength.

The resolution of the exciton peaks is much better in this material than MV348 and this is due to a number of reasons. The smaller number of wells means that any variation in well width will have less of an effect: there will be less well to well variation and the number of heterostructure interfaces is reduced, reducing the well fluctuations through island formation. Also, the lower doping concentration in the intrinsic layer of A77 leads to a smaller variation in the electric field strength across the MQW region and hence reduces the variation in resonance energies of the indvidual wells.

Section 4.3 ELECTRO–ABSORPTION IN MQW STRIPE WAVEGUIDES.

The need for improvements in modulators in integrated optics has lead to the interest in the electro–absorption effect in multiple quantum well material. Devices have been demonstrated in a planar configuration with light propagating perpendicular to the quantum well layers [Singh et al '88, Wood et al '84] and in a waveguide configuration [MacBean et al '87]. In the latter configuration, the devices are compatable with monolithic integration of devices with semiconductor lasers and the anisotropic nature of quantum wells with polarisation can be examined [Weiner et al '86(b)].

Section 4.3.1 Experimental Method.

A study of the wavelength sensitivity of the the electro–absorption effect in the stripe waveguides fabricated in the MQW material was carried out. Stripe loaded waveguides with ohmic contacts on the p– and n– faces were fabricated in samples of MV348 and A77, cleaved to lengths of 1mm and mounted as described in chapter 3. To examine the electro–absorption in the waveguides, light from a tunable Styryl–9 dye laser was end fired into the waveguide whilst applying a voltage to the waveguide via a probe, as shown in the photograph in figure 3.17. The change in transmission through the waveguide at a fixed wavelength was measured as the voltage applied across the waveguide was stepped up from zero volts to 10 volts. The laser light was chopped at 1kHz before being end fired into the waveguide to allow the use of a lock–in amplifier, and the transmitted light was focused onto a Si detector. A horizontal slit was placed before the detector to reduce the amount of unguided light incident on the detector. The voltage source to the waveguide was a Digital to Analogue Converter (D/AC) of an IBM/PC and the amplified detector signal from the lock–in amplifier was measured by an Analogue to Digital Converter (A/DC) of the IBM/PC. The experiment was carried

out using MV348 and A77 3μm wide stripe waveguides with propagating modes TE_0 and TM_0, and the results are presented below.

Section 4.3.2 Electro–Absorption In MV348 Stripe Waveguides.

The electric field dependence of absorption in MV348 waveguides was examined and the results of the change in absorption, measured in dB/cm at a range of discrete wavelengths approaching the band gap are shown in figures 4.7 and 4.8 for the TE_0 and TM_0 propagating modes respectively. All measurements were made at photon energies below the band gap, ranging from 75meV to 34meV below the e1–hh1 exciton transition for TE polarisation and 85meV to 36meV below the e1–lh1 exciton transition for TM polarisation.

The measured absorption change shows the expected increase in absorption associated with the shifting of the exciton peaks via the quantum confined Stark effect (QCSE) [Miller et al '84]. The photocurrent measurements taken from a sample of MV348 and presented in section 4.2.4 show that the material does exhibit a good QCSE and it is of value to discuss the electro–absorption results in relation to these measurements. At the wavelengths close to the absorption edge, the large $\Delta\alpha$ begins as soon as the voltage is applied to the guide. For instance, at 865nm (20nm from the band–gap for TE polarisation) an absorption change ($\Delta\alpha$) of 50dB/cm was measured for a revese bias voltage of 3 volts, rising non linearly to 300dB/cm for an applied voltage of 6 volts. However, at wavelengths further from the absoption edge, the absorption change is less than 10dB/cm, and for lower voltages the transmission is dominated by Fabry–Perot resonances. It is not until a voltage is reached at which the edge of the shifting excitonic band edge reaches the photon energy of the incident light that any change in absorption is observed. For instance, at the wavelengths of 885nm and 890nm, there is negligible electro–absorption until 6V is applied which, from photocurrent measurements, corresponds to the edge of the exciton reaching these wavelengths. The magnitude of $\Delta\alpha$ at these wavelengths for both polarisations is reduced to less than 40dB/cm, primarily because the effect of the red shifting exciton is much less at these wavelengths.

The shorter wavelengths required to observe the electro–absorption for TM polarisation result from the absence of the heavy hole transitions for that polarisation, leading to an increase in the band gap [Weiner et al '85(a)] and the anisotropic electro–absorption [Weiner et al '85(b)]. The separation of the 1hh–1e and 1lh–1e transitions of approximately 6nm measured from the photocurrent

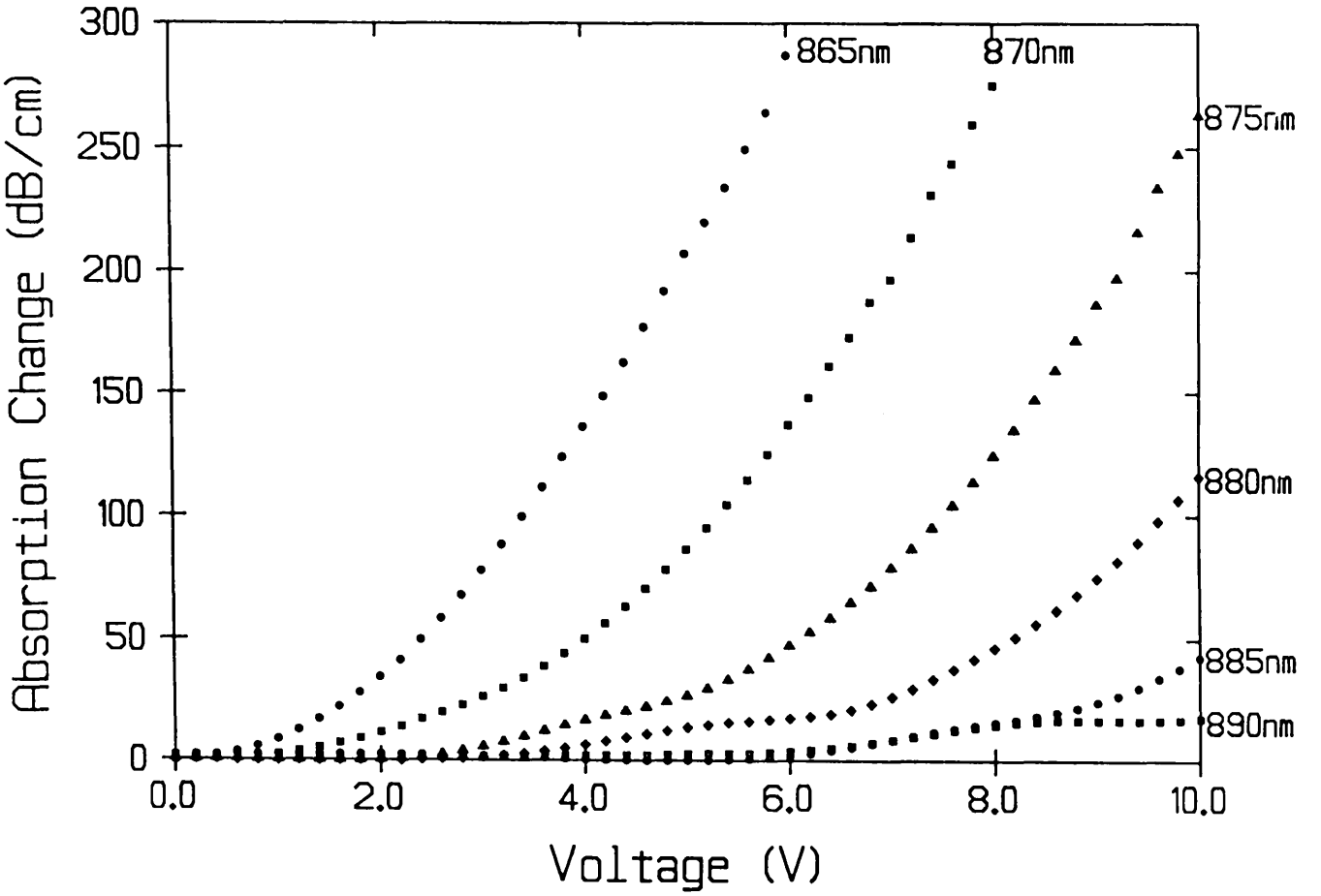

Figure 4.7
Electro-absorption for TE polarisation in 3 μm wide stripe waveguides fabricated in MQW material MV348. Change in absorption (dB/cm) measured as a function of reverse bias voltage across the waveguide and at a number of wavelengths close to the e1-hh1 exciton transition at 845nm.

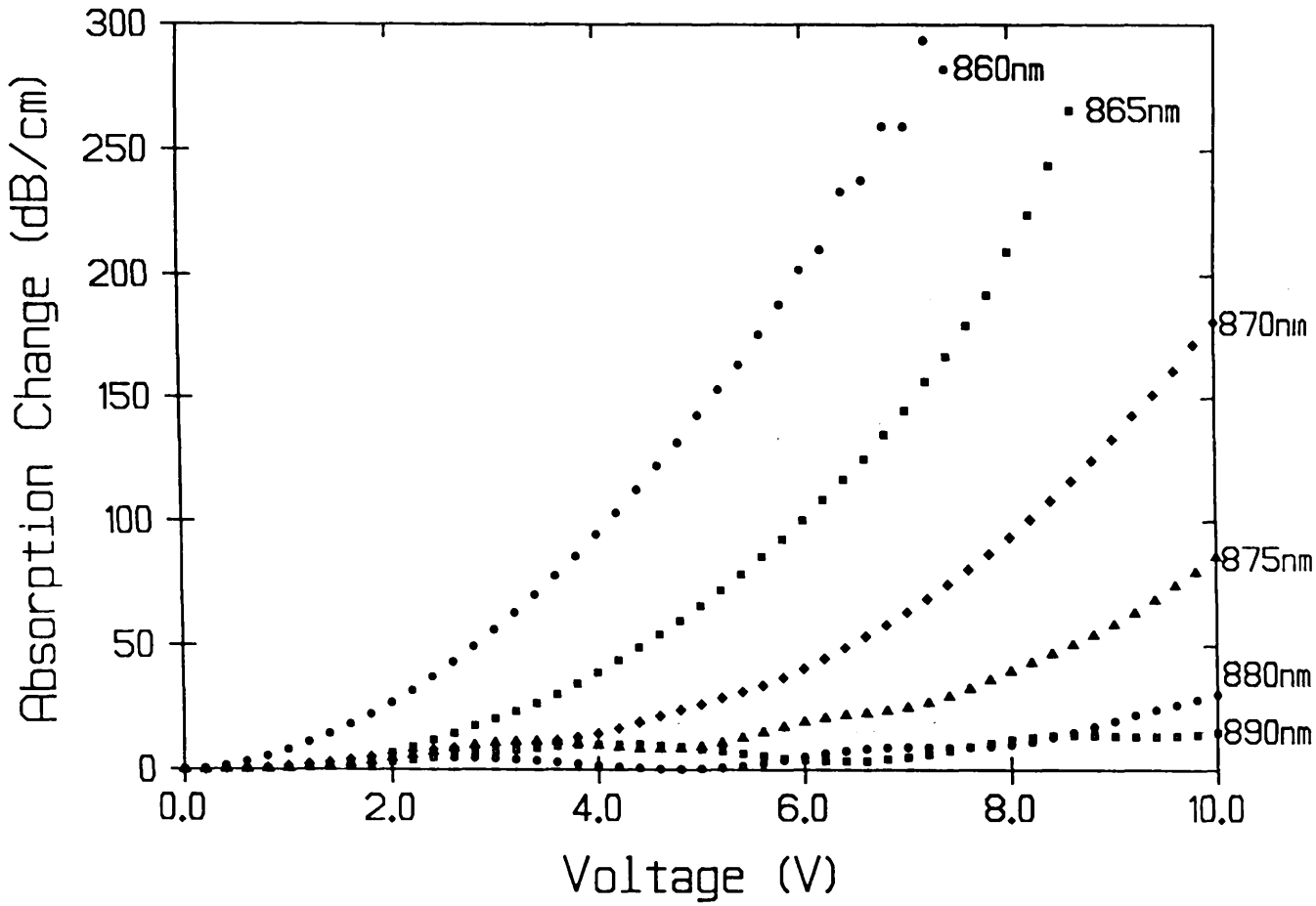

Figure 4.8
Electro-absorption for TM polarisation in 3μm wide stripe waveguides fabricated in MQW material MV348. Change in absorption (dB/cm) measured as a function of reverse bias voltage across the waveguide and at a number of wavelengths close to the e1-lh1 exciton transition at 839nm.

spectroscopy is consistent with the anisotropy of electro–absorption with polarisation observed in the waveguides.

Section 4.3.3 Electro–Absorption in A77 Stripe Waveguides.

Measures of the electro–absorption in A77 waveguides were carried out in the same way as for MV348 waveguides. However, the smaller number of quantum wells in these waveguides meant that the electro–absorption could be studied at wavelengths closer to the band gap, allowing electro–absorption measurements to be carried out at photon energies above the zero volt band gap of the material. The results of measuring the absorption change in the waveguides with voltage are shown for TE_0 and TM_0 propagating modes in figures 4.9 and 4.10 respectively.

Electro–Absorption near the Band–gap.

The electro–absorption in A77 waveguides at wavelengths greater than 860nm and 855nm for TE_0 and TM_0 propagating modes respectively are qualitatively similar to those obtained from MV348. Again there is a marked increase in the electro–absorption for decreasing wavelength and $\Delta\alpha$ is non linear with voltage. The anisotropic electro–absorption with TE and TM polarisation [Weiner et al '85(b)] is again clear, and is consistent with the separation of the e1–hh1 and e1–lh1 exciton transitions as measured by the photocurrent.

The magnitude of $\Delta\alpha$ for A77 waveguides is, however, less than for MV348 by a factor of at least 3 for similar photon energies from the band–gap. The reduction in $\Delta\alpha$ is not only due to the reduced number of wells in the A77 waveguides, but also because of the reduced back ground doping in the intrinsic layer of A77 compared to MV348. The work by [Bradley et al '89(a)] demonstrated that the modulation depth observed in an MQW p–i–n electro–absorption waveguide modulator was greatly enhanced by increasing the doping of the intrinsic layer within the range $2x10^{15}cm^{-3}$ and $5x10^{16}cm^{-3}$. Since A77 and MV348 are at the extremes of this range, the large difference in modulation depth was to be expected. The increase in $\Delta\alpha$ at the higher doping concentrations is due to the larger variation in the electric field across the intrinsic region of the p–i–n diode and the resultant broadening of the exciton peak with electric field strength.

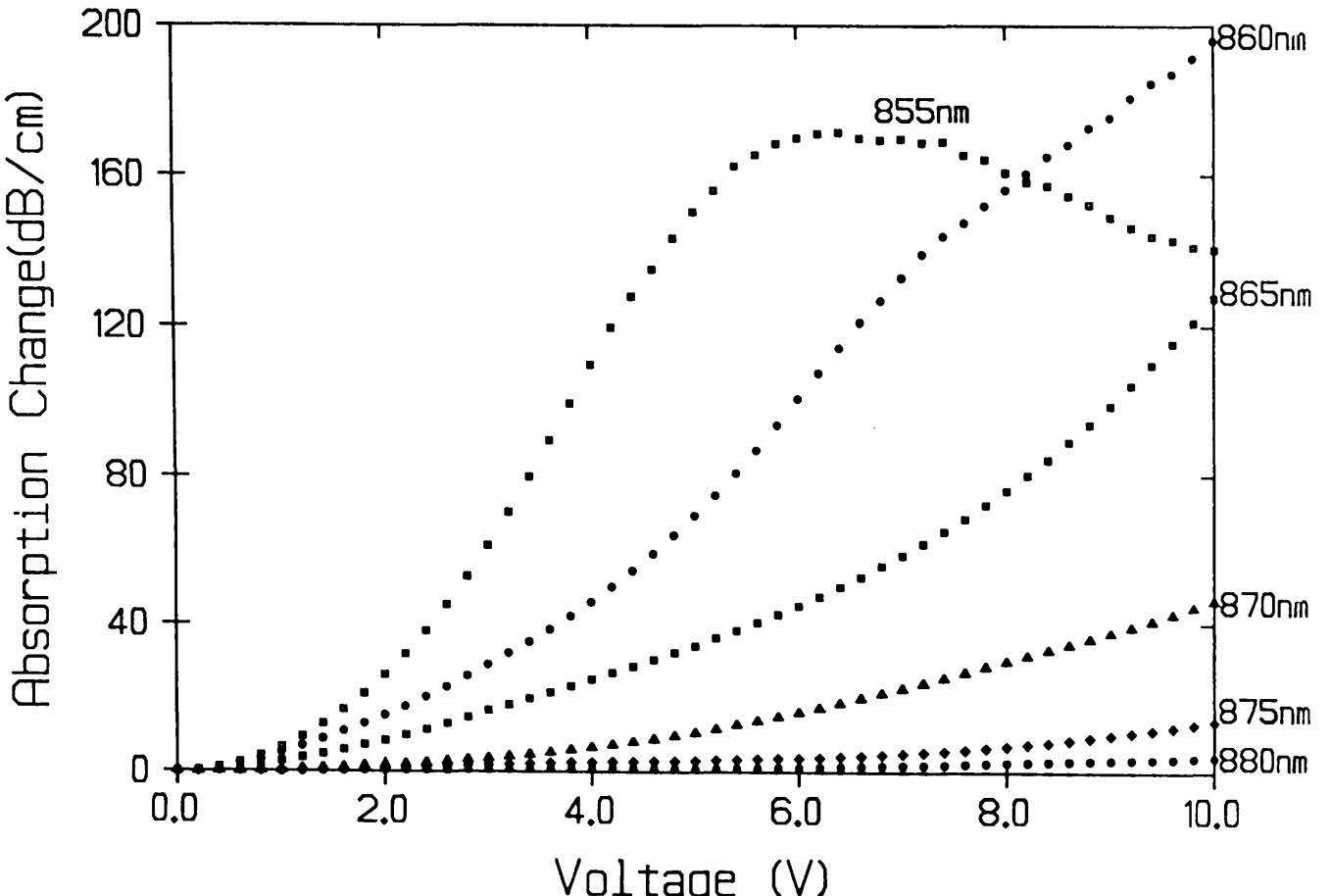

Figure 4.9
Electro-absorption for TE polarisation in 3 μm wide stripe waveguides fabricated in MQW material A77. Change in absorption (dB/cm) measured as a function of reverse bias voltage across the waveguide and at a number of wavelengths close to the e1-hh1 exciton transition at 851nm.

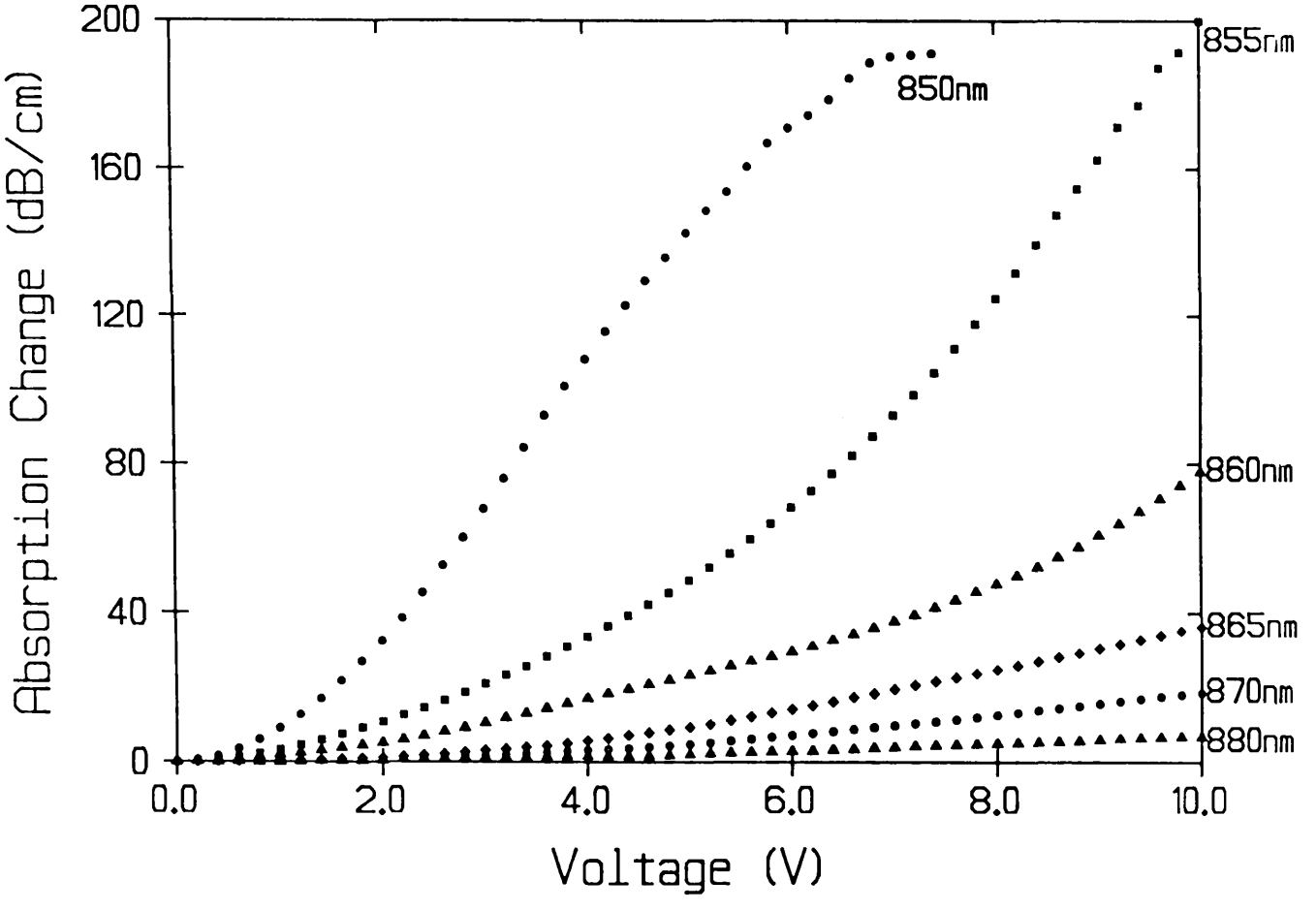

Figure 4.10
Electro-absorption for TM polarisation in 3 μm wide stripe waveguides fabricated in MQW material A77. Change in absorption (dB/cm) measured as a function of reverse bias voltage across the waveguide and at a number of wavelengths close to the e1-hh1 exciton transition at 845nm.

Electro– Absorption at the excitonic band– gap.

For wavelengths closer to the band– gap, the absorption change becomes qualitatively very different, with the absorption in the waveguide beginning to decrease with applied voltage, showing some interesting features. The onset of this change can be seen at wavelengths 855nm for TE polarisation and 850nm for TM polarisation in figures 4.9 and 4.10 respectively, where the absorption in the waveguide actually begins to fall with applied voltage. Figure 4.11 shows the results taken whilst concentrating on the electro– absorption at wavelengths close to the e1– hh1 exciton transition for TE polarisation.

At a wavelength of 855nm, 7meV from the e1– hh1 exciton transition, figure 4.11(a) shows an increase in $\Delta\alpha$, up to a peak of 170dB/cm at a voltage of 6 volts as the red shifting e1– hh1 exciton moves to this wavelength. Comparing this with the photocurrent measurements, the peak in $\Delta\alpha$ corresponds with the e1– hh1 exciton peak being at a position of 855nm. The insert of figure 4.11(a) shows more detailed measurements of $\Delta\alpha$, starting from a voltage of 3.8 volts.

Moving to a wavelength of 850nm (1.5meV from the exciton transition), the electro– absorption measurements show an increase in absorption associated with the e1– hh1 exciton to a peak of only 3dB/cm at 3 volts reverse bias. For voltages larger than 3V, $\Delta\alpha$ decreases since the wavelength is now positioned at the high energy side of the shifting exciton. The minimum in $\Delta\alpha$ at 6V corresponds to the dip in the absorption between the e1– hh1 and e1– lh1 exciton transitions. The second peak in $\Delta\alpha$ corresponds to the shifting of the e1– lh1 exciton. The absorption change of the e1– lh1 peak is negative in relation to the zero volt absorption on two accounts. Firstly the oscillator strength of the e1– hh1 exciton is approximately 1/3 that of the e1– lh1 exciton transition [Weiner et al '85(a)]. Secondly, broadening and quenching of the peak with field as discussed in section 4.2.2 further reduces the oscillator strength and hence reduces the absorption associated with the peak.

At the wavelength of 847nm, 7meV higher in energy than the zero volt e1– hh1 exciton peak, the electro– absorption shows an intial decrease in absorption as the e1– hh1 exciton peak shifts to larger wavelengths with applied voltage. The increase in absorption at 7 volts is then due to the red shifted e1– lh1 exciton peak. Once this peak has passed the wavelength of 847nm, the absorption continues to fall for the voltages measured as the quenching of the exciton peak with increasing field takes place.

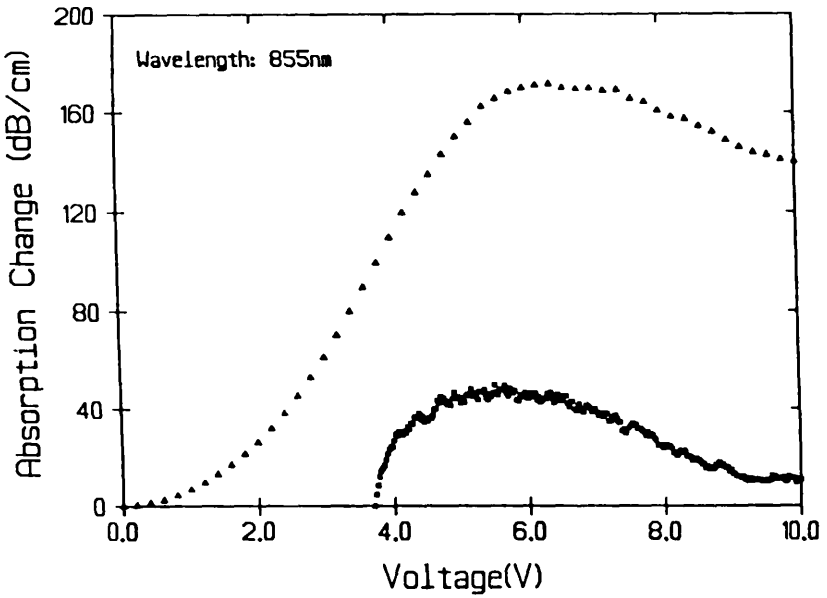

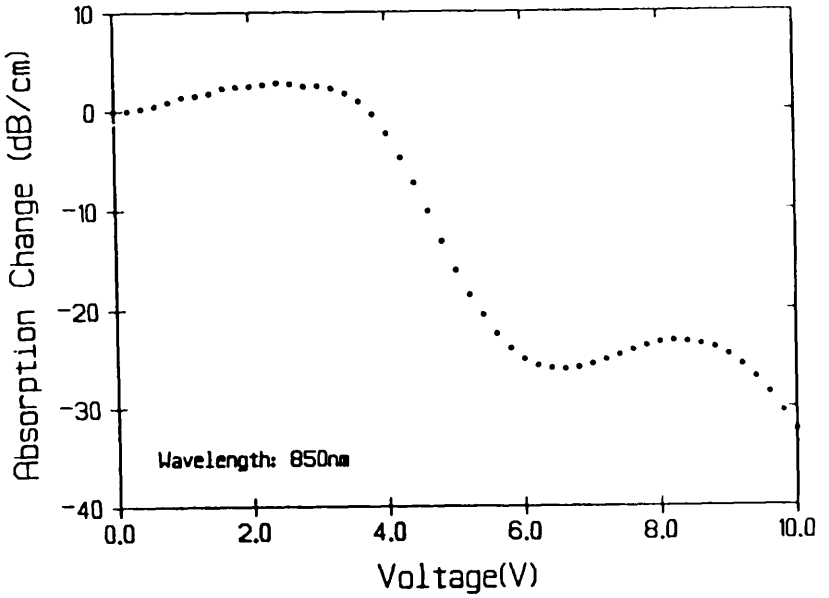

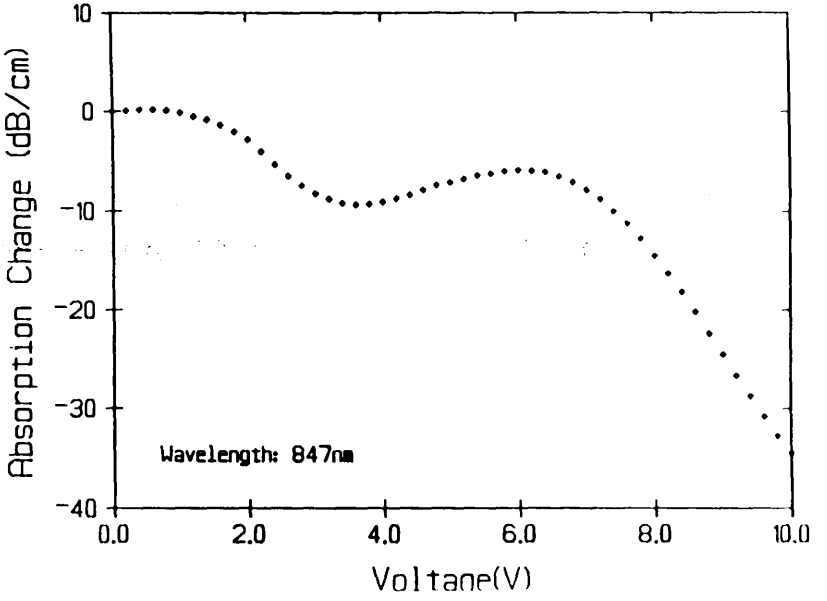

Figure 4.11
Electro-absorption in 3μm wide stripe waveguides on wafer MV348. The measurements, taken at 3 wavelengths close to the e1-hh1 exciton transition, show the resonant wavelength of the exciton shift through the operating wavelength of the laser. The results taken at 855nm show the absorption change at 855nm and taking both zero volts and 3.8 volts as the zero absorption change reference.

Section 4.4 CONCLUSIONS.

Photocurrent spectroscopy on two MQW GaAs/AlGaAs wafers, one containing 7x10.1nm GaAs quantum wells and a second containing 25x8.5nm GaAs quantum wells showed that the quantum confined Stark effect (QCSE) was demonstrated in both samples on application of an electric field perpendicular to the plane of the wells. The exciton peaks remained resolved to an electric field strength of $1.5x10^5$V/cm in both instances. The appearance of interband transitions which are parity forbidden at zero field become dominant in the absorption spectrum of MQW material at large field strengths, with the n= 1 interband transitions becoming extensively quenched. The shift in the resonance energy of the exciton peaks associated with the n= 1 interband transitions was shown to be quadratic with electric field strength, with a constant of proportionality of $1.5x10^{-9}$meV/(cm/V)^2 and $1.2x10^{-9}$meV/(cm/V)^2 for the heavy and light hole transitions respectively.

A highly wavelength dependant electro– absorption effect related to the QCSE was demonstrated in the two MQW wafers. Measurements in 3μm wide stripe waveguides demonstrated changes in absorption of 300dB/cm at photon energies 40meV below the lowest energy exciton peak, which for a device of length 500μm leads to an on/off modulation of 15dB.

CHAPTER 5 ELECTRO-OPTIC EFFECTS IN MULTIPLE QUANTUM WELL WAVEGUIDES

SECTION 5.1 INTRODUCTION.

In integrated optics, a number of device operations are based on the electro-optic effect. Devices receiving attention which utilise the effect include phase modulators [Bradley et al '89(b)], Mach-Zehnder modulators [Zucker et al '90] and directional coupling switches [Zucker et al '89(b)] in both bulk and MQW III-V materials. Within integrated optics, it is hoped to obtain monolithic integration of such devices with lasers which requires waveguide device lengths of the order of 100's of microns. The presence of a quadratic electro-optic effect which is related to electro-refraction in III-V semiconductors has been demonstrated theoretically [Hiroshima '87] and experimentally [Glick et al '86 and '87] to give an enhanced electro-optic effect in MQW material. The enhanced electro-optic effect enables shorter length devices, making monolithic integration more feasible.

The MQW waveguides examined in chapter 4 demonstrated strong electro-absorption at wavelengths close to the band-edge, indicating that there should be an enhancement of the electro-optic effect. The waveguides were therefore examined in order to study the electro-optic effects exhibited by MQW GaAs/AlGaAs at wavelengths close to the band edge. The wavelength dependence of the effect was studied and the refractive index change separated into two components: a linear and a quadratic elctro-optic effect.

SECTION 5.2 METHODS OF ELECTRO-OPTIC MEASUREMENTS.

With the interest in the electro-optic effects in MQW GaAs/AlGaAs waveguides as mentioned above, a suitable method of measuring the change in refractive index in the waveguides had to be developed. A description of the methods used will be given in this section, together with a discussion of the merits of each method.

Section 5.2.1 Fabry Perot Measuring System

During the measurements of the electro–absorption effect in the waveguides, the narrow linewidth of the Coherent 599 dye laser lead to Fabry–Perot resonances in the transmission against voltage. These peaks result from the changes in the optical path length of the waveguide (through the electro–optic effect) which swept the waveguide through Fabry–Perot resonances. The change in the optical path length (ΔOPL) between successive passes of a waveguide of length l and effective index n as a result of an index change Δn is given by:

$$\Delta OPL = \Delta n.\ 2nl \qquad (5.1)$$

The separation of the Fabry–Perot resonance peaks is equivalent to ΔOPL of one wavelength, such that the index change ($\Delta n'$) required to pass between two resonance peaks is given by:

$$\Delta n' = \lambda/2l \qquad (5.2)$$

The measurement of the index change in the waveguides was carried out in exactly the same way as the electro–absorption measurements as described in chapter 4.

Results and Discussion

The results of measuring the change in transmission through a 1mm long stripe waveguide in MV348 and observing the Fabry–Perot resonances are shown in figure 5.1 for two wavelengths (882.4nm and 885nm). The graph of transmission at a wavelength of 882.4nm shows well resolved Fabry–Perot resonances. For this wavelength, however, the resonances are lost for voltages greater than 8V as the increase in absorption through electro–absorption prevents multiple passes through the waveguide. From these measurements, a limited number of data points of Δn against voltage can be measured by noting the position of the peaks and troughs. For a wavelength only 2.6nm closer to the band gap, the increase in both absorption and electro–absoption in the waveguide further limits the extent to which the electro–optic effect can be studied by this method. The measurements obtained from this method could be extended to larger fields by shortening the waveguides. The data points would, however, still be limited by the position and number of peaks and troughs in the transmission curves.

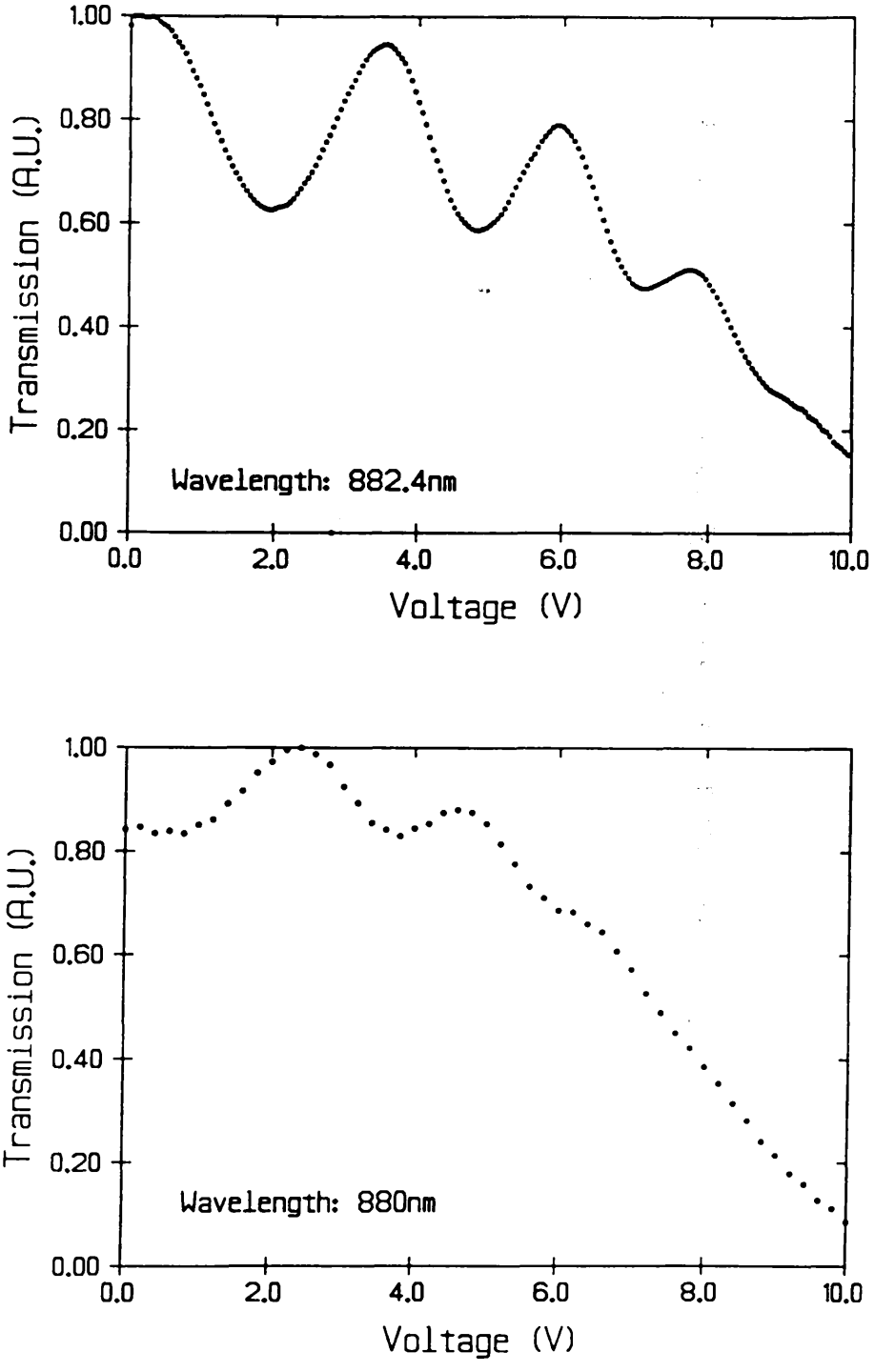

Figure 5.1
Transmission through a stripe waveguide at wavelengths 882nm and 880nm as a function of reverse bias voltage. Fabry-Perot resonances in the transmission are the result of the electro-optic effect in the waveguides. The poorer finesse at 880nm is due to higher absorption at that wavelength.

Conclusion

Monitoring the Fabry– Perot resonances in the waveguides was shown to be an effective, but limited method of studying the electro– optic effects in MQW waveguides at wavelengths close to the band gap. Although this was not used as the main method of studying the electro– optic effects in the waveguides, results taken using this technique were used to verify the results obtained using a Mach– Zehnder interferometer system which is described below.

Section 5.2.2 Mach– Zehnder Interferometer.

Using a Mach– Zehnder interferometer is one technique used for measuring the change in refractive index or phase modulation of a waveguide. The Mach– Zehnder interferometer system is shown in fig 5.2(a).

In one arm of the interferometer, light from a tunable dye laser passes through a waveguide mounted in the end fire rig. The other arm carries a reference beam which, on recombination with the light from the waveguide, creates an interference pattern. Any change in the relative phase of the two beams, for instance from a change in the refractive index change (Δn) of the waveguide, leads to a shift in the fringe pattern. By measuring the resulting fringe shift ($\Delta\varphi$), the refractive index change of the waveguide can be calculated from the expression:

$$\Delta n = \frac{\Delta\varphi . \lambda}{2\pi . l} \qquad \text{Equ.(5.3)}$$

where λ is the wavelength and l is the waveguide length.

Section 5.2.3 Mach– Zehnder Interferometer: Experiment Using A Hamamatsu Camera.

To obtain a clear and stable fringe pattern from the interferometer, great care had to be taken in setting up the interferometer. Because of the importance of mechanical stability in any interferometic system, all the optical components of the were mounted on rigid mounts with an optical axis as close to the bench top as practically possible (optical axis 75mm from the bench top). Also for any interferometer, the path difference of the two interferometer beams has to be kept within the coherence length of the light source, and using the Coherent 599 Dye laser it was necessary to restrict the path difference to 5mm.

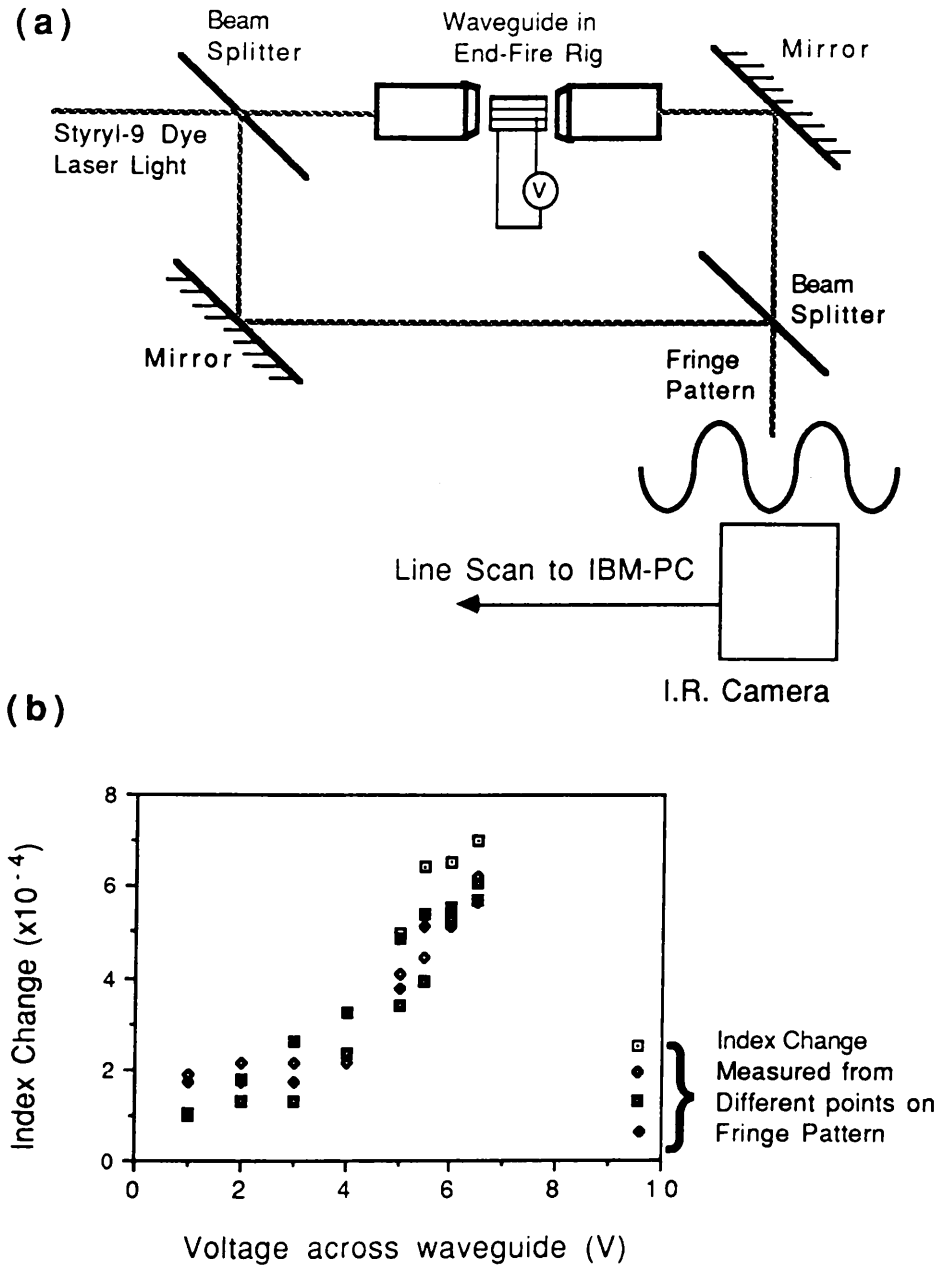

Figure 5.2
(a) Mach-Zehnder interferometer using I.R. camera and line scan to measure phase modulation in a waveguide.
(b)Typical set of results of index change of an MQW waveguide stucture for a wavelength of 860nm obtained using the interferometric system.

For the interfering beams to form a good image on recombination, the image of the output from the waveguide had to be slightly de-focused, increasing the spatial extent of the fringe pattern by smearing out the image of the waveguide output. This increases the area over which the reference beam and waveguide output had comparable intensities, a situation necessary to get good fringe modulation. The fringe pattern was then expanded by a large aperture x40 microscope objective to give an image on an IR camera.

The fringe shifts of the interferometer were measured by imaging the fringe pattern onto a Hamamatsu camera, as shown in fig 5.2(a), which gave an intensity profile plot of the fringe pattern. The progression of the fringe pattern then was monitored by measuring the position of the peaks and troughs in the interference pattern. A line scan of the fringe patten was taken from the camera for each voltage applied to the waveguide.

Results and Conclusion.

Fig 5.2(b) shows a plot of Δn 'v' Voltage using this method for a stripe waveguide in A77 for TE polarised light. Each set of points in each graph represents the progression of a particular peak or trough across a single fringe pattern and it is apparent that the measurements from just one fringe pattern at each wavelength yield a large uncertainty to the index change.

This method was found to be unsuitable for making extensive measurements of electro-optic effects in the waveguides at a range of wavelengths close to the absorption edge of the material. It was found to be inaccurate on two accounts. First, identifying the peaks and troughs of the fringe pattern became increasingly difficult as the fringe modulation was reduced with the onset of electro-absorption in the waveguide. Secondly, the periodicity of the fringe pattern varied across the pattern, giving a systematic error in the fringe shift measurements, since the periodicity of a peak or trough varied as it progressed across the fringe pattern. The method was also very time consuming.

The time involved in obtaining results and the inaccuracy of the results made the above method impractical for carrying out extensive measurements of the electro-optic effect in the waveguides. Although this method was not used, it did lead to a much quicker and more accurate method which will be described in the following section.

Section 5.2.4 Mach– Zehnder Interferometer Incorporating Control System.

With the motivation of getting a measuring technique which was both more accurate and less time consuming, the system shown in fig 5.3 was set up. The general principle is the same as in the method described in section 5.2.3, but rather than measuring the fringe shift, the phase compensation of a piezo– electric mirror holding the fringe pattern stationary was measured.

The fringe pattern, expanded by a x40 miroscope objective, was focused onto a two element detector (A and B) with element separation of 50μm and the signals from the detector elements were input to channels A and B of a lock– in amplifier. An amplified output signal α(A– B) was fed back to the high voltage amplifier of the piezo– electrical mirror, settling the fringe pattern over the detectors such that (A– B) was minimised, as shown in figure 5.3. If there was any shift in the fringe pattern, the signal to the high voltage amplifier became non zero and the piezo electric mirror moves to return the fringe pattern back to its original position such that A– B= 0. However, a finite signal is required to hold the piezo electric mirror at its new position and there was a small error in the position of the fringe pattern. If the gain in the feed back is large enough, then this error is small and monitoring the signal α(A– B) gives a measure of the shift of the fringe pattern. As a voltage was applied to the waveguide, the resulting change in the relative optical path length of the two arms of the interferometer was then compensated for by the movement of the piezo electric mirror. By monitoring the signal α(A– B) to the high voltage amplifier of the piezo– electric mirror, the resulting phase modulation of the waveguide could be calculated.

Experimental Details.

The sensitivity of the control system was dependent upon the modulation depth of the fringe pattern and the fringe periodicity relative to the detector size. Both of these had to be optimised if the measuring system was to prove to be effective.

To optimise the size of the fringe pattern on the detector, the signal obtained from each detector element was modelled by integrating a sinusoidal fringe pattern across a detector element:

$$A = \int_0^q 1 - m\cos(\theta)\, d\theta \qquad (5.4)$$

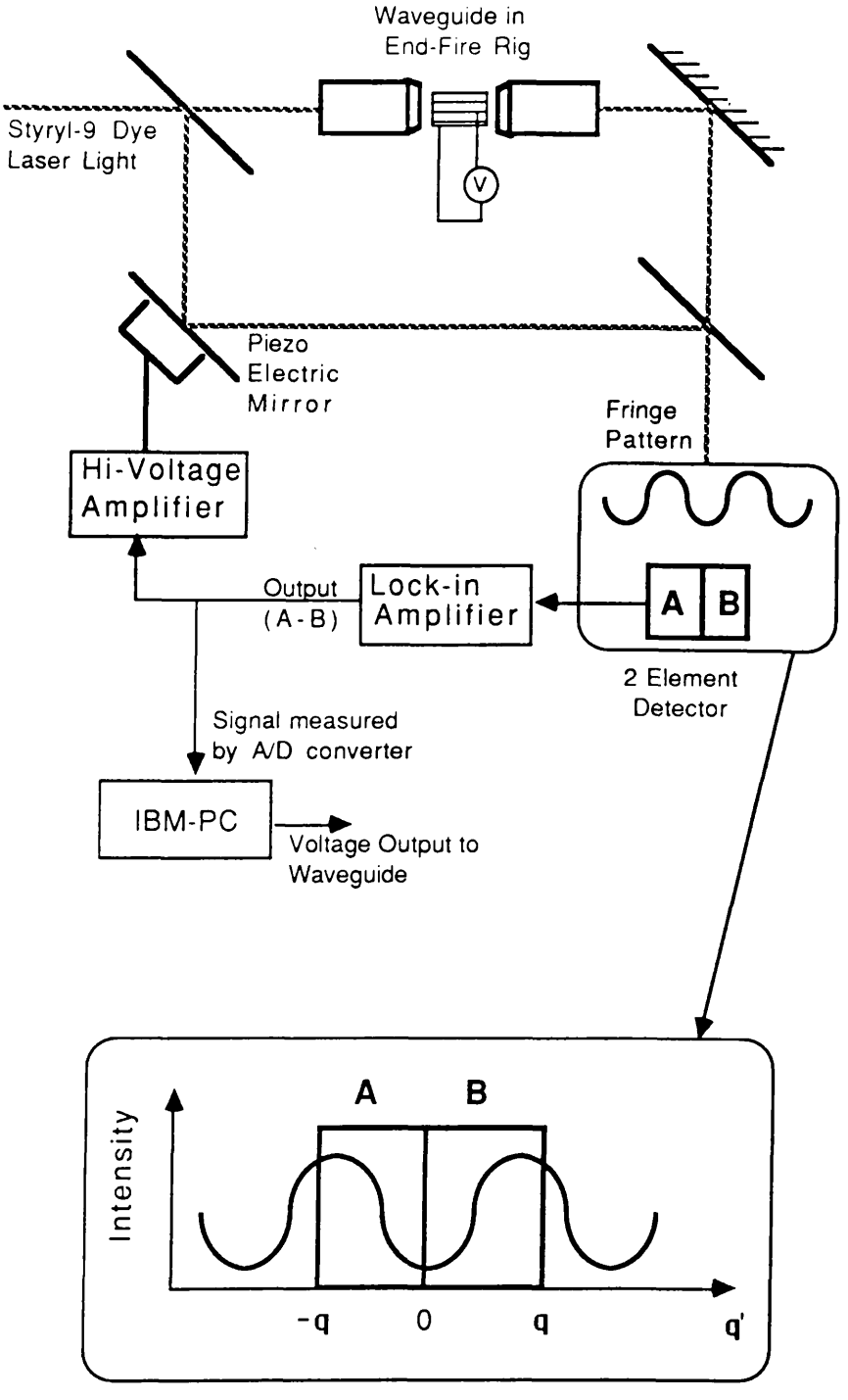

Figure 5.3
Mach-Zehnder Interferometer incorporating control loop for measuring phase modulation in a waveguide.
The insert shows the extent of the fringe pattern focused onto the two element detector.

where $\theta = 0$ is the minimum of the fringe at the interface of the two detector elements and $\theta = q$ is the phase of the fringe pattern at the edge of the detector, as shown in the insert of figure 5.3. From the calculated signal, (A− B) was calculated to be most sensitive to fringe shifts for a value of $q = \pi/2$. The image of the fringe pattern was thus expanded onto the two element detector using a microscope objective such the size of the fringe pattern was in this regime. The fringe pattern was also adjusted such that when the piezo− electric mirror was modulated, the signals A and B were modulated in antiphase and with a maximum amplitude.

The electro− optic measurements were to be carried out at wavelengths close to the material band gap, where large electro− absorption has been demonstrated. To obtain a good modulation depth at the fringe pattern, the waveguide output intensity and reference beam intensity had to be comparable. The intensity of the interfering beams therefore had to be balanced in such a way that the modulation of the fringe pattern was maintained as a reverse bias voltage was applied to the waveguide.

Since path differences of the order of 10nm were being monitored, the system was very sensitive to vibrations. It was therefore necessary to mount the chopper both off the bench top and away from the interferometer to prevent vibrations and air currents from destabilising the fringe pattern. A chopping frequency of 800Hz was used to allow a short integration time of 3ms to be used, which increased the stability of the feedback system at high gain. The output smoothing of the lock− in amplifier was kept 'slow', increasing the response time of the system and hence improving the stability at high gain. Stability was also highly dependent on fringe modulation and intensity, so was set for each experiment at a value x5 less than the gain at the onset of instability.

The experiment was fully controlled by an IBM− PC, with voltages being applied to the waveguide from a Digital− Analogue Converter (D/AC), and the output from the lock− in amplifier being measured by a Analogue− Digital converter (A/DC). The execution of the experiment is given in the explanation below.

Before running the experiment, the piezo− electric mirror was always positioned such that the signal Vpzt was zero when zero volts was applied to the waveguide. This was essential if the experiment was to be correctly calibrated. The range of voltages to be applied to the waveguide (V_{wg}), from zero to a maximum value (V_{max}), and the voltage increment (V_{step}) were initialised. Then, starting

from zero volts, the voltage across the waveguide was increased incrementally and the voltage $\alpha(A-B)$ from the the lock–in amplifier to the high voltage amplifier of the piezo–electric mirror (V_{pzt}) was measured for each voltage applied to the waveguide. The voltages V_{wg} and V_{pzt} were taken as the measurement of phase modulation against voltage in the waveguide. From these, the index change against voltage could be calculated after calibration.

Calibration.

A calibration of the phase compensation of the piezo–electric mirror was necessary at the end of each experiment as a consequence of hysteretic nature of the piezo–electric mirror with applied voltage. For the calibration, the feedback from the lock–in amplifier to the piezo–electric mirror was removed and a voltage was applied directly from the D/AC of the IBM–PC. No voltage was applied to the waveguide.

From the experiment, it was known that by applying a voltage to the waveguide ranging from zero to a maximum value led to a voltage from zero to a maximum value $V_{pzt(max)}$ being applied to the high voltage amplifier. For the calibration, this same range of voltages was applied to the pzt whilst monitoring the output A from the lock–in amplifier. The measured signal was sinusoidal, with a varying period as a result of the nonlinear movement. The measured signal was scaled between ±1 as shown in fig 5.4(a) and the arc sine of these scaled values were calculated. This gave the phase compensation $\Delta\varphi$ as a function of voltage to the high voltage amplifier as shown in figure 5.3(b).

Calculating Index changes (Δn).

From the experiment and calibration data, the change in refractive index of the waveguide was calculated. A least squares fit of the calibration data gave a fourth order polynomial to $\Delta\varphi(V)$. This allowed the values of Vpzt measured during the experiment to be related directly to a phase modulation in the waveguide by substituting the signal from the lock–in amplifier measured during the experiment into the polynomial. The index change of the waveguide could then be calculated using equation 5.3.

In order to confirm that the values of Δn measured using the interferometer were true values, results obtained from waveguides in MV348 by this method were compared with those obtained using Fabry–Perot resonances in the waveguide.

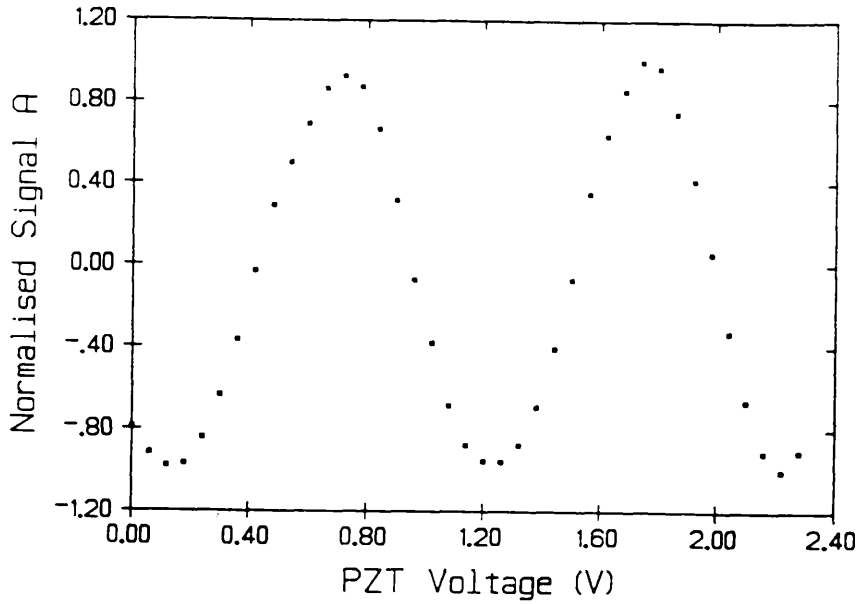

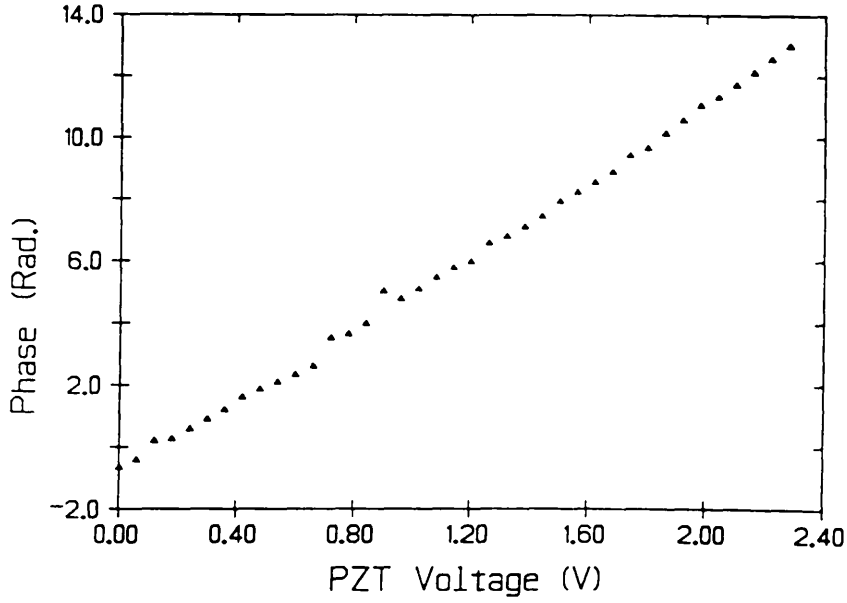

Figure 5.4
Calibration of the piezo electric mirror.
(a) Normalised output from one detector element as the voltage to the Hi-Voltage amplifier scans the piezo-electric mirror through 2 fringe periods.
(b) Phase shift of the interferometer fringe pattern as a function of the voltage to the Hi-Voltage amplifier.

Figure 5.5 shows a comparison for measurements from the two techniques taken at 3 different wavelengths. The lines are results from the interferometeric method and the points are taken from the Fabry–Perot method. The figure shows good agreement between the results of the two methods, verifying the measurements from the interferometer are true values of Δn.

Conclusion.

The interferometer and control system were therefore shown to be a reliable method for measuring the electro–optic effect in the waveguides, so giving an effective method of carrying out an extensive study of the electro–optic effect in MQW GaAs/AlGaAs waveguides.

SECTION 5.3 ELECTRO–OPTIC MEASUREMENTS.

The quantum well waveguide structures grown had been shown to exhibit strong electro–absorption through the shifting of the band edge. This had been demonstrated by the photocurrent measurements and electro–absorption measurements in the waveguide configuration. The large shift observed in the band edge should contribute to a large change in refractive index in the material through the electro–refractive effect, enhancing the electro–optic effect [Glick et al '86]. To examine this effect, the stripe waveguides were fabricated on material MV348 with the direction of propagation of the waveguides was along the crystalographic axes [1$\bar{1}$0] and [110]. The electro–optic effects were then measured in these guides for modes propagating with TE polarisation and TM polarisation at a range of wavelengths approaching the material band edge.

Section 5.3.1 Experiment with MV348 Stripe Waveguides

To study the electro–optic effects in MV348, the fabricated waveguides were cleaved to lengths of 800μm and 1mm for guides propagating along [1$\bar{1}$0] and [110] respectively. These lengths gave easily measureable phase modulations of approximately 2π for a reverse bias voltage of 10 volts with the attenuation from electro–absorption in the guides remaining acceptably low. The Mach–Zehnder interferometer described in section 5.2 was used to make measurements of changes in refractive index (Δn) in the waveguides at a number of discrete wavelengths approaching the material band edge. For these measurerments, a reverse bias voltage was applied to the waveguides up to a maximum of 10 volts. All measurments were carried out on stripe waveguides with a nominal width of 3μm.

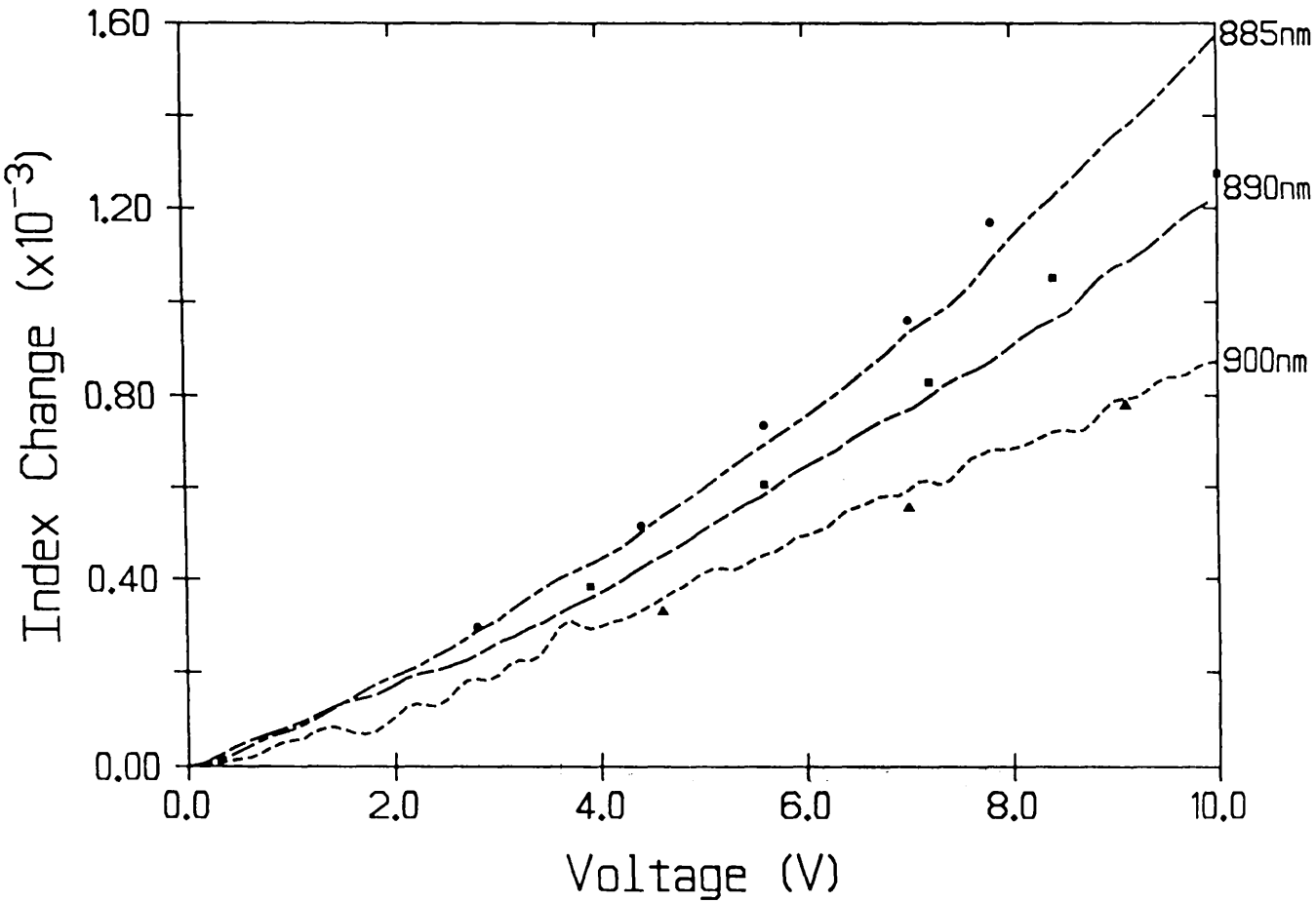

Figure 5.5
Change in effective index of MV348 waveguides with applied voltage as measured at three wavelengths as measured by two methods:
(i) Fabry-Perot method (points) and
(ii) Mach-Zehnder interferometer (lines).

Measurements were carried out for TE polarisation at wavelengths in the range 910nm to 865nm. This was equivalently a range of photon energies 105meV to 34meV below the resonance energy of the e1−hh1 exciton transition which has a resonance energy of 1.471eV. For TM polarisation, the wavelength range of 910nm to 855nm was equivalently a range of 115meV to 28meV from the e1−lh1 exciton transition which has a resonance energy of 1.481eV. These transitions define the band edge of the material for their respective polarisations and it is the shifting of these transitions to lower energies when an electric field is applied perpendicular to the plane of the quantum wells that enhances the electro−optic effect in MQW GaAs/AlGaAs.

At wavelengths approaching the material band gap, the absorption changes ($\Delta\alpha$) dominate the electro−optic properties of the MQW structure. So at wavelengths close to the band gap, the fringe contrast of the interferometer became increasingly poor when a voltage was applied to the waveguide and electro−absorption decreased the waveguide output intensity. As a result, the control loop could not hold onto a shifting fringe over a large range of voltages and for wavelengths of less than 880nm, the maximum voltage for which Δn could be monitored was limited by absorption changes resulting from electro−absorption in the waveguide.

Section 5.3.2 Results From MV348 Waveguides.

TE Polarisation.

The measurements of Δn against reverse bias voltage for TE polarisation and propagation along [1$\bar{1}$0] and [110] are shown in figures 5.6 and 5.7 respectively. It is important to note that the measured Δn values are in fact the change in effective index of the waveguides, and not the change in index of the MQW region.

There are two most prominent features of figs 5.6 and 5.7. Firstly, for both of these propagation directions there is a large spectral variation in the electro−optic effect, with Δn increasing dramatically for wavelengths approaching the exciton resonance. Secondly, the change in index is nonlinear with voltage, unlike that of both bulk GaAs [Suzuki et al '84] which exhibits very little electro−refraction [Van Eck et al '86] or MQW GaAs/AlGaAs away from the band edge [Glick et al '85]. In both of these instances the linear electro−optic effect dominates and it is only when the shifting band edge of the MQW material

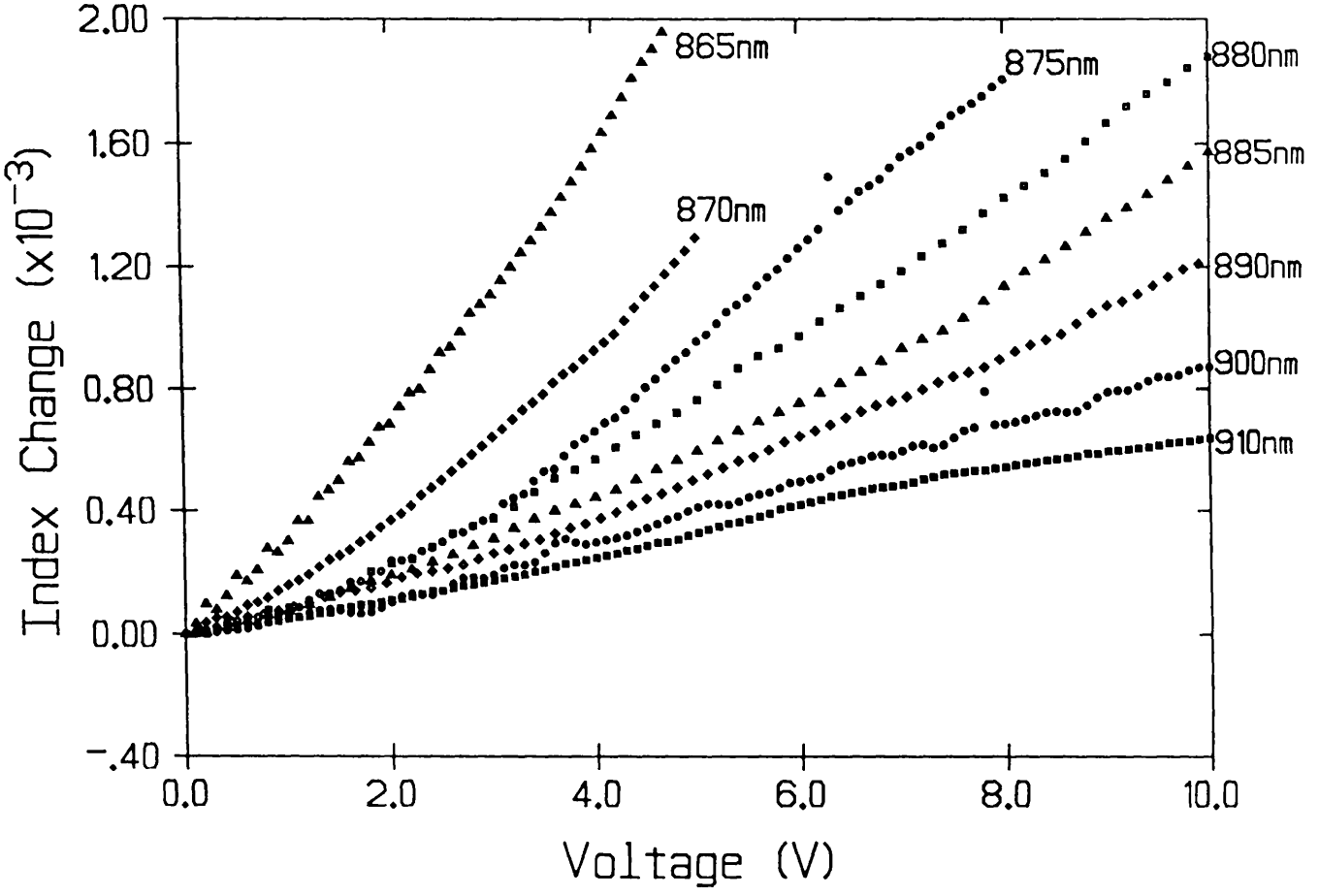

Figure 5.6
Change in refractive index with applied voltage at a number of wavelengths in 3μm wide stripe waveguides fabricated in wafer MV348. The direction of propagation is along the crystalographic direction [1$\bar{1}$0], and polarisation is TE.

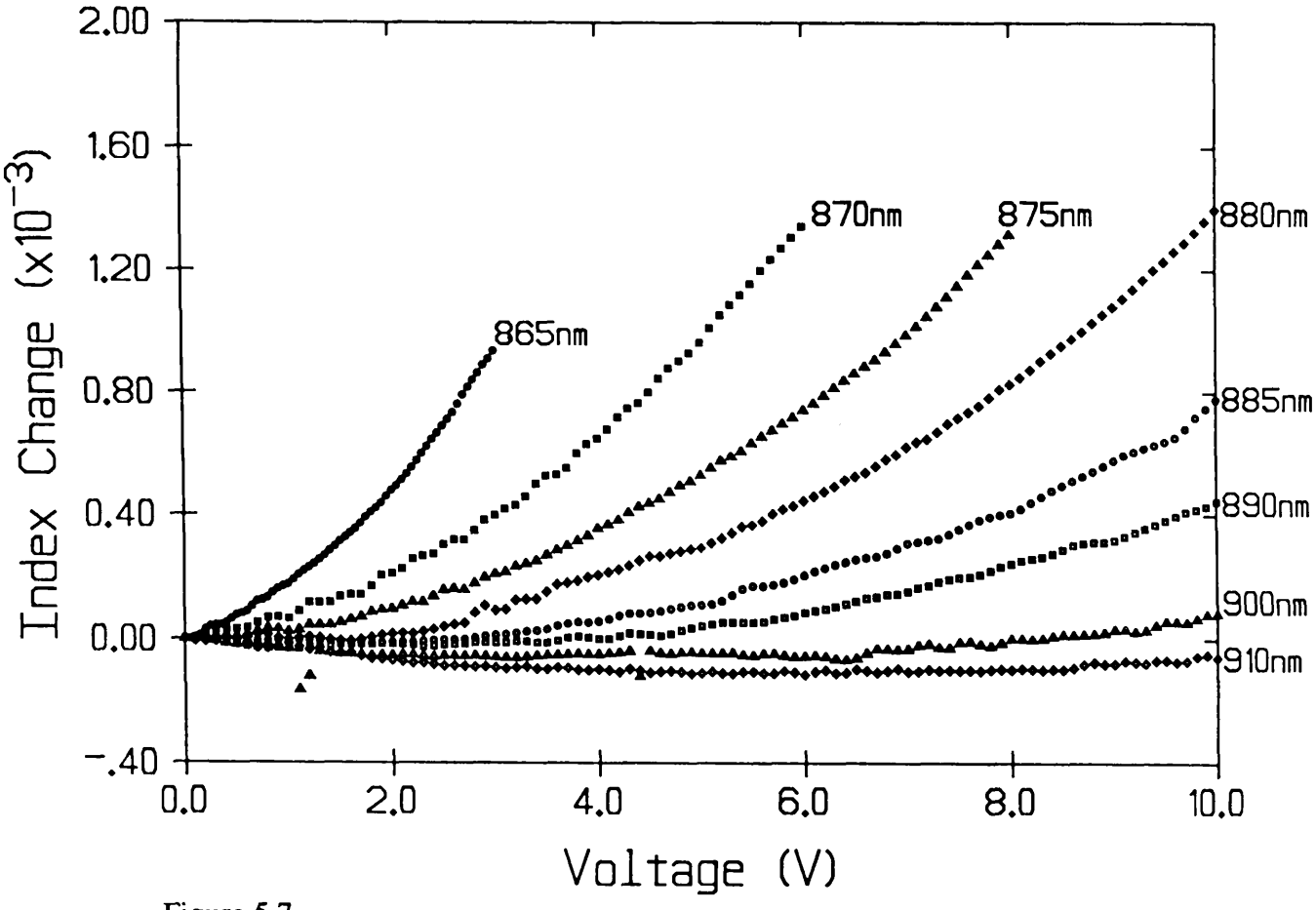

Figure 5.7
Change in refractive index with applied voltage at a number of wavelengths in 3μm wide stripe waveguides fabricated in wafer MV348. The direction of propagation is along the crystalographic direction [110], and polarisation is TE.

contributes to a large electro-refractive effect close to the band edge that Δn becomes non linear with voltage.

It is interesting to examine the magnitude and spectral varition of Δn for propagation along [1$\bar{1}$0], for which the linear electro-optic and electro-refractive effects add constructively. For an applied voltage of 10V, an index change of 0.6×10^{-3} at a wavelength of 910nm (112meV away from the exciton resonance) increases by a factor of 3 to 1.9×10^{-3} for a wavelength of 880nm. These values are large compared with a value of 0.4×10^{-3} expected from a waveguide in bulk GaAs using a value of 1.1×10^{-12}m/V for r_{41} [Yariv '85]; a factor of up to 4.5 increase. Considering the low $\Delta\alpha$ measured at a reverse bias voltage of 880nm (15dB/cm), the enhancement of the electro-optic effect at short wavelengths demonstrates the advantages in using quantum well material over bulk material for phase modulator applications.

Examining the index change for propagation along [110], the size of Δn is less than for propagation along the perpendicular direction of [1$\bar{1}$0]. This is a result of the directional dependence of the linear electro-optic (LEO) effect [Faist et al '87] leading to the linear electro-optic and electro-refractive effects having opposing signs for propagation along the crystalgraphic direction [110]. The maximum Δn observed is therefore reduced to 1.3×10^{-3} compared with 1.8×10^{-3} for similar wavelengths and voltages for propagation along [1$\bar{1}$0].

As with propagation along [1$\bar{1}$0], the electro-refactive effect becomes much stronger at photon energies close to the band-edge, increasing the resultant index change. At the longer wavelengths of 900-910nm, away from the band-edge, the LEO and electro-refactive effects are of the same magnitude and of the opposite scence, thus cancelling one another out and resulting in an index change which remains close to zero and is slightly negative.

TM Polarisation

The results of measuring the electro-optic effect for TM polarisation in the waveguides propagating along the crystalographic direction [1$\bar{1}$0] in MV348 are shown in figure 5.8. With polarisation perpendicular to the plane of the quantum wells, the transition e1-hh1 is forbidden and the band edge is defined by the higher energy e1-lh1 exciton transition. As a result, the electro-optic measurements for TM polarisation could be made at shorter wavelengths than for TE polarisation.

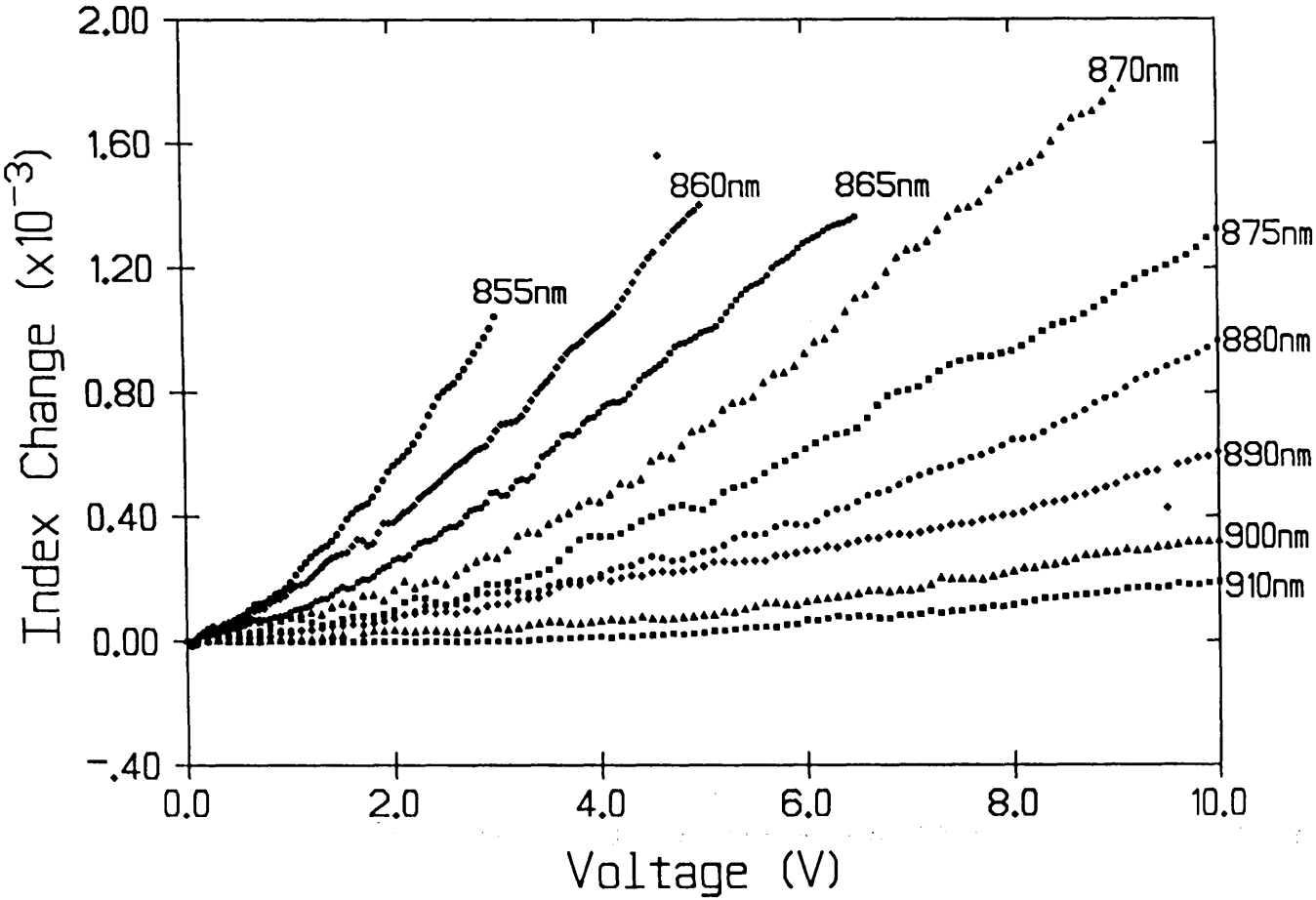

Figure 5.8
Change in refractive index with applied voltage at a number of wavelengths in 3μm wide stripe waveguides fabricated in wafer MV348. The direction of propagation is along the crystalographic direction [1$\bar{1}$0], and polarisation is TM.

As with TE polarisation, the index change is non-linear with voltage and highly wavelength dependent. At the longest wavelength of 910nm, 115meV from the e1-hh1 transition, no index change is observed until a voltage of 4V is applied to the waveguide. This is in contrast to TE polarisation for which a comparabl index change was measured at this wavelength for [1$\bar{1}$0] propagation and a negative index change was observed for propagation along [110].

Measurements of Δn were carried out for propagation along both [1$\bar{1}$0] and [110] crystalographic directions with TM polarisation and the results taken at two repesentative wavelengths are shown in figure 5.9. The difference in the electro-optic effect for these propagation directions was within the accuracy of the measuring system showing that the electro-optic effect for TM polarisation was directionally independent. This will be discussed in further detail in section 5.5.

SECTION 5.4 ISOLATING THE LINEAR ELECTRO-OPTIC AND ELECTRO-REFRACTIVE EFFECTS IN MQW WAVEGUIDES.

Although it has been noted in section 5.3 that the electro-refractive effect in the waveguides is nonlinear with applied voltage, the dependence of Δn with voltage has not been examined. In considering the electro-refractive effect in relation to the Franz-Keldysh effect in bulk III-V semiconductors, [Bennet et al '87] showed theoretically that, close to the band edge, the index change is quadratic with field strength. The quadratic nature of the electro-refractive effect has also been demonstrated experimentally in MQW GaAs/AlGaAs [Glick et al '86] and InGaAs/GaAs [Das et al '88] at wavelengths close to the band edge. In both these instances the linear and quadratic effects were isolated by using the directional dependence of the linear electro-optic effect [Faist et al '87].

This technique has also been used in the present work to isolate the components of Δn which vary linearly and quadratically with electric field strength. The electro-refactive effect is predicted to have a quadratic dependence on electric field strength, such that the index change in the waveguides can be expressed as:

$$\Delta n(E) = \tfrac{1}{2} n_0^3 [\pm \Gamma_1 r_{63} E_z + \Gamma_2 s E_z^2] \qquad (5.5)$$

where $\Delta n(E)$ is the change in the effective index of the waveguide in an electric field E_z which is in the direction perpendicular to the plane of the quantum well

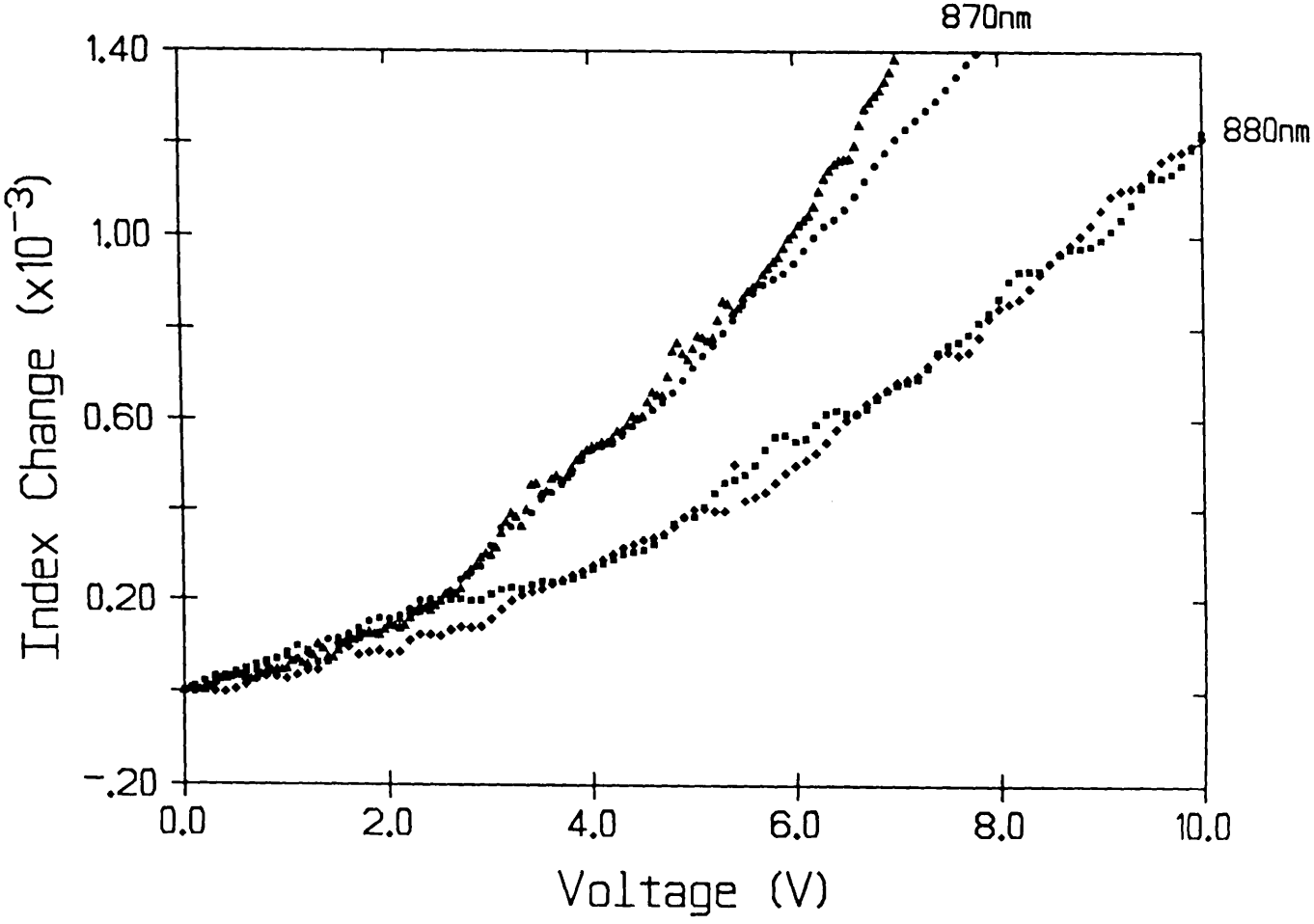

Figure 5.9
Directional dependence of the electro-optic effect in MQW waveguides with TM polarisation. Comparison of the change in refractive index of MV348 stripe waveguides for TM polarisation propagating in the two crystal directions [1$\bar{1}$0] and [110]

layers, and r_{63} and s are the linear and quadratic electro–optic coefficients respectively. Γ_1 and Γ_2 are the confinement factors of the optical field to the active region of the waveguide for the LEO and quadratic electro–optic (QEO) effects respectively.

The sign of the LEO is positive for light propagating along [1$\bar{1}$0] and negative for propagation along [110]. It is therefore possible to isolate the linear electro–optic (LEO) and quadratic electro–optic (QEO) effects by the procedure of subtracting or adding the measured values of Δn for the two propagation directions respectively:

$$-\tfrac{1}{2}\, r_{63}\, E_z\, \Gamma_1 = \tfrac{1}{2}\, [\, \Delta n[1\bar{1}0] - \Delta n[110]\,] \qquad (5.3(a))$$

and

$$\tfrac{1}{2}\, s\, E_z\, \Gamma_2 = \tfrac{1}{2}\, [\, \Delta n[1\bar{1}0] + \Delta n[110]\,] \qquad (5.3(b))$$

where $\Delta n[1\bar{1}0]$ and $\Delta n[110]$ are the changes in the effective index of the MQW waveguide in an electric field E_z for their respective propagation directions. These equations are only valid if the index change can be expressed by the two terms: LEO and QEO.

Section 5.4.1 Calculating The Confinement Factors Γ_1 and Γ_2

The measured values of the change in effective index of the waveguides gave a weighted average index change; weighted by both the intensity of the confined light and the electric field strength in the different regions of the guide. To calculate the coefficients r_{63} and s, the LEO and QEO effects respectively, the confinement of the light to the active region of the waveguide had to be calculated.

The confinement under the stripe of the waveguides was tight. This was apparent fom the WAVE calculations discussed in chapter 3 and also from observing the waveguide output on an IR camera. With the light tightly confined, the majority of the guided light was directly under the electrode and thus experienced the effects of the electric field. It was therefore decided to use the confinement factor of the slab waveguide to represent the confinement of the stripe waveguides.

The overlap of the intensity of the optical mode and the applied electric field of the slab guide is shown schematically in figure 5.10 for both the LEO and

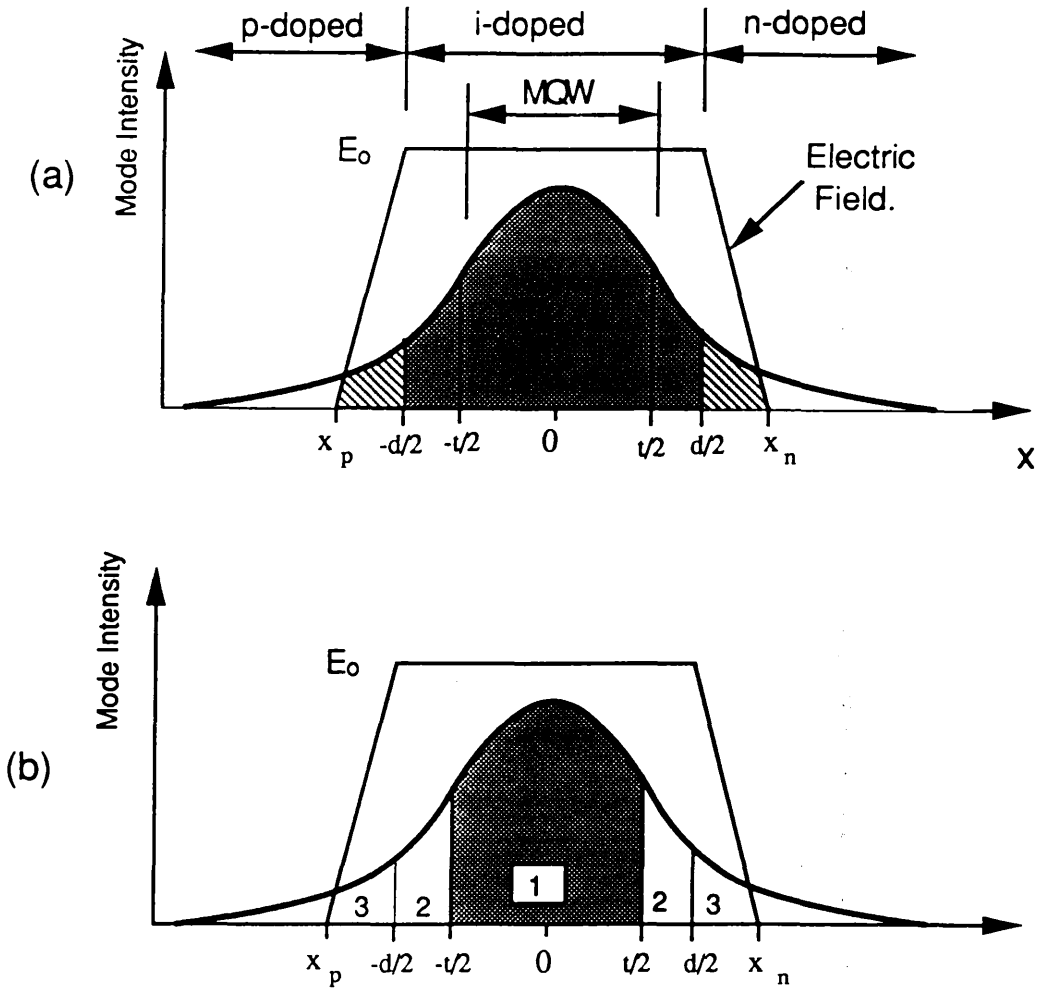

Confinement in active intrinsic region of waveguide

Confinement in active depletion region of waveguide

Region 1: i-doped MQW Guide $\psi_1 = \cos(2ux/t)$

Region 2: i-doped AlGaAs Cladding
Region 3 Depletion region of doped cladding
} $\psi_2 = \cos(u).\exp[w(1-2x/t)]$

Figure 5.10
Confinement of the guided mode to the active region of an MQW waveguide for:
(a) Linear Electro-optic effect and
(b) Quadratic Electro-optic effect.

QEO effects. In order to obtain the relevant confinement factor, expressions for a confinement factor to the active region, weighted with the electric field strength in each region of the waveguide, were derived. The confinement factors Γ_1 and Γ_2 were then obtained from these expressions.

Section 5.4.2 Linear Confinement Γ_1

When considering the LEO effect, the intrinsically doped AlGaAs spacer region of the cladding layer experiences the large electric field of the reverse biased p− i− n diode. As a result, this region also contributes to the change in the effective index of the waveguide through the LEO effect. Hence, in calculating the confinement factor Γ_1, the intrinsically doped spacer layer has to be included in the overlap integral. Calculating the partial confinement factors γ_1 and γ_2 for regions 1 and 2 of figure 5.10(a) simply involved including regions 1 and 2 in the integration of Ψ in the numerator of the confinement factor:

$$\gamma_1+\gamma_2 = \frac{\int_{-t/2}^{t/2} E_0 \, |\Psi_1(x)|^2 \, dx \; + \; 2\int_{t/2}^{d/2} E_0 \, |\Psi_2(x)|^2 \, dx}{\int_{-\infty}^{\infty} |\Psi(x)|^2 \, dx \quad \int_{-d/2}^{d/2} E_0 \, dx} \qquad (5.7)$$

Ψ_1 and Ψ_2 are the guided mode functions of the waveguide in the guiding region and cladding layers and are given by:

$$\Psi_1 = \cos(2ux/t)$$

and

$$\Psi_2 = \cos(u).\exp[\, w(1- |x|/t) \,]$$

where t is the width of the guiding region and u and w are given by:

$$u = \pi t/\lambda \; (n_1^2 - n_e^2)^{\frac{1}{2}}$$

and

$$w = \pi t/\lambda \; (n_e^2 - n_2^2)^{\frac{1}{2}}$$

with n_1 and n_2 being the refractive indices of the MQW guide layer and AlGaAs cladding layer respectively and n_e the effective index of the waveguide.

The electric field strength in the intrinsic region was been approximated to a constant E_0, although in reality there is a variation of $3\text{x}10^{-4}$ V/cm across the region in wafer MV348. Substituting the relevant expressions for Ψ into equation 5.7, the following expression was derived for the confinement factor to regions 1 and 2:

$$\gamma_1 + \gamma_2 = 1 - \frac{1/w.\ \cos^2(u).\ \exp[\ 2w(1-d/t)\ ]}{1 + 1/(2u).\ \sin(2u) + 1/w.\cos^2(u)} \qquad (5.8)$$

For a given wavelength, the value of $\gamma_1 + \gamma_2$ is constant for all voltages applied to the waveguide since the width of the region does not vary. However, in calculating the confinement to region 3, the variation in the depletion widths x_p and x_n had to be taken into account, together with the x dependence of the electric field strength. This was calculated, and found to contribute less than 1% to the confinememt factor and so was neglected.

Section 5.4.3 Quadratic Confinement Γ_2.

Calculating Γ_2, the confinement of the optical field in the active region for the QEO, was less complex. Since the QEO in bulk GaAs [Van Eck et al '86] is 2 orders of magnitude less than in MQW GaAs [Glick et al '87], the confinement of the optical field in the MQW guiding region need only be considered. Hence, the standard expression for the confinement factor of a guided mode can be used :

$$\Gamma_2 = \frac{1 + 1/(2u).\ \sin(2u)}{1 + 1/(2u).\ \sin(2u) + 1/w.\ \cos^2(u)} \qquad (5.9)$$

Section 5.4.4 Evaluating Γ_1 and Γ_2.

The confinement factors Γ_1 and Γ_2 were used in calculating the linear and quadratic electro–optic coefficients, r_{63} and s, of the MQW material at a number of wavelengths approaching the material band gap. It must be noted that these confinement factors varied with wavelength on two accounts. Firstly, the confinement has a wavelength dependency through u and w. Secondly, the wavelength dependency of the refractive index of both the MQW guiding region and the AlGaAs cladding also affects the effective index of the waveguide and hence u and w. The effective index of the waveguides was therefore calculated at each wavelength before Γ_1 and Γ_2 could be obtained.

To calculate the effective index of the waveguide, the values of the refractive index of the AlGaAs cladding layer were calculated for each wavelength [Adachi '85]. For the MQW guiding region, the values of the refractive index were taken from direct measurements of the refractive index of MQW waveguides [Chen et al '87]. The MQW structure used for these measurements was very similar to that of MV348, consisting of 25 periods of 8nm GaAs wells and 8nm AlGaAs barriers with

fractional Al composition of x= 0.26. Using these values was considered more accurate than calculating them using the rms values [Ohke et al '85] because the large dispersion of refractive index at wavelengths so close to the excitonic band edge is not taken into account by the rms method. Using these values of refractive index, the effective index of the slab waveguide was calculated using the effective index method and the confinement factors Γ_1 and Γ_2 calculated.

SECTION 5.5 LINEAR ELECTRO–OPTIC EFFECT (LEO) IN MV348 WAVEGUIDES.

Section 5.5.1 Isolating the LEO Effect.

TE Polarisation.

To isolate the LEO effect from the measurements of Δn against voltage, the data shown in figures 5.6 and 5.7 for the propagation directions [1$\bar{1}$0] and [110] was substituted into equation 5.6(a). The isolated refractive index change plotted against electric field strength (E) in figure 5.11(a) then gave the values of the LEO coefficient r_{63} at the different wavelengths. The index changes as a function of electric field lie essentially on a single straight line for all the wavelengths measured, indicating two important features. First, a LEO has been isolated, implying that no other significant electro–optic effect which has the directional dependence exists in the waveguides. Second, the LEO is not highly wavelength dependent for photon energies in the range 105meV to 34meV below the e1–hh1 exciton peak.

The gradient of the curves, substituted into equation 5.6(a) together with the confinement factor (Γ_1), gave the value of the LEO coefficient r_{63}. The dispersion of the MQW refractive index was also taken into account for the n_0^3 term in equation 5.6(a) by using values of the calculated waveguide effective index at each wavelength.

The wavelength dependence of the cefficient r_{63} is plotted in fig. 5.11(b), showing as a general trend a decrease in the LEO coefficient r_{63} with wavelength. The values of the LEO coefficient are comparable with the measured values of 1.7×10^{-12}m/V and 1.6×10^{-12}V/m at wavelengths 30meV and 50meV from the exciton respectively [Glick et al '87].

(a)

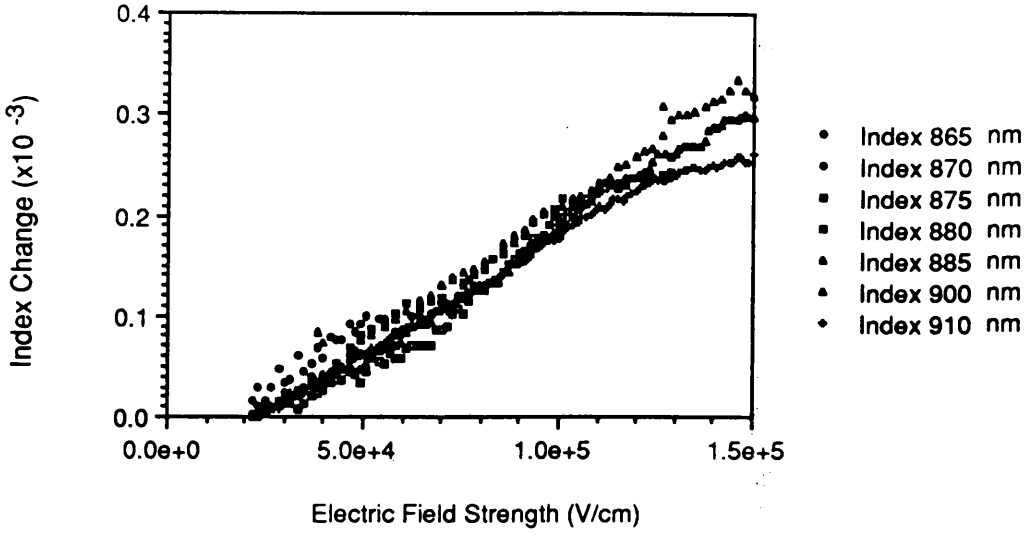

(b)

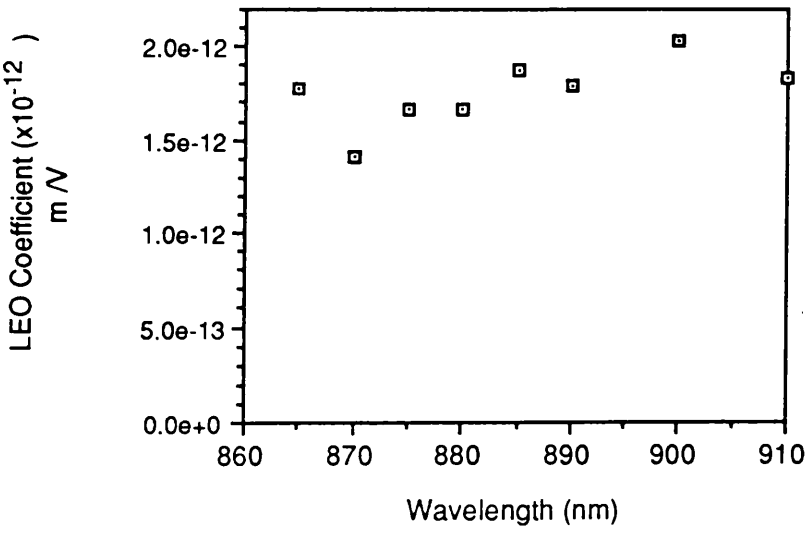

Figure 5.11
Directionally dependant electro-optic effect in MQW waveguides in MV348.
(a) Isolated refractive index change at a number of wavelengths as labelled at the side of the graph.
(b) Wavelength dependance of the linear electro-optic (LEO) coefficient in MQW material MV348.

TM Polarisation.

Measurements of Δn for TM polarisation with propagation along both the crystalographic directions [110] and [1$\bar{1}$0] were carried out. The difference in the index change for these two directions was not as significant, in contrast to TE polarisation. For comparison, figure 5.9 shows measurements of Δn for propagation along the crystalographic directions [1$\bar{1}$0] and [110] with TM polarisation at two wavelengths.

Within the accuracy of the measuring system, there appears to be no difference between the electro-optic effect for these two propagation directions. The indication from this is that the linear electro-optic effect is absent from MQW GaAs with polarisation perpendicular to the quantum wells. This is observed in bulk GaAs [Faist et al '87] and also predicted by crystal symmetry for bulk crystals with point group symmetry $\bar{4}3m$ in an electric field along the direction of polarisation (Section 2.5.1).

Section 5.5.2 Discussion of LEO Effect in MQW GaAs/AlGaAs.

In discussing the results for isolating the LEO effect in GaAs/AlGaAs MQW the results will be compared with data and theoretical studies published in the literature. The LEO effect in MQW material has received limited attention because of the dominance of the quadratic effect close to the band edge. However, to compare the above measured values of the LEO coefficient with those measured by others in both MQW and bulk GaAs, table 5.1 has been included, listing the values published in the literature.

Experimental Studies of LEO in MQW Materials.

Measurements have been carried out at wavelengths both close to and far from the band edge of MQW GaAs [Glick et al '85, '86 and '87] and also far from the band edge in bulk GaAs [Glick et al '88]. Measurements made at two wavelengths 50 and 30meV from the 1e-1hh transition [Glick et al '87] showed the variation in r_{63} of 0.1×10^{-12}m/V, within experimental error. The indication from these measurements is that any dipersion in r_{63} in MQW GaAs/AlGaAs is not significant.

In assessing whether there are any advantages in utilising the LEO effect in MQW GaAs over bulk GaAs, a comparison of the LEO effect in the two material

Material	Well Width (nm)	Wavelength (μm)	ΔE (meV)	Polarisation	Electro-Optic Coefficent		
					Linear	Quadratic ($x10^{-20}$ m^2/V^2)	
					r_{63} ($x10^{-12}$ m/V)	s_{33}	$(R_{33}-R_{13})$
GaAs/AlGaAs (1)	12.2		50	TE	-1.6		6
			30	TE	-1.7		19
GaAs/AlGaAs (2)	10.0		34	TE	-1.6	300	
GaAs/AlGaAs (3)	10.0		40	TM	-7.34	187	
GaAs/AlGaAs (4)	9.4		60	TM		47	
GaAs/AlGaAs (5)	9.4		21	TE		2000	
			16	TE		4300	
			12	TM		4600	
GaAs/AlGaAs (6)	12.2	1.15		TE	-1.47		0.52
	6.6	1.15		TE	-1.52		
	Bulk	1.15		TE	-1.43		37.4
GaAs (7)	Bulk	1.06		TE	-1.65		2.5
InGaAs/GaAs (8)	10.0	1.06	25	TE	1.82		
		1.15	115	TE	0.26		

(1) Glick et al '87,
(2) Bradley et al '89,
(3) Zucker et al '88,
(4) Weiner et al '87,
(5) Wood et al '87,
(6) Glick et al '88,
(7) Faist et al '87,
(8) Das et al '88.

Table 5.1:
Measured values of the LEO and QEO Coefficients for MQW and bulk and MQW III/V materials.

types was carried out at 1.15μm [Glick et al '88]. They found a variation of only 3% in the LEO coefficient r_{63} for the three stuctures examined. This variation is more likely to originate from the difference in the average Al concentration of the samples, rather than the different material types.

Theoretical Models of LEO in GaAs.

With the similarity in r_{63} between MQW and bulk GaAs, it is worth while looking at the theoretical models for the LEO in bulk GaAs. The LEO effect as studied by [Adachi et al '84] in bulk GaAs looked at the variation of both r^{S}_{41} and r^{P}_{41}, the strain free and stress free LEO coefficients respectively, at wavelengths approaching the band gap. The model predicted a constant, negative value for r_{41} at wavelengths away from the band gap with a sharp increase in $|r_{41}|$ for wavelengths within 200meV of the band gap.

This is however in contrast to both the calculations and measurements of r_{41} made by [Suzuki '84] on bulk GaAs. Both the model and experimental measurements show a steady decrease in r_{41} from 1.55×10^{-12} to 1.33×10^{-12}m/V across the wavelength range 1.55 to 1.06μm. This spectral variation is of the same order as the variations found in the present measurements on MQW waveguides, thus reinforcing the similarities of the LEO in bulk GaAs and MQW GaAs/AlGaAs which were indicted by [Glick et al '88].

Section 5.5.3 Conclusions.

The LEO effect has been successfully isolated from the measurements of the electro-optic effect in MQW GaAs/AlGaAs waveguides and the LEO coefficient r_{63} evaluated. This has been done for TE propagating modes at photon energies from 105meV to 34meV below the e1-hh1 exciton peak. The magnitude of r_{63} has been shown to be comparable to that measued in bulk GaAs, indicating that utilising the LEO effect in MQW GaAs/AlGaAs offers no advantages over bulk GaAs.

The results have shown that there is a small decrease in r_{63} at wavelengths approaching the material band gap, which is again similar to the effect seen in bulk GaAs. This is, however, in contrast to the LEO in InGaAs/GaAs MQW waveguides, where measurements have shown that there is a large increase in the LEO coefficient at wavelengths close to the absorption edge [Das et al '88].

From measurements of the electro–optic effect with TM polarisation, the LEO effect has been shown to be absent. For this polarisation and electric field direction, crystals with point group symmetry $\bar{4}3m$ such as GaAs exhibit no LEO effect. This is indicated by the tensor equation (2.25), and so the absence of the effect is therefore consistent with the point group symmetry of the MQW materials.

SECTION 5.6 QUADRATIC ELECTRO–OPTIC EFFECT (QEO) IN MV348 WAVEGUIDES.

Section 5.6.1 Isolating the QEO.

TE Polarisation.

The results of Δn against voltage shown in figures 5.6 and 5.7 were used to isolate the QEO effect in the waveguides by substitution of the data points into equation 5.6(b). As with the LEO, the electric field strength in the p–i–n structure was calculated for the voltages, and in order to verify that this directionally independent electro–refractive effect is quadratic with electric field strength, the isolated index change was plotted against E^2 (figure 5.12). The curves are linear for all wavelengths with the index changes increasing dramatically for wavelengths approaching the e1–hh1 exciton peak. This indicates that, in a wavelength range of 105meV up to 34 meV below the excitonic band edge, the electro–refractive effect leads to a change in refractive index (Δn) which is quadratic with electric field and that no other directionally independent electro–optic effect was present in the waveguides.

To calculate the quadratic electro–optic coefficients s_{33} at each wavelength, a least squares fit to the gradients of the curves in figure 5.12 was substituted into equation 5.6(b) together with the calcuated confinement factor to give the QEO coefficient s_{33}. The wavelength dependence of s_{33}, plotted in figure 5.13, shows a non linear increase in the electro–refractive effect, with the effect increasing dramatically at wavelengths in the spectral region of large electro–absorption.

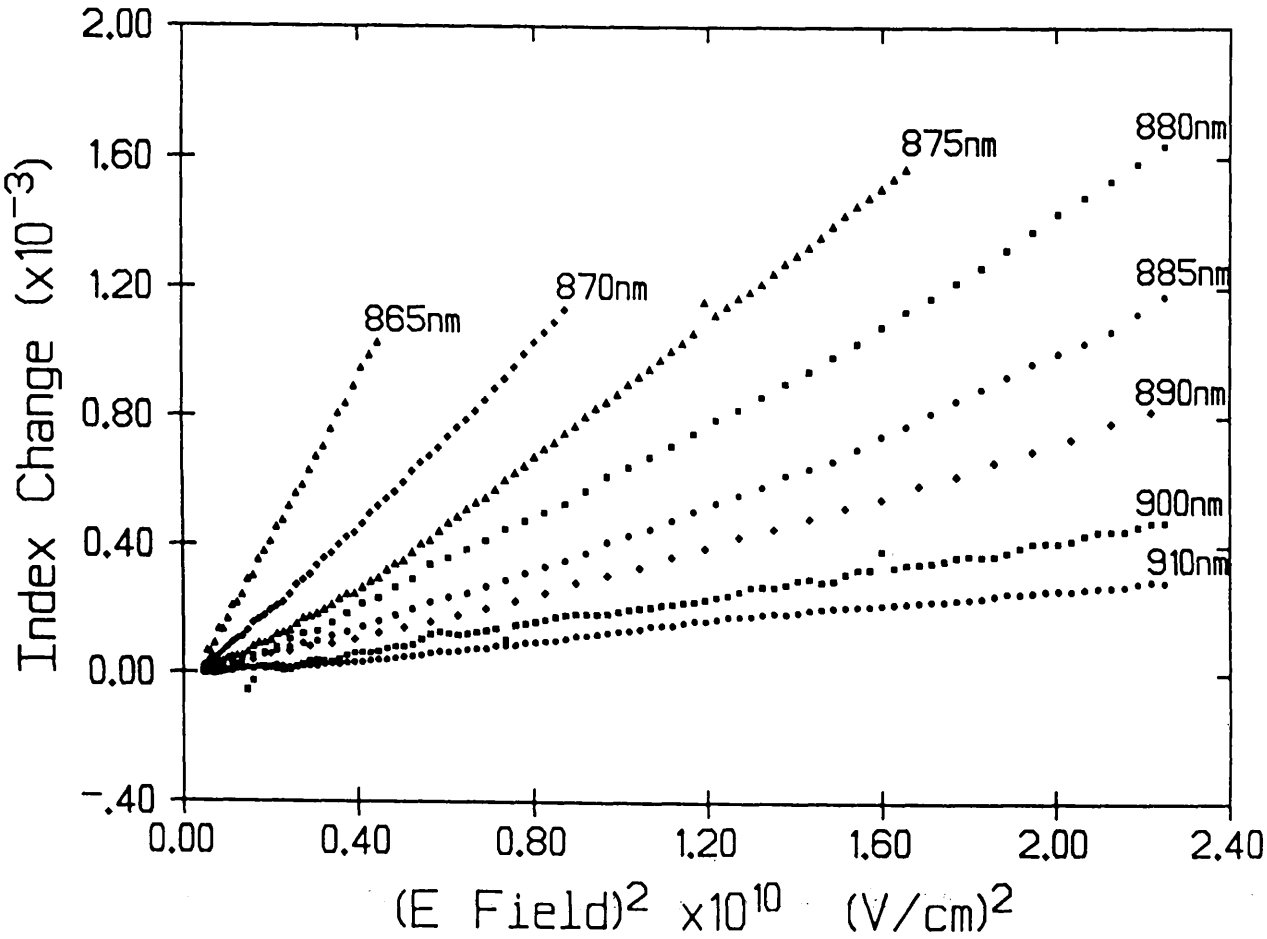

Figure 5.12
Isolated refractive index (Δ n) resulting from an electro-optic effect which shows no dependance on propagation direction for TE polarisation in MV348 stripe waveguides. Δ n plotted against electric field squared to show the quadratic nature of the electro-optic effect and the wavelength dependancy

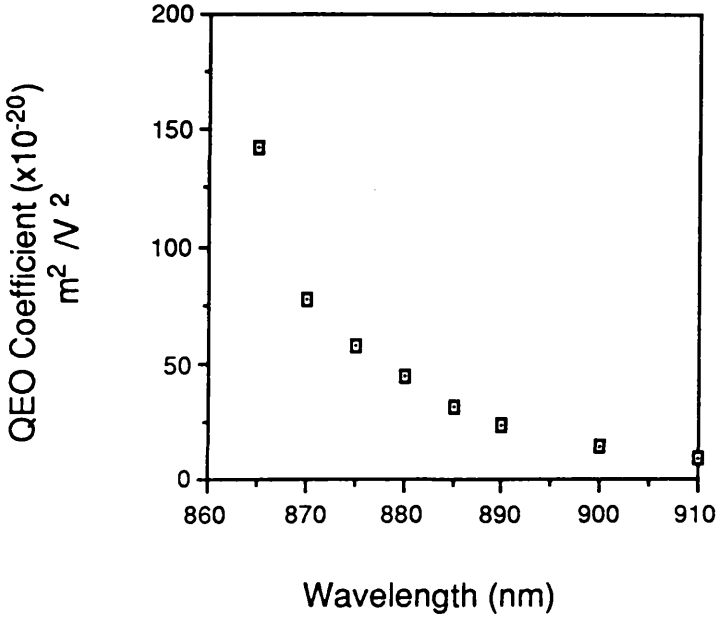

Figure 5.13
The wavelength dependance of the quadratic electro-optic coefficient s for TE polarisation in MQW material MV348 at wavelengths close to the material band gap.

TM Polarisation.

It has already been verified that no LEO effect was found in the waveguides for TM polarisation (section 5.5.1) and that the measured electro–optic effect shows no dependence on the direction of propagation of the waveguides. Plotting the measured index change (Δn) for TM polarisation as a function of E^2 (figure 5.14) shows a clear quadratic dependence of Δn with electric field strength. As with the TE polarisation, there is a significant increase in the measured Δn for wavelengths approaching the absorption edge. With the absence of the LEO effect in the waveguides, the only significant electro–optic effect is therefore the directionally independent electro–refractive effect and this can be described as a QEO effect in the wavelength range 115meV to 28meV from the band gap.

The QEO coefficients s_{33} were calculated for each wavelength in the same way as with TE polarisation. For the confinement factor Γ_1, the effective index of the waveguides was calculated using the values of MQW refractive index for TM polarisation [Chen et al '87], so that the absence of the e1–hh1 exciton transition was taken into account. The resulting values of s_{33} against wavelength, shown in figure 5.15 show the same functional form as for TE polarisation.

Section 5.6.2 Comparison of QEO in MQW material for TE and TM polarisation

There appear to be large similarities in the QEO effect in the waveguides for TE and TM polarisations. For both polarisations, the QEO effect is directionally independent, and shown to increase with the same functional form in both instances.

To compare the QEO effect for the two polarisations, the coefficient s_{33} has been plotted in figure 5.16 as a function of $(\lambda - \lambda_g)$, where λ_g is the wavelength of peak absorption of the e1–hh1 and e1–lh1 exciton for TE and TM polarisation respectively. The strong similarity of the coefficients implies that just below the band gap in the waveguides, the QEO effect is dominated by the electro–refraction associated with the lowest energy exciton peak. This is supported by calulations of electro–refraction in quantum well GaAs/AlGaAs [Hiroshima '87] which showed that there is a large index change in the vicinity of the excitonic peaks in an electric field.

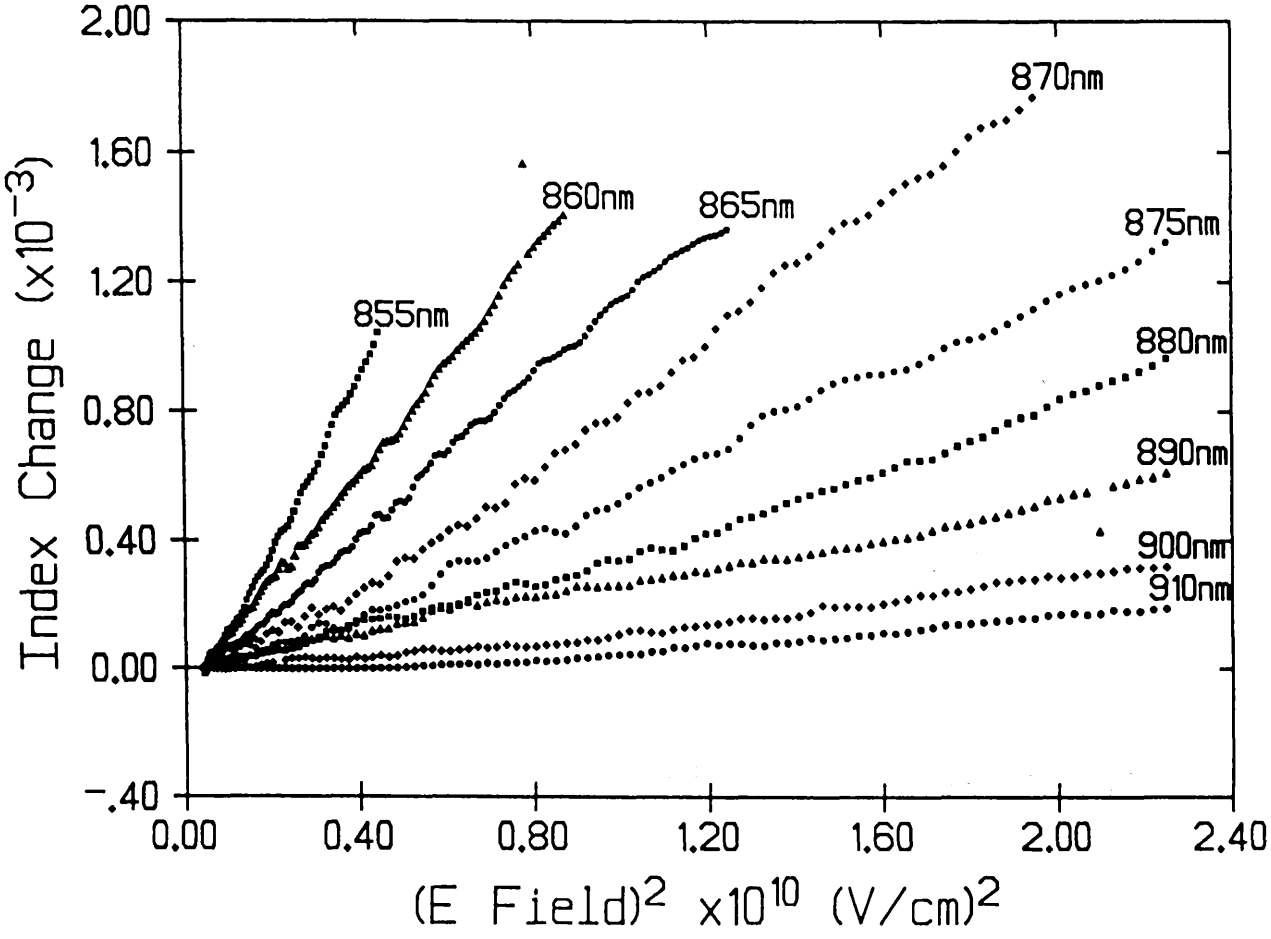

Figure 5.14
Refractive index change (Δn) for TM polarisation in MV348 stripe waveguides plotted against electric field squared, showing the quadratic nature of the electro-optic effect and the waavelength dependancy.

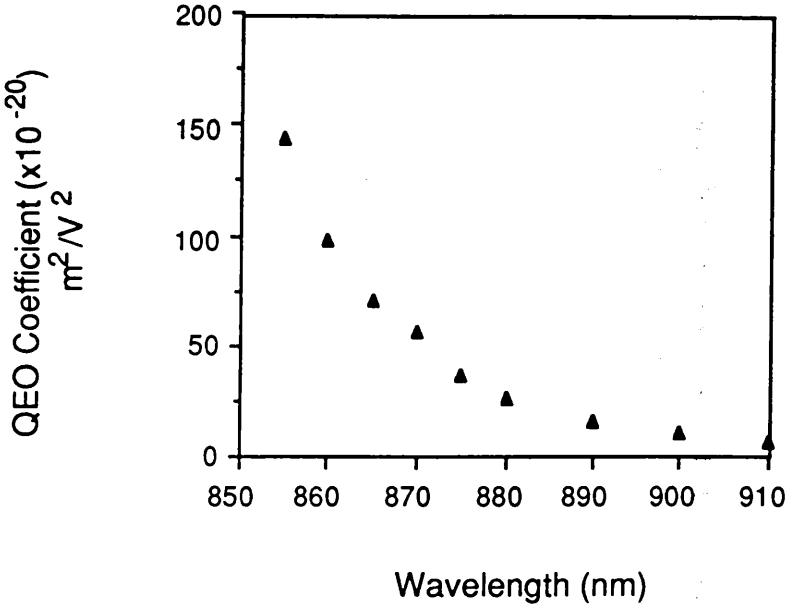

Figure 5.15
The wavelength dependance of the quadratic electro-optic (QEO) coefficient s for TM polarisation in MQW material MV348 at wavelengths close to the material band gap.

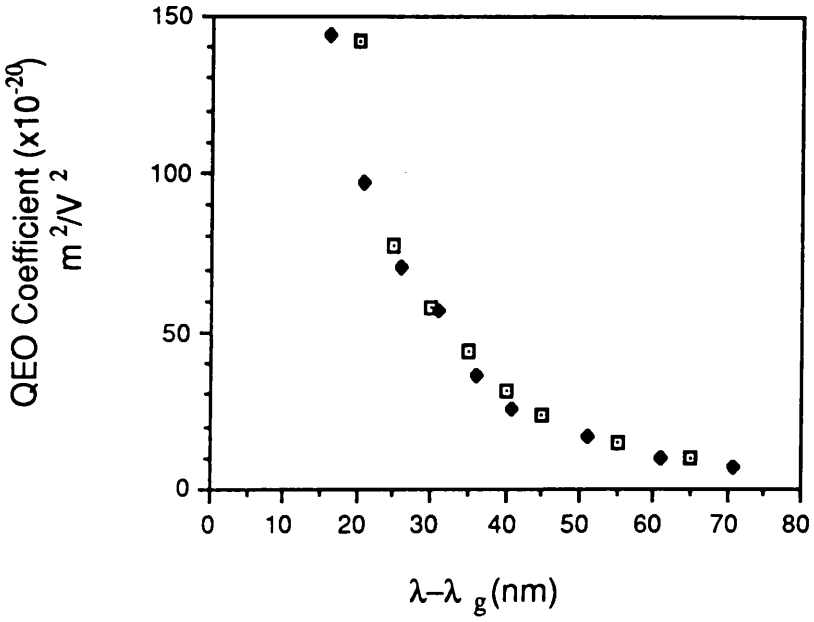

Figure 5.16
Comparison of the Quadratic Electro-Optic Coefficient for TE (□)and TM (♦) polarisation in MQW sample MV348 as a function of wavelength from band-gap ($\lambda-\lambda_g$) where λ_g is the wavelength of the e1-hh1 and e1-lh1 exciton transition for TE and TM polarisation respectively.

Section 5.6.3 Discussion of the QEO Effect In MQW Material.

In assessing the measured values of the QEO coefficient, the studies of the QEO carried out by others in both MQW and bulk GaAs will be discussed. The values of the QEO coefficients published for both MQW and bulk materials have been included in table 5.1.

With the exception of [Zucker et al '88(b)], no study of the full spectral dependence of the QEO effect at photon energies close to the band edge of MQW material has been reported, with most workers measuring at the most two wavelengths. Zucker used a Mach–Zehnder interferometer system to measure the change in refractive index through the electro–optic effect of a slab waveguide containing two 9.4nm quantum wells and showed large index changes at wavelengths close to the exciton resonances.

To obtain the LEO and QEO coefficients r and s, Zucker fitted the values of $\Delta n(E)$ to the equation:

$$\Delta n(E) = -\tfrac{1}{2} n_0^3 (rE + sE^2) \qquad (5.10)$$

for wavelengths between 10 and 70 meV below the band gap and for both TE and TM propagating modes. The values quoted for r_{63} and s_{33} are not included in table 5.1 since no correction for the confinements Γ_1 and Γ_2 was made, preventing a direct comparison of the QEO in the samples. However, the wavelength dependence of the QEO coefficient s_{33} showed similar trends to those seen in MV348, although the values of s_{33} for TE polarisation range from $-1.5\times10^{-20}m^2/V^2$ to $+1.5\times10^{-20}m^2/V^2$. Within this same wavelength range, the LEO coefficient is seen to vary from $-3.8\times10^{-12}m/V$ to $-0.2\times10^{-12}m/V$, a variation much larger than seen in the present work or by others [Glick et al '88]. For TM polarised light, the LEO was shown to have a finite value of $r_{33}\approx\pm0.3\times10^{-12}m/V$.

Fitting experimental data to equation 5.10 was also used in assessing a phase modulator [Zucker '88(a)] propagating a TM polarised mode. This yielded a LEO coefficient $r_{33}= 7.34\times10^{-12}$ m/V, a x5 increase on that of TE polarised light. It has, however, been shown in the present work and by others [Glick et al '88] that the LEO effect is absent in MQW material for TM polarisation. It therefore appears that this method does not effectively identify the origins of the index change, ie whether the index change originates from the LEO or QEO effects. There is therefore some doubt in the work reported by [Zucker et al '88(b)] on

the QEO coefficients s_{33} of GaAs/AlGaAs MQW.

The spectral dependence of the QEO coefficient ($R_{33}-R_{13}$), the difference in the QEO effect between TE and TM polarised light, in slab waveguides containing 30 x 12.2nm quantum wells was examined by [Glick et al '87]. An increase in the QEO coefficient was observed in going from a wavelength 50meV to 30meV below the band gap. In order to compare the values of QEO coefficients measured by [Glick et al '88] with the present values, the difference between the coefficients for TE and TM polarisation must be considered. Using the coefficients shown in figure 5.13 for TE polarisation and figure 5.15 for TM polarisation, we obtain:

$$s_{33}(TE) - s_{33}(TM) = 21.5 m^2/V^2 \text{ at } \Delta E=50meV$$
$$s_{33}(TE) - s_{33}(TM) = 72 \ m^2/V^2 \text{ at } \Delta E=34meV$$

Although larger by a factor of 3.5 than those reported by Glick et al, the increase across the wavelength range in both cases is a factor of 3.2. Comparing the published values of the QEO coefficient s_{33} in MQW waveguides, [Bradley et al '89(a)] have obtained a single value of s_{33} comparable with the present by asssuming the LEO ceofficient of $1.6x10^{-12}m/V$ as measured by [Glick et al '86], and then fitting the $\Delta n(E)$ data to equation 5.6(b).

Considering other material types, the electro-optic effect in InGaAs/GaAs stripe waveguides was measured to be highly wavelength dependant [Das et al '88] for both the LEO and QEO effects. The dispersion of the LEO effects in InGaAs/GaAs MQW material is consistent with the LEO effect in bulk InGaAs.

Theoretical Modeling of the QEO in MQW Material.

Considering the dominance of the electro-refractive effect which manifests as a QEO effect in MQW material at wavelengths close to the band gap, modelling of the effect has received little attention, the most comprehensive being that of [Hiroshima '87]. The absorption edge of MQW GaAs/AlGaAs was modelled, taking into account both the allowed exciton transitions e1-hh1 and e1-lh1 and also the forbidden exciton transition e1-hh2, which becomes allowed in the presence of an electric field [Collins et al '86]. To calculate the refractive index change resulting from the QCSE, the Stark shift of the excitons [Miller et al '84] and the changing oscillator strength of the exciton transitions [Whitehead et al '88(a)] were modelled. The broadening of the exciton line width was neglected, although this is seen to be a significant effect in the electro-absorption of the present material MV348. The

change in refractive index, calculated at wavelengths both above and below the absorption edge, using the Kramers–Kronig transform, showed the refractive index of the material increasing by approximately 10^{-2} in an electric field of 80kV/cm for wavelengths 20meV from the e1–hh1 exciton transition. Measurements in the present work were only carried out for wavelengths up to 30meV from the e1–hh1 exciton transition, showing Δn of $\approx 10^{-3}$ at field strengths of 80kV/cm. The calculations would therefore seem to have reasonable agreement with the present measurements.

Both measurements [Bach et al '83] and calculations [Alping et al '87] indicate that the electro–refractive effect observed in bulk III–V semiconductors is two orders of magnitude less than in MQW materials. In bulk semiconductors, electro–refraction is related to the Franz–Keldysh effect for which the absorption changes exhibited are smaller, and so the electro–refraction is correspondingly smaller.

Section 5.6.4 Conclusion.

An electro–optic effect in MQW GaAs/AlGaAs which is independent of the direction of propagation of the waveguides (crystallographic directions [1$\bar{1}$0] or [110]) has been isolated. This effect has been shown to be highly wavelength dependent at photon energies close to the absorption edge and to be present for both TE and TM propagating modes. The refractive index change, resulting from electro–refraction associated with the quantum confined Stark shifting of the exciton resonances, manifests as a quadratic electro–optic effect. The quadratic electro–optic coefficients s_{33} associated with the electro–refraction have been measured and shown to increase rapidly at wavelengths approaching the exciton resonances. Comparison of s_{33} for TE and TM polarisation has shown that, at photon energies a few 10's of meV below the band gap, the refractive index changes are dominated by the Stark shifting of the lowest energy exciton. The refractive index changes are also 2 orders of magnitude greater than those seen in bulk GaAs. As such, the enhanced electro–optic effect in MQW GaAs/AlGaAs offers advantages over bulk GaAs in electro–optic devices.

SECTION 5.7 CONCLUSIONS.

The electro–optic effect exhibited by MQW GaAs/AlGaAs waveguides has been studied using a Mach–Zehnder interferometer system for measuring the phase modulation in the waveguides. In the analysis of the electro–optic effects in the waveguides, the spectral range concentrated on was the region where the material exhibited strong electro–absorption through the QCSE. In this region, the waveguides therefore showed a large phase modulation through the electro–refractive effect.

The electro–optic measurements were carried out on stripe waveguides with direction of propagation along the crystalographic directions [1$\bar{1}$0] and [110] and for polarisation in the plane of the quantum wells (TE polarisation) and perpendicular to the plane of the quantum wells (TM polarisation). With an electric field applied perpendicular to the plane of the wells, the electro–optic effect was shown to be directionally dependant for TE polarisation, with Δn being largest for propagation along [1$\bar{1}$0] and highly wavelength dependant for both TE and TM polarisations

The index change was separated into two components. The first was the linear electro–optic (LEO) effect which was only exhibited for TE polarisation, and was shown to have a directional dependance which gave rise to a negative Δn for propagation along [110] and positive for propagation along [1$\bar{1}$0]. The LEO coefficient r_{63} was calculated to be 1.6×10^{-12}cm/V for TE polarisation and was shown to be independent on wavelength in the wavelength range studied. This is comparable with the LEO coefficient found in bulk GaAs, which also shows minimal wavelength dependancy. The absence of the LEO effect for TM polarisation is consistent with the result in bulk III–V semiconductors with the given electric field direction. It can therefore be concluded that the LEO effect exhibited by MQW GaAs/AlGaAs does not significantly differ from the effect exhibited by bulk GaAs.

The second component to the electro–optic effect was present for both TE and TM polarisations and showed no directional dependance. The index change, which was shown to be a quadratic electro–optic (QEO) effect was however highly wavelength dependant, with Δn increasing dramatically with wavelength. This electro–optic effect is due to the electro–refraction associated to the QCSE in the MQW material. A QEO coefficient was calculated for both TE and TM polarisation at all the wavelengths considered and was found to be highly dependant upon $\lambda - \lambda_g$, where λ is the wavelength of the light and λ_g is the wavelength for

which the absorption of the e1−hh1 and e1−lh1 exciton peaks are maximum. It was therefore concluded that, at photon energies just below the material absorption edge, the electro−refraction is dominated by the shifting of the lowest energy exciton peak. In comparing the QEO effect exhibited by bulk GaAs with that measured in the GaAs/AlGaAs MQW waveguides, the change in refractive index was found to be greatly enhanced in MQW GaAs/AlGaAs.

Chapter 6 ELECTRO–OPTIC DIRECTIONAL COUPLING SWITCH.

Section 6.1 INTRODUCTION.

The electro–optic effect exhibited by MQW GaAs/AlGaAs stripe waveguides has been shown to be enhanced at wavelengths close to the material absorption edge due to the electro–refractive effect. It should be possible to utilise the large changes in refractive index experienced in intensity modulators [Soref et al '88] or phase modulators [Bradley et al '89(b)]. In some of these devices, there are associated problems with the large electro–absorption [Bradley et al '89(a)] experienced by the material. For instance, simultaneous amplitude modulation in MQW phase modulator waveguides is not a desirable feature and in integrated Mach–Zehnder modulators [Zucker et al '90], a loss of power in one arm of the device can lead to poor modulation .

One device which avoids the problem of electro–absorption is the electro–optic direction coupling switch (EODCS) which has been demonstrated in bulk GaAs/AlGaAs waveguides [Takeuchi et al '86]. Passive directional couplers have been demonstrated in MQW GaAs/AlGaAs waveguides [MacBean et al '86(b)] and now the design, fabrication and successful demonstration of the EODCS in MQW GaAs/AlGaAs waveguides is described in this Chapter.

Section 6.2 DESIGN OF DIRECTIONAL COUPLER.

Section 6.2.1 Principle of Operation of the Device.

The operation of a directional coupling switch is outlined in this section, beginning with a passive directional coupler. The devices considered here are directional couplers consisting of two identical parallel stripe waveguides which are close together ($3\mu m$ wide waveguides separated by $3\mu m$ in this instance). Light is coupled into one of these waveguides (say waveguide 1) and the coupling of the evanescent tail of the confined mode leads to the light being coupled into the adjacent waveguide (say waveguide 2). Assuming that the power of light P_0 is coupled into waveguide 1 of a lossless coupler, then the power in waveguides 1 and 2 at a point y along the length of the device is given by:

$$P_1(y) = P_0 \frac{K^2}{(K^2 + \delta^2)} \cos^2[\ (K^2 + \delta^2)^{\frac{1}{2}}\ y] \qquad (6.1a)$$

$$P_2(y) = P_0 - P_1(y) \qquad (6.1b)$$

where K is the coupling coefficient between the waveguides and δ is the mismatch between the waveguides. Thus, along the length of the device, light transfers from one waveguide of the device to the adjacent waveguide. If the waveguides are identical, $\delta = 0$ so power varies as $\cos^2(Ky)$ along the device length and at the coupling length L_c the condition $KL_c = \pi/2$ is reached and the light transfers completely from waveguide 1 to waveguide 2.

By perturbing one of the waveguides, the change in the effective index (Δn) introduces a difference in the propagation constant (β) between the two waveguide modes, where $\Delta\beta$ is given by $\Delta\beta = 2\pi\ \Delta n/\lambda_g$, where λ_g is the wavelength of the light in the waveguide. The perturbation changes the coupling length of the device, such that the power output from waveguides 1 and 2 of a device of length $KL = \pi/2$ is given by [Soref et al '88]:

$$P_1(\text{output}) = P_0 \exp\left[\ \frac{\Delta\beta L}{\rho}\ \right] \left|\cos(gL) \pm (i-1/\rho)\ \left[\ \frac{\Delta\beta L}{2gL}\ \right] \sin(gL)\right|^2 \qquad (6.2a)$$

$$P_2(\text{output}) = P_0 \exp\left[\ \frac{-\Delta\beta L}{\rho}\ \right] \left|\ \frac{i\pi}{2gL}\ \sin(gL)\ \right|^2 \qquad (6.2b)$$

where $(gL)^2 = (1 + i/\rho)^2 . (\Delta\beta L/2)^2 + (\pi/2)^2$

and $\rho = \Delta n/\Delta k$.

With $\Delta\beta = 0$ the output from waveguide 2 of the device is P_0, but by introducing a perturbation $\Delta\beta L = \sqrt{3}.\pi$ there is a total transfer of power away from waveguide 2 into waveguide 1. The choice of device length: $KL = \pi/2$ leads to the situation where total transfer of power between waveguides is possible. A more general form of equation (6.2) [Soref et al '88] shows that for a device of length $KL = \pi$ (ie when $\Delta\beta = 0$ then the power along the length of the device couples from waveguide 1 to 2 and back to 1) the best switching that can be achieved in the device is 50%. The devices considered here were therefore of length $KL = \pi/2$.

Changing the effective index of one of the waveguides can be achieved either by using the intensity dependent refractive index of the MQW waveguiding material [Jensen '82, Jin et al '88] or by using the electro–optic effect [Takeuchi et al '86, Zucker et al '89]. In the latter, the device is refered to as an electro–optic

directional coupling switch (EODCS), and the enhanced electro–optic effect exhibited by MQW GaAs/AlGaAs at wavelengths close to the absorption edge indicates that switching should be achievable at low voltages and for shorter device lengths. In the devices being studied here, the $\Delta\beta$ is achieved through the electro–optic effect in the MQW waveguide. Associated with the required Δn, there is however a large $\Delta\alpha$ experienced in the waveguide through the QCSE, as demonstrated in chapters 4. Analysis of the directional coupling switch [Soref et al '88] which includes both the $\Delta\alpha$ and Δn terms in the device model shows that the attenuation of the signal is minimised by applying an electric field across the waveguide 2. The devices designed and fabricated therefore had the electric field applied to waveguide 2.

Section 6.2.2 Design of Electro–optic Directional Coupling Switch.

To design the EODCS, a passive directional coupling device first had to be designed. The waveguide structure also had to have good electro–optic properties and so a planar MQW GaAs/AlGaAs waveguide structure identical to MV348 was used since this had been shown to exhibit good electro–optic properties. The full design of the wafer and the characterisation of the grown wafer A163 is given in chapter 3. A modification to the MQW planar waveguide design MV348 was incorporated in the wafer A163. The thickness of the i–doped layer was increased to bring the i–doping 0.3μm into the top AlGaAs cladding layer of the planar waveguide as shown in figure 3.5 in an attempt to isolate electrically the adjacent stripe waveguides of the device.

The passive directional coupler was then designed on the basis of using stripe waveguides 3μm in width separated by 3μm and optimising the etch depth of the stripes to maximise the coupling coefficient K of the device. The modified effective index method (MEIM) was used to model the devices, and an etch depth of 1.7μm for the stripe waveguides (leaving an outer slab thickness of 1.3μm) was calculated to give a maximum coupling coefficient and a coupling length of 2.3mm. This relatively long coupling length was due to the a 3μm separation of the waveguides, a parameter chosen to ease the fabrication. Reducing the separation to 1μm would have reduced the coupling length.

The mask for defining the devices consisted of sets of five devices with different interaction lengths. The input end of waveguide 1 of the devices extended to the edge of the samples. However, waveguide 2 of the individual devices was then staggered by intervals of 0.25mm from the edge of the sample, giving

different interaction lengths of the five devices on the sample, extending over a range of 1mm.

Section 6.3 DEVICE FABRICATION AND INITIAL TESTING.

The wafer A163 was grown by MBE in the Department of Electronics and Electrical Engineering, Glasgow for the purpose of fabricating electro–optic directional coupling switches (EODCS) in an MQW structure. The characterisation of the grown structure, described in Chapter 3, showed the wafer to contain a planar MQW waveguide and a p–i–n diode. Two types of waveguide samples were therefore prepared: one containing stripe waveguides similar to those used for electro–optic measurements and another containing directional coupler devices. The stripe waveguides were fabricated to enable the electro–optic effect in the material to be characterised before the directional coupling switches were studied. All waveguide devices were fabricated with the direction of propagation along the crystalographic direction [1$\bar{1}$0], since this yielded the maximum change in refractive index through the electro–optic effect (Chapter 5).

The design of the passive directional couplers showed that the etch depth of the devices was critical in optimising the interaction length. The thickness of the cladding layer in the grown structure was determined directly by imaging the epitaxial layers in a scanning electron microscope (SEM). A freshly cleaved edge of a A163 sample was stained by immersing it in 25% ammonia solution: deionised water (5:95 by volume) for 8 seconds, rinsing in deionised water and blow drying in dry nitrogen immediately before mounting the sample in the SEM. This treatment etches slightly the GaAs with respect to the AlGaAs layers and when viewed in the SEM showed quite clearly the epitaxial layers (figure 6.1). The thicknesses of the cladding layer and the MQW region could then be measured (figure 6.1(a)). Measurements from the micrographs coupled with the known well and barrier thickness calculated from growth conditions [Stanley '89] indicated that the cladding layer thickness was 1.5μm rather than the 2μm in the original design. The more detailed view of the MQW region of figure 6.1(b) clearly shows the individal wells indicating an average well and barrier width of 7.2nm. This measurement, coupled with the known well/barrier widths of 7.5nm from photoluminescence measurements, was used to estimate the tilt of the sample in the SEM, allowing a correction to the measurement of the cladding width.

The fabrication of the EODCS devices involved the same processing steps as

(a)

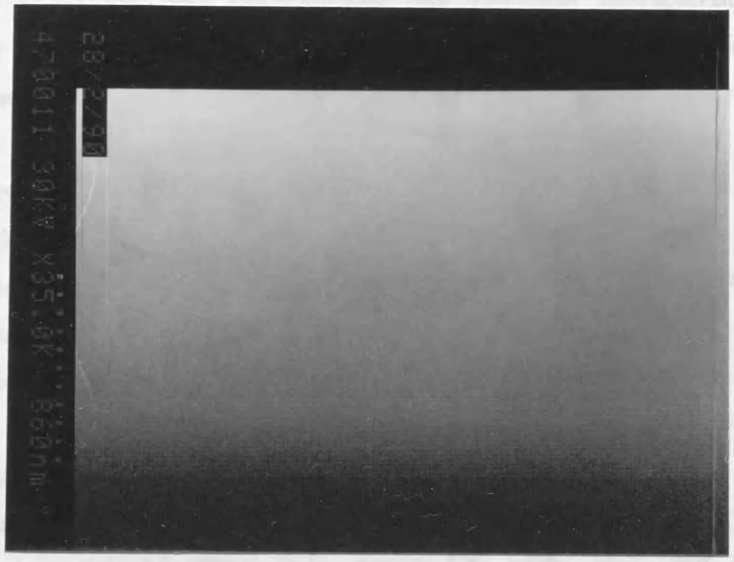

(b)

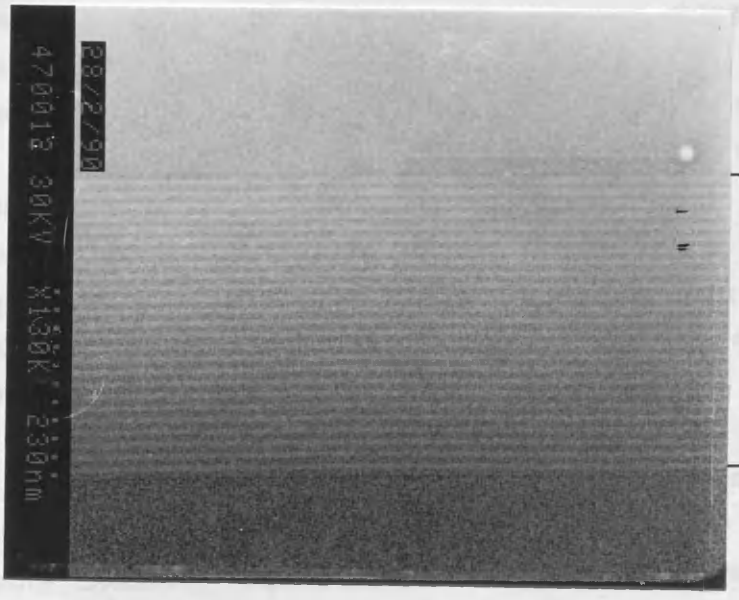

Figure 6.1
SEM micrographs showing the epitaxial layers of grown wafer A163.
(a) Upper cladding layer, measured to be 1.7 μm thick with the MQW layer visible beneath.
(b) MQW layers giving an average well/barrier width of 7.1nm.

the fabrication of the stripe waveguide devices as described in Chapter 3. Once the stripe waveguides had been etched, the electrical characteristics of the devices were tested to ensure that a reverse bias voltage could be applied to the device with low leakage current. Waveguide and directional coupling devices with reverse break down voltages of 42V and dark currents of 50nA were successfully fabricated. However, a second requirement on the directional coupler devices was that a large electric field applied to one waveguide of the device must not be experienced by the adjacent waveguide. This was not satisfied by the devices fabricated, and so a method of isolating adjacent waveguides was required. Passivation of III–V semiconductors by exposure to a hydrogen plasma has been studied in terms of dry etch damage [Dautremont–Smith et al '86]. To take advantage of this passivation, the samples were electrically isolated by exposing them to a hydrogen plasma in an Electrotek 340 plasma etcher under the following conditions: Hydrogen gas flow 25 sccm, pressure 10mTorr, R.F. power 100 watts, D.C. self bias 825 volts, time 15 minutes.

Figure 6.2(a) shows the configuration used for measuring the electrical isolation of adjacent waveguides of an EODCS. The voltage between waveguide 1 and the substrate was monitored, whilst the voltage between waveguide 2 and the substrate was swept from −10 volts to 2 volts. Carrying out the measurements on a fabricated device before being exposed to the hydrogen plasma, the voltage applied to waveguide 2 was measured at waveguide 1, indicating that there is no isolation between the waveguides. After exposure to the plasma, the voltage measured at waveguide 2 was reduced, giving approximately 2 volts at waveguide 1 for an applied voltage of 10 volts to waveguide 2, thus showing the adjacent waveguides had been isolated. An SEM micrograph of a completed device is shown in figure 6.3.

The adjacent waveguides of the EODCS, having been shown to be effectively isolated by exposure to a hydrogen plasma, had then to be shown to operate as passive directional coupling devices. The samples fabricated contained directional coupler devices with different interaction lengths, thus allowing the passive coupling of devices one sample to be studied without having to sequentially cleave. To measure the coupling efficiency at various interaction lengths, light from a Styryl–9 dye laser operating at a fixed wavelength of 870nm and chopped at 1kHz was end fired into the waveguide 1 of a device. The light coupled into the adjacent waveguide was focused onto a Si detector and measured using a lock–in amplifier. This was carried out for the devices of different interaction lengths which had been etched to a depth of 1μm and the measured coupled power against interaction

(a)

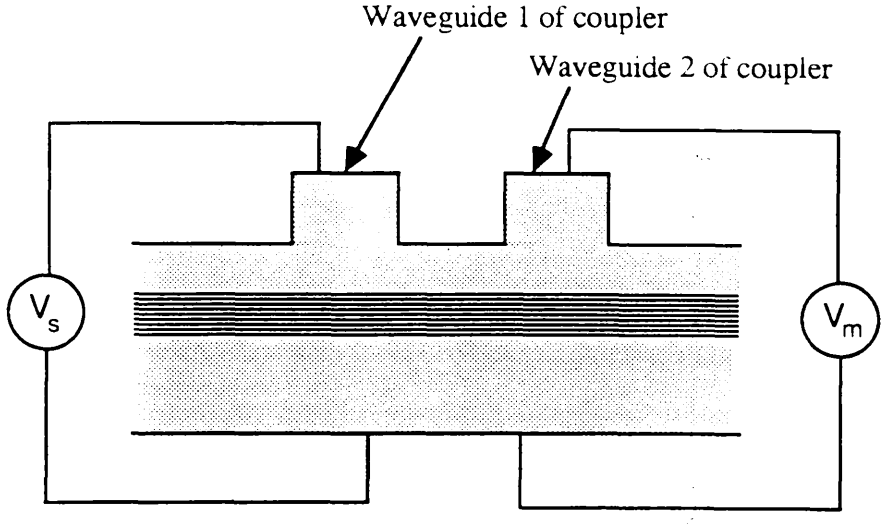

V_S = Voltage applied to waveguide 1
V_m= Voltage measured at waveguide 2

(b)

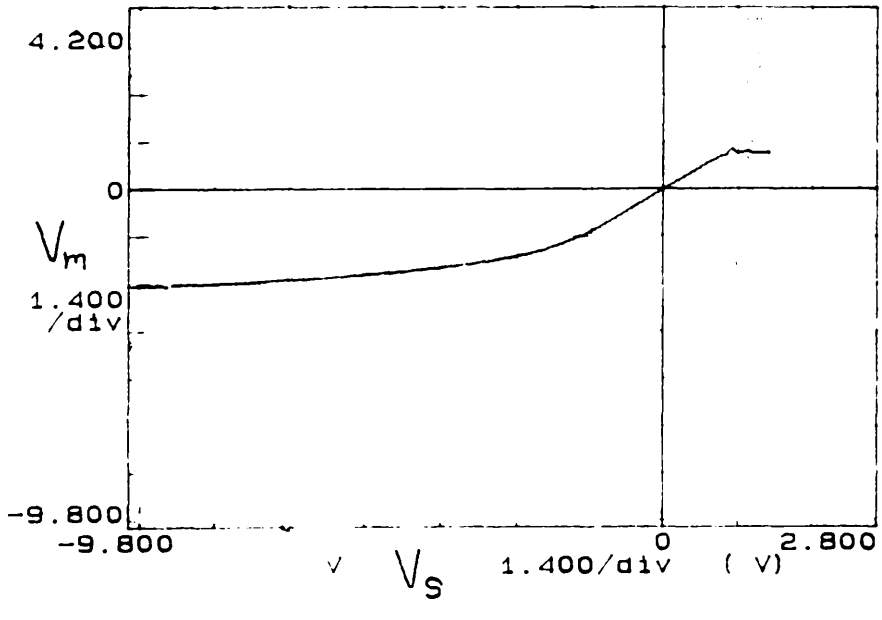

Figure 6.2
(a) Probe arrangement for measuring the electrical isolation of adjacent waveguides of an electro-optic directional coupling switch.
(b) Plot showing the voltage measured across waveguide 2 as a voltage was applied to waveguide 1 in a device after exposure to a hydrogen plasma.

length are shown in figure 6.4. A coupling length for complete transfer from waveguide 1 to waveguide 2 was calculated to be 3.4mm for these devices.

The devices fabricated had therefore been demonstrated to be passive directional couplers with a coupling length of 3.4mm. The adjacent waveguides of a device had also been successfully electrically isolated, and so the device operation as an EODCS was investigated.

Section 6.4 CHARACTERISATION OF DIRECTIONAL COUPLING SWITCHES.

The advantages of using MQW material for electro-optic switching lies in the enhancement of the electro-optic effect through electro-refraction, as studied in chapter 5. The enhancement of the effect in the waveguides fabricated in wafer A163 first had to be verified and characterised before the EODCS devices were investigated. The electro-optic effect in A163 stripe waveguides was measured at a series of wavelengths approaching the e1-hh1 exciton peak using the system described in chapter 5. The measured change in refractive index as a function of reverse bias voltage to the waveguide is shown in figure 6.5 at wavelengths ranging from 880nm to 850nm. The measurements show the highly wavelength dependent and non linear increase in refractive index of the waveguides with applied voltage as seen in MV348 stripe waveguides (Chapter 5). The enhanced electro-optic effect exhibited in the MQW waveguides therefore indicates that the EODCS should switch at low voltages.

Section 6.4.1 Demonstration of the Electro-Optic Directional Coupling Switch.

To demonstrate the electro-optic switching in the direction coupling devices, light from the Styryl-9 dye laser, chopped at 1kHz, was endfired into the waveguide 1 of a device which had an interaction length close to the measured coupling length. The light transmitted via waveguide 2 was focused onto a Si detector, the signal input to a lock-in amplifer and the output from the lock-in amplifier monitored at the analogue to digital converter (A/D C) of an IBM-PC. To minimise the detection of light from the waveguide 1, a vertical slit was placed in front of the Si detector. During the measurements, the device output was also focused onto an I.R. camera and observed on a monitor.

Voltages were applied to the waveguides 1 and 2 from the digital to analogue converter (D/A C) of an IBM-PC via probes. The voltage to the waveguide 2 was

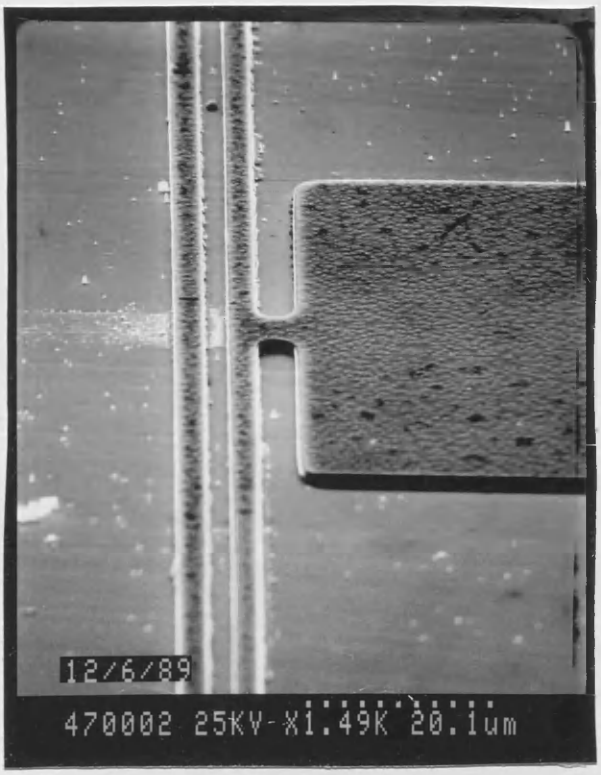

Figure 6.3
SEM micrograph of a directional coupling switch, showing the waveguides of nominal width of 3μm separated by 3μm. The micrograph shows an electrical contact pad attached to waveguide 2 on the right.

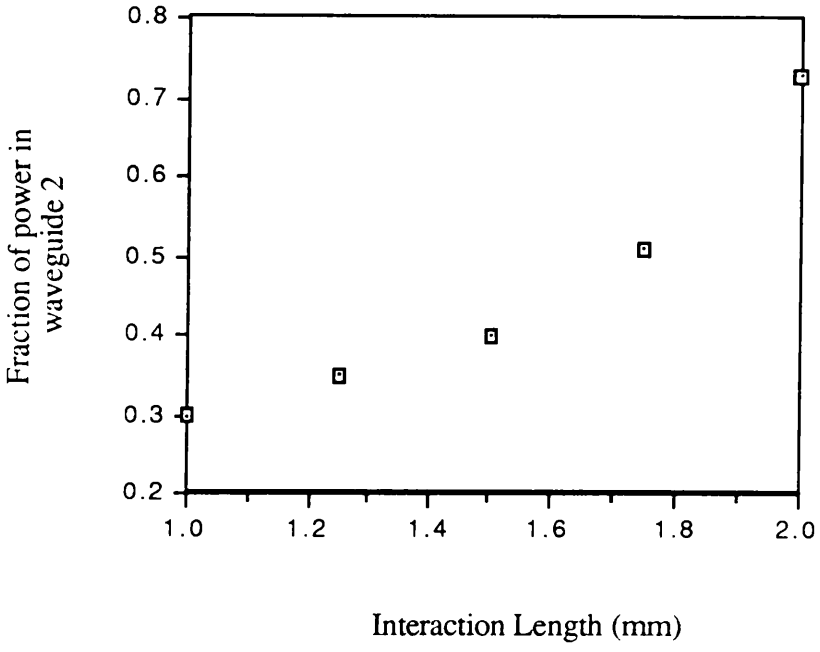

Figure 6.4
Passive coupler fabricated on wafer A163. Waveguide width and separation was 3μm, and etch depth of stripes was 1μm.

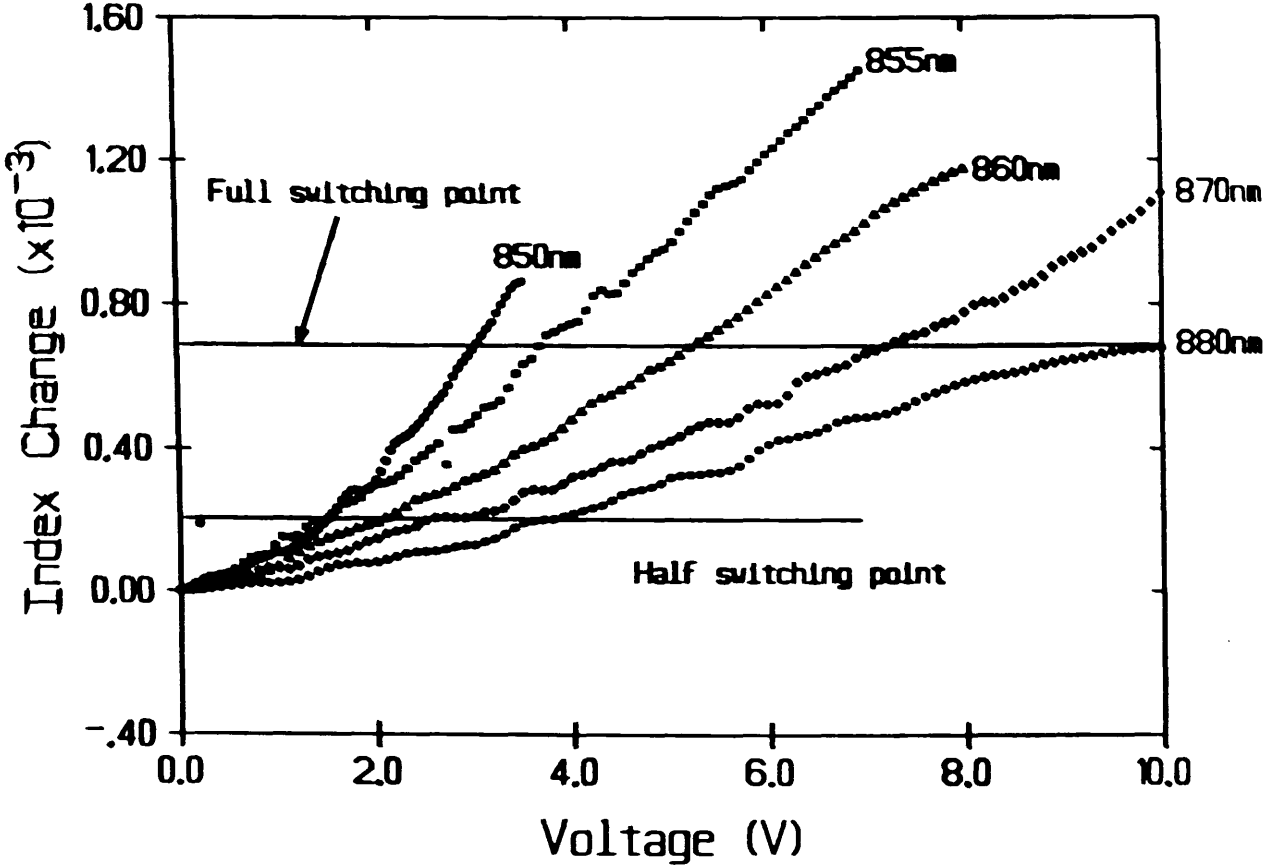

Figure 6.5
Change in refractive index (Δn) with applied voltage in 3μm wide stripe waveguides propagating along tjhe [1$\bar{1}$0] crystalographic direction in wafer A163. Also indicated is the Δn required to obtain half and full switching in the final EODCS devices.

held at zero volts, whilst the voltage to the waveguide 1 and device substrate had a variable positive voltage V applied. In this way, the waveguide 1 which was electrically isolated from waveguide 2 was not reverse biased, whilst a variable reverse bias voltage V was applied to the waveguide 2. The configuration of probes adopted overcame the problem that the D/A C could only apply positive voltages.

The light transmitted through the device was observed using the I.R. camera, and the intensity of light transmitted through the waveguide 2 was measured at the lock–in amplifier whilst the voltage V was swept from zero to 10 volts. The image on the monitor showed the intensity of the light from waveguide 2 decreasing as a voltage was applied and the output power was transfered to the waveguide 1. To measure the intensity output from waveguide 1 of the device, the output beam was then diverted so that light transmitted through the waveguide 1 was focused onto the detector. The measurements were then repeated, monitoring the intensity of light from waveguide 1 as the voltage V was swept from zero to 10 volts. The device performance was studied by carrying out the measurements at wavelengths ranging from 880nm to 860nm.

Section 6.4.2 Results and Discussion.

The switching characteristics was measured from a device etched to a depth of 1.1 μm with the two waveguides successfully isolated and with an interaction length of 2.9mm. The output intensity from waveguides 1 and 2 was measured as described in section 6.4.1 at an operating wavelength of 870nm. Photographs of the device output, taken directly from the monitor screen, at three applied voltages are shown in figure 6.6. For this particular device, the interaction length was less than that required for the passive directional coupler to obtain complete transfer of the guided mode from waveguide 1 to waveguide 2. A weak output from waveguide 1 is therefore visible in figure 6.6(a) for zero volts is applied to waveguide 2.

As a voltage was applied to waveguide 2, the switching of the light from waveguide 2 to waveguide 1 is clearly visible in the photographs (figure 6.6) and the guided modes of the two waveguides are well resolved. At zero volts the device output is dominated by waveguide 2 on the right, by 4.2 volts the device output is shared equally by waveguides 1 and 2 and for an applied voltage of 10 volts, the device output is completely from waveguide 1 on the left. The switch operation is also represented in figure 6.7, with the output intensities of waveguides 1 and 2 measured using the lock–in amplifier plotted as a function of voltage applied across waveguide 2. Also plotted is the sum of the outputs 1 and 2 to

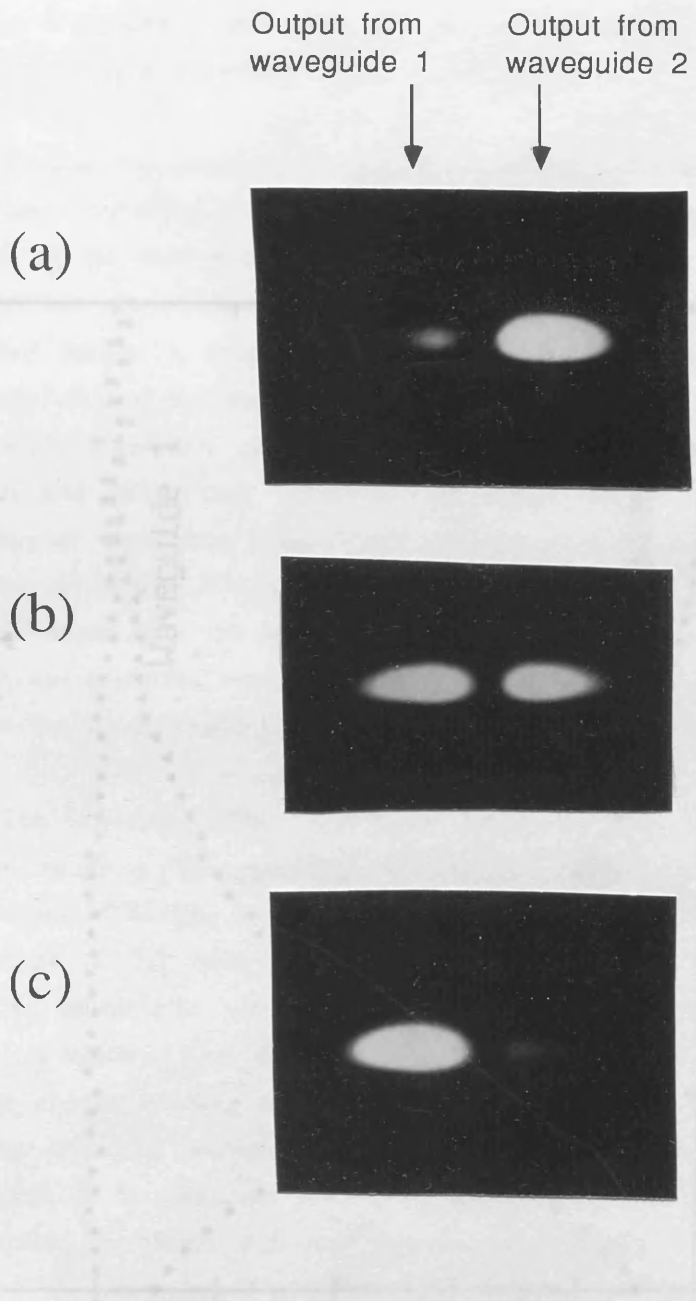

Figure 6.6
Photographs taken from the monitor screen of an IR camera showing the output from an operating directional coupling switch device of interaction length 1.9mm.
(a) Zero bias voltage across waveguide 2, with most of light coupled into waveguide 2.
(b) 4.2 reverse bias voltage across waveguide 2, leading to equal output intensities from waveguides 1 and 2.
(c) 10 volt reverse bias voltage across waveguide 2, leading to all output intensity from waveguide 1.

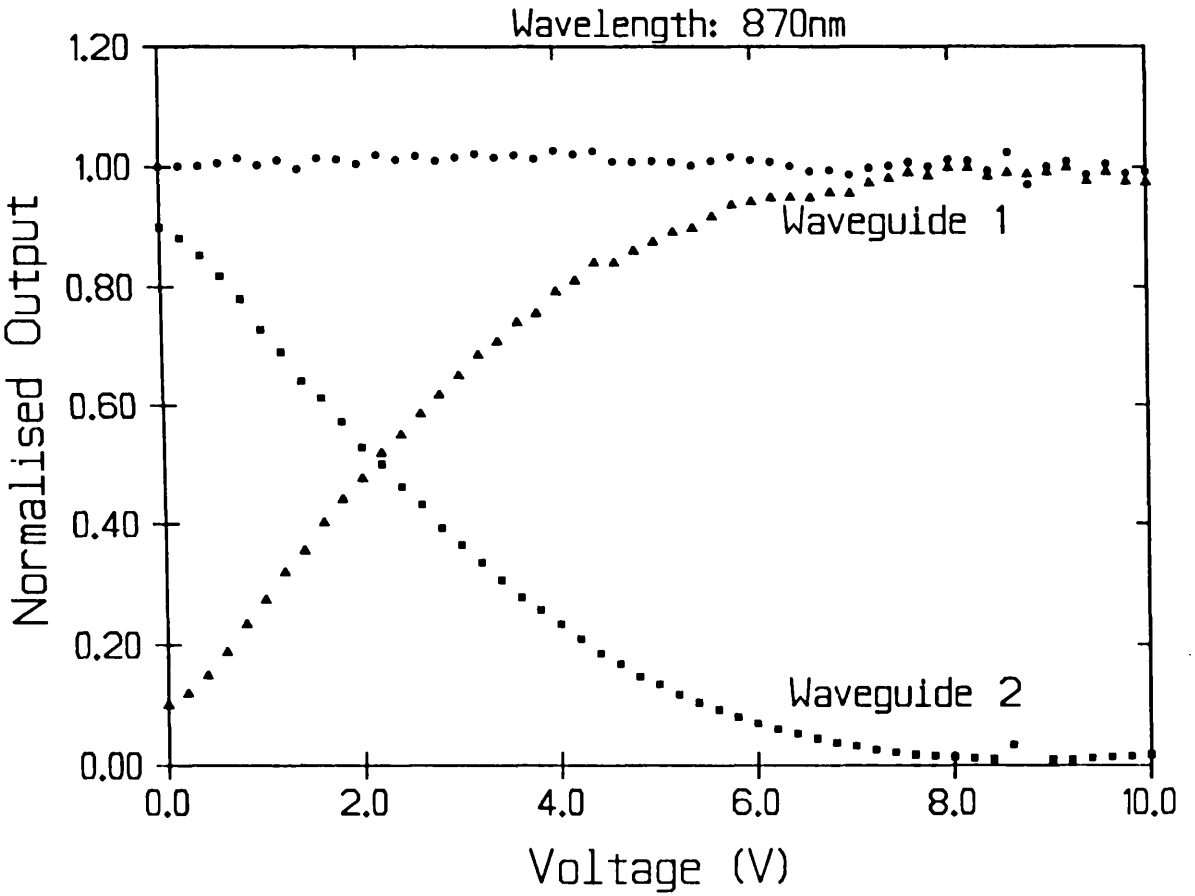

Figure 6.7
Device characteristics of an electro-optic directional coupling switch of length 2.9mm and operating at a wavelength of 870nm. The plot shows the normalised output power from waveguides 1 and 2 as a function of voltage applied to waveguide 2 and also the sum of the output powers from the two waveguides.

show that the loss of signal through electro–absorption in the waveguides is negligible. The switching of the device output from waveguide 2 to 1 as the voltage is applied is seen with the complete transfer at 8 volts giving a switching ratio of 30dB, a respectable device characteristic.

Because the interaction length of the device tested was not optimised, a device with an interaction length of 3.4mm, slightly longer than the optimum coupling length of the passive device was studied. Unfortunately, the mode quality in this device was poorer than the previous device and so that even at the optimum coupling length, a coupling efficiency of only 95% was achieved. The switching characteristics of the device were measured at a number of wavelengths approaching the MQW absorption edge and the measured characteristics at wavelengths 880nm, 870nm and 860nm are represented in figure 6.8. These plots show the output intensity of waveguides 1 and 2 of the device and the sum of the two outputs as a function of reverse bias voltage. Because the interaction length of the waveguide is slightly longer than the coupling length of the device, the low voltage ($V < 1$ volt) switch characteristics show an initial transfer of the output signal to waveguide 2 before the signal transfers to waveguide 1.

The interesting feature of the device is the reduction in voltage required to obtain switching for operating wavelengths which give the largest Δn. At a wavelength of 885nm, the switching is not complete at 10 volts whereas at 860nm a voltage of 3.5 volts gives complete switching. The voltages required for the different wavelengths are consistent with the electro–optic measurements made on stripe waveguides. Two voltage reference points were used to verify this: first, the voltage change required to switch from maximum signal in waveguide 2 to a 50% a signal split and second, the voltage required to switch from maximum signal in waveguide 2 to maximum transfer of signal to waveguide 1. These voltages are represented in figure 6.5 and show that index changes of $0.2\text{x}10^{-3}$ and $0.75\text{x}10^{-3}$ were required at all the wavelengths tested to obtain a 50% signal split and maximum switching respectively. Refering to equation 6.2, recall that to obtain 100% switching in the EODCS the condition of $\Delta\beta L = \sqrt{3}.\pi$ is required. For a device of length 3.4mm, this corresponds to an index change in the waveguide of $\Delta n = 0.22\text{x}10^{-3}$. The discrepancy between the required Δn and calculated Δn could be explained in terms of the waveguides in a device not being completely isolated, so that a small index change is experienced in waveguide 1, thus reducing the effective $\Delta\beta$. Alternatively, it could be because the device does not fulfill the criterion $KL = \pi/2$ nescesary for equation 6.2 to be valid. At the short wavelengths coupling back into waveguide 2 was observed. This behaviour is predicted by

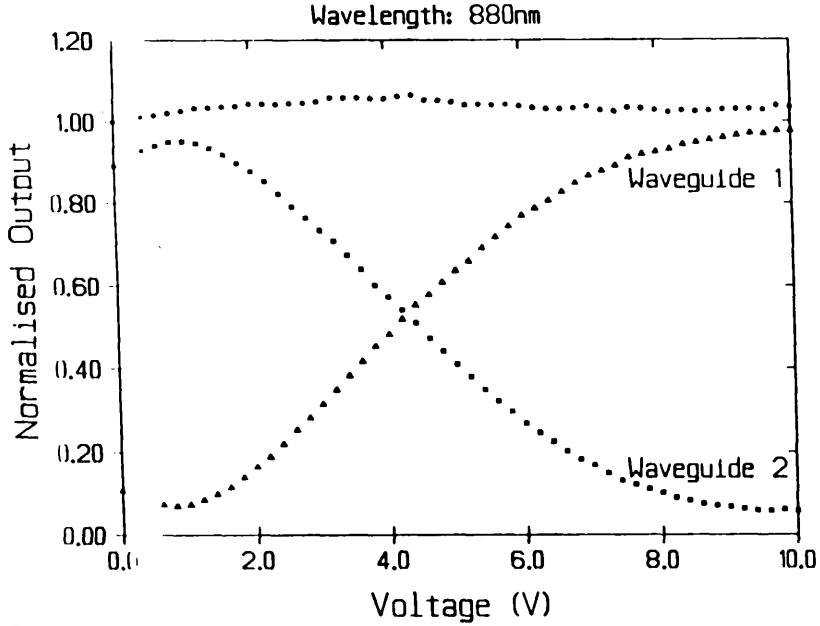

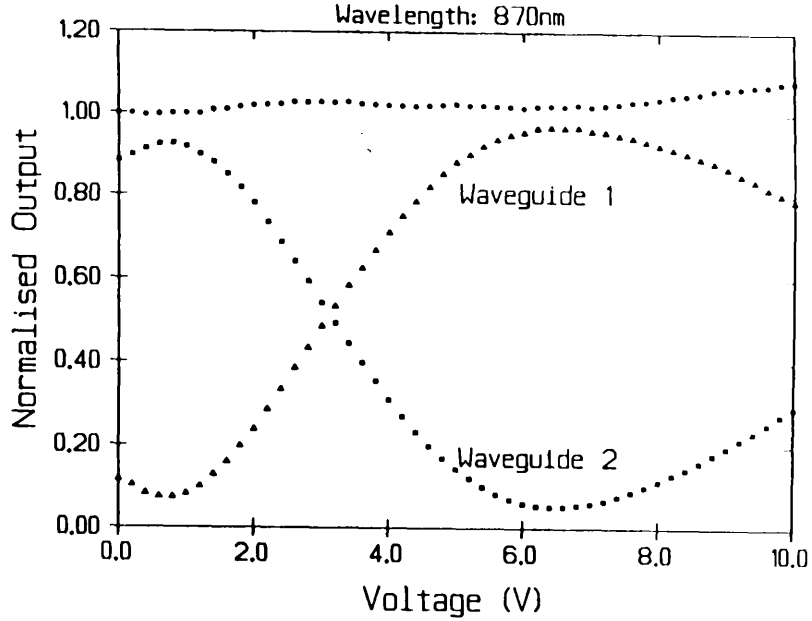

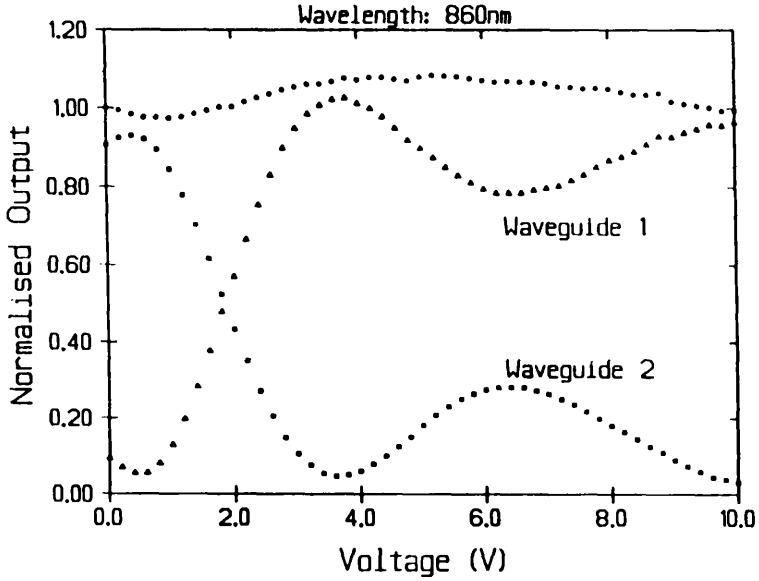

Figure 6.8
Device characteristics of an electro-optic directional coupling switch of length 3.4mm at 3 wavelengths approaching the excitonic band gap. The switching voltage is seen to reduce at wavelengths with enhanced Δn, whilst the electro-absorption in the device does not reduce the output power.

equation 6.2 and was shown in the modelling of the device by [Soref et al '88].

Whilst large electro–absorption was observed in the stripe waveguides, the loss in signal from the EODCS devices was negligible, even with 10 volts applied to the device and at an operating wavelength of 860nm. Thus, advantage has been taken of the enhanced electro–optic effect in the devices, whilst not suffering from the problem of large electro–absorption. Comparing the device characteristics to the modulation experienced in electro–absorption modulators in material MV348, the advantages in using EODCS modulators becomes apparent.

Section 6.5 CONCLUSION.

The operation of an electro–optic directional coupling switch which utilises the strong electro–refraction in MQW GaAs/AlGaAs has been successfully demonstrated. The device operates at low voltages and, because of the large Δn experienced by the material, shows potential for shorter device lengths. Switching characteristics show an extinction ratio of 30dB in the device and the configuration of the device allows the large electro–refraction in the MQW material to be exploited, without the disadvantages of the associated electro–absorption. Further optimisation of the device design such as decreasing the waveguide separation would reduce the device length making it a more practical device.

Chapter 7 CONCLUSIONS.

This thesis began with an over–view of the optical and electro–optic properties of multiple quantum well materials, concentrating on the GaAs/AlGaAs system. The dominance of the 2 dimensional density of states and excitonic features on the absorption edge have far reaching effects on the electro–optic effects of the material when the electric field is applied perpendicular to the plane of the wells. The exciton resonances remain resolved in the absorption spectrum of the material for electric field strengths up to fifty times the classical ionisation field and the resonance energies shift to lower energies by as much as five times the binding energy in an effect termed the quantum confined Stark effect (QCSE). It is the associated change in absorption and refractive index of the material and device applications that have been studied, and this has been carried out with the light propagating through the material in a stripe waveguide embedded in a pin diode to allow large electric fields to be applied to the quantum wells. Three waveguide structures were grown and characterised, two containing 25 quantum wells and a third containing 7 quantum wells.

Initial photocurrent measurements with light propagating normal to the quantum well layers were carried out on two of the waveguide structures grown verifing that the material exhibited the QCSE. In both wafers, the e1–hh1 and e1–lh1 exciton resonances shift quadratically with electric field strength, consistent with calculations of a finite potential well in an electric field, and remain resolved in electric field strengths upto 1×10^5V/cm. Furthermore, exciton resonances which are forbidden in the absence of an electric field were seen to begin to dominate the absorption spectrum in the presence of an electric field.

Having established the presence of the QCSE, a study of the wavelength dependance of the electro–absorption in the material in a waveguide configuration demonstrated a rapid increase in absorption change ($\Delta\alpha$) at wavelengths approaching the excitonic absorption edge. The absorption changes are qualitatively related to photocurrent measurements and measurements of the electro–absorption at wavelengths a few nm below the e1–hh1 exciton resonance show peaks in $\Delta\alpha$ as the resonant wavelengths of the e1–hh1 and e1–lh1 exciton pass through the measuring wavelength. This decrease in absorption with increasing voltage is characteristic of the situation required for the operation of SEED devices. If a waveguide structure was optimised such that the exciton resonances observed in the electro–absorption measurements are sharp, it should be possible to get SEED devices operating in a waveguide structure. With the increased interaction length of

the waveguide compared to present SEED devices which have light propagating normal to the quantum well layers, it may be possible to improve the modulation depth of the devices.

The enhanced electro-refraction which is associated with the large shifts in the absorption edge of MQW material was studied in an investigation of the wavelength dependance of the electro-optic effect at wavelengths approaching the excitonic absorption edge for both TE and TM polarisation. It was shown that a linear electro-optic (LEO) effect in MQW GaAs/AlGaAs material is very similar to the effect observed in bulk GaAs, whilst a quadratic electro-optic (QEO) effect in MQW GaAs/AlGaAs is greatly enhanced and is highly wavelength dependant. The LEO effect with TE polarisation results in a positive Δn for propagation along the crystallographic direction [1$\bar{1}$0] and negative for propagation along [110], the LEO coefficient does not show any strong wavelength dependance ($\bar{r}_{63} = -1.75$ x10^{-12}m/V for the wavelengths considered) and the effect is absent for TM polarisation. With the QEO effect, which results from the electro-refraction in the material, a large Δn is experienced for both TE and TM polarisations in the waveguide and the magnitude of the QEO coefficients increase dramatically for photon energies approaching the material band gap. The results show 2 orders of magnitude increase in the QEO coefficient s_{33} over the photon energy range of 30meV to 100meV below the lowest energy exciton. The changes in refractive index experienced below the band gap are dominated by presence of the lowest energy exciton resonance. This results in equal values of s_{33} for TE and TM polarisations for photon energies below the band gap.

The enhanced electro-absorption and electro-optic effects in MQW GaAs/AlGaAs have direct applications in integrated optic devices such as absorption modulators (utilising electro-absorption effect), phase moulators (utilising electro-optic effect) and intensity modulators (utilising either electro-absorption or electro-optic effects), all of which have applications in fibre optic communications and integrated optics. A full understanding of the effects is therefore necessary for the optimisation of devices and in the results reported here, a comprehensive study of the wavelength dependence of the effects has been given.

Intensity modulation devices which rely on the modulation of refractive index include Mach-Zehnder interferometers and directional coupling switches in waveguide configuration and Fabry-Perot devices in a planar structure. The enhanced operation of an electro-optic directional coupling switch in MQW GaAs/AlGaAs waveguides has been demonstrated by utilising the electro-refraction

in the material. The device has not been optimised to give a short device length or low operating voltages and so further work to obtain a device which is practical for integrated optics and communication purposes are necessary. The devices does, however, switch with voltages less than 4 volts, although this was in the spectral region of high absorption. The on/off ratio of each channel of the directional coupling switch was demonstrated to be as high as 30dB. It is in such devices the full use of the electro–optic effects of MQW structures can be successfully ulilised for optical communication systems.

Through this work three waveguide modulators have examined: absorption modulators, phase modulators and electro–optic directional coupling switches; the operation of all these devices being enhance by the QCSE. Further work in the optimisation of devices which utilise these enhanced effects includes the following:

1 Optimisation of the EODCS to reduce the length of the device and/or operating voltage.

2 Investigation to enhance the modulation depth of SEED's by using a waveguide structure since the modulation depth of present planar SEED's of ≈5dB is a weak point of these devices.

3 Development of Fabry–Perot reflection devices which can be switched on/off resonance using either the enhanced electro–absorption or the electro–optic effect.

REFERENCES.

S. Adachi and K. Oe;
"Linear electro– optic effects in zincblende– type semiconductors: Key properties of InGaAsP relevent to device design", J. Appl. Phys. **56**, 74 (1984).

S. Adachi;
"GaAs, AlAs and $Al_xGa_{1-x}As$: Material parameters for use in research and device applications", J. Appl. Phys. **58**, R1 (1985).

A. Alping and L.A. Coldren;
"Electro– refraction in GaAs and InGaAs and its application to phase modulators", J. Appl. Phys. **61**, 2430 (1987).

H.G. Bach, J. Krauser, H.P. Nolting, R.A. Logan and F.K. Reinhart;
"Electro– optical light modulation in InGaAs/InP double heterostructure diodes", Appl. Phys. Lett. **42**, 692 (1983).

G. Bastard, E.E. Mendez, L.L. Chang and L.Esaki;
"Exciton binding energy in quantum wells", Phys. Rev. B **26**, 1974 (1982).

G. Bastard, E.E. Mendez, L.L. Chang and L. Esaki;
"Variational calculation on a quantum well in an electric field", Phys. Rev. B **28**, 3214 (1983).

G. Bastard and J.A. Brum;
"Electronic states in semiconductor heterostructures", IEEE J. Quantum Electron. **22**, 1625 (1986).

G. Bastard;
"Wave mechanacs applied to semiconductor heterostructures", Les Ulis press (1988).

B.R. Bennett and R.A. Soref;
"Electrorefraction and electroabsorption in InP, GaAs, GaSb, InAs, and InSb", IEEE J. Quantum Electron. **23**, 2159 (1987).

P.J. Bradley, M. Whitehead, G. Parry, P. Mistry nad J.S. Roberts.
"Effect of device length and background doping on the relative magnitudes of phase and amplitude modulation in GaAs/AlGaAs PIN multiple quantum well waveguide optical modulators", Applied Optics **28**, 1560 (1989(a)).

P.J. Bradley and G. Parry;
"Optimised multiple quantum well phase modulator", Electron. Lett. **25**, 1349 (1989(b)).

J.A. Brum and G. Bastard;
"Electric field induced disociation of excitons in semiconductor quantum wells", Phys. Rev. B **31**, 3893 (1985).

H.C. Cassey Jr., D.D. Sell and M.B. Panish;
"Refractive index of $Al_xGa_{1-x}As$ between 1.2 and 1.8eV", Appl. Phys. Lett. **24**, 63 (1974).

J.R. Chelikowski and M.L. Cohen;
Phys. Rev. B **14**, 556 (1974).

D.S. Chemla, T.C. Damen, D.A.B. Miller, A.C. Gossard and W. Wiegmann;
"Electroabsorption by Stark effect on room temperature excitons in GaAs/AlGaAs multiple quantum well structures", Appl. Phys. Lett. **42**, 864 (1983).

D.S. Chemla, D.A.B. Miller, P.W. Smith, A.C. Gossard and W. Wiegman;
"Room temperature excitonic nonlinear absorption and refraction in GaAs/AlGaAs multiple quantum well structures", IEEE J. Quantum Electron. **20**, 265 (1984).

D.S. Chemla and D.A.B. Miller;
"Room–temperature excitonic nonlinear–optical effects in semiconductor quantum–well structures", J. Opt. Soc. America B **2**, 1155 (1985).

D.S. Chemla and D.A.B. Miller;
"Physics and applications of excitons confined in semiconductor quantum wells", Internal Report AT&T Bell Labs 1987.

D.S. Chemla, I. Bar–Joseph, J.M. Kuo, T.Y. Chang, C. KLingshirn, G. Livescu and D.A.B. Miller;
"Modulation of absorption in field–effect quantum well structures", IEEE J. Quantum Electron. **24**, 1664 (1988).

Y.J. Chen, E.S. Koteles, B.S. Elman, S.W. Brown and G.J. Sonek;
"Multiple quantum well GaAs/AlGaAs waveguides for integrated optics", Proceedings from fourth Conf. on Integrated Optics, 86 (1987).

R.T. Collins, K.v. Klitzing and K. Ploog;
"Photocurrent spectroscopy of GaAs/AlGaAs quantum wells in an electric field", Phys. Rev. B **33**, 4378 (1986).

U. Das, Y. Chen, P.K. Bhattacharya and P.R. Berger;
"Orientation dependent phase modulation in InGaAs/GaAs multiquantum well waveguides", Appl. Phys. Lett. **53**, 2129 (1988).

W.C. Daultemont–Smith, J.C. Nabity, V. Swaminathan, M. Stavola, J. Chevallier, C.W. Tu and S.J. Pearton;
"Passivation of deep level defects in molecular beam epitaxial GaAs by hydrogen passivation", Appl. Phys. Lett. **49**, 1098 (1986).

P. Dawson, K.J. Moore, G. Duggan, H.I. Ralph and C.T.B. Foxon;
"Unambiguous observation of the 2*s* state of the light– and heavy–hole excitons in GaAs–(AlGa)As multi–quantum–well structures", Phys. Rev. B **34**, 6007 (1986).

B. Deveaud, T.C.Damen, J. Shah and C.W. Tu;
"Dynamics of exciton transfer between monolayer–flat islands in single quantum wells", Appl. Phys. Lett. **51**, 828 (1987).

B. Deveaud, J. Shah, T.C. Damen, B. Lambert, A. Chommette and A. Regreny;
"Optical studies of perpendicular transport in semiconductor superlattices", IEEE J. Quantum Electron. **24**, 1641 (1988).

R. Dingle, W. Wiegmann and C.H. Henry;
"Quantum states of confined carriers in very thin $Al_xGa_{1-x}As$–GaAs–$Al_xGa_{1-x}As$ hetrtostructures" Phys. Rev. Lett. **33**, 827 (1974).

J.D. Dow and D. Renfield;
"Electroabsorption in semiconductors: The excitonic absorption edge", Phys. Rev. B **1**, 3358 (1970).

J. Faist, F.K. Reinhart, D. Martin and E. Runcel;
"Orientation dependence of the phase modulation in a p–n junction $GaAs/Al_xGa_{1-x}As$ waveguide", Appl. Phys. Lett. **50**, 68 (1987).

J.E. Fouquet and R.D. Burnham;
"Recombination dynamics in $GaAs/Al_xGa_{1-x}As$ quantum well structures", IEEE J. Quantum Electron. **22**, 1799 (1986).

M. Glick and F.K. Reinhart;
"Electro–optical light modulation in GaAs/AlGaAs multiquantum well heterostructures", Helvetica Physica Acta **58**, 403 (1985).

M. Glick, F.K. Reinhart, G. Weimann and W. Schlapp:
"Quadratic electro–optic light modulation in a GaAs/AlGaAs multiquantum well heterostructure near the excitonic gap", Appl. Phys. Lett. **48**, 989 (1986).

M. Glick, D. Pavuna and F.K. Reinhart;
"Electro–optic effects and electroabsorption in GaAs/AlGaAs multiquantum well heterostructures near the bandgap", Electron. Lett. **23**, 1235 (1987).

M. Glick, F.K. Reinhart nad D. Martin:
"Linear electro–optic effect: Comparison of GaAs/AlGaAs multi–quantum–well hetreostructures with AlGaAs solid solution at 1.1523μm", J. Appl. Phys. **63** , 5877 (1988).

R.L. Greene, and K.K. Baja;
"Binding energy of Wannier excitons in GaAs–$Al_xGa_{1-x}As$ quantum well structures", Solid State Comm. **45**, 831 (1983).

D.W. Hewak and J.W.Y. Lit;
"Generalized dispertion properties of a four layer thin–film waveguide", Appl. Optics **26**, 833 (1987).

T. Hiroshima;
"Electric field induced refractive index changes in $GaAs/Al_xGa_{1-x}As$ quantum wells", Appl. Phys. Lett. 50, 968 (1987).

K. Hofler and K. Wellerdieck;
"RF sputtering for substrate cleaning", Balzers: Technical report.

S. Hong and J. Singh;
"Excitonic energies in inhomogenous line broadening effects in InAlAs/InGaAs modulator structures" J. Appl. Phys. 62, 1994 (1987).

H. Iwamura, T. Saku, and H. Okamoto;
"Optical absorption of GaAs–AlGaAs superlattice under electric field", Jpn. J. Appl. Phys. 24, 104 (1985).

S.M Jensen;
"The nonlinear coherent coupler", IEEE J. Quantum Electron. 18, 1580 (1982).

B. Jensen and A. Torabi;
"Dispertion of refractive index of GaAs and AlGaAs", IEEE J. Quantum Electron. 19, 877 (1983).

R. Jin, C.L. Chuang, H.M. Gibb and S.W. Koch;
"Picosecond all–optical switching in single mode GaAs–AlGaAs strip loaded nonlinear waveguide directional coupler", Appl. Phys. Lett. 53, 1791 (1988).

F.Y. Juang, J. Singh and P.K. Bhattacharya;
"Field–dependent line width and luminescence energies in GaAs–AlGaAs multiquantum well modulators", Appl. Phys. Lett 48, 1246 (1986).

K.B. Kahen and J.P. Leburton;
"Structure variation of the index of refraction of GaAs–AlAs superlattices and multiple quantum wells', Appl, Phys. Lett. 47, 508 (1985).

Y. Kan, H. Nagai and M. Yamanishi;
"Field effects on the refractive index and absorption coefficient in AlGaAs quantum well structures and their feasibility for electrooptic device applications", IEEE J. Quantum Electron. 23, 2167 (1987).

H. Kawaguchi;
"GaAs rib waveguide directional coupler switch with schottky barriers", Elect. Lett. **14** 387 (1978).

H. Kawai, K. Kaneko and N. Watanabe;
"Photoluminescence of AlGaAs/GaAs quantum wells grown by metalorganic chemical vapor deposition", J. Appl. Phys. **56**, 463 (1984).

L.V. Keldysh;
"The effect of a strong electric field on the optical properties of insulating crystals", Soviet Phys. JETP **34(7)**, 788 (1958).

C. Kittel;
"Introduction to solid state physics" 6^{th} edition, Wiley, New York (1986).

H. Kogelnik and V. Ramaswamy;
"Scaling rules for thin– film optical waveguides", Appl. Optics **13**, 1857 (1974).

U. Koren, T.L. Koch, H. Presting, and B.I. Miller;
"InGaAs/InP multiple quantum well waveguide phase modulator", Appl. Phys. Lett. **50**, 368 (1987(a)).

U. Koren, B.I. Miller, T.L. Koch, G. Eisenstein, R.S. Tucker, I. Bar– Joseph and D.S. Chemla;
"Low– loss InGaAs/InP multiple quantum well optical electroabsorption waveguide modulator", Appl. Phys. Lett. **51**, 1132 (1987(b)).

M.D.A. MacBean;
"Mulitple quantum well GaAs– AlGaAs heterostructures as optical waveguides", PhD Thesis, Dept of Electronics abd Electrical Engineering, Univ. of Glasogw (1986).

M.D.A. MacBean, O. Mikami, C.D.W. Wilkinson, P.Mistry and J.S. Roberts;
"Optical properties of (Al,Ga)As/GaAs multiple quantum well planar waveguides and fabrication of single mode rib waveguides and directional couplers by reactive ion etching", Appl. Optics **26**, 2625 (1987).

W.F. Marshal and J. Katz;
"Waveguide PIN junction electrooptic phase modulators: theoretical analysis and design criteria" Appl. Optics **24**, 1996 (1985).

W.T. Massenlink, P.J. Pearah, J. klem, C.K. Fenk, H. Morkok, G.D. Sanders and Y. Chang;
"Absorption coefficients and exciton oscillator strengths in AlGaAs– GaAs superlattices", Phys. Rev. B **32**, 8027 (1985).

M. Massumoto and T. Kamizato;
"Subbands and excitons in a quantum well in an electric field", Phys. Rev. B **33**, 8385 (1986).

E.E. Mendez, G. Bastard, L.L. Chang, L. Esaki, H. Moroc and R. Fischer;
"Effect of an electric field on the luminescence of GaAs quantum wells", Phys. Rev. B **26**, 7101 (1982).

J.G. Mendoza– Alvarez, L.A. Coldren, A. Alping, R.H. Yan, T. Hauseken, K. Lee and K. Pedrotti;
"Analysis of depletion edge translation lightwave modulators", J. of Lightwave Technology **6**, 793 (1988).

R.C. Miller, D.A. Kleinman, W.A. Nordland Jr. and A.C Gossard;
"Luminescence studies of optically pumped quantum wells in GaAs– $Al_xGa_{1-x}As$ multilayer structures" Phys. Rev. B **22**, 863 (1980).

R.C. Miller, D.A. Kleinman, O. Munteaun and W.T. Tsang;
"New transitions in the photoluminescence of GaAs quantum wells", Appl. Phys. Lett. **39**, 1 (1981(a)).

R.C. Miller D.A. Kleinman, W.T. Tsang and A.C. Gossard;
"Observation of the excited level of excitons in GaAs quantum wells", Phys. Rev. B **24**, 1134 (1981(b)).

R.C. Miller, D.A. Kleinman and A.C Gossard;
"Band– gap discontinuities and effective masses for GaAs– $Al_xGa_{1-x}As$ quantum wells", Phys. Rev. B **29** 7085 (1984).

D.A.B. Miller, D.S. Chemla, T.C. Damen, A.C.Gossard, W. Wiegman, T.H. Wood and C.A. Burrus;
"Band– edge electroabsorption in Quantum Well Structures: The Quantum Confined Stark Effect", Phys. Rev. Lett. **53**, 2173 (1984).

D.A.B. Miller, D.S. Chemla, T.C. Damen, A.C.Gossard, W. Wiegman, T.H. Wood and C.A. Burrus;
"Electric field dependence of optical absorption near the band gap of quantum– well structures", Phys. Rev. B **32**, 1043 (1985).

D.A.B. Miller, J.S. Wiener and D.S.Chemla:
"Electric field dependence of linear optical properties in quantum well structures: Waveguide electroabsorption and sum rules", IEEE J. Quantum Electron. **22**, 1816 (1986(a)).

D.A.B. Miller, D.S. Chemla and S. Schmitt–Rink;
"Relation between electroabsorption in bulk semiconductors and in quantum wells: The quantum confined Franz–Keldysh effect", Phys Rev B **33**, 6976 (1986(b)).

D.A.B. Miller, D.S. Chemla and S. Schmitt–Rink;
"Electroabsorption of highly confined systems: Theory of the quantum–confined Franz–Keldysh effect in semiconductor quantum wires and dots", Appl. Phys. Lett. **52**, 2154 (1988).

T. Miyoshi, Y. AoYagi, A. Yadama, Y. Segawa, S. Namba and N. Sano;
"Effect of electric field on transient characteristics of luminescence from GaAs/$Ga_{0.6}Al_{0.4}As$ multi–quantum–wel structure", Jpn. J. Appl. Phys. **25**, 504 (1986).

H. Nagai, M. Yamanishi, Y. Kan, I. Suemune;
"Field–induced modulations of refractive index and absorption coefficient in a GaAs/AlGaAs quantum well structure", Electron. Lett. **22**, 888 (1986).

M. Naganuma, T. Ishibashi and Y. Horikoshi;
"The electric field induced photoluminescence properties of GaAs/$Al_xGa_{1-x}As$ quantum–well structures grown by molecular–beam epitaxy", J. Appl. Phys. **62**, 644 (1987).

D.J. Newson and A. Kurobe;
"Effect of residual doping on optimum structure of multiquantum–well optical modulators", Electron. Lett. **23**, 439 (1987).

K. Nishi and T. Hiroshima;
"Enhancement of quantum confined Stark effect in a graded gap quantum well",

Appl. Phys. Lett. **51**, 320 (1987).

Nye;
"Physical properties of crystals", Clarendon Press, Oxford (1957).

G. Oelgart, R. Schwabe, M. Heider and B. Jacobs;
"Photoluminescence of $Al_xGa_{1-x}As$ near the $\Gamma-X$ crossover", Semicond. Sci. Technol. **2**, 468 (1987).

M. Ogawa;
"Alloying behavior of Ni/Au–Ge films on GaAs",J. Appl. Phys. **51**, 406 (1980).

S. Ohke, T. Vmeda and Y. Cho;
"Optical waveguides using GaAs–Al_x–$Ga_{1-x}As$ mulitiple quantum well", Optical Comm. **56**, 235 (1985).

J.I. Pankove;
"Optical processes in sumiconductors", Dover Publications Inc., New York (1971).

W. Patrick
"The fabrication of very short gate–length field effect transistor devices", PhD Thesis, Dept. of Electronics and Electrical Engineering, Univ. of Glasgow, 1985.

J.D. Ralston, W.J. Schaff, D.P. Bour and L.F. Eastman;
"Room–temperature exciton electroabsorption in partially intermixed GaAs/AlGaAs quantum well waveguides", Appl. Phys. Lett. **54**, 534 (1989).

V.L. Rideout;
"A review of the theory and technology for ohmic contacts to group III–V compound semiconductors", Solid State Electronics **18**, 541 (1975).

G.D. Sanders and K.K. Baja;
"Electronic Properties and optical–absorption spactra of GaAs–$Al_xGa_{1-x}As$ quantum wells in externally applied electric fields", Phys. Rev. B **35**, 2308 (1987).

F.P. Schafer;
"Dye lasers", Topics in applied physics Vol. 1 pp1–83 1977.

S. Schmitt–Rink, D.S. Chemla and D.A.B. Miller;

Linear and non−linear optical properties of semiconductor quantum wells", Advances in Physics **38**, 89 (1989).

M.F.H. Schuurmans and G.W.'t Hooft;
"Simple calculations of confinement states in a quantum well", Phys. Rev. B **31**, 8041 (1985).

D.D. Sell, S.E. Stokowski, R. Dingle and J.V. DiLorenzo;
"Polariton reflectance and photoluminescence in high−purity GaAS", Phys. Rev. B **7**, 4568 (1973).

A.Ya Shik;
"Superlattices− periodic semiconductor structures (review)", Sov. Phys. Semicond. **8**, 1195 (1975).

J. Shimizu, T. Hiroshima, A. Ajisawa, M. Sugimoto and Y. Ohta;
"Measurements of the polarisation dependence of field−induced refractive index changes in GaAs/AlGaAs multiple quantum well structures", Appl. Phys. Lett. **53**, 86 (1988).

J. Singh, S, Hong, P.K. Bhattacharay, R. Sahai, C. Lastufka and H.R. Sobel.
"System requirements and feasibility studies for optical modulators based on GaAs/AlGaAs multiquantum well structures for optical modulators", J. of Lightwave Technology **6**, 818 (1988).

R. Sooryakumar;
"Valence band mixing and optical emission in modulation doped GaAs−(AlGa)As heterostructures", IEEE J. Quantum Electron. **22**, 1645 (1986).

R.A. Soref;
Guided−wave intensity modulators using amplitude−and−phase perturbations", J. of Lightewave Tech. **6**, 437 (1988).

C.R. Stanley;
A private communication, Dept of Electronics and Electrical Engineering, Univ. of Glasgow (1989).

P.J. Stevens, M. Whitehead, G.Parry and K. Woodbridge;
"Computer modeling of the Electric field dependent absorption spectrum of multiple

quantum well material", IEEE J. Quantum Electronic. **24**, 2007 (1988).

Y. Suzuki and H. Okamoto;
"Refractive index of GaAs– AlAs superlattice grown by MBE", J. Electron. Mat. **12**, 397 (1983).

S.M. Sze;
"Physics of Semiconductor Devices", John Wiley and Sons, Second Edition, (1981).

H. Takeuchi, K. Nagata, H. Kawaguchi and K. Oe;
"GaAs/AlGaAs directional coupler switch with submillimetre device length". Elec. Lett. **22**, 1241 (1986).

H. Thomas, D. Morgan, B. Thomas, J.E. Aubery and G.B. Morgan;
"Gallium Arsenide for devices and integrated circuits" Proceedings of the UWIST GaAs school (1986).

H.K. Tsang and I.H. White;
"Polarisation characteristics of the optical plasma effect in GaAs/AlGaAs quantum well waveguides", Proc. of the 9th National Quantum Electronics conf. Oxford 130 (1989).

T.E. Van Eck, L.M. Walpita, W.S.C. Chang and H.H. Wieder;
"Franz– Keldysh electrorefraction and electroabsorption in bulk InP and GaAs", Appl. Phys. Lett. **48**, 451 (1986).

L. Vina, R.T. Collins, E.E. Mendez and W.I. Wang;
"Excitonic coupling in GaAs/AlGaAs quantum wells in an electric field", Phys. Rev. Lett. **58**, 832 (1987).

R.G. Walker;
"Broadband (6GHz) GaAs/AlGaAs electro– optic modulator with low drive power", Appl. Phys. Lett. **54**, 1613 (1989).

K. Wakita, Y. Kawamura, Y. Yoshikuni and H. Asahi;
"High– temperature excitons and enhanced electroabsorption in InGaAs/InAlAs multiple quantum wells", Electron. Lett. **21**, 574 (1985).

J.S. Weiner, D.S. Chemla, D.A.B. Miller, H.A. Hause, A.C. Gossard, W.

Wiegman and C.A. Burrus;
"Highly anisotropic optical properties of single quantum well waveguides", Appl. Phys. Lett. **47**, 664 (1985(a)).

J.S. Weiner, D.A.B. Miller, D.S. Chemla, T.C. Damen, C.A. Burrus, T.H. Wood, A.C. Gossard and W. Wiegman;
"Strong polarisation–sensitive electroabsorption in GaAs/AlGaAs quantum well waveguides", Appl. Phys. Lett **47**, 1148 (1985(b)).

J.S. Weiner, D.A.B. Miller and D.S. Chemla;
"Quadratic electro–optic efffect due to the quantum–confined Stark effect in quantum wells", Appl. Phys. Lett. **50**, 842 (1987).

C. Weisbuch, R. Dingle, A.C.Gossard and W. Wiegmann;
"Optical characterisation of interface disorder in GaAs–$Ga_{1-x}Al_xAs$ multi–quantum well structures", Solid State Comm. **38**, 709 (1981).

M. Whitehead, G. Parry, K. Woodbridge, P.J. Dobson and G. Duggan;
"Experimental confirmation of a sum rule for room temperature electroabsorption in GaAs–AlGaAs multiple quantum well structures", Appl. Phys. Lett. **52**, 345 (1988(a)).

M. Whitehead, P. Stevens, A. Rivers, G. Parry, J.S. Roberts, P. Mistry, M. Pate and G. Hill;
"Effects of well width on the characteristics of GaAs/AlGaAs multiple quantum well electroabsorption modulators", Appl.Phys. Lett. **53**, 956 (1988(b)).

D.R. Wight, A.M. Keir, G.J. Pryce, J.C.H. Birbeck, J.H. Heaton, R.J. Norcross and P.J. Wright;
"Limits of electro–absorption in high purity GaAs and the optimisation of waveguide devices", IEEE Proc. **135**, 39 (1988).

T.H. Wood, C.A. Burrus, D.A.B. Miller, D.S. Chemla, T.C. Damen, A.C. Gossard and W. Wiegmann;
"High–speed optical modulation with GaAs/AlGaAs quantum wells in a p–i–n diode structure", Appl. Phys. Lett. **44**, 16 (1984).

T.H. Wood;
"Direct measurement of the electric–field–dependent absorption coefficient in

GaAs/AlGaAs multiple quantum wells", Appl. Phys. Lett. **48**, 413 (1986).

T.H. Wood, R.W. Tkach and A. R. Chraplyvy;
"Observation of the large quadratic electro–optic effect in GaAs/AlGaAs multiple quantum wells", Appl. Phys. Lett. **50**, 798 (1987).

H. Yamamoto, M. Asadat, Y. Suematsu;
"Electric–field induced refractive index variation in quantum well structure", Electron. Lett. **21**, 579 (1985).

K. Yamanaka, T. Fukunaga, N. Tsukada, K.L.I. Kobayshi and M. Ishi;
"Photocurrent spectroscopy in GaAs/AlGaAs multiple quantum wells under a high field perpendicular to the heterointerface", Appl. Phys. Lett. **48**, 840 (1986).

H. Yamamoto, M. Asada and Y. Suematsu;
"Theory of refractive index variation in quantum well structure and related intersectional optical switches", J. of Lightwave Technology **6**, 1831 (1988).
A. Yariv;
"Optical electronics", Holt Reinhart and Wilson, Third Edition (1985).

J.E. Zucker, T.L. Hendrickson and C.A. Burrus;
"Low–voltage phase modulation in GaAs/AlGaAs quantum well optical waveguides", Electron. Lett. **24**, 112 (1988(a)).

J.E. Zucker, T.L. Hendrickson and C.A. Burrus;
"Electro–optic phase modulation in GaAs/AlGaAs quantum well waveguides", Appl. Phys. Lett. **52**, 945 (1988(b)).

J.E. Zucker, I. Bar–Joseph, B.I. Miller and U. Koren;
"Quarternary quantum wells for electro–optic intensity and phases modulation", Appl. Phys. Lett. **54**, 10 (1989(a)).

J.E. Zucker, K.L. Jones, M.G. Young, B.I. Miller and U. Koren;
"Compact directional coupler switches using quantum well electrorefraction", Apl. Phys. Lett. **55**, 2280 (1989(b)).

J.E. Zucker, I. Bar–Joseph, B.I. Miller and U Koren;
"Miniature Mach–Zehnder InGaAsP quantum well waveguide interferometer for 1.3μm", IEEE Photonics Tech. Lett. **2**, 32 (1990).